

Radiation Dose and Diagnostic Accuracy in Pediatric Computed Tomography

by

Xiang Li

Medical Physics Graduate Program
Duke University

Date: _____

Approved:

Ehsan Samei, Ph.D., Supervisor

Donald P. Frush, M.D.

W. Paul Segars, Ph.D.

James G. Colsher, Ph.D.

Terry T. Yoshizumi, Ph.D.

G. Allan Johnson, Ph.D.

Dissertation submitted in partial fulfillment of
the requirements for the degree of Doctor of Philosophy in the
Medical Physics Graduate Program in the Graduate School
of Duke University

2010

ABSTRACT

Radiation Dose and Diagnostic Accuracy in Pediatric Computed Tomography

by

Xiang Li

Medical Physics Graduate Program
Duke University

Date: _____

Approved:

Ehsan Samei, Ph.D., Supervisor

Donald P. Frush, M.D.

W. Paul Segars, Ph.D.

James G. Colsher, Ph.D.

Terry T. Yoshizumi, Ph.D.

G. Allan Johnson, Ph.D.

An abstract of a dissertation submitted in partial
fulfillment of the requirements for the degree
of Doctor of Philosophy in the
Medical Physics Graduate Program in the Graduate School
of Duke University

2010

Copyright by
Xiang Li
2010

Abstract

Since its inception in the 1970's, computed tomography (CT) has revolutionized the practice of medicine and evolved into an essential tool for diagnosing numerous diseases not only in adults but also in children. The clinical utility of CT examinations has led to a rapid expansion in CT use and a corresponding increase in the radiation burden to patients. CT radiation is of particular concern to children, whose rapidly growing tissues are more susceptible to radiation-induced cancer and who have longer life spans during which cancerous changes might occur. In recent years, the increasing awareness of CT radiation risk to children has brought about growing efforts to reduce CT dose to the pediatric population. The key element of all dose reduction efforts is to reduce radiation dose while maintaining diagnostic accuracy. Substantiating the tradeoff between the two is the motivation behind this dissertation work.

The first part of this dissertation involved the development of an accurate method for estimating patient-specific radiation dose and potential cancer risk from CT examinations. A Monte Carlo program was developed and validated for dose simulation in a state-of-the-art CT system. Combined with realistic computer models of patients created from clinical CT data, the program was applied to estimate patient-specific dose from pediatric chest and abdomen-pelvic CT examinations and to investigate the dose variation across patients due to the variability of patient anatomy and body habitus. The

Monte Carlo method was further employed to investigate the effects of patient size and scan parameters on dose and risk for the entire pediatric population.

The second part of this dissertation involved the development of tools needed to study the diagnostic accuracy of small lung nodules on pediatric CT images. A prior method for modeling two-dimensional symmetric liver/lung lesions was extended to create three-dimensional nodules with asymmetric shapes and diffused margins. A method was also developed to estimate quantum noise in the lung region of a CT image based on patient size.

The last part of this dissertation involved assessment of diagnostic accuracy using receiver operating characteristic (ROC) observer experiments. A pilot study of 13 pediatric patients (1-7 years old) was first conducted to evaluate the effect of tube current on diagnostic accuracy, as measured by the area under the ROC curve (A_z). A study of 30 pediatric patients (0-15 years old) was then conducted to assess protocol- and scanner-independent relationships between image quality (nodule detectability and noise) and diagnostic accuracy. The relationships between diagnostic accuracy and nodule detectability, between noise and scan parameters, and between dose/risk and scan parameters were lastly combined to yield the relationship between diagnostic accuracy and dose/risk.

For pediatric patients in the same weight/protocol group, organ dose variation across patients was found to be generally small for large organs in the scan coverage (< 10%), larger for small organs in the scan coverage (1-18%), and the largest for organs partially or completely outside the scan coverage (6-77%). Across the entire pediatric population, dose and risk associated with a chest scan protocol decreased exponentially with increasing patient size. The average chest diameter was found to be a stronger predictor of dose and risk than weight and total scan length.

The effects of bowtie filter and beam collimation on dose and risk were small compared to the effects of helical pitch and tube potential. The effects of any scan parameter were patient size-dependent, which could not be reflected by the difference in volume-weighted CT dose index ($CTDI_{vol}$).

Over a nodule detectability (product of nodule peak contrast and display diameter to noise ratio or $CDNR_{display}$) range of approximately 52-374 mm with an average of 143 mm, tube current or dose had a weak effect on the diagnostic accuracy of lung nodules. The effect of 75% dose reduction was comparable to inter-observer variability, suggesting a potential for dose reduction.

Diagnostic accuracy increased with increasing nodule detectability over the range of 25-374 mm, but reached a plateau beyond a threshold of ~ 99 mm. The trend was analogous to the relationship between A_z and signal-to-noise ratio and suggested

that the performance of the radiologists saturates (or increases slowly) beyond a threshold nodule detectability level; further reducing noise or increasing contrast to improve nodule detectability beyond the threshold yields little gain in diagnostic accuracy.

For a typical product of nodule contrast and physical diameter (1400 HU·mm) and a set of most commonly used scan parameters (tube potential of 120 kVp, helical pitch of 1.375, slice thickness of 5 mm, gantry rotation period of 0.4 second, image pixel size of 0.48 mm), diagnostic accuracy increased with effective dose and effective risk for a given patient size, but reached a plateau beyond a threshold dose/risk level. At a given effective dose, A_z increased with decreasing patient size, i.e., the dose needed to achieve the same noise and hence diagnostic accuracy increased with patient size. To achieve an A_z of 0.90, the dose needed for a 22-cm diameter (male) patient was about quadruple of that for a 10-cm diameter patient. While the effective risk associated with achieving the same diagnostic accuracy also increased with patient size, the risk associated with an A_z of 0.90 was only twice as high for a 22-cm diameter (male) patient than for a 10-cm diameter patient due to the older age of the larger patient.

The research in this dissertation has two important clinical implications. First, the quantitative relationships between patient dose/risk and patient size, between patient dose/risk and scan parameters, between diagnostic accuracy and image quality, and

between diagnostic accuracy and radiation dose can guide the design of pediatric CT protocols to achieve the desired diagnostic accuracy at the minimum radiation dose. Second, patient-specific dose and risk information, when included in a patient's dosimetry and medical records, can inform healthcare providers of prior radiation exposure and aid in decisions for image utilization, including the situation where multiple examinations are being considered.

In memory of my beloved mother, Yumei Zhang
To my father, Baolin Li, and my husband, Gang Lu

Contents

Abstract	iv
List of Tables.....	xvii
List of Figures	xxi
Acknowledgements	xxviii
1. Introduction	1
1.1 Clinical Benefits and Radiation Risk.....	1
1.2 Radiation Dose Estimation.....	3
1.3 Influence of Dose Reduction on Diagnostic Accuracy	5
1.4 Design and Objectives of the Dissertation	7
Part I: Radiation Dose Studies.....	9
2. A Monte Carlo Method for Estimating Patient-Specific Radiation Dose and Cancer Risk in CT.....	9
2.1 Introduction.....	9
2.2 Materials and Methods	11
2.2.1 CT Scanner.....	11
2.2.2 CT System Modeling.....	12
2.2.2.1 Analytical simulation of X-ray energy spectra	12
2.2.2.2 Monte Carlo simulation of radiation transport	13
2.2.3 Effective Beam Width Measurements	16
2.2.4 Dose Measurements	17

2.2.4.1	Dose measurements in air.....	18
2.2.4.2	Dose measurements in a cylindrical phantom.....	18
2.2.4.3	Dose measurements in anthropomorphic phantoms	20
2.2.5	Dose Simulations	22
2.2.5.1	Dose simulations in the air and in the cylindrical phantom.....	22
2.2.5.2	Dose simulations in the anthropomorphic phantoms	26
2.2.6	Patient-Specific Dose and Risk Estimation	28
2.2.6.1	Patients	28
2.2.6.2	Patient-specific computer models.....	29
2.2.6.3	Organ dose simulations	32
2.2.6.4	Effective dose and effective risk calculations.....	34
2.3	Results	36
2.3.1	In-Air Results	36
2.3.2	Effective Beam Width Results.....	37
2.3.3	Cylindrical-Phantom Results.....	38
2.3.4	Anthropomorphic-Phantom Results	39
2.3.5	Patient-Specific Dose and Risk Results	43
2.4	Discussions	46
3.	Patient-Specific Dose Estimation for Pediatric Chest CT	52
3.1	Introduction.....	52
3.2	Materials and Methods.....	53
3.2.1	Patients.....	53

3.2.2 Patient-Specific Computer Models	54
3.2.3 Monte Carlo Simulations.....	59
3.2.4 Effective Dose Calculations.....	61
3.2.5 Data Analysis	61
3.3 Results	62
3.4 Discussions	67
4. Patient-Specific Dose Estimation for Pediatric Abdomen-Pelvis CT.....	70
4.1 Introduction.....	70
4.2 Materials and Methods	71
4.2.1 Patients.....	71
4.2.2 Patient-Specific Computer Models	71
4.2.3 Monte Carlo Simulations.....	72
4.2.4 Effective Dose Calculations.....	73
4.2.5 Data Analysis	74
4.3 Results	74
4.4 Discussions	79
5. Patient-Specific Radiation Dose and Cancer Risk in Pediatric Chest CT: A Systematic Evaluation of the Effects of Patient Size and Scan Parameters.....	82
5.1 Introduction.....	82
5.2 Materials and Methods	83
5.2.1 Patients.....	83
5.2.2 Patient-Specific Computer Models	84

5.2.3 CT Scanner and Protocols	85
5.2.4 Radiation Dose and Cancer Risk Estimations	86
5.2.5 Data Analysis	88
5.3 Results	89
5.3.1 Effects of Patient Size	89
5.3.2 Effects of Scan Parameters.....	109
5.4 Discussions	113
Part II: Tool Development.....	120
6. Three-Dimensional Simulation of Lung Nodules for Pediatric Multidetector Array CT	120
6.1 Introduction.....	120
6.2 Materials and Methods	121
6.2.1 Image Selection.....	121
6.2.2 Nodule Characterization	122
6.2.3 Nodule Simulation Method	124
6.2.4 Comparison between Real and Simulated Nodules: Physical Characteristics	128
6.2.5 Comparison between Real and Simulated Nodules: Observer Experiment...	131
6.3 Results	134
6.3.1 Physical Characteristics	134
6.3.2 Observer Experiment	137
6.4 Discussions	141
7. Comparison of Patient Size Based Methods for Estimating Quantum Noise in CT Images of the Lung	146

7.1 Introduction.....	146
7.2 Materials and Methods.....	147
7.2.1 Noise-Diameter Relationship in Water Phantoms.....	147
7.2.2 Noise in the Lung Measured Using Image-Subtraction Method.....	150
7.2.3 Noise in the Lung Estimated Using Patient Size Based Methods	151
7.3 Results	155
7.3 Discussions	157
Part III: Diagnostic Accuracy Studies.....	160
8. Pediatric MDCT: Towards Assessing the Diagnostic Influence of Dose Reduction on the Detection of Small Lung Nodules	160
8.1 Introduction.....	160
8.2 Materials and Methods	162
8.2.1 Clinical Cases	162
8.2.2 Noise Simulation	163
8.2.3 Nodule Simulation	168
8.2.4 Observer Experiment.....	169
8.2.5 Data Analysis	170
8.3 Results	171
8.3.1 Evaluation and Calibration of Noise Addition Software	171
8.3.2 Observer Experiment.....	176
8.4 Discussions	177
9. Lung Nodule Detection in Pediatric CT: Quantitative Relationship between Image Quality and Radiologist Performance.....	182

9.1 Introduction.....	182
9.2 Materials and Methods.....	183
9.2.1 Clinical Cases	184
9.2.2 Noise Simulation	184
9.2.3 Nodule Simulation	188
9.2.4 Observer Experiment.....	190
9.2.5 Data Analysis	191
9.2.5.1 Relationship between nodule detectability and diagnostic accuracy.....	192
9.2.5.2 Effect of location in the lung.....	195
9.2.5.3 Relationship between noise and diagnostic accuracy.....	195
9.3 Results.....	196
9.3.1 Extended Calibration of Noise Addition Software.....	196
9.3.2 Relationship between Image Quality and Diagnostic Accuracy	198
9.4 Discussions	201
10. Lung Nodule Detection in Pediatric CT: the Tradeoff between Diagnostic Accuracy and Radiation Dose or Cancer Risk.....	206
10.1 Introduction.....	206
10.2 Materials and Methods.....	207
10.3 Results	211
10.4 Discussions	213
11. Conclusions, Implications, and Future Directions.....	217
11.1 Summary and Conclusions	217

11.2 Clinical Implications	222
11.3 Future Directions	222
References	226
Biography	243

List of Tables

Table 1: Scan protocols used to collect TLD dose measurements from the pediatric one-year-old and the adult female phantoms.....	22
Table 2: Simulation parameters and variance reduction techniques used for dose simulations in the air and the cylindrical phantom.	24
Table 3: CT examinations undergone by the two patients in our study. Each patient underwent a combined chest-abdomen-pelvis (CAP) examination consisting of a chest scan and an abdomen-pelvis scan.	29
Table 4: Summary of organs in the computer models of the two patients.	30
Table 5: Measured and simulated in-air dose at the isocenter of the LightSpeed VCT scanner for single axial scans. Error figures reflect one standard deviation.	36
Table 6: Effective beam widths measured for both focal spot sizes and for three most commonly used collimation settings.....	38
Table 7: Summary of discrepancies between simulated and measured dose in the cylindrical and anthropomorphic phantoms.	39
Table 8: Organ and effective dose of the two patients from their CT examinations. Each patient underwent a combined chest-abdomen-pelvis (CAP) examination consisting of a chest scan and an abdomen-pelvis scan.	43
Table 9: Lifetime risks of cancer incidence for the two patients attributable to their CT examinations. Each patient underwent a combined chest-abdomen-pelvis (CAP) examination consisting of a chest scan and an abdomen-pelvis scan.	45
Table 10: Comparison between volume-weighted CT dose index ($CTDI_{vol}$) and patient-specific organ dose, and comparison between effective dose derived from DLP and effective dose estimated using patient-specific organ dose values.....	45
Table 11: Summary of organs included in the computer models of the seven pediatric patients.	56

Table 12: Variations across patients in normalized organ dose from chest MDCT scan and correlations of normalized organ dose with chest size and organ volume for selected organs.	64
Table 13: Variations across patients in normalized organ dose from an abdomen-pelvis MDCT scan and correlations of normalized organ dose with abdominopelvic size.	77
Table 14: CT protocols investigated in this study.	85
Table 15: Body size indices and their correlations with average chest diameter.....	89
Table 16: Protocol A (120 kVp, pediatric body scan FOV, small bowtie filter, 1.375 pitch, 40 mm collimation): correlations of organ dose, effective dose, cancer risk to individual organs, and effective risk with three body size indices: average chest diameter, total scan length (a surrogate for chest height), and weight, and the results of exponential fits $y = \exp(ax + b)$ to the relationships between dose/risk estimates and average chest diameter.....	94
Table 17: Protocol B (120 kVp, medium body scan FOV, medium bowtie filter, 1.375 pitch, 40 mm collimation): correlations of organ dose, effective dose, cancer risk to individual organs, and effective risk with three body size indices: average chest diameter, total scan length (a surrogate for chest height), and weight, and the results of exponential fits $y = \exp(ax + b)$ to the relationships between dose/risk estimates and average chest diameter.....	96
Table 18: Protocol C (120 kVp, large body scan FOV, large bowtie filter, 1.375 pitch, 40 mm collimation): correlations of organ dose, effective dose, cancer risk to individual organs, and effective risk with three body size indices: average chest diameter, total scan length (a surrogate for chest height), and weight, and the results of exponential fits $y = \exp(ax + b)$ to the relationships between dose/risk estimates and average chest diameter.....	98
Table 19: Protocol D (120 kVp, pediatric body scan FOV, small bowtie filter, 1.375 pitch, 20 mm collimation): correlations of organ dose, effective dose, cancer risk to individual organs, and effective risk with three body size indices: average chest diameter, total scan length (a surrogate for chest height), and weight, and the results of exponential fits $y = \exp(ax + b)$ to the relationships between dose/risk estimates and average chest diameter.....	100

Table 20: Protocol E (120 kVp, pediatric body scan FOV, small bowtie filter, 0.984 pitch, 40 mm collimation): correlations of organ dose, effective dose, cancer risk to individual organs, and effective risk with three body size indices: average chest diameter, total scan length (a surrogate for chest height), and weight, and the results of exponential fits $y = \exp(ax + b)$ to the relationships between dose/risk estimates and average chest diameter.....	102
Table 21: Protocol F (80 kVp, pediatric body scan FOV, small bowtie filter, 1.375 pitch, 40 mm collimation): correlations of organ dose, effective dose, cancer risk to individual organs, and effective risk with three body size indices: average chest diameter, total scan length (a surrogate for chest height), and weight, and the results of exponential fits $y = \exp(ax + b)$ to the relationships between dose/risk estimates and average chest diameter.....	104
Table 22: Protocol G (100 kVp, pediatric body scan FOV, small bowtie filter, 1.375 pitch, 40 mm collimation): correlations of organ dose, effective dose, cancer risk to individual organs, and effective risk with three body size indices: average chest diameter, total scan length (a surrogate for chest height), and weight, and the results of exponential fits $y = \exp(ax + b)$ to the relationships between dose/risk estimates and average chest diameter.....	106
Table 23: Protocol H (140 kVp, pediatric body scan FOV, small bowtie filter, 1.375 pitch, 40 mm collimation): correlations of organ dose, effective dose, cancer risk to individual organs, and effective risk with three body size indices: average chest diameter, total scan length (a surrogate for chest height), and weight, and the results of exponential fits $y = \exp(ax + b)$ to the relationships between dose/risk estimates and average chest diameter.....	108
Table 24: Summary of <i>t</i> -test results for comparing real and simulated nodule masks in terms of shape and contrast profile irregularities	137
Table 25: Summary of <i>t</i> -test results for comparing real and simulated nodule scores...	139
Table 26: Scan parameters used to acquire noise images from six water phantoms.....	149
Table 27: Coefficients of polynomial equation describing the relationship between quantum noise and diameter in water phantoms on a LightSpeed VCT scanner.....	154
Table 28: Scan parameters used to acquire images from six water phantoms*.....	165

Table 29: Minimum tube-current-time product (mAs)*	174
Table 30: Coefficients of polynomial equations (27) and (28) describing real and simulated noise in images of water phantoms as functions of phantom diameter and tube current.....	175
Table 31: Areas under the ROC Curves ($AUC \pm 0.02$).	177
Table 32: Scan parameters used to acquire images of the water phantoms.	186
Table 33: Coefficients of polynomial Equations (29) and (30) describing real and simulated noise in images of the water phantoms as functions of phantom diameter and tube current-time product (mAs).....	197
Table 34: A_z and associated errors as a function of $CDNR_{display}$, and results of testing the statistical significance of difference between $CDNR_{display}$ bins.....	199
Table 35: A_z and associated errors as a function of location in the lung, and results of testing the statistical significance of difference between lung zones.	199

List of Figures

Figure 1: Lifetime attributable risks of cancer incidence tabulated in BEIR VII report ¹⁴ . Risks for lung cancer and all cancers are shown to illustrate the strong dependence of risk on age and gender.	10
Figure 2: (a) A point source and an effective beam width were used in the simulations to account for the dose delivered by both the umbra and the penumbra regions of the beam. (b) The fan beam was chosen to be just broad enough to cover the imaging object. A pseudo impact detector was added below the bowtie filter at the level of the tungsten cam collimators to register the information of each incident particle in a phase-space file for use in the subsequent simulations of axial and helical scans.	14
Figure 3: (a) Custom-designed CT dose phantom for measuring center-to-periphery dose distributions. The locations of the seven drill holes are numbered. (b) Measurements of dose distribution in the custom-designed phantom. The phantom was attached to one end of the CT table and positioned so that its long axis matched the axis of gantry rotation.	19
Figure 4: Dose measurements in (a) pediatric one-year-old CIRS phantom and (b) adult female CIRS phantom. (c) The phantoms were composed of axially sliced, 25 mm thick, contiguous sections. Each section contained one or more 5 mm diameter through-holes at various organ locations.	20
Figure 5: Model of the ion chamber (model 10×5-0.18/9015, Radcal Corporation, Monrovia, CA) used in the Monte Carlo simulations. “C552” here refers to C552 air-equivalent plastic. Material data file for polyoxymethylene was used for the polyacetal cap.	23
Figure 6: Simulated X-ray energy spectra at the exit of the X-ray tube and before filtration by the bowtie filter (pre-bowtie spectra).	37
Figure 7: Measured and simulated dose distributions in the custom-designed cylindrical phantom for single axial scans at four kVp values using the (a) small, (b) medium, and (c) large bowtie filters and a 40-mm beam collimation. Simulated dose values are shown by lines. Measured dose values are shown by symbols, and their error bars reflect one standard deviation. Most error bars are too small to appreciate.	39

Figure 8: Measured and simulated dose from a single axial scan in (a) the pediatric and (b) the adult female phantoms. Error bars reflect one standard deviation. Percent discrepancies between simulation and measurement are labeled on the bottom. 40

Figure 9: Measured and simulated dose from (a) a full-body helical scan in the pediatric phantom and (b) a chest scan in the adult female phantom. Error bars reflect one standard deviation. The degrees are X-ray tube start angles relative to 12 o'clock. Percent discrepancies between simulation (averaged over tube starting angles) and measurement are labeled on the bottom. At four organ locations in the adult female phantom, one of the two TLD chips was cracked during the experiment; dose uncertainty could not be assessed for these four locations. 41

Figure 10: Coronal dose distributions in the two patients, resultant from their CT examinations: (a) chest scan of the newborn patient, (b) abdomen-pelvis scan of the newborn patient, (c) chest scan of the teenager patient, and (d) abdomen-pelvis scan of the teenager patient. The coronal plane was taken about half-way in between the anterior and posterior surfaces of each patient. The computer model of each patient with organs shown on a gray scale was overlaid with a semi-transparent colored image of the dose distribution. The noise in the dose distribution is reflective of the limited number of photos used in the simulations. As organ dose was an average over the entire organ volume, the uncertainty associated with organ dose was less than 1% for all organs in the scan coverage and less than 3% for other organs (see Section 2.2.6.3)..... 42

Figure 11: Surface rendered views of the three-dimensional anatomy in the computer models of the youngest (16 months old) and the oldest (6 years old) patients in our study. 58

Figure 12: Coronal dose distributions in three 2-year-old patients, determined from the chest MDCT scan. The coronal plane was taken about half-way in between the anterior and posterior surfaces of each patient. The computer model of each patient with organs shown on a gray scale was overlaid with a semi-transparent colored image of the normalized dose distribution. 63

Figure 13: Normalized absorbed dose (mGy/100mAs) to the lung and the heart from the chest MDCT scan as a function of mid-chest equivalent diameter and the results of regression analysis. The mid-chest equivalent diameter was defined as the diameter of a circle having the same area as the mid-chest (half-way between lung apex and lung base) area of the patient model. 65

Figure 14: Normalized effective dose (mSv/100mAs) from the chest MDCT scan as a function of patient model weight and the result of regression analysis. Because the weights of the patient models were not perfectly matched to the actual patient weights (discrepancy < 5 kg), the weights of the patient models were used here for the regression analysis. 66

Figure 15: Coronal dose distribution in a 2-year-old patient, determined from the abdomen-pelvis MDCT scan. The coronal plane was taken about half-way in between the anterior and posterior surfaces of the abdominopelvic region of the patient. The computer model of the patient with organs shown on a gray scale was overlaid with a semi-transparent image of the normalized dose distribution on a colored scale. The patient's arms are out of this coronal plane. 76

Figure 16: (a) Normalized absorbed dose (mGy/100mAs) to the kidney and the adrenal gland from the abdomen-pelvis MDCT scan as a function of mid-liver equivalent diameter and the results of regression analysis. (b) Normalized absorbed dose (mGy/100mAs) to the small intestine from the abdomen-pelvis MDCT scan as a function of mid-intestine equivalent diameter and the result of regression analysis. The mid-liver/mid-intestine equivalent diameter was defined as the diameter of a circle having the same area as the cross-sectional area of the patient model on the plane halfway in between the inferior and posterior ends of the liver/small intestine. 78

Figure 17: Normalized effective dose (mSv/100mAs) from the abdomen-pelvis MDCT scan as a function of patient model weight and the result of regression analysis. The weights of the patient models were not perfectly matched to the actual patient weights (discrepancy < 5 kg). The weights of the patient models were used here for the regression analysis. 79

Figure 18: Examples of normalized dose to individual organs, resultant from Protocol A, as a function of average chest diameter for (a) large organs and centrally-located tubular organs inside the chest scan coverage, (b) small organs inside the chest scan coverage, (c) organs on the periphery or outside the chest scan coverage, and (d) distributed organs. The symbols represent dose to the organs of individual patients. The lines are exponential fits $y = \exp(ax + b)$ to the data. The quantity r is the Pearson sample correlation coefficient. 91

Figure 19: Examples of normalized cancer risk to individual organs, resultant from Protocol A, as a function of average chest diameter for (a) large organs inside the chest scan coverage, (b) small organs inside the chest scan coverage, (c) organs on the periphery or outside the chest scan coverage, and (d) distributed organs. Risk of colon

cancer was assessed using dose to the large intestine, and risk of leukemia was assessed using dose to the red bone marrow. The symbols represent the risks of individual patients. The lines are exponential fits $y = \exp(ax + b)$ to the data. The quantity r is the Pearson sample correlation coefficient. 92

Figure 20: Normalized effective dose and effective risk, resultant from Protocol A. The symbols represent effective dose and effective risk estimated for individual patients. The lines are exponential fits $y = \exp(ax + b)$ to the data. The quantity r is the Pearson sample correlation coefficient. 93

Figure 21: Effects of scan parameters (bowtie filter, collimation, helical pitch, and peak tube potential) on radiation dose and cancer risk, using lung dose, large intestine dose, effective dose (male), and effective risk (male) as examples. The error bar on each curve reflects the root-mean-square of the residuals associated with the exponential fit; it represents the average discrepancy between dose/risk values predicted by the fitting function and the dose/risk results estimated by the Monte Carlo method. Volume-weighted CTDI ($CTDI_{vol}$) were shown for comparison. The letters A-H refer to Protocols A-H..... 112

Figure 22: Three-dimensional characteristics of small lung nodules on pediatric MDCT images as exemplified by a nodule in our study. The nodule was clearly visible on 3 contiguous CT slices with slice thickness of 5 mm and reconstruction interval of 2.5 mm. The regions of interest (ROIs) are 30 mm in size with the nodule located centrally..... 122

Figure 23: A variety of nodule appearances existed as exemplified by 18 real nodules in our study. Only the central slice of each nodule is shown. All ROIs are 20 mm in size with nodules located centrally. 123

Figure 24: (a) For a 3-D nodule with diameter $2R_o$ of 6 mm, its radii on a 5-mm thick CT slice are 3, 3, and 2.83 mm for the vertical (z -direction) locations 1, 2, and 3, respectively. Assuming the peak contrast of the nodule to be proportional to its diameter subtended by the CT slice and defining its peak contrast at vertical locate on 1 as C_o , its peak contrasts at vertical locations 2 and 3 are $4C_o/5$ and $2C_o/5$, respectively. When changing reconstruction interval from (b) half of the slice thickness to (c) one slice thickness, the occupation and the appearance of a nodule on contiguous CT slices also change. 124

Figure 25: An example simulated (single-component) nodule in three dimensions. The nodule was simulated with $2R_o = 5$ mm and $C_o = 350$ HU on 5 contiguous CT slices with slice thickness of 5 mm and reconstruction interval of 2.5 mm. All ROIs are 30 mm in size with the nodule located centrally. 128

Figure 26: Examples of simulated nodules used in the observer experiment: the central slices of (a) 18 single-component and (b) 18 double-component nodules. All ROIs are 20 mm in size with nodules located centrally..... 132

Figure 27: Sample results of curve fitting performed for normalized contrast profiles of 20 real nodule masks. Contrast profiles are represented by symbols, and their fits to Equation (22) are represented by solid lines. All R' , $R^{(1)}$, and $R^{(2)}$ values are in the unit of mm. (a) An excellent fit with small residues. (b) Another excellent fit, where the general trend of the contrast profile was well described by Equation (22), despite the relatively large residues. (b) is also an example fit that yielded large R' and n' values. The corresponding $R'_{0.05}$ and η values were 3.3 mm and 2.1, respectively, more suitable to describe the visual radius and steepness of this contrast profile than the original R' and n' values. (c) and (d) are two examples of not excellent, but acceptable fits to Equation (22). Excellent fits, however, were obtained when fitting these two contrast profiles to the double-component version of Equation (22), as demonstrated by the thick dashed lines. 135

Figure 28: Scatter plots of visual steepness (inversely related to η) versus visual radius $R'_{0.05}$ for real, simulated single-component (SSC), and simulated double-component (SDC) nodule masks. 136

Figure 29: Results of ROC analysis. Simulated nodules were defined as positive cases; true-positive fraction (TPF) was the likelihood of a simulated nodule being identified as simulated, while false-positive fraction (FPF) was the likelihood of a real nodule being identified as simulated. Error figures refer to standard errors. 138

Figure 30: Results of equivalence tests based on confidence intervals of the differences in population mean score between simulated and real nodules ($\Delta\bar{\mu} = \bar{\mu}_{\text{simulated}} - \bar{\mu}_{\text{real}}$). The zone of equivalence was defined as $<\sigma(x_{\text{real}})>_{\text{observer}}$, the standard deviation of real nodule scores averaged across observers. 140

Figure 31: Histograms of score assignments for (a) observer 1, (b) observer 2, (c) observer 3, and (d) observer 4. Scores of 100 were included in the last bin of each histogram. 140

Figure 32: Six water phantoms representing body size ranging from infant, to adolescent, to young adult: (a) five custom-built phantoms with diameters of 12.7, 15.3, 17.8, 23.3, and 27.0 cm, and (b) 20-cm-diameter GE quality-assurance water phantom. 148

Figure 33: (a) A CT slice from the chest section of the anthropomorphic phantom acquired at 95 mA. (b) The noise map of (a) obtained by subtracting two copies of (a) and dividing the subtraction image by $\sqrt{2}$. Standard deviations of pixel values within six 50-pixel-diameter ROIs evenly distributed in the lung region were averaged to yield a single noise figure for the CT slice..... 151

Figure 34: Quantum noise in the lung measured using the image-subtraction method from the 28 contiguous CT slices of the anthropomorphic phantom’s chest section at 95 and 20 mA. The error bar reflects the standard deviation of the six measurements on each CT slice. The distance to lung apex was calculated as the z-distance between a given CT slice and the CT slice associated with the most superior position of the lung. 155

Figure 35: Four definitions of patient size calculated for the 28 contiguous CT slices of the anthropomorphic phantom’s chest section, including water-equivalent diameters derived from chest area ($d_w^{(CA)}$), water-equivalent area ($d_w^{(WEA)}$), non-lung area ($d_w^{(NLA)}$), and water-equivalent path length ($d_w^{(WEPL)}$). The error bar on $d_w^{(WEPL)}$ reflects the standard deviation of the ten $d_w^{(WEPL)}$ ’s calculated for each CT slice. The distance to lung apex was calculated as the z-distance between a given CT slice and the CT slice associated with the most superior position of the lung..... 156

Figure 36: Accuracies of quantum noise in the lung estimated by $d_w^{(CA)}$, $d_w^{(WEA)}$, $d_w^{(NLA)}$, and $d_w^{(WEPL)}$ for the 28 contiguous CT slices of the anthropomorphic phantom’s chest section at (a) 95-mA and (b) 20-mA scans. Errors of $\pm 30\%$, the magnitude of noise variation across the lung volume, are indicated by thick dashed lines. 157

Figure 37: Diagram showing the preparation of image samples used for the ROC observer experiment. 169

Figure 38: Noise texture of (a) real (small bowtie filter, 120 kVp, 60 mA) and (b) simulated (small bowtie filter, 120 kVp, nominal simulation tube current of 60 mA, simulated from an actual image acquired at 200 mA) CT images of the 20-cm water phantom. A 64-pixel ROI from the center of each image was blew up by 4 times and displayed at the lower right hand corner of each image to allow a close view of the noise texture. (c) Normalized noise power spectra (NNPS) of real and simulated CT images of the 20-cm water phantom acquired using the small bowtie filter at tube potential of 120 kVp and tube current of 100 mA. The NNPS were further normalized relative to their respective peak values in order to compare spectral shapes. The spectral shapes of NNPS at other kVp and mA settings were similar. 172

Figure 39: (a) Average CT number as a function of mAs measured from real images of the 20-cm water phantom at 80 kVp and 140 kVp for the small, medium and large bowtie filters. The average CT number was calculated as the average of mean pixel values within central ROIs of the selected CT slices. (b) An image of the 20-cm water phantom acquired at 80 kVp and 4 mAs (i.e. 10 mA, 0.4-second gantry rotation period) using the medium bowtie filter. Severe photon starvation caused a shift in CT number of ~ 40 HU at the center of the image which would otherwise look uniform as in Figure 38. 173

Figure 40: ROC curves for (a) observer 1, (b) observer 2, and (c) observer 3 at three nominal tube current (dose) levels: 70 mA, 35 mA, and 17.5 mA..... 176

Figure 41: Diagram showing the preparation of image samples used in the ROC observer experiment. Because nodule locations and characteristics (size, shape, and contrast) were randomized, the nodules in any series were different from the nodules in any other series within a patient or cross patients..... 189

Figure 42: Diagnostic accuracy, A_z , as a function of nodule detectability, $CDNR_{display}$ 198

Figure 43: Diagnostic accuracy, A_z , as a function of noise for (a) a nodule with a diameter of 4 mm and a peak contrast of 200-500 HU and (b) a nodule with a peak contrast of 350 HU and a diameter of 3-5 mm..... 200

Figure 44: The relationship between average non-lung area diameter $d_w^{(NLA)}$ and average chest diameter d 212

Figure 45: For the detection of lung nodules with a typical contrast-diameter product of 1400 HU·mm, diagnostic accuracy A_z as a function of (a) effective dose and (b) effective risk of male patients from a chest examination. The chest examination employed tube potential of 120 kVp, helical pitch of 1.375, slice thickness of 5 mm, and gantry rotation period of 0.4 second. A typical pixel size of 0.48 mm was assumed. The effects of bowtie filter and collimation on dose and risk were assumed to be small¹⁶⁴. 212

Acknowledgements

I owe my deepest gratitude to my advisor, Dr. Ehsan Samei, who has been an extremely supportive and caring mentor to me over the past four years and has taught me every aspect of being an imaging researcher, from strategic thinking and effective writing to productive collaboration and viewing every obstacle in a positive light. My deepest gratitude also goes to Dr. Donald Frush, my co-advisor, who has taught me abundantly about the clinical aspects of CT imaging and has always offered me critical guidance and thorough reviews of my work. I am also deeply indebted to the other professors on my PhD committee. I am grateful to Dr. James Colsher for teaching me amply about the physics and engineering aspects of CT and for inspiring me with his enthusiasm for work even after his retirement. My deep appreciation is also due to Dr. Paul Segars, who has been incredibly patient and tireless in addressing my requests and giving me support. I am extremely thankful to Dr. Terry Yoshizumi for teaching me the fundamentals of radiation dosimetry and for helping me tremendously with experimental measurements from the beginning to the end of my project. Last but not least, I am grateful to Dr. Allan Johnson for his insightful guidance on the direction of the work.

I greatly appreciate the help received from many other mentors, colleagues, and friends at Duke University. The pediatric radiologists, Drs. Ana Maria Gaca, Caroline

Hollingsworth, Charles Maxfield, and Caroline Carrico spent many long hours participating in the observer studies. The experimental parts of the project were only possible with help from the following individuals: Greta Toncheva and Samuel Brady (who has recently become Dr. Brady!) of the Radiation Dosimetry Laboratory, Carolyn Lowry and Halaine Grubaugh of the Department of Radiology, Christina Shafer of the Biomedical Engineering Department, and Robert Jones and Matthew McCarthy of the School of Medicine. Sincere thanks are also due to all members of the Carl E. Ravin Advanced Imaging Laboratories for their constant help and support.

I dedicate this dissertation to my parents, Yumei Zhang and Baolin Li, who instilled in me the value of hard work and commitment, and to my husband, Gang Lu, who has always supported me with unconditional love, care, and encouragement.

1. Introduction

1.1 *Clinical Benefits and Radiation Risk*

Since its inception in the 1970s¹, computed tomography (CT) has surpassed projection radiography as the first imaging modality to picture the inner depth of human body in a slice-by-slice manner. With the advents of helical technology in the late 1980s²⁻⁴ and multi-detector array (MDCT) technology in the late 1990s, CT has demonstrated advantages over other imaging modalities, thanks to its sub-millimeter spatial resolution, sub-second gantry rotation time, and large anatomical coverage. The accuracy, speed, and versatility of CT examinations have been essential for the diagnosis of numerous diseases not only in adult but also in children. CT has proved of value for virtually the entire spectrum of pediatric thoracic disease⁵ and is the most frequently used imaging modality for evaluating abdominal disease of children⁶.

The clinical benefits of CT have led to a rapid increase in CT use. It is estimated that the annual number of CT examinations in the United States rose from 2.8 million in 1981⁷ to 20 million in 1995⁸, and to 62 million in 2006⁹. The estimated proportion of CT examinations in children increased from about 4% in 1989¹⁰, to an average of 6% in 1993¹¹, and to about 11% in 1999¹².

With this rapid increase in CT use comes great concern over CT radiation exposure. By its nature, CT delivers substantially higher radiation dose to the patient than conventional radiography. For a 5-year-old child, the radiation dose from a chest

CT scan is estimated to be equivalent to 150 chest radiography examinations¹³. Consequently, CT examinations pose substantially higher health risk to patients¹⁴, especially to children whose rapidly growing tissues are more susceptible to radiation-induced cancer and who have longer life spans during which cancerous changes might occur. An article in 2001¹⁵ estimated that of approximately 600,000 abdominal and head CT examinations annually performed in the United States in children under the age of 15 years, 500 individuals might ultimately die from cancer attributable to the CT radiation. A review article in 2007¹⁶ again emphasized the radiation risk from CT, particularly in children.

The increasing awareness of CT radiation risk to children has brought about efforts to reduce CT dose. The dose reduction efforts of healthcare providers (radiologists, medical physicists, and radiological technologists) have focused on the judicious choice of CT scan parameters, avoidance of unnecessary CT examinations, and the use of shielding for radiosensitive organs¹⁷. The dose reduction efforts of CT manufacturers (engineers and medical physicists) have focused on efficient use of X-ray beam (e.g., reducing over-beaming and over-ranging distances), proper design of X-ray filtration (e.g., bowtie filter design), implementation of automatic tube current modulation, and optimization of image reconstruction algorithms (e.g., iterative reconstruction method¹⁸ and noise reduction filter¹⁹). The key element of all dose reduction efforts is to reduce radiation dose while maintaining diagnostic accuracy.

Substantiating the tradeoff between the two is the motivation behind this dissertation work.

1.2 Radiation Dose Estimation

As a result of the aforementioned dose reduction efforts and the continuous advance of CT technology, CT scanning protocols and scanner designs have become increasingly complex, and there is a growing need to accurately estimate radiation dose from CT, not only for the purpose of assessing life-time cancer risk which can be useful during discussions with healthcare providers, parents, regulatory bodies, and ethics committees, but also for the purposes of comparing and optimizing CT technologies and scan protocols.

Currently, two types of dosimetric quantities are being used in CT. The first type is reference dose quantities: CT dose index (CTDI), weighted CT dose index (CTDI_w), volume-weighted CT dose index (CTDI_{vol}), and dose length product (DLP)²⁰. The reference dose quantities are based on measurements made within standard CT dose phantoms: polymethylmethacrylate (PMMA) cylinders with diameters of 32 cm (adult body) and 16 cm (adult head and pediatric body). The reference dose quantities are useful for comparing exposure levels of different CT protocols or scanners; however, they do not reflect the actual dose received by the patient and cannot be used to directly estimate cancer risk. The second type of dosimetric quantity is patient dose quantities: organ dose and effective dose. Organ dose refers to the mean absorbed dose received by

an organ of the patient and is directly related to the cancer risk of that organ¹⁴. Effective dose is the summation of organ dose values weighted by the relative radiosensitivity of the organs; it expresses the radiation detriment of a non-uniform exposure in terms of an equivalent whole body exposure²¹. Despite the recent debate on its concept²², effective dose has been and remains the most widely used dosimetric quantity related to the overall cancer risk of the patient.

Because it is impossible to measure organ dose directly from patients, three methods are currently being used to estimate organ and effective dose from CT examinations using patient phantoms/models. The first method is to measure organ dose within physical anthropomorphic phantoms using point dosimeters^{23, 24}. Though a direct approach, this method does not provide average organ dose values desired for the calculation of effective dose. The second method is to simulate organ dose using Monte Carlo radiation transport algorithms coupled with mathematical or voxelized models of patients²⁵⁻³². Compared with the first method, Monte Carlo based approach is more flexible; scan parameters currently not available on clinical CT scanners (e.g., an arbitrary pitch or tube potential) can be investigated. This approach can also be very accurate, provided that the simulation code is carefully benchmarked against experimental measurements³³⁻³⁵. Lastly, organ and effective dose has been estimated from CTDI or DLP using conversion coefficients derived from the first two methods^{23, 24, 36-38}. The common limitation of the current methods is that they are largely patient-

generic; phantoms/models have only been developed for standard/limited patient sizes at discrete ages (e.g., 0, 1, 5, 10, 15 years old) and do not reflect the variability of patient anatomy and body habitus. Therefore, dose information for individual patients is currently not available. Furthermore, current protocol designs rely on dose as a surrogate for risk of cancer incidence, neglecting the fact that the same dose delivered to two patients may entail substantially different risks due to age and gender differences.

1.3 Influence of Dose Reduction on Diagnostic Accuracy

When other scan parameters are kept constant, the noise variance in a CT image is inversely proportional to tube current and hence radiation dose to the patient³⁹. Therefore, dose reduction often comes at the expense of increased image noise. Because some clinical tasks (e.g., organ volume estimation) have more tolerance for increased noise than others (e.g., lesion detection), the influence of dose reduction on diagnostic accuracy cannot be addressed in a general sense and must be evaluated in terms of a chosen clinical task. The clinical task targeted by this dissertation was the detection of small lung nodules in pediatric patients.

Owing to the superior resolutions of modern MDCT, chest CT examination for the detection of lung nodules is often standard for pediatric cancer staging and surveillance. In such examinations, the presence of even one small lung nodule may have tremendous prognostic and therapeutic implications⁴⁰. Several previous studies on the pediatric population⁴¹⁻⁴³ have suggested that diagnostic-quality images of the lung

could be obtained at significantly reduced tube-current (dose) levels. However, those studies were preference-based; reduced-dose images were evaluated by assigning subjective image quality scores to known anatomical structures. Results of those studies do not necessarily reflect the actual performance of radiologists in terms of lung nodule detection at reduced dose levels. Performance-based evaluations have been hindered by three major challenges: (a) the occurrence of isolated small lung nodules in the pediatric population is low, making it difficult to research with real lung nodules, (b) ethical concerns prohibit repeated scans to be taken on the same patients at different dose levels, and (c) the performances of radiologists measured at multiple tube currents cannot be easily generalized to different scan protocols and CT scanner models.

The first challenge may be overcome by the simulation of lung nodules⁴⁴⁻⁴⁸. However, most prior studies on nodule simulation have not aimed to emulate the features of real lung nodules, validated by observer studies of nodule appearances. In two recent studies which have offered an exception^{46, 47}, the modeled nodule characteristics were typical of large (> 5 mm) nodules, a range that is larger than what would be subtle enough for most technique optimization studies in MDCT, particularly in pediatric applications⁴⁸. To overcome the second challenge, one may add noise to existing CT data to simulate reduced dose conditions⁴⁹⁻⁵⁶. However, most noise simulation techniques operate on raw projection data, which are cumbersome to store and transfer and often require scanner processors for image reconstruction. In addition,

prior techniques have not been validated in terms of both the magnitude and the texture of the simulated noise. To overcome the last challenge, one may assess the performances of the radiologists at multiple noise levels. However, it is often difficult to reliably and accurately measure the quantum noise in actual patient images due to the underlying anatomy (anatomic noise)⁵⁷.

1.4 Design and Objectives of the Dissertation

This dissertation addressed the relationship between diagnostic accuracy and radiation dose in pediatric CT in three parts.

The first part aimed to estimate patient-specific organ dose and cancer risk in pediatric CT. In Chapter 2, a Monte Carlo program was developed to model a state-of-the-art CT system. The accuracy of this program was validated against experimental measurements using cylindrical and anthropomorphic phantoms. As a demonstration of its utility, the program was used to estimate organ dose, effective dose, and risks of cancer incidence for CT examinations of two representative pediatric patients. The Monte Carlo program was subsequently applied to estimate organ and effective dose for chest (Chapter 3) and abdomen-pelvis (Chapter 4) examinations of seven pediatric patients in the same size group to investigate the dose variation across patients due to the variability of patient anatomy and body habitus. In Chapter 5, the effects of body size and scanner acquisition parameters on dose and risk estimates were systematically evaluated for the entire pediatric size range.

The second part aimed to develop software tools to address the challenges associated with performance-based studies. In Chapter 6, a technique was developed to simulate realistic small lung nodules in three dimensions on pediatric MDCT images and was validated in a receiver operating characteristic (ROC) observer experiment. In Chapter 7, a method was developed to estimate quantum noise in the lung region of CT images based on patient size.

The last part of this dissertation aimed to conduct ROC observer experiments to assess the diagnostic accuracy of radiologists in detecting small lung nodules. A proprietary noise addition software tool, which adds noise directly to reconstructed CT images, was evaluated and calibrated in terms of both noise texture and magnitude. Combined with the nodule simulation technique and the noise estimation method, images simulated at reduced tube currents (with increased noise) were used to evaluate the effect of tube current (Chapter 8) and image quality (Chapter 9), including nodule detectability and noise, on the performance of radiologists. The relationship between nodule detectability and diagnostic accuracy, between noise and scan parameters, and between dose/risk and scan parameters were lastly combined to yield a generalizable relationship between diagnostic accuracy and dose/risk (Chapter 10).

Part I: Radiation Dose Studies

2. A Monte Carlo Method for Estimating Patient-Specific Radiation Dose and Cancer Risk in CT*

2.1 Introduction

Computed tomography (CT) is the single largest source of medical radiation exposure to the US population, constituting half of the total medical exposure in 2006⁵⁸. The last few years have witnessed growing societal efforts to manage radiation dose in CT, particularly efforts to adapt CT scanning technique to patient sizes^{20, 59, 60}. These efforts can greatly benefit from a dose-reporting system that provides radiation dose and potential cancer risk estimates that are specific to each patient and each CT scan. Such a system could serve as the basis for individualized protocol design and optimization. For patients who undergo sequential examinations over an extended period of time, knowledge of dose and risk could also aid in deciding the necessity and frequency of examinations. Moreover, as there is an increasing call for radiation dose tracking from medical examinations and procedures^{61, 62}, patient-specific dose and risk estimations could offer an additional opportunity to be accountable for serial examinations.

The current dose-reporting method, however, is patient-generic; a patient's dosimetry report only includes reference dose quantities such as CT dose index (CTDI)⁶³ measured in a standard-size cylindrical phantom (e.g., 32-cm diameter phantom for

* This chapter is based on a manuscript with the same title submitted to the journal *Medical Physics*.

adult body). While a myriad of physical^{24, 64} and computerized⁶⁵⁻⁷⁰ anthropomorphic phantoms exist for dosimetric applications, they only represent standard or limited patient sizes at discrete reference ages (e.g., 0, 1, 5, 10, 15 years of age) and do not reflect the size and hence dose variations from patient to patient. Furthermore, current protocol designs rely on dose as a surrogate for risk of cancer incidence, neglecting the fact that the same dose delivered to two patients may entail substantially different risks due to age and gender differences. Figure 1 illustrates the strong dependence of risk on age and gender using lung cancer and all cancers combined as examples.

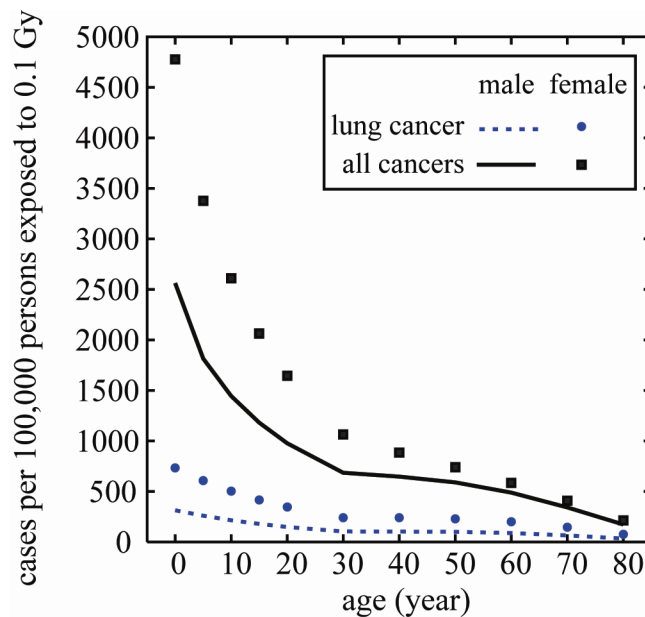


Figure 1: Lifetime attributable risks of cancer incidence tabulated in BEIR VII report¹⁴. Risks for lung cancer and all cancers are shown to illustrate the strong dependence of risk on age and gender.

The goal of this work is to develop a method for estimating patient-specific radiation dose and cancer risk in CT. A Monte Carlo program was developed to model a CT system. Its accuracy was validated using cylindrical and anthropomorphic phantoms for both axial and helical scanning modes. As a demonstration of its utility, the Monte Carlo program was used to estimate organ dose in CT examinations of two pediatric patients (a newborn and a teenager), for whom patient-specific full-body computer models were recently developed. The organ dose values were then used to calculate risks of cancer incidence for radiosensitive organs and to derive effective dose, the most widely accepted dose descriptor, and effective risk, a newly proposed concept for overall radiation risk assessment⁷¹.

2.2 Materials and Methods

2.2.1 CT Scanner

A multi-detector array CT scanner (LightSpeed VCT, GE Healthcare, Waukesha, WI) was used in all measurements and simulations. The CT scanner was equipped with 64 arrays/rows of detectors, allowing the user to select a beam collimation of 1.25-40 mm. It could operate in both axial and helical scanning modes with a helical pitch of 0.516-1.375. Three bowtie filters (small, medium, and large) were available on the scanner to provide size-adapted compensation for the variation of body thickness from the center to the periphery of the scan field-of-view (SFOV) in order to reduce dose and achieve more uniform X-ray intensity at the detector. The appropriate bowtie filter could

be selected based on patient size and scanned body region via the proper choice of SFOV type. The scanner automatically switched between a large and a small spot size based on tube current. The distance between focal spot and isocenter was 54.1 cm. The user could select a tube potential of 80, 100, 120, or 140 kVp and a gantry rotation period of 0.4-2.0 seconds. While tube-current modulation techniques were available on the CT scanner, this study focused on fixed tube current techniques.

2.2.2 CT System Modeling

2.2.2.1 Analytical simulation of X-ray energy spectra

The X-ray energy spectra at the exit of the X-ray tube and before filtration by the bowtie filter (referred to as the pre-bowtie spectra) were simulated by an X-ray modeling program (xSpect, version 3.3, Henry Ford Health System). An initial set of pre-bowtie spectra for the four kVp values was simulated for constant/high-frequency tube potentials based on the target material, target angle, and inherent tube filtration data provided by the manufacturer. The pre-bowtie spectra were then numerically filtered by the thinnest central region of the small bowtie filter to obtain a set of post-bowtie spectra. The half-value layers (HVLs) of the post-bowtie spectra estimated using xSpect were matched to the HVLs reported by the manufacturer for each kVp (at the center of the beam) by making small adjustments to the amount of inherent aluminum filtration. The above procedure was implemented to ensure that the beam qualities in our simulations match that in the actual CT scanner.

2.2.2.2 Monte Carlo simulation of radiation transport

Monte Carlo code: We developed a Monte Carlo program to simulate radiation transport in the CT system. The program was based on a benchmarked Monte Carlo subroutine package for photon, electron, and positron transport (PENELOPE, version 2006, Universitat de Barcelona, Spain)^{72, 73}. The example main program PENMAIN.F included in the standard PENELOPE distribution was modified to simulate radiation transport in the bowtie filter, to model X-ray tube motions during axial and helical scans, and to transport radiation through voxel geometry. All material definition files used in the simulations were generated by running the program MATERIAL.F of PENELOPE, which has a large database of pre-defined common materials in addition to allowing the user to input the atomic compositions and mass densities of user-defined materials.

Radiation transport in bowtie filters: Based on the geometry data provided by the manufacturer, each bowtie filter available on the CT scanner was modeled using the geometry package PENGEOM of PENELOPE as a group of simple objects limited by quadric surfaces. In the actual CT scanner, a cone beam of X-ray with a semi-beam angle of $\sim 27.5^\circ$ first passes through the bowtie filter and is subsequently restricted by a pair of tungsten cam collimators⁷⁴. In our simulations, the collimators were not explicitly modeled, but a fan beam of X-ray defined by the collimators was transported through the bowtie filter. Using a point source, we chose an effective beam width to account for the dose delivered by both the umbra and the penumbra regions of the beam (Figure 2a).

The effective beam width was measured using a ready-pack X-ray film. The methods are detailed in the next section. The semi-angle of the fan beam was chosen to be broad enough to cover the imaging object (Figure 2b). A pseudo impact detector was added below the bowtie filter at the level of the tungsten cam collimators to register the state (type of particle, energy, position coordinates, directional cosines, weight, etc.) of each incident particle in a phase-space file for use in the subsequent simulations of axial and helical scans. The width of the impact detector was equal to the aperture of the tungsten cam collimators and its length was just slightly larger than the divergence of the X-ray beam (Figure 2b).

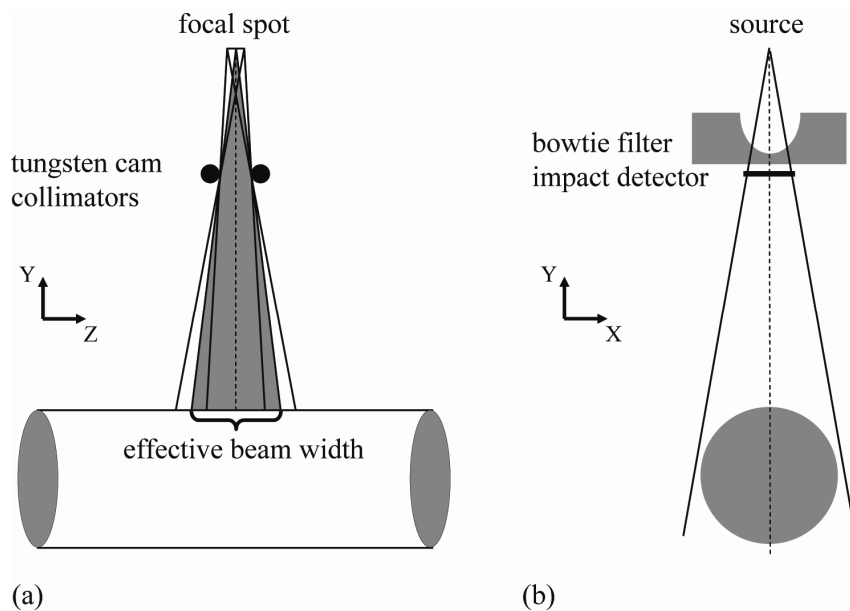


Figure 2: (a) A point source and an effective beam width were used in the simulations to account for the dose delivered by both the umbra and the penumbra regions of the beam. (b) The fan beam was chosen to be just broad enough to cover the imaging object. A pseudo impact detector was added below the bowtie filter at the level of the tungsten cam collimators to register the information of each incident particle in a phase-space file for use in the subsequent simulations of axial and helical scans.

Axial and helical scans: To model the effect of X-ray tube motion during an axial or helical scan, the initial state of each particle was first read from the pre-calculated phase-space file. Before the particle was released for transport in the imaging object, rotational and translational transforms were performed on the initial coordinates and the directional cosines of the particle with rotational angle and translational distance calculated as

$$\beta = \alpha \text{RAND} \text{ and } d = \frac{\beta}{2\pi} s + z_0, \quad (1)$$

respectively, where α is the total gantry rotation angle during the scan and equals 2π for single axial scans, RAND is a random value between 0 and 1, s is table increment per gantry rotation (equals zero for a single axial scan), and z_0 is the start location of the scan. Considering the limited size of the phase-space file, each particle was split into 12 equivalent particles with weights equal to 1/12 of the original particle weight at the beginning of the particle track. We have verified that the particle splitting technique did not affect the simulation results.

Radiation transport in voxel geometry: Realistic representation of human anatomy in Monte Carlo simulations frequently requires the use of voxel geometry. Earlier computer models of patients were generated from direct segmentation of the three-dimensional matrices of voxels in the patients' tomographic datasets^{66, 67, 75, 76}; every voxel was assigned to the appropriate organ or tissue based on grayscale values. Modern computer modeling of human anatomy employs more flexible mathematical surfaces,

most notably the non-uniform rational B-spline (NURBS) surfaces, which are fits to the segmented tomographic data⁷⁷. The complexity of such surfaces, however, prohibits particle locations to be solved efficiently during Monte Carlo simulations. As such, NURBS surfaces based computer models are often voxelized before inputting into Monte Carlo simulations³².

As it is impractical and inefficient to individually define all the planes and voxels in a voxel geometry using the original geometry routine PENGEOm of PENELOPE, we developed a new geometry routine, named PENVOME (i.e., PENGEOm for voxelized models). PENVOME conveniently labels each voxel by its matrix indices; boundary planes of the voxel are only calculated when the voxel is reached by a particle. This circumvents the need to store surface/body definitions and to sort through a genealogical tree of a large number of bodies. The accuracy of PENVOME was validated against PENGEOm in terms of simulated dose in a simple object of 18 voxels, and the results were identical within the statistical constraints of the Monte Carlo simulation. As such, the Monte Carlo program can be used to transport radiation for dose simulation in both quadric and voxel geometries.

2.2.3 Effective Beam Width Measurements

The effective beam width (along z direction) was determined for the small and large focal spots and for three most commonly used collimation settings: 40, 20, and 10 mm. At each combination of collimation and focal spot setting, a ready-pack X-ray film

(PPL, Eastman Kodak Company, Rochester, NY) was centered on the surface of the gantry bore and exposed in a single axial scan that delivered dose values within the responsive range of the film. The developed film was digitized (Expression 10000 XL, Seiko Epson Corporation, Japan) at a resolution of 72 points per inch (ppi), resulting in a 16-bit image. From the image, three pixel intensity profiles were measured across the X-ray beam along the beam width (z) direction. The pixel intensity profiles were converted into net optical density profiles, which were linearly proportional to the dose profiles over the range of net optical densities in our experiment. As each film was exposed twice in a single axial scan at two different source-to-film distances, each dose profile was the superposition of two profiles, representing the divergences of the beam at two source-to-film distances. The effective beam width at each source-to-film distance was defined as the distance between two points where the dose fell off most rapidly. Such two points were determined by differentiating the dose profile to find the points of maximum/minimum slopes. The effective beam widths measured at the two source-film distances were then converted to that at the isocenter of the CT scanner using known source-to-isocenter distance and gantry bore size.

2.2.4 Dose Measurements

A series of dose measurements were performed to calibrate and validate the accuracy of our CT model and Monte Carlo code.

2.2.4.1 Dose measurements in air

To quantify the absolute outputs of the X-ray tube for converting Monte Carlo results to absolute dose, free-in-air exposure was measured for all combinations of bowtie filters and kVps with a calibrated ion chamber and its corresponding electrometer (model 10×5-0.18/9015, Radcal Corporation, Monrovia, CA). The ion chamber was positioned at the isocenter of the CT scanner with its long axis aligned with the axis of gantry rotation. Single axial scans were performed with the X-ray beam centered on the active volume of the ion chamber. For each combination of bowtie filter and kVp, five to seven repeated measurements were taken at a beam collimation of 40 mm, a tube current of 30 or 60 mA, and a gantry rotation period of 1 second, and the results were averaged. All measured exposures in Roentgen (R) were converted to dose in cGy using $1 \text{ R} = 0.876 \text{ cGy}$.

2.2.4.2 Dose measurements in a cylindrical phantom

It is well known that a single axial scan generally delivers more radiation dose to the periphery than the center of a cylindrical phantom, affected by beam quality, phantom attenuation, and the spatial variation of beam intensity. We were motivated by this fact to design a CT dose phantom that allows center-to-periphery dose distributions to be measured for comparison with Monte Carlo simulated results. Initially focused on pediatric CT applications, we built a cylindrical phantom to represent a pediatric torso (Figure 3a). The phantom was made of a 7-inch diameter and 7-inch long

polymethylmethacrylate (PMMA) cylinder. Seven through-holes, 1.4 cm in diameter, were drilled parallel to its long axis to allow the placement of ion chambers at incremental distances away from the central axis. The holes, which could be filled with similar diameter PMMA rods, were arranged in a spiral pattern to minimize their overlap in the CT projections.

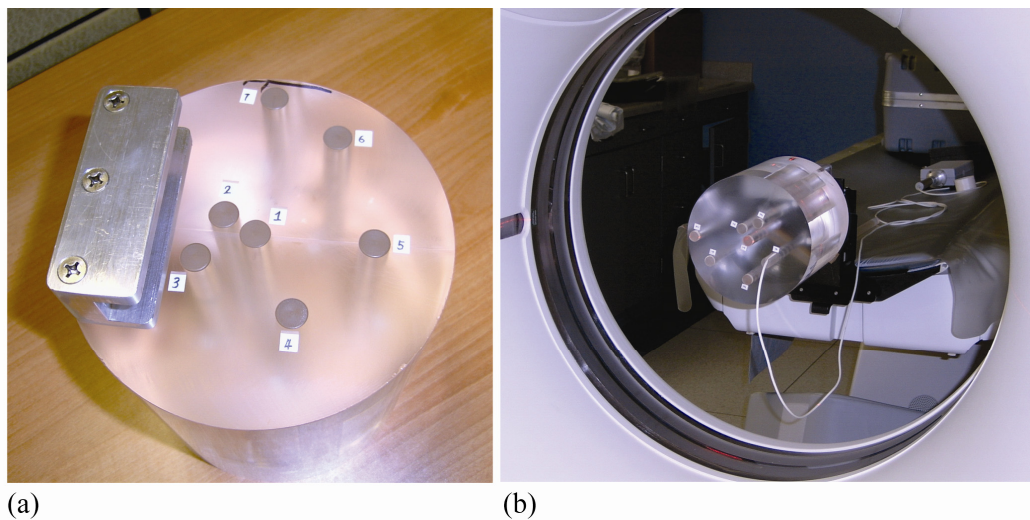


Figure 3: (a) Custom-designed CT dose phantom for measuring center-to-periphery dose distributions. The locations of the seven drill holes are numbered. (b) Measurements of dose distribution in the custom-designed phantom. The phantom was attached to one end of the CT table and positioned so that its long axis matched the axis of gantry rotation.

Radial dose distributions in the phantom from single axial scans were measured with the ion chamber. The phantom was attached to one end of the CT table using a phantom holder supplied with the CT system and positioned so that its long axis matched the axis of gantry rotation (Figure 3b). Exposure was measured for each hole individually with the ion chamber positioned mid-way inside the hole and the X-ray

beam centered on the active volume of the ion chamber. The remaining volume of that hole was filled with two half-length PMMA rods. All other holes also were filled. For each of the three bowtie filters, dose distribution was measured at the four kVp values with a beam collimation of 40 mm, a tube current between 200 and 300 mA, and a gantry rotation period of 1 second. Five to seven repeated measurements were taken at each hole location, and the results were averaged.

2.2.4.3 Dose measurements in anthropomorphic phantoms

To further validate the accuracy of our Monte Carlo method for dose estimation in human anatomical structures, we measured dose in two anthropomorphic phantoms, a pediatric one-year-old phantom and an adult female phantom (ATOM, Models 704-D and 702, CIRS, Norfolk, VA) shown in Figure 4a and Figure 4b.

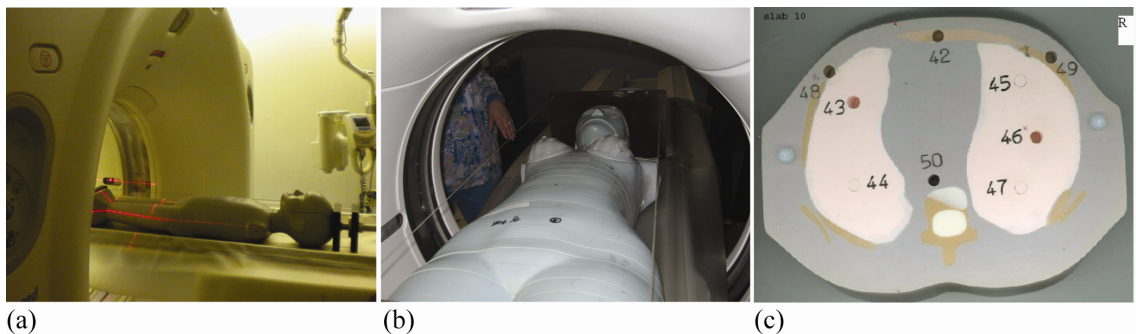


Figure 4: Dose measurements in (a) pediatric one-year-old CIRS phantom and (b) adult female CIRS phantom. (c) The phantoms were composed of axially sliced, 25 mm thick, contiguous sections. Each section contained one or more 5 mm diameter through-holes at various organ locations.

The phantoms were composed of axially sliced, 25 mm thick, contiguous sections. Each section contained one or more 5 mm diameter through-holes at various organ locations (Figure 4c). The holes could be filled with similar size plugs or dosimeter holders. We used thermoluminescent dosimetry (TLD) chips (Harshaw TLD-100, Thermoscientific, Oakwood Village, OH), which were calibrated against a pre-calibrated ion chamber (model 10×5-6/9015, Radcal Corporation, Monrovia, CA) at appropriate beam energies; calibration was performed either in the CT beam of interest or in an X-ray beam of a radiography system where the beam was hardened with a copper filter to match the half-value layer of the CT beam at the tube potential of interest. At each selected organ location, the hole plug was removed, cut in half, and used to sandwich a pair of two TLD chips before refilling the hole. The average of the two TLD readings at each organ location was used as the measured dose at that location; the standard deviation of the two readings was used to assess the uncertainty of the measurement. For each anthropomorphic phantom, two sets of TLD chips were used to measure dose from a single axial scan and a helical scan, respectively (Table 1). The single axial scan was centered on a chest section in which TLD chips were embedded. The helical scan was a full-body scan for the pediatric phantom and a chest scan for the adult female phantom.

Table 1: Scan protocols used to collect TLD dose measurements from the pediatric one-year-old and the adult female phantoms.

	pediatric phantom		adult female phantom	
	single axial	helical	single axial	helical
body region	chest	whole body	chest	chest
kVp	100	100	120	120
mA	250	250	250	250
gantry rotation period (second)	1	1	1	1
scan FOV (bowtie filter)	pediatric body (small bowtie)	pediatric body (small bowtie)	large body (large bowtie)	large body (large bowtie)
collimation (mm)	40	20	40	40
pitch	–	0.531	–	0.516
slice thickness (mm)	2.5	2.5	5	5
reconstruction interval (mm)	2.5	2.5	5	5

2.2.5 Dose Simulations

The dose measurements conducted in the air and in the three phantoms were simulated using the developed Monte Carlo program.

2.2.5.1 Dose simulations in the air and in the cylindrical phantom

Computer models of the ion chamber (model 10×5-0.18) and the cylindrical phantom were created using the geometry package PENGINE. The head of the ion chamber was modeled as a group of simple objects limited by quadric surfaces (Figure 5), based on the chamber geometry data provided by Radcal Corporation. The stem of the ion chamber, which contains metal conductors, was not explicitly modeled but was

approximated by a small PMMA cylinder. The small air gaps left in between the ion chamber and the phantom were also assumed to be filled with PMMA.

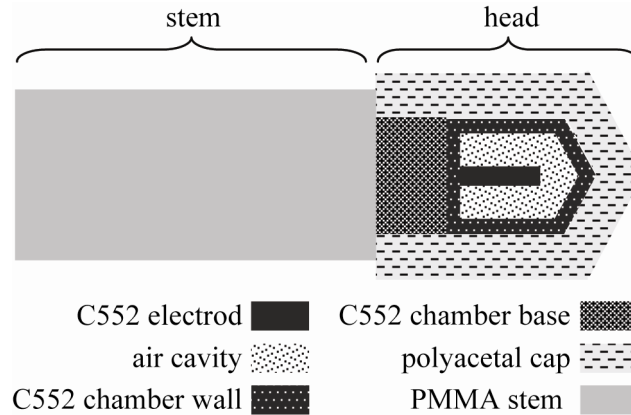


Figure 5: Model of the ion chamber (model 10×5-0.18/9015, Radcal Corporation, Monrovia, CA) used in the Monte Carlo simulations. “C552” here refers to C552 air-equivalent plastic. Material data file for polyoxymethylene was used for the polyacetal cap.

Energy deposited in the air cavity of the ion chamber was accumulated and used to calculate dose. When choosing simulation parameters, we referenced the recipe prescribed by Sempau et al.⁷⁸. Analogue simulation was employed in the air cavity and a speedup parameter⁷⁸ of $a = 1$ was used for the chamber wall. Table 2 summarizes the simulation parameters and variance reduction techniques used for air, C552 air-equivalent plastic, polyacetal (polyoxymethylene), and PMMA. In the polyacetal cap and the PMMA stem, electrons were not transported but were assumed to be absorbed locally when produced. This is because even if electrons were transported in these objects, they could not arrive at the air cavity, thus having no effect on the air cavity dose. For the same reason, electrons were not transported in the PMMA phantom. For

each combination of bowtie filter and kVp, center-to-periphery dose distribution in the phantom was obtained by running the simulation seven times with the ion chamber placed in a different hole each time. For all simulations in the phantom, the number of photon histories was chosen to obtain relative errors in dose of 1% or below. The relative error was defined as one standard deviation divided by the average tally result. When simulating the in-air measurements, the volume occupied by the phantom was replaced by air leaving only the model of the ion chamber; the number of photon histories was chosen to obtain relative errors of 0.5% or below.

Table 2: Simulation parameters and variance reduction techniques used for dose simulations in the air and the cylindrical phantom.

	electron absorption energy (keV)	photon absorption energy (keV)	speedup parameter ⁷⁸ <i>a</i>	variance reduction technique ⁷²
air cavity	5 ^a	kVp energy /1000	0	photoelectric interaction forcer = 50 Compton interaction forcer = 50
chamber wall	5	kVp energy /1000	1	photoelectric interaction forcer = 50 Compton interaction forcer = 50
chamber base	5	kVp energy /1000	1	No
polyacetal	kVp energy	kVp energy /1000	N/A	No
PMMA	kVp energy	kVp energy /1000	N/A	No

^aThe absorption energy of electrons in the air was chosen to be 5 keV, half the kinetic energy of an electron that has a continuous slowing down approximation (CSDA) range approximately equal to the thickness of the air in the cavity⁷⁸.

The above simulations produced air cavity dose in the unit of cGy per photon emitted from the source. The total number of photons emitted from the source during a CT scan was calculated as

$$N = n \cdot \Omega \cdot \text{mAs}, \quad (2)$$

where n , the number of photons emitted from the source per solid beam angle per mAs, was calculated from the energy spectra simulated by xSpect, and Ω is the solid angle of the fan beam. Absolute dose values in the unit of cGy were then equal to

$$D_{sim} = d_{sim} \cdot N, \quad (3)$$

where d_{sim} is Monte Carlo simulated dose in the unit of cGy per photon emitted from the source. We first calculated the absolute dose for each of the in-air dose simulations and compared it with the corresponding measured dose. The ratio of the measured to the simulated in-air dose was defined as an output correction factor (OCF):

$$OCF = \frac{D_{meas, in-air}}{D_{sim, in-air}}. \quad (4)$$

As mentioned earlier, HVL matching served to ensure the accurate *shapes* of the pre-bowtie spectra. Here the OCF values serve to correct for inaccuracy in the *magnitudes* of the pre-bowtie spectra. In other words, they correct for inaccuracy, tube-to-tube variation, or tube variation over time in the values of n . To calculate the absolute dose for all simulations in the phantoms and the patients, the total number of photons emitted from the source was calculated as

$$N' = N \cdot OCF. \quad (5)$$

2.2.5.2 Dose simulations in the anthropomorphic phantoms

A full-body computer model was created for each anthropomorphic phantom based on the phantom's CT images. The method was similar to that reported recently for creating NURBS models of pediatric CT patients⁷⁹ and is briefly described below. Initially, the images of each phantom were segmented using a graphical software application developed in our laboratory. Segmented organs and tissues included soft tissue, lung, bone, spinal cord, and spinal disc. The brain of the pediatric phantom, the breasts of the adult female phantom, and large unfilled air holes were also segmented. The TLD chips were not explicitly segmented, but each was modeled as a 1-mm tall cylinder with a 3-mm diameter to emulate the actual dimensions of the TLD chips. Following the segmentation, three-dimensional polygon models were created for each structure using the marching cubes algorithm^{80, 81}. Typically, three-dimensional NURBS surfaces would be then be fit to the polygon models to provide a more compact and flexible definition for each structure. The advantage of using NURBS surfaces would be to allow for the simulation of anatomical variations or motion. In this case, since only static phantoms were needed for dose simulation purposes, each phantom was left as a collection of polygon models. As only the chest part of the adult female phantom was scanned during the TLD dose measurements, the initial computer model of that phantom only included this region. To simulate dose to organ locations outside the chest

scan image volume, images of the entire adult female phantom were acquired (after the TLD chips were removed) to allow the remaining parts of the phantom to be modeled.

To account for the effect of CT table attenuation on dose, a computer model of the CT table (table case and table interior) was also created via manual segmentation of the table from a patient CT image with a large reconstruction field-of-view.

The model of each phantom with the table attached was voxelized at resolutions comparable to the original image resolutions. Each organ and structure was assigned a material based on the elemental composition and mass density information tabulated in the CIRS manual. Soft tissue material was used for the tissue-equivalent TLD chips. The interior of the CT table (acrylic foam) was modeled as low-density acrylic per information provided by the manufacturer. The case of the CT table (carbon fiber) was modeled as carbon with density of 1.7 g/cm³.

The location and coverage of the axial and helical scans in the actual experiments were reproduced in the simulation. For the helical scans, the total scan length was calculated as the total image coverage plus the overranging distance (additional scan length necessary for data interpolation in helical reconstruction)⁸². The overranging distance was estimated from the scanner console parameters as “table speed (cm/s) × total scan time (s) – image coverage (cm)”. In a helical scan, the X-ray tube starting angle is not fixed and thus different each time (per private communication with the manufacturer). As the tube starting angles in the actual experiments were unknown,

each helical scan was simulated six times with tube starting angle differing by 60 degrees each time.

For the range of photon energies in CT, the ranges of the secondary electrons in tissue materials are generally much smaller than the voxel sizes in the phantoms. Therefore, electrons were not transported during the simulations; their energies were deposited locally immediately after they were produced. The transport of a photon was terminated if the photon energy dropped below one thousandth of the kVp energy⁷². Energy deposited in the TLD chips was tallied and used to calculate dose, following the procedure of dose calculation performed for the cylindrical phantom. The number of photon histories was chosen to obtain relative errors in dose of 5% or below.

2.2.6 Patient-Specific Dose and Risk Estimation

2.2.6.1 Patients

The validated Monte Carlo program was applied to estimate organ dose and potential cancer risk for CT examinations of two patients: a newborn (5 weeks, female) and a teenager (12 years, male). Both patients underwent 64-slice CT examinations (LightSpeed VCT, GE Healthcare, Waukesha, WI) of the chest, abdomen, and pelvis at our institution in 2006 using our size-based pediatric protocols at the time that employed fixed tube currents (Table 3).

The study was approved by our institutional review board (IRB), who determined that it was in compliance with the Health Insurance Portability and Accountability Act (HIPAA), and did not require informed consent.

Table 3: CT examinations undergone by the two patients in our study. Each patient underwent a combined chest-abdomen-pelvis (CAP) examination consisting of a chest scan and an abdomen-pelvis scan.

	newborn (5 weeks, female)		teenager (12 years, male)	
	chest	abdomen-pelvis	chest	abdomen-pelvis
image coverage	from lung apex to top of liver	from 0.75 cm above top of liver to 1.25 cm below bottom of ischium	from 1 cm above lung apex to top of liver	from 1 cm above top of liver to just above bottom of ischium
kVp	100	120	120	120
mA	55	70	90	110
gantry rotation period (s)	0.4	0.4	0.4	0.4
scan FOV (bowtie filter)	pediatric body (small)	pediatric body (small)	medium body (medium)	medium body (medium)
collimation (mm)	40	40	40	40
pitch	0.984	0.984	1.375	1.375
slice thickness (mm)	3.75	3.75	5	5
reconstruction interval (mm)	2.5	2.5	5	5

2.2.6.2 Patient-specific computer models

For each patient, a NURBS-based full-body computer model was created based on the patient’s clinical CT data⁷⁹. Large organs and structures inside the image volume (backbone, ribcage, lungs, heart, liver, gall bladder, stomach, spleen, and kidneys) were individually segmented and modeled. Other organs were created by morphing existing adult male or female full-body computer models (developed from visible human data)⁸³

to match the framework defined by the segmented organs, referencing the organ volume and anthropometry data in ICRP Publication 89⁸⁴. The resultant full-body models possessed a total of 44 and 43 organs for the newborn and the teenager, respectively, including most of the radiosensitive organs defined by ICRP Publication 103²¹ (Table 4).

Table 4: Summary of organs in the computer models of the two patients.

organ/structure	density (g cm ⁻³) ^g	material (ICRU 46) ^g	mass (g) ⁱ	
			newborn (5 weeks, female)	teenager (12 years, male)
respiratory system				
pharynx-larynx ^a	1.03	average soft tissue ^h	1.6	17.3
trachea-bronchi	1.03	average soft tissue	1.0	13.7
lungs*	0.26	lung (adult, healthy, inflated)	57.9	445.3
alimentary system				
esophagus	1.03	average soft tissue	1.5	18.0
stomach ^b	1.03	average soft tissue	39.4	282.9
pancreas	1.03	average soft tissue	9.2	82.1
liver*	1.03	average soft tissue	104.5	961.5
gall bladder	1.03	average soft tissue	4.1	24.6
small intestine	1.03	average soft tissue	70.7	558.3
large intestine	1.03	average soft tissue	63.9	436.5
circulatory system				
heart*	1.03	average soft tissue	51.2	459.8
urogenital system				
kidneys*	1.03	average soft tissue	21.5	189.3
urinary bladder	1.03	average soft tissue	5.4	63.8
prostate ^c	1.03	average soft tissue	–	3.1
testes	1.03	average soft tissue	–	3.9
ovaries	1.03	average soft tissue	0.5	–
uterus	1.03	average soft tissue	3.2	–
vagina	1.03	average soft tissue	0.4	–
skeletal system^d				
cranium	1.4 ^d	average skeleton ^d	257.5	941.9
mandible	1.4	average skeleton	20.5	99.4
clavicles	1.4	average skeleton	1.2	42.9
scapulea	1.4	average skeleton	6.3	164.6

Table 4: Continued.

sternum	1.4	average skeleton	2.5	32.1
ribs*	1.4	average skeleton	25.5	302.9
cervical vertebrae*	1.4	average skeleton	7.1	74.4
thoracic vertebrae*	1.4	average skeleton	23.5	233.7
lumbar vertebrae*	1.4	average skeleton	16.6	186.7
pelvis	1.4	average skeleton	25.6	492.6
sacrum	1.4	average skeleton	10.9	152.7
upper humeri	1.4	average skeleton	5.1	175.9
lower humeri	1.4	average skeleton	3.7	125.1
radii, ulnae	1.4	average skeleton	6.1	185.9
wrist and hand bones	1.4	average skeleton	4.6	132.1
upper femora	1.4	average skeleton	10.9	439.6
lower femora	1.4	average skeleton	15.0	543.9
tibiae, fibiae, patellae	1.4	average skeleton	21.5	765.5
ankle and foot bones	1.4	average skeleton	12.1	420.1
integumentary system				
skin (torso only) ^e	1.03	average soft tissue	49.3	452.4
additional organs/tissues				
brain	1.03	average soft tissue	400.3	1488.4
eyes	1.03	average soft tissue	6.8	14.6
thyroid	1.03	average soft tissue	1.6	11.2
breasts	0.96	breast (50/50)	0.7	2.2
thymus	1.03	average soft tissue	16.3	37.5
spleen*	1.03	average soft tissue	8.1	215.1
adrenal glands	1.03	average soft tissue	6.5	10.6
residual soft tissues ^f	1.03	average soft tissue	2348.2	30226.5

^a Combined organ of pharynx and larynx, combined organ of trachea and bronchi, and esophagus were modeled as tubular organs with air-fill lumens. The wall thickness of these tubular organs was assumed to be 2 mm for the newborn and 3 mm for the teenager. It was independently verified that, over the range of 1-3 mm, the effect of wall thickness on organ dose was less than 1%. Dose to combined organ of pharynx and larynx was used as a surrogate for dose to salivary glands, oral mucosa, and extra-thoracic (ET) region.

^b Alimentary tract organs (stomach, small intestine, large intestine), heart, gall bladder, and urinary bladder were modeled as single homogenous organs without delineation of walls and contents.

^c Prostate, testes, ovaries, uterus, and vagina are gender-specific organs and were included in the models of their respective genders only.

^d The skeleton was modeled as a homogeneous mixture of its component tissues, namely cortical bone, trabecular bone, yellow marrow, red marrow, and various connective tissues. The atomic composition and mass density data published by Cristy and Eckerman⁶⁵ for the skeletons of newborn and adult were used for the newborn and the teenager patients, respectively.

Table 4: Continued.

^c The torso of the NURBS model of each patient was covered with a skin layer to allow dose estimations for the skin. The skin thickness was assumed to be 1 mm and 2 mm for the newborn and the teenager patients, respectively, resulting in a 1-2 voxel definition of the skin in the Monte Carlo simulations. Whole body skin dose was calculated as torso skin dose multiplied by the ratio of torso skin area to whole body skin area, where skin areas were estimated from the NURBS model of each patient.

^f Residual soft tissues included skeletal muscle, adipose tissue, cartilage, blood, lymphatic tissues, and connective tissues. Dose to residual soft tissues was used to approximate dose to skeletal muscle and lymphatic nodes.

^g The atomic composition and mass density data tabulated in ICRU Publication 46⁸⁵ were used for all organs and tissues with the exception of the skeleton (see footnote d).

^h Average soft tissue of adult male was used.

ⁱ Organ/tissue mass in the voxel models.

* Organs individually segmented from CT images of the patients.

While each patient's three-dimensional CT dataset may also serve as his/her patient-specific computer model³⁵, the full-body models in our study allowed dose to be estimated for not only organs within the image volume, but also organs in the overranging distance and those outside the scan coverage.

2.2.6.3 Organ dose simulations

The NURBS model of each patient was "positioned" on the CT table in a supine position with arms elevated above the head to mimic actual patient posture during CT examinations. The models were voxelized at 0.5- and 1-mm isotropic resolutions for the newborn and the teenager, respectively. Each organ/structure was assigned a material (Table 4) based on the elemental composition and mass density information tabulated in ICRU Publication 46⁸⁵ with the exception of the skeleton, for which the material information published by Cristy and Eckerman⁶⁵ for the skeletons of newborn and adult was used for the newborn and the teenager patients, respectively.

The scan coverage in the actual patient examinations (Table 3) was reproduced in the simulations. As was done for the anthropomorphic phantoms, the total scan length in a helical scan was calculated as the total image coverage plus the overranging distance. As the exact tube starting angles in the patients' examinations were unknown, a zero degree (12 o'clock) tube starting angle was assumed.

Energy deposited in organs and tissues was tallied and used to calculate dose. Because bone marrow and bone surface were not explicitly modeled, the following methods were used to estimate dose to these two organs. To assess dose to the red bone marrow, volume-averaged photon fluence spectrum was tallied individually at each skeletal site and used to calculate dose to the red bone marrow via the fluence-to-dose conversion coefficients published by Cristy and Eckerman⁶⁵. A single active marrow dose was then calculated as its skeletal average using the age-dependent fractional distribution of active marrow tabulated in ICRP Publication 89⁸⁴. Dose to the bone surface was approximated by the mass-weighted average of dose to the homogenous bones as recommended by Lee et al.⁸⁶.

In terms of simulation time requirement, using a single processor on a 2.3 GHz Linux server with 20 GB of random access memory (RAM), a 30-minute runtime plus another 30 minutes of input/output operation time was needed to finish ~7 million photon histories, resulting in relative dose error of less than 1% for all organs in the scan coverage and less than 10% for other organs. In this study, 80 million photon histories

(6.5-hour user time) were used to simulate each CT scan of each patient, resulting in relative dose error of less than 1% for all organs in the scan coverage and less than 3% for other organs.

2.2.6.4 Effective dose and effective risk calculations

Simulated organ dose values were used to calculate effective dose for the examination of each patient as

$$E = \sum_T w_T H_T, \quad (6)$$

where H_T is the equivalent dose for organ/tissue T and w_T is the tissue weighting factor defined by ICRP Publication 103²¹. Dose to radiosensitive organs that were not explicitly modeled was approximated by dose to neighboring organs (Table 4). Dose to the breasts was only included in the effective dose calculations for the female patient.

While widely used as a surrogate for radiation risk, effective dose is defined for a reference hermaphrodite person; the tissue weighting factors are mean values representing averages over many individuals of different genders and age groups²¹. To more accurately estimate individual patient risks, we used the recently proposed concept of effective risk⁷¹ defined as

$$R = \sum_T r_T H_T, \quad (7)$$

where r_T is the gender-, age-, and tissue-specific risk coefficient (cases/100,000 exposed to 0.1 Gy) tabulated in BEIR VII report¹⁴ for lifetime attributable risk of cancer incidence

(Figure 1). Thus, $r_T H_T$ is the lifetime attributable risk of cancer incidence for organ/tissue T . Values of r_T are available for leukemia and for cancer of 8-9 high-risk organs of each gender at discrete ages of 0, 5, 10, 15, 20, 30, 40, 50, 60, 70, 80 years¹⁴, from which we linearly interpolated the values of r_T at other ages. Cancer of other radiosensitive organs shares a collective risk coefficient (r_{other})¹⁴. This risk coefficient was applied to a weighted average dose of other radiosensitive organs, defined as¹⁵

$$H_{\text{other}} = \frac{\sum_{T \in \{\text{other organs}\}} w_T H_T}{\sum_{T \in \{\text{other organs}\}} w_T}, \quad (8)$$

where the other radiosensitive organs included heart, kidney, gall bladder, spleen, pancreas, adrenal glands, thymus, small intestine, salivary glands, extrathoracic region, lymph node, muscle, oral mucosa, bone surface, brain, skin, testes (male only), and esophagus, among which the reminder organs, as defined by ICRP Publication 103²¹, were each assigned a tissue-weighting factor of 0.01.

To compare patient-specific organ dose estimation with the current dose-reporting method, volume-averaged CTDI (CTDI_{vol}) was also calculated for each patient's each CT scan using the CTDI_{100} table and the tables of technique adjustment factors in the technical reference manual of the LightSpeed VCT scanner. CTDI_{vol} values estimated this way agreed with those in the patients' dosimetry reports within about 5%.

Lastly, as effective dose is frequently calculated using the dose-length product (DLP) to effective dose conversion coefficients^{37, 38, 87}. DLP was calculated for each CT

scan and used to derive effective dose using the conversion coefficients published by Shrimpton³⁶. The conversion coefficients for children at 0 and 10 years of age were used for the newborn and the teenager patients in our study, respectively.

2.3 Results

2.3.1 In-Air Results

Simulated dose in the air was lower than measured dose for all combinations of kVps and bowtie filters (Table 5), resulting in OCF values (Equation 4) greater than unity. As OCFs calibrated the magnitudes of the pre-bowtie spectra, they had little dependence on bowtie filter type (Table 5). Thus, results averaged across bowtie filters were used in subsequent dose calculations.

Table 5: Measured and simulated in-air dose at the isocenter of the LightSpeed VCT scanner for single axial scans. Error figures reflect one standard deviation.

kVp	bowtie filter	in-air dose (cGy/100mAs)		OCF	mean ^a	standard deviation ^a	coefficient of variation ^{a,b}
		measured	simulated				
80	small	1.145 ± 0.004	0.896 ± 0.004	1.278	1.290	0.020	1.5%
	medium	1.151 ± 0.003	0.900 ± 0.004	1.279			
	large	0.835 ± 0.003	0.636 ± 0.003	1.313			
100	small	1.901 ± 0.003	1.515 ± 0.006	1.255	1.270	0.014	1.1%
	medium	1.907 ± 0.004	1.498 ± 0.006	1.273			
	large	1.481 ± 0.003	1.155 ± 0.005	1.283			
120	small	2.776 ± 0.004	2.337 ± 0.009	1.188	1.196	0.016	1.4%
	medium	2.775 ± 0.005	2.340 ± 0.009	1.186			
	large	2.262 ± 0.001	1.862 ± 0.008	1.215			
140	small	3.744 ± 0.006	3.187 ± 0.013	1.175	1.177	0.003	0.3%
	medium	3.736 ± 0.007	3.178 ± 0.013	1.176			
	large	3.144 ± 0.005	2.664 ± 0.012	1.180			

Table 5: Continued.

^a The mean, standard deviation, and coefficient of variation of the OCF values across bowtie filters.

^bCoefficient of variation = (standard deviation / mean) × 100%.

Figure 6 illustrates the results of our analytical simulation of the X-ray energy spectra at the exit of the X-ray tube and before filtration by the bowtie filter. The magnitudes of the spectra have been corrected using the OCF results.

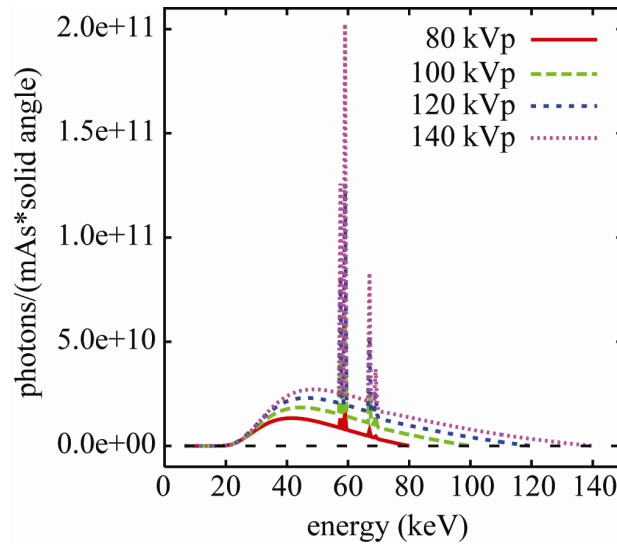


Figure 6: Simulated X-ray energy spectra at the exit of the X-ray tube and before filtration by the bowtie filter (pre-bowtie spectra).

2.3.2 Effective Beam Width Results

Results of effective beam width measurements are summarized in Table 6. Good agreements were found between the results derived from the two source-to-film distances. Furthermore, the effect of focal spot size was not statistically significant ($p =$

0.06-0.94). We defined the penumbra of the beam as the effective beam width minus the nominal collimation setting. As the differences between the penumbras at different collimation settings were small, the results were averaged to obtain a single penumbra value, which was added to each collimation setting to serve as the effective beam width at each collimation setting for the Monte Carlo simulations.

Table 6: Effective beam widths measured for both focal spot sizes and for three most commonly used collimation settings.

focal spot size	collimation (mm)	effective beam width at isocenter (mm)			penumbra ^b (mm)
		derived from near SFD ^a	derived from far SFD	average	
small	40	42.2 ± 0.6	42.4 ± 0.2	42.3	2.3
large	40	41.9 ± 0.0	42.7 ± 0.2	42.3	2.3
small	20	22.1 ± 0.6	21.7 ± 0.2	21.9	1.9
large	20	22.1 ± 0.6	23.1 ± 0.2	22.6	2.6
small	10	12.7 ± 0.0	12.1 ± 0.0	12.4	2.4
large	10	12.7 ± 0.0	12.8 ± 0.4	12.7	2.7
				average=	2.3

^aSFD = source-to-film distance

^bPenumbra is defined here as the effective beam width minus the nominal collimation setting.

2.3.3 Cylindrical-Phantom Results

Comparisons between measured and simulated dose distributions in the custom-designed cylindrical phantom are shown in Figure 7. Across all bowtie filter and kVp settings, simulations agreed very well with measurements. Percent differences between simulations and measurements at individual data points ranged from -4.8% to 2.2% with an average magnitude of 1.3%.

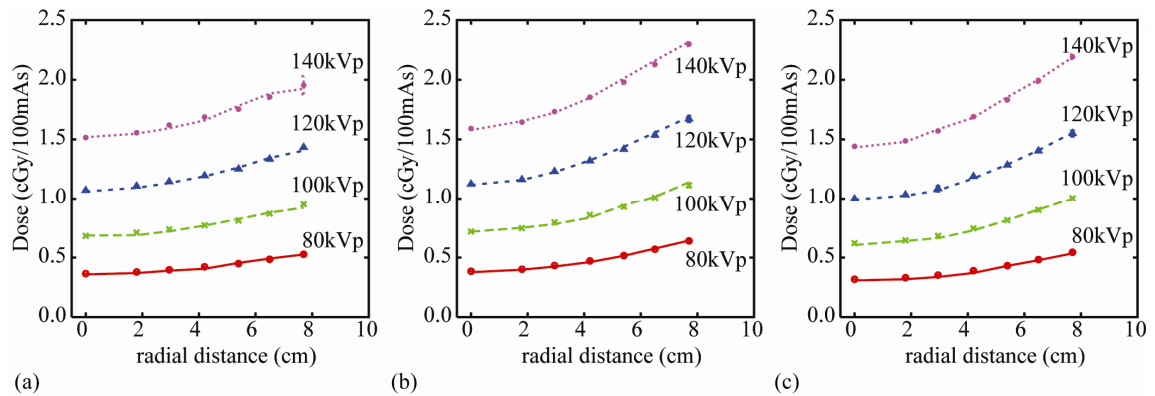


Figure 7: Measured and simulated dose distributions in the custom-designed cylindrical phantom for single axial scans at four kVp values using the (a) small, (b) medium, and (c) large bowtie filters and a 40-mm beam collimation. Simulated dose values are shown by lines. Measured dose values are shown by symbols, and their error bars reflect one standard deviation. Most error bars are too small to appreciate.

2.3.4 Anthropomorphic-Phantom Results

Figure 8 and Figure 9 illustrate measured and simulated dose values in the pediatric and adult female anthropomorphic phantoms. For the axial scans performed in both phantoms, excellent match was found between simulations and measurements at all organ locations. For the helical scans, simulations agreed well with measurements for the pediatric phantom, yet slightly underestimated measurements for the adult female phantom. Results are also summarized in Table 7.

Table 7: Summary of discrepancies between simulated and measured dose in the cylindrical and anthropomorphic phantoms.

	cylindrical phantom		pediatric phantom		adult female phantom	
	single axial		single axial	helical ^a	single axial	helical ^a
range	(-4.8%, 2.2%)		(-8.1%, 8.1%)	(-2.1%, 13.0%)	(-7.2%, 6.1%)	(-17.2%, 3.8%)
average magnitude	1.3%		6.2%	4.0%	3.4%	11.1%

^a Simulated dose averaged across tube starting angles was used for the comparison.

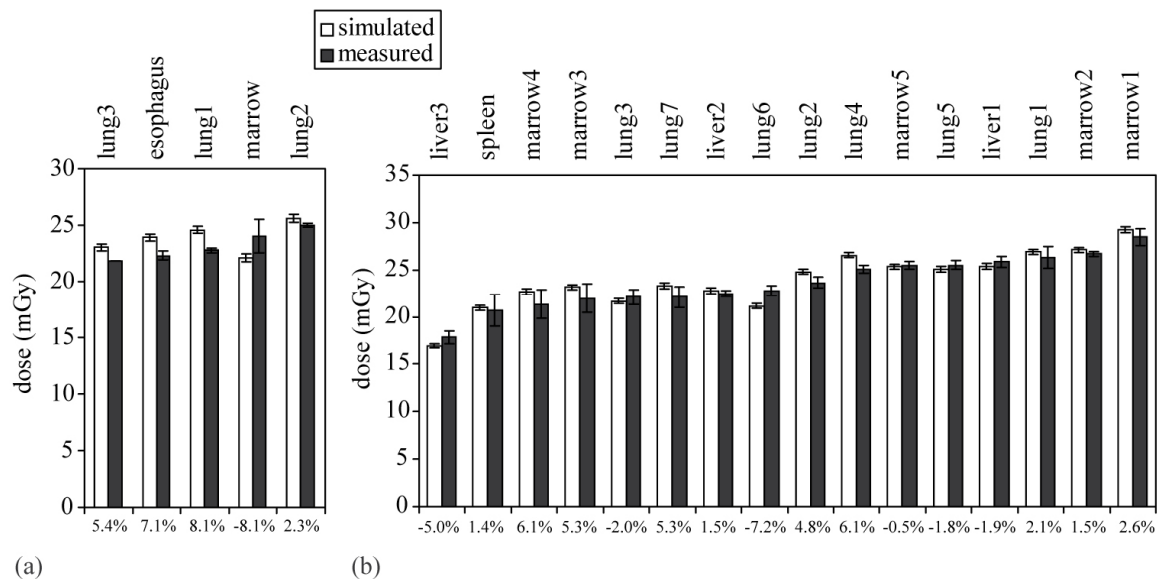
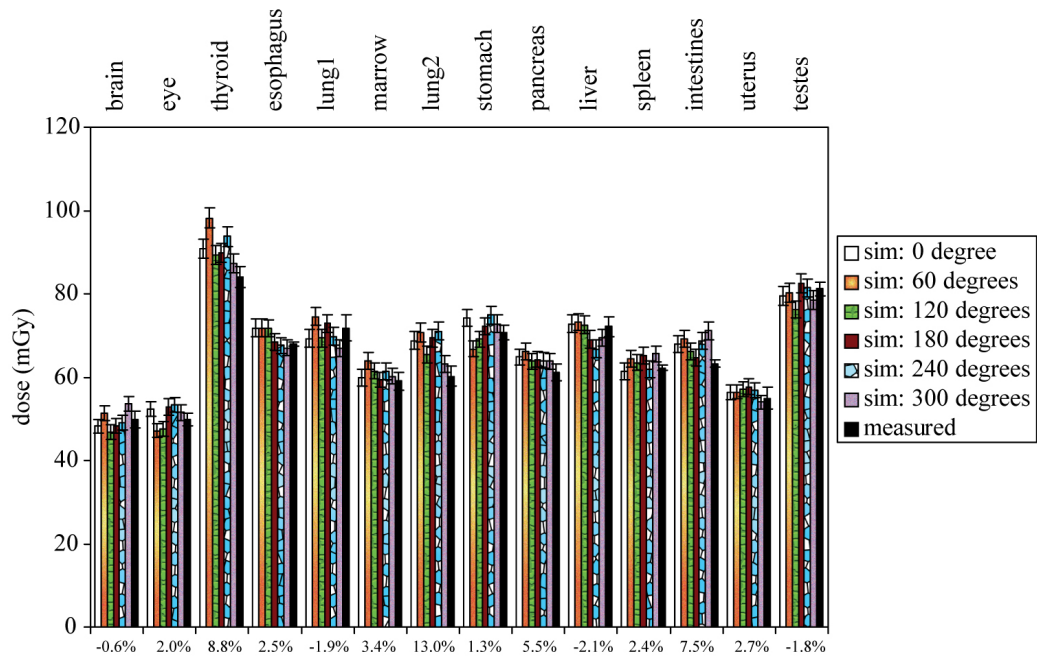
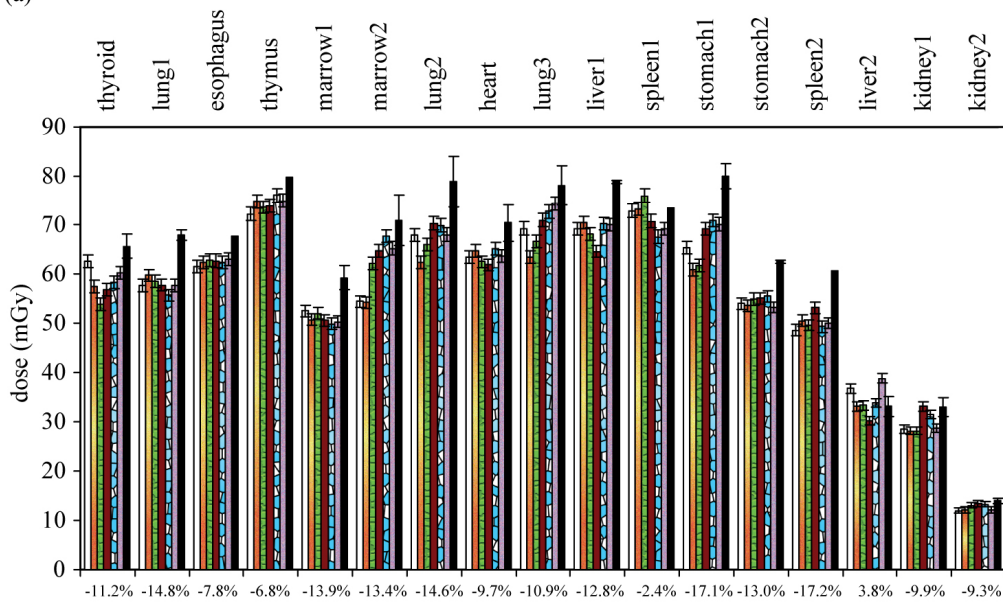


Figure 8: Measured and simulated dose from a single axial scan in (a) the pediatric and (b) the adult female phantoms. Error bars reflect one standard deviation. Percent discrepancies between simulation and measurement are labeled on the bottom.



(a)



(b)

Figure 9: Measured and simulated dose from (a) a full-body helical scan in the pediatric phantom and (b) a chest scan in the adult female phantom. Error bars reflect one standard deviation. The degrees are X-ray tube start angles relative to 12 o'clock. Percent discrepancies between simulation (averaged over tube starting angles) and measurement are labeled on the bottom. At four organ locations in the adult female phantom, one of the two TLD chips was cracked during the experiment; dose uncertainty could not be assessed for these four locations.

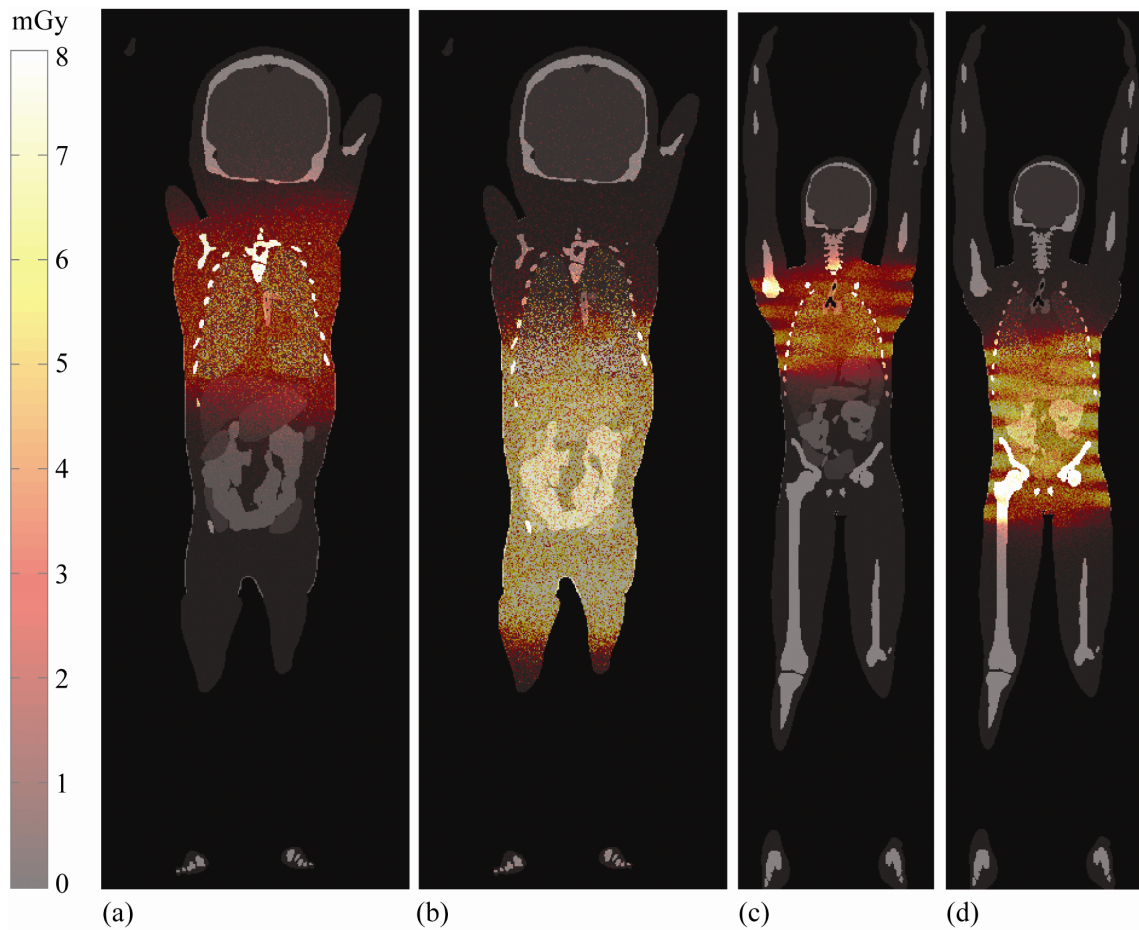


Figure 10: Coronal dose distributions in the two patients, resultant from their CT examinations: (a) chest scan of the newborn patient, (b) abdomen-pelvis scan of the newborn patient, (c) chest scan of the teenager patient, and (d) abdomen-pelvis scan of the teenager patient. The coronal plane was taken about half-way in between the anterior and posterior surfaces of each patient. The computer model of each patient with organs shown on a gray scale was overlaid with a semi-transparent colored image of the dose distribution. The noise in the dose distribution is reflective of the limited number of photos used in the simulations. As organ dose was an average over the entire organ volume, the uncertainty associated with organ dose was less than 1% for all organs in the scan coverage and less than 3% for other organs (see Section 2.2.6.3).

2.3.5 Patient-Specific Dose and Risk Results

Examples of dose distributions in the two patients from their CT examinations are illustrated in Figure 10. The dose distribution was more uniform in the newborn patient (pitch of 0.984) than in the teenager patient (pitch of 1.375). As a result of the overranging distance, a large portion of the abdomen (chest) was irradiated in the chest (abdomen-pelvis) scan.

Table 8 summarizes the organ and effective dose values. The corresponding risks of cancer incidence are tabulated in Table 9. For the newborn patient, lung dose from the abdomen-pelvis scan was comparable to that from the chest scan. For both patients, the effective dose from the abdomen-pelvis scan was more than double that from the chest scan. While the organ and effective dose of the two patients was similar, the organ and effective risk of the newborn patient was up to 23 times higher. $CTDI_{vol}$ underestimated dose to large organs in the scan coverage by 30-48%, and effective dose derived from DLP differed from that estimated using patient-specific organ dose values by -30% to 42% (Table 10).

Table 8: Organ and effective dose of the two patients from their CT examinations. Each patient underwent a combined chest-abdomen-pelvis (CAP) examination consisting of a chest scan and an abdomen-pelvis scan.

organ	dose (mGy)					
	newborn (5 weeks, female)			teenager (12 years, male)		
	chest	abdomen-pelvis	CAP ^a	chest	abdomen-pelvis	CAP ^a
respiratory system						
pharynx-larynx	1.95	0.24	2.18	1.09	0.06	1.15
trachea-bronchi	3.28	0.58	3.86	3.72	0.38	4.09
lungs	3.68	3.56	7.24	3.93	2.50	6.43

Table 8: Continued.

alimentary system						
esophagus	3.21	1.58	4.79	3.34	1.35	4.69
stomach	1.49	6.39	7.88	1.61	5.06	6.67
pancreas	0.34	6.40	6.74	0.58	4.97	5.55
liver	2.01	6.56	8.57	1.84	4.94	6.77
gall bladder	0.97	6.89	7.86	0.41	5.20	5.60
small intestine	0.27	7.07	7.35	0.15	5.51	5.66
large intestine	0.24	6.77	7.00	0.11	5.08	5.19
circulatory system						
heart	3.57	4.33	7.90	4.16	2.63	6.80
urogenital system						
kidneys	1.43	6.10	7.53	0.65	4.55	5.20
urinary bladder	0.03	6.27	6.30	0.02	5.45	5.47
prostate	-	-	-	0.01	3.98	3.99
testes	-	-	-	0.00	4.19	4.19
ovaries	0.05	6.11	6.16	-	-	-
uterus	0.04	6.06	6.10	-	-	-
vagina	0.03	6.32	6.35	-	-	-
skeletal system						
bone surface	1.81	3.36	5.17	1.45	2.68	4.13
red bone marrow	0.93	1.60	2.52	1.04	1.91	2.95
integumentary system						
skin	0.55	1.70	2.25	0.60	1.24	1.83
additional organs/tissues						
brain	0.12	0.05	0.17	0.07	0.01	0.08
eyes	0.09	0.03	0.12	0.05	0.01	0.05
thyroid	2.86	0.38	3.23	4.78	0.23	5.01
breasts	2.89	2.27	5.16	2.57	1.45	4.02
thymus	3.54	0.75	4.29	3.87	0.51	4.39
spleen	2.62	5.71	8.33	1.26	4.65	5.91
adrenal glands	1.98	6.06	8.04	1.24	4.11	5.36
residual soft tissues	0.99	2.79	3.78	0.72	1.44	2.16
effective dose (mSv)	1.7	4.1	5.8	1.4	3.0	4.4

^a Dose from the combined chest-abdomen-pelvis (CAP) examination, i.e., the summation of dose from the chest scan and that from the abdomen-pelvis scan.

Table 9: Lifetime risks of cancer incidence for the two patients attributable to their CT examinations. Each patient underwent a combined chest-abdomen-pelvis (CAP) examination consisting of a chest scan and an abdomen-pelvis scan.

	lifetime attributable risk of cancer incidence (cases / 1000 exposed)					
	newborn (5 weeks, female)			teenager (12 years, male)		
	chest	abdomen-pelvis	CAP ^a	chest	abdomen-pelvis	CAP ^a
thyroid cancer	0.180	0.024	0.203	0.021	0.001	0.022
breast cancer	0.337	0.265	0.602	0.000	0.000	0.000
lung cancer	0.269	0.260	0.529	0.080	0.051	0.132
stomach cancer	0.015	0.064	0.079	0.008	0.026	0.035
liver cancer	0.006	0.018	0.024	0.007	0.020	0.028
colon cancer	0.005	0.148	0.154	0.002	0.116	0.119
bladder cancer	0.001	0.132	0.133	0.000	0.078	0.078
prostate cancer	-	-	-	0.000	0.025	0.025
ovary cancer	0.001	0.063	0.064	-	-	-
uterus cancer	0.000	0.030	0.030	-	-	-
leukemia	0.017	0.029	0.046	0.012	0.022	0.034
other cancer	0.251	0.405	0.656	0.055	0.131	0.185
effective risk	1.1	1.4	2.5	0.2	0.5	0.7

^a Risk from the combined chest-abdomen-pelvis (CAP) examination, i.e., the summation of risk from the chest scan and that from the abdomen-pelvis scan.

Table 10: Comparison between volume-weighted CT dose index (CTDI_{vol}) and patient-specific organ dose, and comparison between effective dose derived from DLP and effective dose estimated using patient-specific organ dose values.

	newborn (5 weeks, female)		teenager (12 years, male)	
	chest	abdomen-pelvis	chest	abdomen-pelvis
large organ dose (mGy) ^a				
approximated by CTDI _{vol}	2.21	4.77	2.24	2.74
estimated for specific patient	3.63	6.82	4.05	5.23
discrepancy	-39%	-30%	-45%	-48%
effective dose (mSv)				
derived from DLP	1.2	5.2	2.0	4.1
estimated using patient-specific organ dose	1.7	4.1	1.4	3.0
discrepancy	-30%	26%	42%	36%

^a Average dose to large organs inside the scan coverage, represented by lung and heart for the chest scan and liver and small intestine for the abdomen-pelvis scan.

2.4 Discussions

In this work, we reported a Monte Carlo method for estimating patient-specific radiation dose and potential cancer risk associated with CT examinations. To ensure the accuracy of our Monte Carlo method, we modeled the CT system in great detail, including explicit modeling of the X-ray source energy spectra, the three-dimensional geometry of the bowtie filters, and the trajectories of CT tube motions during axial and helical scans. The results of our effective beam width measurements were consistent with those reported earlier by other authors, who measured the effective beam widths on the LightSpeed VCT scanner using rod optically stimulated luminescence (OSL) dosimeters.⁸⁸ The results of our dose simulation showed good agreement with ion chamber and TLD measurements. Excellent match (Figure 7) was found between simulated and measured radial dose distributions in the cylindrical phantom for all combinations of kVp and bowtie filter settings (discrepancy < 4.8%). As radial dose distribution is highly dependent on the quality of the X-ray beam and the filtration of the CT system, these results are strong evidence of the accuracy of our spectrum and filtration models.

To our knowledge, this work is the first effort to validate Monte Carlo simulated dose inside anthropomorphic phantoms for helical scans. Prior work was limited either to single axial scans^{34, 35, 89} or to the surfaces of an anthropomorphic phantom³³. For the pediatric phantom in our study, excellent agreement was found between simulations

and measurements for both axial and helical scans (Figure 8a and Figure 9a) (discrepancy < 13%). Our simulations showed that the tube starting angle has a discernable effect on dose even at small helical pitch values (~ 0.5), contributing to the uncertainty in dose estimation. Such dependence has also been reported recently at higher pitch values (0.75-1.5) and has been exploited as dose reduction strategies⁹⁰. For the adult female phantom, simulations agreed well with measurements for the single axial scan (discrepancy < 7.2%), yet slightly underestimated measurements for the helical scan (discrepancy < 17.2%). Nevertheless, considering the complexity of the simulations and the large number of factors that influence the results, discrepancies of less than 20% from measurements are generally considered as good matches³⁵.

Results of patient-specific dose estimations for the two patients showed that overranging and scattered radiation contribute significantly to the dose received by organs on the edges and outside of the image volume (Figure 10 and Table 8). This is especially apparent for the newborn patient whose lung dose in the abdomen-pelvis scan was comparable to that in the chest scan. This result highlighted the importance of reducing or eliminating overranging distances⁹¹, especially for smaller patients. For both patients, the effective dose from the abdomen-pelvis scan was more than double that from the chest scan. This may be explained by the higher technique (kVp and/or mA) and the larger irradiated body volume in the abdomen-pelvis scan.

It is generally accepted that when the same scan technique is used, a smaller patient receives higher radiation dose^{30, 92}. Due to the size-based pediatric CT protocols in use at our institution, which uses lower scan techniques for smaller patients, organ and effective dose received by the newborn patient were only slightly higher but comparable to that of the teenager patient. When the risks of cancer incidence were assessed, however, the newborn had up to 23% times higher risks than the teenager, due to the differences in age and gender. As the same dose may entail substantially different risks to patients of different ages and genders, patient-specific risk estimates should be used together with dose estimates to guide the design and optimization of CT technologies and scan protocols. Knowledge of the risks to a specific patient may have potential influence on decisions for imaging in clinical scenarios; even assuming that the effect may be trivial, it is important that those involved with ordering, performing, and assuring quality for CT examinations understand the range of potential biological effects, such as cancer, from these examinations. In addition, patient-specific dose information may be extremely helpful for institutional review of scientific investigations using CT examinations. Finally, patient-specific dose estimations afford more individualized and expanded application of dose tracking from medical radiation exposures^{61, 62}.

To further demonstrate the inadequacy of the current patient-generic dose reporting method, we compared $CTDI_{vol}$ with patient-specific dose to large organs in the

scan coverage. For the two patients in our study, $CTDI_{vol}$ grossly underestimated (-30 to -48%) dose to large organs in the scan coverage, primarily because the newborn and the teenager patients had average trunk diameters of 9.7 and 21.7 cm, respectively, much smaller than the diameters of the standard CTDI phantoms (i.e., 16- and 32-cm diameter PMMA or equivalently 18- and 36-cm diameter water⁹³), on which the respective $CTDI_{vol}$ values were based. As such, $CTDI_{vol}$ should not be used as a surrogate for radiation dose in CT. Furthermore, we showed that the effective dose values derived from DLP can differ substantially (-30% to 42%) from that calculated using patient-specific organ dose values. Part of the difference may be attributed to the differences in tissue-weighting factors (w_T) used in the two methods; the DLP method was based on the w_T values in ICRP Publication 60⁹⁴, whereas our calculation of effective dose for specific patients employed the w_T values in ICRP 103²¹. However, the patient-generic nature of the DLP method was likely the main cause of the discrepancy, leading to under- or over-estimation of dose depending on the patient. With the development of a large library of patient-specific compute models⁷⁹, it is possible to match any new patient to an existing patient in the library based on age, gender, and body habitus. This will allow more accurate dose and risk estimates or pseudo-patient-specific estimates to be included in all patients' dosimetry and medical records.

Our study has several limitations. Firstly, it is limited to a single CT scanner model and to the fixed tube-current techniques. However, the methods developed in our

study can be readily extended to other CT scanner models and to tube-current-modulated techniques. Furthermore, other authors have shown, with small numbers of patient and scanner models, that when organ dose estimates are normalized by CTDI values appropriate for the patient size (e.g., $CTDI_{vol}$ in a cylindrical phantom with the same circumference as the patient), the variations across CT scanner models are small^{10,95}. Thus, our method may be extended to provide patient-specific normalized dose and risk estimates independent of scanner models, although this requires further testing and validation. Secondly, we and other authors⁹⁰ have shown that tube starting angle has sizable effects on patient dose. However, as the two patients in our study underwent CT examinations four years ago, it was not possible for us to obtain the actual tube starting angles in the patients' examinations (part of the raw CT data, not archived) and reproduce that in our dose simulations. This potentially introduced errors in the dose results. Lastly, the accuracy of our risk estimations is limited by the accuracy/uncertainties of the current cancer risk models,¹⁴ which are largely based on the life-span studies of atomic-bomb survivors and limited number of studies on occupational exposures. Furthermore, as the risk coefficients are still statistical averages over many individuals of the same gender and similar age, they can not reflect individual vulnerability due to genetic factors. As such, the cancer risks we reported do not represent the true risk of an individual from his/her CT examination but rather our current best knowledge of the potential risk to a patient from his/her CT examination,

knowing the patient's age and gender. Therefore, care should be exercised when interpreting the risk results. Nevertheless, the patient-specific risk information, as presented by our study, represents a step forward beyond effective dose towards personalized patient care.

3. Patient-Specific Dose Estimation for Pediatric Chest CT*

3.1 Introduction

With the growing use of computed tomography in children^{96, 97} and the increasing awareness of CT radiation risk to this population^{15, 16, 60}, there is a greater need to accurately estimate radiation dose from CT examinations, not only for the purpose of assessing life-time cancer risk which can be useful during discussions with healthcare providers, regulatory bodies, parents, and ethics committees, but also for the purposes of comparing and optimizing CT technologies and scan protocols. Despite the recent debate on its concept²², effective dose remains the most widely used dose descriptor for radiological procedures including CT. Its calculation requires the knowledge of dose delivered to individual organs.

With no practical technique to measure organ dose directly from patients, three methods are currently being used to estimate organ and effective dose from CT examinations using patient phantoms/models: (a) experimental measurement on physical anthropomorphic phantoms^{23, 24}, (b) Monte Carlo simulation using mathematical or voxelized models of patients^{25-27, 29-32, 98}, and (c) calculation of organ and effective dose from CT dose index (CTDI) or dose-length product (DLP) using conversion coefficients derived via the first two methods^{23-25, 36-38}. Current methods are

* This chapter is based on an article with the same title published in the journal *Medical Physics*.

limited in that they are largely patient-generic. Phantoms/models have only been developed for standard/limited patient sizes at discrete ages (e.g. 0, 1, 5, 10, 15 years old) and do not reflect the variability of patient anatomy and body habitus. Therefore, dose information for individual patients is currently not available. In a recent study³², the effect of body weight on organ dose was studied for 15-year-old adolescents using NURBS (non-uniform rational B-spline) based computer models created at 10th, 50th, and 90th weight percentiles. The authors reported up to ~30% dose errors when reference patient models were used to represent overweight patients. This highlighted the need for patient-specific dose estimations.

The goal of this work is to use multi-detector array CT (MDCT) data of multiple pediatric patients in the same size/protocol group to investigate dose variations across patients due to the variability of patient anatomy and body habitus and to explore methods for patient-specific dose estimations.

3.2 Materials and Methods

3.2.1 Patients

This study was approved by our institutional review board (IRB), who determined that it was in compliance with the Health Insurance Portability and Accountability Act, and did not require informed consent. The study included seven pediatric patients (3 boys and 4 girls; median age, 2 years old; age range, 1-6 years old; median weight, 12.9 kg; weight range, 11.9-18.2 kg) who underwent 64-slice MDCT

examinations (LightSpeed VCT, GE Healthcare, Waukesha, WI) of the chest, abdomen, and pelvis.

3.2.2 Patient-Specific Computer Models

In CT examinations, three sources of exposure contribute to organ dose: direct primary exposure, exposure from overranging (additional scan length necessary for data interpolation in helical reconstruction), and scattered radiation. While the first source of exposure has higher contribution than the other two and can be modeled with the actual patient CT data, the other two sources contribute notably to organ dose as well and can only be adequately modeled using full-body patient models.

A full-body computer model of each patient was created to enable dose estimations for organs both inside and outside the image volume. The initial anatomy of the model was defined by segmenting the patient's MDCT data using a software application developed in our laboratory⁹⁹. The heart, liver, gall bladder, stomach, spleen, and kidneys were manually segmented by contouring from each CT slice. The lungs and bones were semi-automatically segmented using thresholding. Once a dataset was segmented, three-dimensional polygon models were generated for each structure using the marching cubes algorithm^{80, 81}. Three-dimensional NURBS surfaces were then fit to the polygon models using NURBS modeling software (Rhinoceros, McNeel North America, Seattle, WA) to create the initial patient-specific model.

Other organs and structures, not easily segmented or visible in the scan coverage, were defined by morphing an existing male or female full-body adult model (developed from visible human data)⁸³ to match the framework defined by the segmented organs. The morphing was performed manually using the affine transformations of Rhinoceros. The volumes of the organs and structures defined in this manner for each pediatric model were checked and scaled, if necessary, to match age-interpolated organ volume and anthropometry data in ICRP Publication 89⁸⁴.

The resultant full-body pediatric male and female models possessed a total of 26 and 27 organs, respectively, including most of the radiosensitive organs defined by ICRP Publication 103²¹ (Table 11). Figure 11 illustrates surface rendered views of the three-dimensional anatomy in the computer models of the youngest (16 months old) and the oldest (6 years old) patients in our study.

A computer model of the CT table (table case and table interior) was also created via manual segmentation of the table from an adult CT image with a large scan field-of-view, referencing the dimensional data provided by the manufacturer. The model of each patient was “positioned” on the table in a supine position with arms elevated above the head to mimic actual patient posture during CT examinations.

The NURBS model of each patient with the table attached was voxelized at 2-mm isotropic resolution, resulting in a three-dimensional matrix of voxels, each assigned an integer labeling a specific organ or object.

Table 11: Summary of organs included in the computer models of the seven pediatric patients.

organ/structure	density (g·cm ⁻³)	material (ICRU 46)	mass (g)		
			mean	(range)	CV ¹
respiratory system					
pharynx-larynx ^a	1.03	average soft tissue ⁱ	7.2	(4.3 - 10.0)	27.6%
trachea-bronchi	1.03	average soft tissue	4.7	(2.6 - 6.6)	31.2%
lungs*	0.26	lung (adult, healthy, inflated)	158.8	(117.6 - 216.6)	22.4%
alimentary system					
esophagus ^b	1.03	average soft tissue	6.7	(1.9 - 10.2)	50.8%
stomach*	1.03	average soft tissue	124.4	(61.9 - 219.6)	46.2%
pancreas	1.03	average soft tissue	33.7	(26.4 - 52.9)	27.2%
liver*	1.03	average soft tissue	484.4	(354.2 - 724.0)	25.7%
gall bladder*	1.03	average soft tissue	6.8	(2.6 - 12.4)	54.4%
small intestine	1.03	average soft tissue	238.0	(190.5 - 343.9)	22.6%
large intestine	1.03	average soft tissue	192.1	(157.6 - 291.7)	23.9%
circulatory system					
heart ^{*c}	1.03	average soft tissue	166.7	(133.6 - 248.7)	23.4%
urogenital system					
kidneys*	1.03	average soft tissue	109.0	(81.3 - 147.6)	22.5%
urinary bladder	1.03	average soft tissue	14.8	(10.4 - 22.4)	26.4%
prostate ^d	1.03	average soft tissue	1.6	(1.6 - 1.7)	0.8%
testes	1.03	average soft tissue	3.3	(3.2 - 3.4)	3.3%
ovaries	1.03	average soft tissue	2.4	(1.8 - 3.3)	29.5%
uterus	1.03	average soft tissue	3.3	(2.6 - 4.3)	23.3%
vagina	1.03	average soft tissue	1.6	(1.4 - 2.1)	20.8%
skeletal system^e					
compact bone ^{*f}	1.75	cortical (5 years)	2303.3	(1875.7 - 2989.5)	16.9%
marrow	1.03	red marrow (adult) ^k	424.5	(270.8 - 701.5)	38.5%
integumentary system					
skin (torso only) ^g	1.03	average soft tissue	440.8	(375.9 - 535.5)	12.5%
additional organs/tissues					
brain	1.03	average soft tissue	1161.6	(1069.4 - 1345.0)	8.0%
eyes	1.03	average soft tissue	12.0	(10.3 - 15.4)	14.2%
thyroid	1.03	average soft tissue	4.1	(2.9 - 7.5)	39.9%
breasts ^h	0.96	breast (50/50)	3.0	(3.0 - 3.1)	1.1%
thymus	1.03	average soft tissue	35.6	(33.3 - 38.3)	5.5%
spleen*	1.03	average soft tissue	86.1	(34.2 - 129.7)	42.0%
adrenal glands	1.03	average soft tissue	7.8	(7.3 - 9.0)	8.3%
residual soft tissues ⁱ	1.03	average soft tissue	10026.0	(7728.8 - 15045.4)	25.1%

^a Dose to combined organ of pharynx and larynx was used as a surrogate for dose to salivary glands, oral mucosa, and extra-thoracic (ET) region.

Table 11: Continued.

^b Esophagus, combined organ of pharynx and larynx, and combined organ of trachea and bronchi were modeled as walled organs with air-fill lumens.

^c Heart, gall bladder, alimentary tract organs (stomach, small intestine, large intestine), and urinary bladder were modeled as single homogenous organs without delineation of walls and contents.

^d Prostate, testes, ovaries, uterus, and vagina are gender-specific organs and were included in the models of their respective genders only.

^e The skeletons were modeled as homogeneous bone marrow encased by homogeneous compact bone. The trabecular bone was not explicitly modeled. The additional dose to bone marrow deposited by photoelectrons released in the trabecular bone was accounted for by applying dose enhancement factors. The dose enhancement factors reported by King and Spiers¹⁰⁰ were interpolated by age at 50 keV, effective energy of the 120 kVp beam.

^f Dose to compact bone was used to approximate dose to bone surface.

^g Skin thickness, wall thicknesses of trachea and esophagus, and thicknesses of compact bones were assumed to be 3 mm given the 2-mm voxel resolution used in this study and the thin thicknesses of these structures in patients of this age range.

^h Breast tissue is underdeveloped in patients of this age range and was not visible in the CT images. A small amount of breast tissue (3.0 g) was “attached” to the chest of each patient model for dose estimation purposes. Dose to the breast was used to study dose variations across the patients, but was not included in the calculation of effective dose.

ⁱ Residual soft tissues include skeletal muscle, adipose tissue, cartilage, blood, lymphatic tissues, and connective tissues. Dose to residual soft tissues was used to approximate dose to skeletal muscle and lymphatic nodes.

^j Average soft tissue of adult male was used.

^k Bone marrow was assumed to be composed entirely of red bone marrow for patients of this age range.

^l CV (coefficient of variation) = standard deviation × 100% / mean.

* Organs individually segmented from CT images of the patients. Individually segmented compact bones included the backbone and the ribcage.



Figure 11: Surface rendered views of the three-dimensional anatomy in the computer models of the youngest (16 months old) and the oldest (6 years old) patients in our study.

3.2.3 Monte Carlo Simulations

The voxelized models of the patients were used as inputs to a PENELOPE⁷² (Universitat de Barcelona, version 2006) based Monte Carlo code, which was previously developed to simulate radiation transport in the LightSpeed VCT scanner¹⁰¹. The three-dimensional geometry of the three bowtie filters on the scanner and the trajectories of X-ray tube motion during axial and helical scans were explicitly modeled by the code. The accuracy of the code was previously validated against experimental measurements in terms of dose distributions in a cylindrical acrylic phantom, and the maximum dose error was found to be less than 5.4%¹⁰¹.

Because it is impractical and inefficient to individually define all the planes and voxels in the patient model using the original geometry routine PENGEO M of PENELOPE, we developed a new geometry routine, named PENVOME (i.e. PENGEO M for voxelized models). PENVOME conveniently labels each voxel by its matrix indices; boundary planes of the voxel are only calculated when the voxel is reached by a particle. This circumvents the needs to store surface/body definitions and to sort through a genealogical tree of a large number of bodies. The accuracy of PENVOME was validated against PENGEO M in terms of simulated dose in a simple object of 18 voxels, and the results were identical within the statistical constraints of the Monte Carlo simulation.

Before incorporating the voxelized model of each patient into Monte Carlo simulation, each organ was assigned a material (Table 11). The case and the interior of

the patient table were modeled as carbon fiber ($\rho = 1.7 \text{ g/cm}^3$) and acrylic foam ($\rho = 0.1 \text{ g/cm}^3$), respectively. The MATERIAL program of PENELOPE was used to generate material definition files based on the elemental composition and mass density information tabulated in ICRU Publication 46⁸⁵.

The simulated scan protocol was the standard, size-based chest scan protocol in place at our institution for the weight range of the patients: 120 kVp, 70 mA (11.5-14.4 kg) or 75 mA (14.5-18.4 kg), 0.4-second gantry rotation period, pitch of 1.375, 20-mm beam collimation, and small body scan field-of-view (corresponding to small bowtie filter). While 40-mm beam collimation is commonly used on the LightSpeed VCT scanner to achieve fast scanning, this protocol used a 20-mm beam collimation because of its higher dose efficiency for small ($< \sim 20 \text{ cm}$) total scan length.

The total scan length of each patient was calculated as the total image coverage plus the overranging distance. The total image coverage was defined as the distance from 1 cm above lung apex to 1 cm below lung base, typical of the clinical image coverage for a chest scan. The overranging distance was estimated from the scanner console parameters as “table speed (cm/s) \times total scan time (s) – image coverage (cm)”. Estimates were found to be independent of slice thickness, reconstruction interval, and image coverage. The start location of the chest scan was, therefore, 1 cm plus half of the overranging distance above lung apex, and the end location was the same distance below lung base.

In terms of simulation time, using a single processor on a 2.3 GHz Linux server with 4 GB of RAM, a 30-minute runtime was needed to finish 10 million photon histories, resulting in percent dose error (1σ standard deviation $\times 100\%$ / mean) of less than 1% for all organs in the scan coverage and less than 15% for other organs.

3.2.4 Effective Dose Calculations

The effective dose of each patient was calculated as the summation of radiosensitive organ dose values weighted by the tissue weighting factors defined by ICRP Publication 103²¹. Dose to radiosensitive organs that were not explicitly modeled was approximated by dose to neighboring organs (footnotes of Table 11). Complying with ICRP Publication 103, the weighting factor for the remainder organs was applied to the arithmetic mean dose of the 13 remainder organs for each gender.

3.2.5 Data Analysis

Variations in organ dose across the patients were quantified by the coefficient of variation (standard deviation $\times 100\%$ / mean) for selected organs both inside and outside the chest scan coverage. The coefficient of variation across the patients was also calculated for the effective dose.

Organ dose was correlated with chest size and organ volume using linear regression analysis. Chest size was expressed in terms of total scan length, a surrogate for chest length, and mid-chest equivalent diameter defined as the diameter of a circle having the same area as the mid-chest (half-way between lung apex and lung base) area

of the patient model. Effective dose was correlated with chest size and body weight of the patient model using linear regression analysis.

3.3 Results

Figure 12 depicts coronal dose distributions resultant from the chest MDCT scan in three 2-year-old patients. Compact bones inside the scan coverage had the highest dose values, a result of having the highest mass energy absorption coefficient. Dose to chest organs was similar for the three patients. However, dose to abdominal organs varied substantially among the patients, affected by the locations of those organs relative to the base of the lung.

The normalized absorbed dose received by large organs in the scan coverage, i.e. the lung, the heart, and the thymus, varied very little across the patients (5.7% - 6.2%) (Table 12). Greater dose variations across the patients were observed for small organs in the scan coverage, i.e. the esophagus (8.6%), the breast (17.7%), and the thyroid (9.1%), but they were generally smaller compared with those for partially or indirectly exposed organs (10.7% - 76.6%) (Table 12). The correlation between dose variations and variations in organ mass was weak (Pearson correlation coefficient: $r = 0.43$). For all the selected organs, the dose error was less than 1%. Therefore, the variations in organ dose reported here were due to the variations in patient anatomy and body habitus, not the uncertainty in dose estimation. The seven patients had a chest MDCT effective dose of

1.1-1.5 mSv, corresponding to normalized effective dose of 3.7-5.3 mSv/100mAs (coefficient of variation: 10.8%).

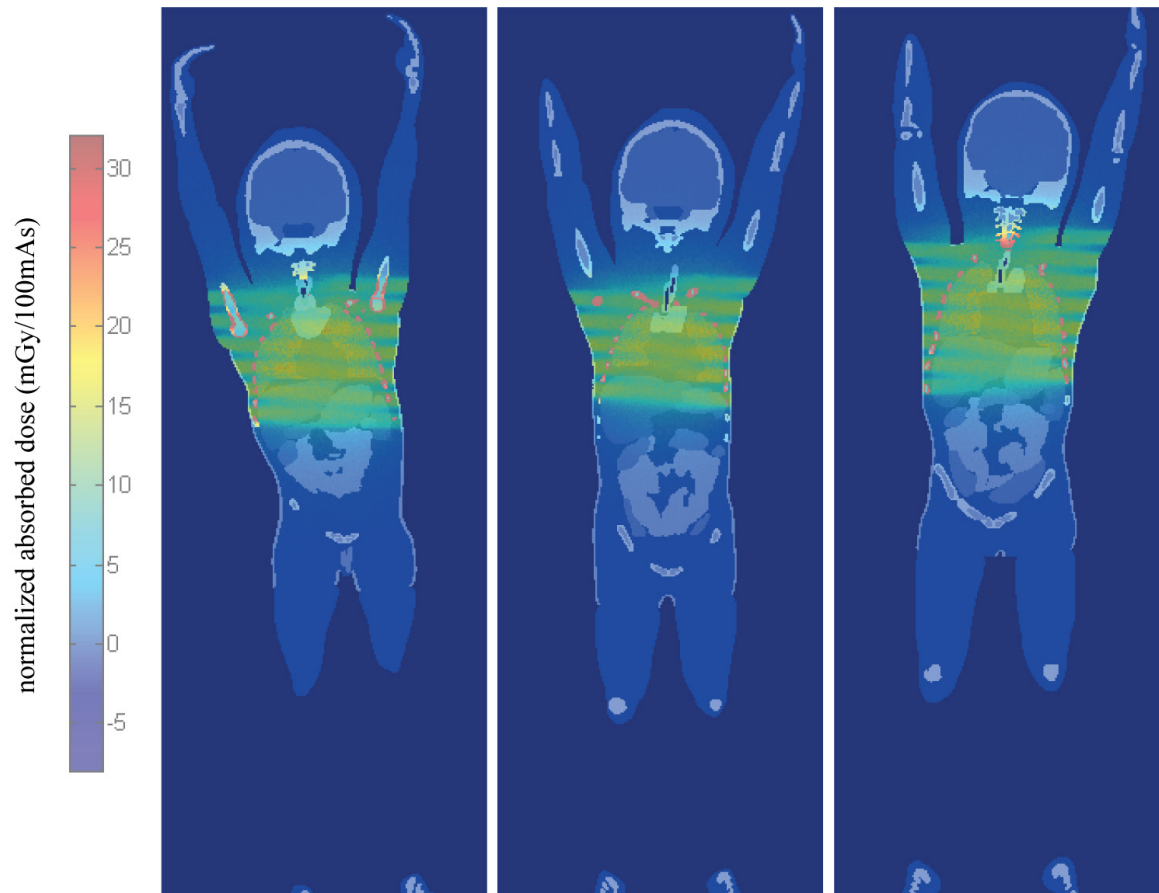


Figure 12: Coronal dose distributions in three 2-year-old patients, determined from the chest MDCT scan. The coronal plane was taken about half-way in between the anterior and posterior surfaces of each patient. The computer model of each patient with organs shown on a gray scale was overlaid with a semi-transparent colored image of the normalized dose distribution.

Table 12: Variations across patients in normalized organ dose from chest MDCT scan and correlations of normalized organ dose with chest size and organ volume for selected organs.

	normalized organ dose (mGy/100mAs)			Pearson correlation coefficient (r) ^b		
	mean	(range)	CV ^a	chest size		organ volume
				mid-chest equivalent diameter	total scan length ^c	
directly exposed large organs						
lung	12.0	(10.4 - 12.6)	6.2%	-0.99	-0.45	-0.51
heart	12.9	(11.2 - 13.3)	5.7%	-0.93	-0.14	-0.94
thymus	11.9	(10.6 - 12.8)	5.8%	-0.76	-0.25	-0.70
directly exposed small organs						
esophagus	9.9	(8.6 - 10.8)	8.6%	-0.49	0.15	-0.07
breast	9.7	(7.2 - 11.7)	17.7%	-0.79	-0.42	- ^d
thyroid	9.5	(8.5 - 11.0)	9.1%	0.11	-0.29	0.17
partially or indirectly organs						
liver	8.0	(6.7 - 9.5)	16.3%	-0.52	0.47	-0.53
gall bladder	3.8	(1.4 - 8.2)	76.6%	-0.41	0.40	0.18
stomach	7.9	(4.8 - 10.9)	26.6%	-0.46	0.13	-0.79
spleen	7.1	(5.3 - 10.0)	22.1%	0.07	0.54	-0.11
kidney	2.6	(1.4 - 4.3)	34.9%	0.03	0.61	0.61
marrow	2.1	(1.9 - 2.5)	10.7%	-0.64	-0.12	-0.88

^a CV (coefficient of variation) = standard deviation \times 100% / mean.

^b The square of r equals R^2 , a measure of goodness-of-fit for linear regression analysis. r values larger than 0.90, corresponding to $R^2 > 0.81$, are highlighted in bold.

^c Total scan length was used as a surrogate for chest length.

^d Correlation of organ dose with organ volume was not calculated for the breast because all patients were arbitrarily assigned the same amount of breast tissue.

Regression analysis of organ dose with respect to chest size indicated that lung dose and heart dose correlated strongly with mid-chest equivalent diameter (lung: $r = -0.99$, heart: $r = -0.93$), but weakly with total scan length (Table 12). Normalized absorbed dose to the lung (D_{lung}) and the heart (D_{lung}) decreased with mid-chest equivalent diameter ($d_{mid-chest}$) as

$$D_{lung} = 22.13 - 0.60 d_{mid-chest}, \text{ and} \quad (9)$$

$$D_{heart} = 22.26 - 0.56 d_{mid-chest}, \quad (10)$$

where $D_{lung/heart}$ and $d_{mid-chest}$ are in the units of mGy/100mAs and cm, respectively (Figure 13). For other organs, the correlations between normalized absorbed dose and chest size were generally weak (Table 12).

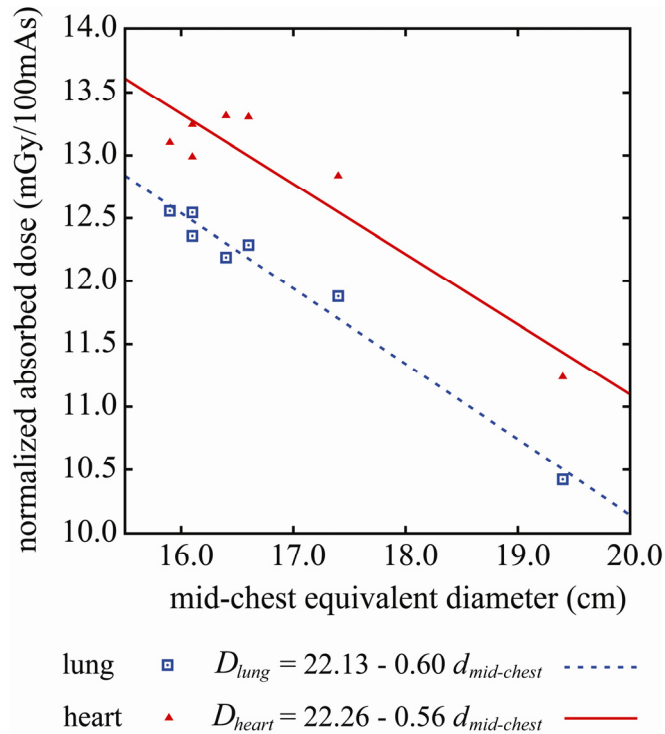


Figure 13: Normalized absorbed dose (mGy/100mAs) to the lung and the heart from the chest MDCT scan as a function of mid-chest equivalent diameter and the results of regression analysis. The mid-chest equivalent diameter was defined as the diameter of a circle having the same area as the mid-chest (half-way between lung apex and lung base) area of the patient model.

Regression analysis of organ dose with respect to organ volume showed that heart dose correlated strongly with heart volume ($r = -0.94$), but for all the other organs, the correlation of dose with organ volume was generally weak (Table 12).

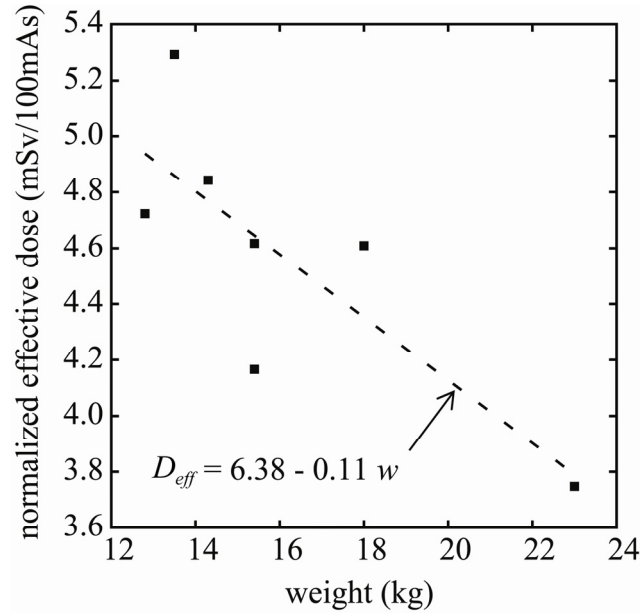


Figure 14: Normalized effective dose (mSv/100mAs) from the chest MDCT scan as a function of patient model weight and the result of regression analysis. Because the weights of the patient models were not perfectly matched to the actual patient weights (discrepancy < 5 kg), the weights of the patient models were used here for the regression analysis.

Normalized effective dose decreased with body weight (Figure 14) as

$$D_{eff} = 6.38 - 0.11 w \quad (11)$$

and with mid-chest equivalent diameter as

$$D_{eff} = 8.87 - 0.26 d_{mid-chest} \quad (12)$$

where D_{eff} and w are in the units of mSv/100mAs and kg, respectively. But the correlations were weak, r equal to -0.80 and -0.64 for body weight and mid-chest

equivalent diameter, respectively. Normalized effective dose had no apparent correlation with total scan length ($r = 0.20$).

For all the correlation relationships studied above, the trends of the data did not suggest the use of non-linear models.

3.4 Discussions

In this work, patient-specific computer models were constructed using the patients' actual MDCT data, which enabled the calculation of dose values that were patient-specific. Using computer models of multiple pediatric patients in the same size/protocol group, we obtained knowledge of dose variations across patients due to the variability of patient anatomy and body habitus, which could not be obtained using previous methods of DLP, Monte Carlo simulation, or physical phantom measurement. We found that, in chest MDCT, variations in normalized organ dose across patients were generally small for large organs in the scan coverage, but large for small organs in the scan coverage and for partially or indirectly exposed organs. Furthermore, dose variations correlated weakly with variations in organ mass, hence organ volume, indicating that variations in organ shape, organ location, and body habitus (e.g. breadth) also contribute to the dose variations across patients. It is necessary to further examine these trends of organ dose variations in future studies of abdominal and pelvis MDCT scans.

Our work also provided a method to determine patient-specific dose information for any other patient in the same size/protocol group (those not included in the study). The formula relating lung dose to mid-chest equivalent diameter (derivable from mid-chest circumference) allows patient-specific lung dose to be estimated with high accuracy. The relationship between heart dose and mid-chest equivalent diameter may also be used for a broad estimation of patient-specific heart dose. The correlation between normalized dose to large organs in the scan coverage and mid-chest equivalent diameter was not surprising. Nickoloff et al.⁹² proposed and verified an exponential relationship between CT dose index (CTDI) and phantom diameter over a wide range of phantom sizes (5-30 cm in diameter, representing new born to large adult). The linear relationships that we found in this study may be understood as an approximation to the exponential relationship over a narrow range of body diameters. The weak correlations between organ dose and patient dimensions (mid-chest equivalent diameter and chest length) for small organs in the scan coverage and for partially or indirectly exposed organs suggested that dose to those organs may only be obtained with high accuracy using patient-specific computer models.

Normalized effective dose was found to decrease with patient weight, consistent with the finding of DeMarco et al.³⁰ who studied the effective dose from a chest scan for eight patients with a much wider weight range (5-100 kg). In either study, the correlation between normalized effective dose and patient weight was weak (DeMarco

study: $R^2 = 0.41$ or $r = -0.64$, our study: $r = -0.79$) and did not warrant inferences to other patients.

We note that this investigation did not use the concept of “effective dose” as originally defined. Effective dose is defined in ICRP Publication 103²¹ for a *reference person*; the tissue weighting factors are mean values representing an average over many individuals of different genders and age groups. Our application of the concept of “effective dose” to individual patients, however, while not being exactly “correct”, is in line with other studies in the literature³⁰ and provides a surrogate for patient risk, using a concept that the medical imaging community is familiar with. For a more proper estimation of patient-specific risk, Martin¹⁰² has recommended the use of age-, sex-, and organ-specific risk coefficients. Perhaps the recently proposed concept of “effective risk”⁷¹ could substitute effective dose for future patient-specific risk estimations.

4. Patient-Specific Dose Estimation for Pediatric Abdomen-Pelvis CT*

4.1 Introduction

The importance of radiation dose in children from multi-detector array CT (MDCT) examinations has been highlighted recently by the launching of the “Image Gently” campaign⁶⁰. The campaign stresses the need to “child-size” CT scan techniques, namely to minimize dose to children by adapting scan techniques to pediatric body sizes or preferably to individual pediatric patients. To this end, dose reported for CT scans should be individualized or at least capture the size variation from patient to patient. Current dose estimation methods, however, are largely patient-generic. The dosimetry report of a patient only includes reference dose quantities such as CT dose index (CTDI) measured in cylindrical phantoms of a single standard size (e.g. 16-cm diameter phantom for pediatric body). While a myriad of physical and computerized anthropomorphic phantoms are available, they only represent standard/limited patient sizes at discrete reference ages (e.g. 0, 1, 5, 10, 15 years of age) and do not reflect the variability in patient anatomy and body habitus within the same size/age group.

Recently, using computer models of pediatric patients created from clinical MDCT data, we developed a method for estimating patient-specific dose from chest

* This chapter is based on a paper with the same title published in the *Proceedings of SPIE*.

MDCT examinations¹⁰³. The purpose of this study is to extend this effort to abdomen-pelvis MDCT examinations.

4.2 Materials and Methods

4.2.1 Patients

This study was approved by our institutional review board (IRB), who determined that it was in compliance with the Health Insurance Portability and Accountability Act (HIPAA), and did not require informed consent. The study included seven pediatric patients (3 boys and 4 girls; age range, 1-6 years old; median age, 2 years old; weight range, 11.9-18.2 kg; median weight, 12.9 kg) who underwent 64-slice CT examinations (LightSpeed VCT, GE Healthcare, Waukesha, WI) of the chest, abdomen, and pelvis.

4.2.2 Patient-Specific Computer Models

A non-uniform rational B-spline (NURBS) based full-body computer model was created for each patient based on the patient's clinical MDCT data¹⁰³. Large organs and structures inside the image volume (backbone, ribcage, lungs, heart, liver, gall bladder, stomach, spleen, and kidneys) were individually segmented and modeled. Other organs were created by morphing existing adult male or female full-body computer models (developed from visible human data)⁸³ to match the framework defined by the segmented organs, referencing the organ volume and anthropometry data in ICRP Publication 89⁸⁴. Li et al.¹⁰³ provided greater details on the process of model construction

and the anatomical data of the models. While a patient's three-dimensional CT data can also serve as his/her patient-specific computer model³⁵, the full-body models in our study allowed dose to be estimated for not only organs within the image volume, but also organs in the over-ranging distance⁸² and those outside the scan coverage.

To account for the effect of CT table attenuation on dose, a computer model of the CT table has also been created via manual segmentation from CT images of the table¹⁰³.

The model of each patient was "positioned" on the table in a supine position with arms raised above the head to mimic actual patient posture during CT examinations. Each model with the table attached was voxelized at 2-mm isotropic resolution for input into Monte Carlo simulations.

4.2.3 Monte Carlo Simulations

A PENELOPE⁷² (Universitat de Barcelona, version 2006) based Monte Carlo code was used. The code was previously developed and benchmarked for dose simulation on the LightSpeed VCT scanner¹⁰¹. The three-dimensional geometry of the bowtie filters on the scanner and the trajectories of X-ray tube motion during axial and helical scans were explicitly modeled by the code. To efficiently transport radiation through voxel geometry, we used the recently developed and validated geometry routine PENVOME¹⁰³ (Carl E. Ravin Advanced Imaging Laboratories, 2008).

The simulated scan protocol was the standard, size-based, abdomen-pelvis scan protocol in place at our institution for the weight range of the seven patients: 120 kVp, 85 mA (11.5-14.4 kg) or 90 mA (14.5-18.4 kg), 0.4-s gantry rotation period, pitch of 1.375, 40-mm beam collimation, and small body scan field-of-view (corresponding to small bowtie filter).

The total scan length of each patient was calculated as the total image coverage plus the overranging distance. The total image coverage was defined as the distance from 1 cm above the top of the liver/diaphragm to the bottom of the ischium, typical of the clinical image coverage for an abdomen-pelvis scan. The overranging distance was estimated from parameters displayed on the scanner console as “table speed (cm/s) × total scan time (s) – image coverage (cm)”. Estimates were found to be independent of slice thickness, reconstruction interval, and image coverage. The start location of the abdomen-pelvis scan was, therefore, 1 cm plus half of the overranging distance above the top of the liver/diaphragm, and the end location was half of the overranging distance below the bottom of the ischium.

4.2.4 Effective Dose Calculations

For each patient, the effective dose was calculated as the summation of radiosensitive organ dose values weighted by the tissue weighting factors defined by ICRP Publication 103²¹. Breast tissue is underdeveloped in patients of this age range and thus was not included in the calculation of effective dose. Dose to radiosensitive organs

that were not explicitly modeled was approximated by dose to neighboring organs¹⁰³. Complying with ICRP Publication 103, the weighting factor for the remainder organs was applied to the arithmetic mean dose of the 13 remainder organs of each gender.

4.2.5 Data Analysis

Dose variation across the patients was quantified by the coefficient of variation (standard deviation \times 100% / mean)¹⁰⁴. Organ dose was correlated with abdominopelvic size using linear regression analysis. Abdominopelvic size was expressed in terms of total scan length, a surrogate for the length of the abdominopelvic cavity, as well as mid-liver and mid-intestine equivalent diameters. The mid-liver/mid-intestine equivalent diameter was defined as the diameter of a circle having the same area as the cross-sectional area of the patient model on the plane halfway in between the inferior and posterior ends of the liver/small intestine. Effective dose was correlated with body weight of the patient model using linear regression analysis.

4.3 Results

Figure 15 illustrates a sample coronal dose distribution resultant from the abdomen-pelvis MDCT scan in a 2-year-old patient.

Organ dose received by the seven patients is summarized in Table 13. In general, dose variation was small for large organs in the scan coverage (mean: 6.6%; range: 4.9%-9.2%), larger for small organs in the scan coverage (mean: 10.3%; range: 1.4%-15.6%), and the largest for organs partially or completely outside the scan coverage (mean:

14.8%; range: 5.7%-27.7%). The uncertainty in the simulated organ dose was less than 2% for the thyroid, the combined organ of pharynx and larynx and the combined organ of trachea and bronchi, less than 5% for the eye, and less than 1% for the rest of the organs. Therefore, the variations in organ dose reported here resulted from variations in patient anatomy and body habitus. The seven patients had an abdomen-pelvis MDCT effective dose of 2.4-2.8 mSv, corresponding to normalized effective dose of 6.6-8.3 mSv/100mAs (coefficient of variation: 7.6%).

Also summarized in Table 13 are correlations of organ dose with abdominopelvic size. With the exception of dose to the testes, organ dose correlated weakly with total scan length. However, the dose to some organs correlated strongly with body diameters. We note in particular that dose to the kidney and the adrenal gland correlated strongly with mid-liver equivalent diameter, $r = -0.97$ and -0.98 , respectively (Figure 16a) and dose to the small intestine correlated strongly with mid-intestine equivalent diameter ($r = -0.97$) (Figure 16b). In addition, normalized effective dose correlated strongly with body weight ($r = -0.94$) (Figure 17).

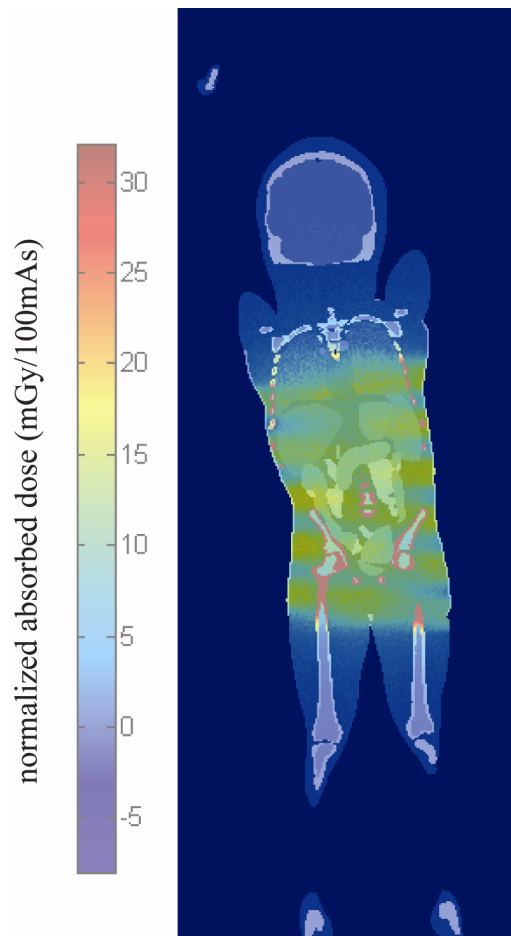


Figure 15: Coronal dose distribution in a 2-year-old patient, determined from the abdomen-pelvis MDCT scan. The coronal plane was taken about half-way in between the anterior and posterior surfaces of the abdominopelvic region of the patient. The computer model of the patient with organs shown on a gray scale was overlaid with a semi-transparent image of the normalized dose distribution on a colored scale. The patient's arms are out of this coronal plane.

Table 13: Variations across patients in normalized organ dose from an abdomen-pelvis MDCT scan and correlations of normalized organ dose with abdominopelvic size.

	Normalized organ dose (mGy/100mAs)			Pearson correlation coefficient (r) ^e		
	Mean	(Range)	CV ^d	Abdominopelvic size		
				Mid-liver equivalent diameter ^f	Mid-intestine equivalent diameter ^f	Total scan length ^g
Large organs in the scan coverage						
Kidneys ^a	11.6	(10.0 - 12.3)	6.6%	-0.97	-0.92	-0.23
Liver ^a	11.5	(10.6 - 12.2)	4.9%	-0.71	-0.54	0.30
Spleen ^a	10.8	(8.9 - 11.7)	9.2%	-0.83	-0.69	-0.31
Stomach ^a	12.0	(10.9 - 12.8)	6.0%	-0.75	-0.57	-0.12
Large Intestine	12.4	(10.6 - 13.0)	6.7%	-0.88	-0.94	-0.35
Small Intestine	13.6	(11.7 - 14.2)	6.2%	-0.90	-0.97	-0.26
Small organs in the scan coverage						
Gall bladder ^a	12.9	(10.2 - 14.6)	12.0%	-0.75	-0.63	-0.01
Pancreas	12.5	(11.0 - 13.4)	6.0%	-0.90	-0.66	0.05
Adrenals	11.2	(9.3 - 11.9)	7.6%	-0.98	-0.91	-0.18
Bladder	11.6	(9.4 - 14.2)	13.4%	-0.56	-0.49	-0.62
Prostate	11.3	(11.2 - 11.5)	1.4%	0.74	0.78	-0.56
Testes	13.0	(11.8 - 14.8)	12.0%	-0.27	-0.32	0.92
Ovaries	11.4	(9.5 - 13.8)	15.6%	-0.54	-0.73	-0.76
Uterus	11.1	(9.6 - 12.6)	11.5%	-0.70	-0.64	-0.51
Vagina	10.5	(9.4 - 11.2)	7.6%	-0.87	-0.88	-0.37
Organs partially or completely outside the scan coverage						
Brain	0.1	(0.03 - 0.07)	24.3%	-0.55	-0.58	-0.81
Eyes	0.0	(0.02 - 0.03)	27.7%	-0.23	-0.37	-0.73
Thyroid	1.1	(1.0 - 1.2)	6.6%	0.47	0.45	0.24
Breasts	7.9	(6.0 - 11.6)	24.7%	-0.24	-0.38	-0.71
Heart ^a	9.4	(8.5 - 10.2)	5.7%	-0.68	-0.71	0.33
Lungs ^a	7.9	(6.7 - 8.8)	8.6%	-0.63	-0.56	-0.35
Thymus	2.7	(2.2 - 3.7)	19.5%	0.22	0.16	0.03
Pharynx-larynx	0.4	(0.3 - 0.6)	19.3%	-0.03	-0.23	-0.80
Trachea-bronchi	1.8	(1.2 - 2.6)	25.1%	0.15	0.28	0.42
Esophagus	5.0	(3.5 - 6.0)	16.0%	-0.01	0.14	0.55
Compact bone ^a	9.1	(7.1 - 10.0)	10.3%	-0.92	-0.83	-0.16
Marrow ^b	5.4	(3.5 - 6.0)	16.4%	-0.91	-0.78	-0.28
Residual soft tissues ^c	4.4	(3.7 - 5.2)	13.3%	-0.49	-0.26	-0.22
Skin (torso only)	9.5	(8.1 - 10.1)	7.7%	-0.82	-0.78	-0.60

Table 13: Continued.

^a Organs individually segmented from CT images of the patients. Individually segmented compact bones included the backbone and the ribcage.

^b Bone marrow was assumed to be composed entirely of red bone marrow for patients of this age range. Additional dose to bone marrow deposited by photoelectrons released in the trabecular bone was accounted for by applying dose enhancement factors of King and Spiers¹⁰⁰.

^c Residual soft tissues included skeletal muscle, adipose tissue, cartilage, blood, lymphatic tissues, and connective tissues.

^d CV (coefficient of variation) = standard deviation \times 100% / mean¹⁰⁴.

^e The square of r equals R^2 , a measure of goodness-of-fit for linear regression analysis. r values larger than 0.90, corresponding to $R^2 > 0.81$, are highlighted in bold.

^f Mid-liver/mid-intestine equivalent diameter was defined as the diameter of a circle having the same area as the cross-sectional area of the patient model on the plane halfway in between the inferior and posterior ends of the liver/small intestine.

^g Total scan length was used as a surrogate for the length of the abdominopelvic region.

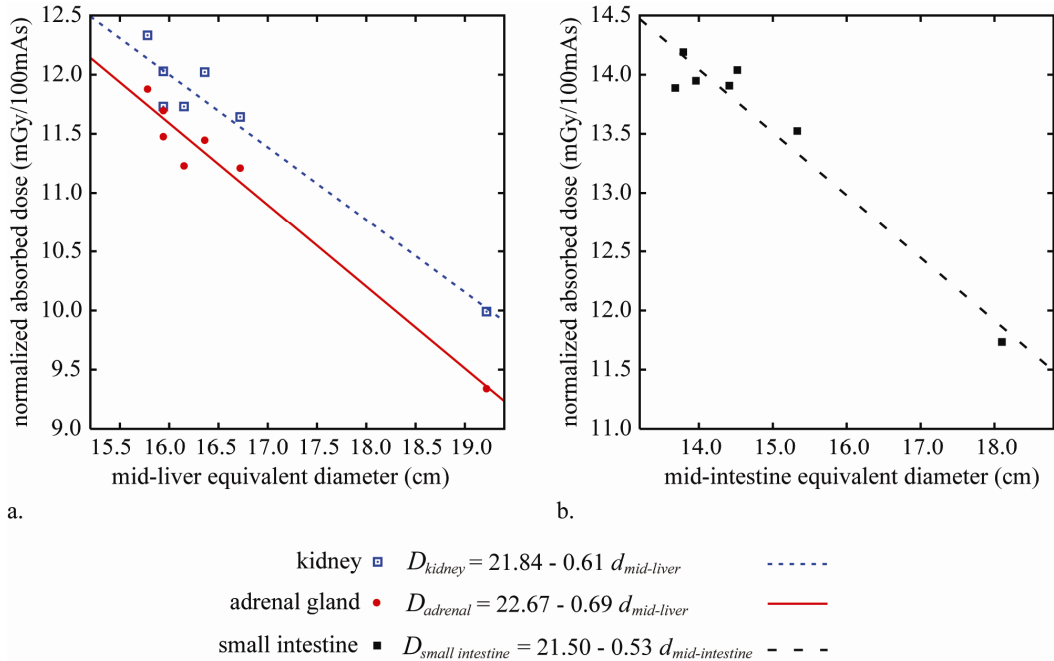


Figure 16: (a) Normalized absorbed dose (mGy/100mAs) to the kidney and the adrenal gland from the abdomen-pelvis MDCT scan as a function of mid-liver equivalent diameter and the results of regression analysis. (b) Normalized absorbed dose (mGy/100mAs) to the small intestine from the abdomen-pelvis MDCT scan as a function of mid-intestine equivalent diameter and the result of regression analysis. The mid-liver/mid-intestine equivalent diameter was defined as the diameter of a circle having the same area as the cross-sectional area of the patient model on the plane halfway in between the inferior and posterior ends of the liver/small intestine.

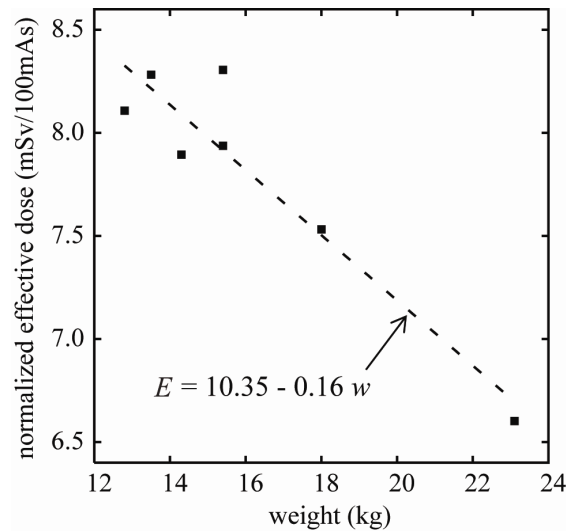


Figure 17: Normalized effective dose (mSv/100mAs) from the abdomen-pelvis MDCT scan as a function of patient model weight and the result of regression analysis. The weights of the patient models were not perfectly matched to the actual patient weights (discrepancy < 5 kg). The weights of the patient models were used here for the regression analysis.

4.4 Discussions

Using patient-specific computer models created from clinical MDCT data, we obtained dose values from an abdomen-pelvis MDCT scan that are patient-specific. Studying multiple patients in the same weight/protocol group provided insight into the magnitude of dose variation across patients due to the variability of patient anatomy and body habitus. Our results show that, in abdomen-pelvis MDCT, dose variations across patients were generally small for large organs in the scan coverage, but large for small organs in the scan coverage and for organs partially or completely outside the scan coverage. These results are consistent with our previous findings for a chest MDCT scan¹⁰³ and suggest that the size of an organ and its location relative to the scanned section of the body play important roles in dose variation across patients. The larger

dose variations exhibited by some small organs in the scan coverage may be attributable to the high helical pitch of 1.375 in our studies which left gaps of tissues unirradiated by the primary beam; the variety of locations that a small organ can take relative to those gaps led to a variation in organ dose. The dose variations exhibited by organs partially or completely outside the scan coverage were most likely caused by the variable locations these organs can take relative to the scanned part of the body.

Our work also suggested a method to estimate patient-specific dose for a larger cohort of patients. The strong correlations of dose to the kidney and the adrenal gland with mid-liver equivalent diameter (derivable from mid-abdomen circumference) and the strong correlation of dose to the small intestine with mid-intestine equivalent diameter (derivable from mid-pelvis circumference) may allow patient-specific dose to these organs be estimated for any other child in this size group provided that these strong relationships are confirmed in a larger scale study. In our previous study of a chest MDCT scan¹⁰³, similar strong correlations with body size were also found for the lung and the heart. We hypothesize that such correlations exist for organs, especially large organs, in the scan coverage that exhibit approximate bilateral symmetry. We will test this hypothesis in future studies involving larger numbers of patients.

Normalized effective dose from an abdomen-pelvis scan was found to decrease with body weight, consistent with the finding of our previous study for a chest scan¹⁰³. The correlation was stronger for an abdomen-pelvis scan ($r = -0.94$) than for a chest scan

($r = -0.80$). DeMarco et al.³⁰ reported an even stronger correlation for a whole-body scan ($R^2 = 0.944$ or $r = -0.97$) for patients of a much wider weight range (5-100 kg). This increase of correlation with total scan length may be explained by the fact that as more radiosensitive organs are included in the scan coverage, their contributions to effective dose become less uncertain, and body weight becomes a more prominent factor affecting effective dose. We note that while this work reports effective dose to individual patients, the ICRP 103 tissue weighting factors are mean values representing averages over both genders and a group of ages. For future studies, perhaps the recently proposed concept of effective risk⁷¹, which employs age- and gender-specific tissue risk coefficients, is a more appropriate metric for reporting risk to individual patients from CT examinations.

5. Patient-Specific Radiation Dose and Cancer Risk in Pediatric Chest CT: A Systematic Evaluation of the Effects of Patient Size and Scan Parameters*

5.1 Introduction

With the expanding use of computed tomography (CT) in children^{96, 97} and the increasing attention to the potential risk of CT radiation to this population^{15, 16}, there have been growing interests to better manage pediatric patient dose from CT examinations¹⁰⁵. Perhaps, the most important of these interests are (1) to eliminate unnecessary or redundant CT examinations, and (2) to adapt CT scan parameters to patient size. The first goal can be facilitated by a dose-reporting system that provides estimates of radiation dose and potential cancer risk specific to each CT examination of each patient. Knowledge of dose and risk may aid in examination justification, including the necessity for and frequency of examinations. The second goal can benefit from an understanding of the quantitative relationship between patient dose/risk and various factors affecting dose/risk, notably patient size/age and CT scan parameters.

Due to the limited designs of pediatric anthropomorphic phantoms, either physical¹⁰⁶ or computational^{65, 68} in nature, efforts to report CT dose and to estimate radiation risk have mainly relied on CT dose index (CTDI) and dose-length product (DLP) determined in standard-size cylindrical phantoms and their conversion coefficients to effective dose derived for patients of standard ages^{36, 38}. As such, dose and

* This chapter is based on a manuscript with the same title that will be submitted to the journal *Radiology*.

risk information specific to individual patients is not available. Similarly, studies that examined the dependence of dose on patient size and scan parameters have mainly been carried out in cylindrical or oval-shaped phantoms^{92, 93, 107}. As such, our knowledge of how actual patient dose depends on body size and scan parameters is less than desirable.

Recently, a library of pediatric computer models were developed in our laboratory based on the clinical CT data of forty pediatric CT patients⁷⁹. The purpose of this study was to combine this unique resource with a validated Monte Carlo technique¹⁰⁸ to estimate patient-specific radiation dose and cancer risk from pediatric chest CT examinations and to conduct a systematic evaluation of factors affecting dose and risk, including patient size/age and scan parameters.

5.2 Materials and Methods

This study was partially funded by GE Healthcare. The authors had complete control over the data and information submitted in this article. Our institutional review board determined that the study was in compliance with the Health Insurance Portability and Accountability Act, and did not require informed consent.

5.2.1 Patients

The study included thirty pediatric patients (16 males and 14 females; median age, 3 years; age range, 0-16 years; median weight, 14 kg; weight range, 2-41 kg), who underwent chest or chest-abdomen-pelvis CT examinations at our institution between

2005 and 2006. All examinations were performed on a clinical CT scanner (LightSpeed VCT or LightSpeed 16, GE Healthcare, Waukesha, WI).

5.2.2 Patient-Specific Computer Models

A non-uniform rational B-spline (NURBS) based full-body computer model⁷⁹ of each patient was created based on the patient's clinical CT data: large organs and structures inside the image volume were individually segmented and modeled; other organs were created by transforming existing adult male or female full-body computer models (developed from visible human data)⁸³ to match the framework defined by the segmented organs, referencing the organ volume and anthropometry data in ICRP Publication 89¹⁰⁹. The resultant full-body model consisted of a total of 43 and 44 organs for female and male patients, respectively, and included most of the radiosensitive organs defined by ICRP Publication 103²¹.

The NURBS model of each patient was voxelized at 1-mm isotropic resolution for input into Monte Carlo simulations, with the exception of two patients who were younger than 2-month old and for whom the voxelization was performed at 0.5-mm isotropic resolution. As clinical CT data of the chest were available for all thirty patients in this study, the chest section of each computer model more closely match the patient anatomy, allowing more reliable estimation of dose and risk for examinations of the chest.

5.2.3 CT Scanner and Protocols

A multi-detector array CT system (LightSpeed VCT, GE Healthcare, Waukesha, WI) was used in this investigation. Organ dose and cancer risk associated with eight scan protocols enabled by the system (Table 14) were estimated to assess the effects of patient size and scan parameters, where the first four protocols were selected from the set of size-based pediatric chest protocols in use at our institution. Protocols A, B, and C were used to examine the effect of bowtie filter choice, Protocols A and D for beam collimation, protocols A and E for helical pitch, and protocols A, F, G, and H for peak tube potential. While other beam collimation and helical pitch settings were also available on the CT system, the values in Table 14 reflect the most frequently used settings for routine examinations of pediatric chest.

Table 14: CT protocols investigated in this study.

protocol ^a	kVp	scan field-of-view (FOV)	bowtie filter	pitch	collimation
A	120	pediatric body	small	1.375	40
B	120	medium body	medium	1.375	40
C	120	large body	large	1.375	40
D	120	pediatric body	small	1.375	20
E	120	pediatric body	small	0.984	40
F	80	pediatric body	small	1.375	40
G	100	pediatric body	small	1.375	40
H	140	pediatric body	small	1.375	40

^a Protocols A, B, and C were used to examine the effect of bowtie filter choice, protocols A and D for beam collimation, protocols A and E for helical pitch, and protocols A, F, G, and H for peak tube potential.

5.2.4 Radiation Dose and Cancer Risk Estimations

Organ dose received by each patient from each scan protocol was estimated using a previously developed Monte Carlo program for dose simulation on the LightSpeed VCT scanner¹⁰⁸. The program explicitly modeled the geometry of the CT system, the three-dimensional geometry of the bowtie filters, and the trajectories of X-ray tube motion during axial and helical scans. The accuracy of the simulated dose was previously validated in a cylindrical phantom and two anthropomorphic phantoms for both axial and helical scanning modes¹⁰⁸. Simulations were found to agree with measurements within 1-11% on average and 5-17% maximum¹⁰⁸.

For each patient, the total scan length was determined as the total image coverage plus the overranging distance (additional scan length necessary for data interpolation in helical reconstruction)⁸². The total image coverage was typical of a clinical chest scan, extending from 1 cm above lung apex to 1 cm below lung base. The overranging distance was dependent on beam collimation and helical pitch and was estimated from the scanner console parameters as “table speed (cm/s) × total scan time (s) – image coverage (cm)”. The start location of the chest scan was, therefore, 1 cm plus half of the overranging distance above lung apex, and the end location was the same distance below lung base.

The organ dose values estimated for each patient were used to calculate effective dose as

$$E = \sum_T w_T H_T, \quad (13)$$

where H_T is the equivalent dose for organ/tissue T and w_T is the tissue weighting factor defined by ICRP Publication 103²¹. Dose to radiosensitive organs that were not explicitly modeled was approximated by dose to neighboring organs¹⁰⁸. Dose to gender-specific organs (i.e., prostate, testes, ovaries, uterus, vagina) was only included in the effective dose calculations for the respective genders, and breast dose was only included in the effective dose calculations for the female patients.

While widely used as a surrogate for radiation risk, effective dose is defined for a *reference hermaphrodite person* and is not suitable for individual patients; the tissue weighting factors are mean values representing averages over many individuals of different genders and age groups²¹. To more accurately estimate individual patient risks, we further implemented the recently proposed concept of effective risk⁷¹ defined as

$$R = \sum_T r_T H_T, \quad (14)$$

where r_T is the gender-, age-, and tissue-specific risk coefficient (cases/100,000 exposed to 0.1 Gy) for lifetime attributable risk of cancer incidence. Thus, $r_T H_T$ represents the lifetime attributable risk of cancer incidence for organ/tissue T . Values for r_T are tabulated in BEIR VII report¹⁴ for leukemia and for cancer of 8-9 high-risk organs of each gender at discrete ages of 0, 5, 10, 15, 20, 30, 40, 50, 60, 70, 80 years¹⁴. Values for r_T at intermediate ages were determined by linear interpolation. Cancer of other

radiosensitive organs shares a collective risk coefficient (r_{other})¹⁴. This risk coefficient was applied to a weighted average dose of other radiosensitive organs, defined as¹⁵

$$H_{\text{other}} = \frac{\sum_{T \in \{\text{other organs}\}} w_T H_T}{\sum_{T \in \{\text{other organs}\}} w_T}. \quad (15)$$

Those organs included heart, kidney, gall bladder, spleen, pancreas, adrenal glands, thymus, small intestine, salivary glands, extrathoracic region, lymph node, muscle, oral mucosa, bone surface, brain, skin, testes (male only), and esophagus, among which the reminder organs, as defined by ICRP Publication 103²¹, were each assigned a tissue-weighting factor of 0.01.

To compare patient-specific dose estimation with current dose-reporting method, volume averaged CTDI (CTDI_{vol})²⁰ was also calculated for the eight CT protocols using the CTDI_{100} table and the tables of technique adjustment factors in the technical reference manual of the LightSpeed VCT scanner. The CTDI_{vol} values estimated in this way agreed with those from patients' dosimetry report to within about 5%.

5.2.5 Data Analysis

For each CT protocol, the estimated organ dose, effective dose, risk of cancer incidence for individual organs, and effective risk were correlated with body size of the patient model using the sample Pearson correlation coefficient¹⁰⁴. Seven indices of body size were initially considered (Table 15). As all indices correlated well with average chest diameter except weight and total scan length, a surrogate for chest height (Table

15), average chest diameter, total scan length, and weight were chosen as the final body size indices to correlate with dose and risk estimates.

Table 15: Body size indices and their correlations with average chest diameter.

body size index ^a	body region	Pearson correlation coefficient with average chest diameter
weight ^b	whole body	0.93
average chest diameter	start: lung apex end: lung base	1
average abdomen diameter	start: liver top end: iliac crest top	0.98
average pelvis diameter	start: iliac crest top end: ischium bottom	0.98
average abdomen-pelvis diameter	start: liver top end: ischium bottom	0.98
average trunk diameter	start: lung apex end: ischium bottom	0.99
total scan length	a surrogate for chest height	0.91

^a The average diameter of a body region (chest, abdomen, pelvis, abdomen-pelvis, trunk) was calculated as

$$d = 2\sqrt{\frac{\text{average cross-sectional area of the region}}{\pi}} = 2\sqrt{\frac{\text{region volume}}{\pi \cdot \text{region height}}} \quad (16)$$

^b Total body weight of the voxelized computer model.

5.3 Results

5.3.1 Effects of Patient Size

For all eight CT scan protocols, normalized dose to individual organs (in the unit of mGy/100mAs) decreased exponentially with increasing average chest diameter (Figure 18 and Table 16 to Table 23). The correlation was strong for large organs and centrally-located tubular organs inside the scan coverage (Figure 18a), but generally weaker for small organs inside the scan coverage (Figure 18b), for organs on the

periphery or outside of the scan coverage (Figure 18c), and for distributed organs (Figure 18d). Similar trend of correlation with average chest diameter was also found for normalized risk of cancer incidence to individual organs (Figure 19 and Table 16 to Table 23); however, cancer risks were gender-dependent. Effective dose and effective risk correlated strongly, decreasing exponentially, with average chest diameter (Figure 20 and Table 16 to Table 23). Effective dose showed slight gender dependence, whereas effective risk was highly gender dependent.

The correlations of dose and risk estimates with total scan length (a surrogate for chest height) and weight were generally weaker than the correlations with average chest diameter (Table 16 to Table 23). As such, curve fitting was not performed for these two patient size indices.

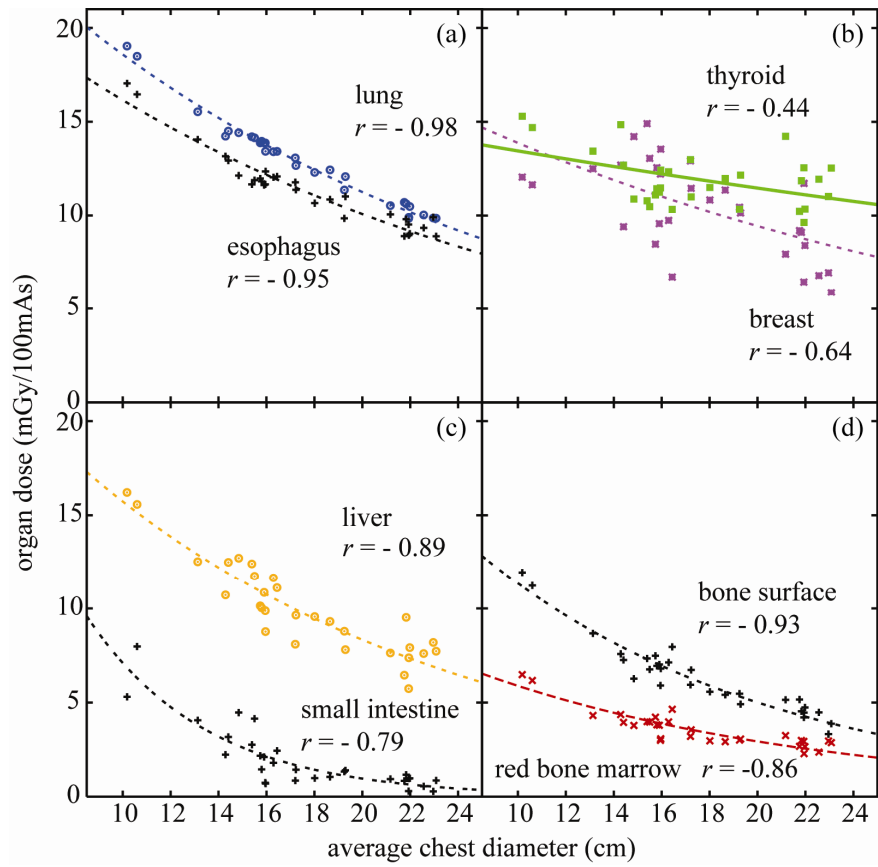


Figure 18: Examples of normalized dose to individual organs, resultant from Protocol A, as a function of average chest diameter for (a) large organs and centrally-located tubular organs inside the chest scan coverage, (b) small organs inside the chest scan coverage, (c) organs on the periphery or outside the chest scan coverage, and (d) distributed organs. The symbols represent dose to the organs of individual patients. The lines are exponential fits $y = \exp(ax + b)$ to the data. The quantity r is the Pearson sample correlation coefficient.

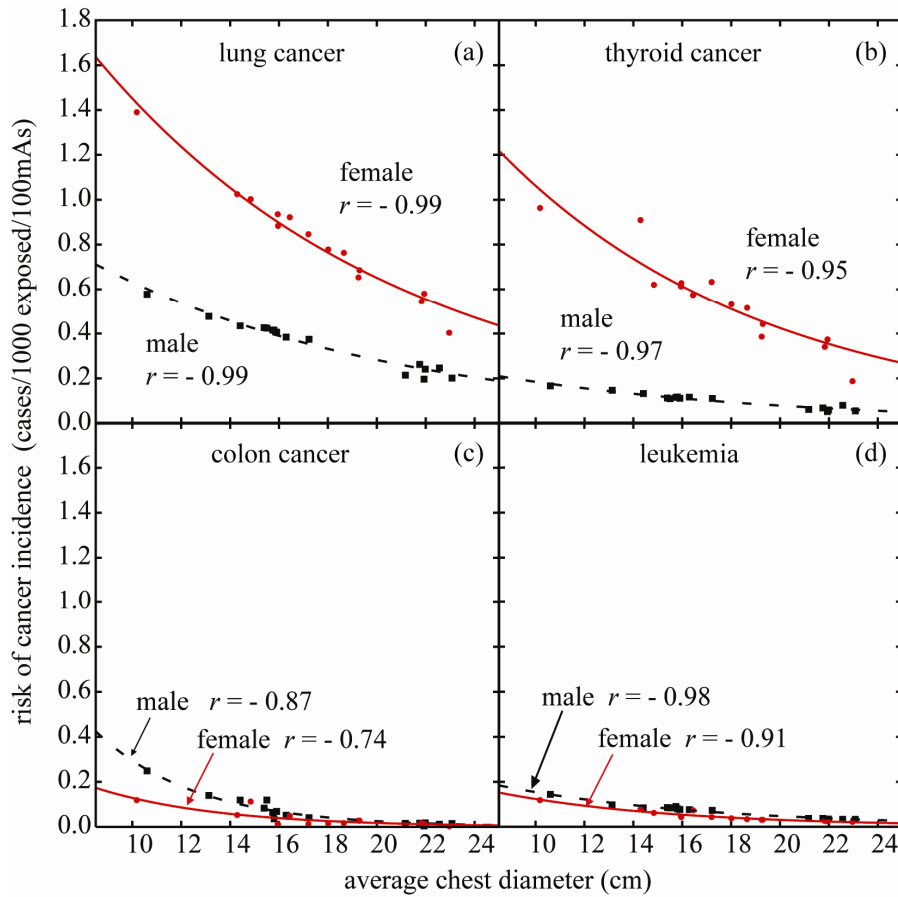


Figure 19: Examples of normalized cancer risk to individual organs, resultant from Protocol A, as a function of average chest diameter for (a) large organs inside the chest scan coverage, (b) small organs inside the chest scan coverage, (c) organs on the periphery or outside the chest scan coverage, and (d) distributed organs. Risk of colon cancer was assessed using dose to the large intestine, and risk of leukemia was assessed using dose to the red bone marrow. The symbols represent the risks of individual patients. The lines are exponential fits $y = \exp(ax + b)$ to the data. The quantity r is the Pearson sample correlation coefficient.

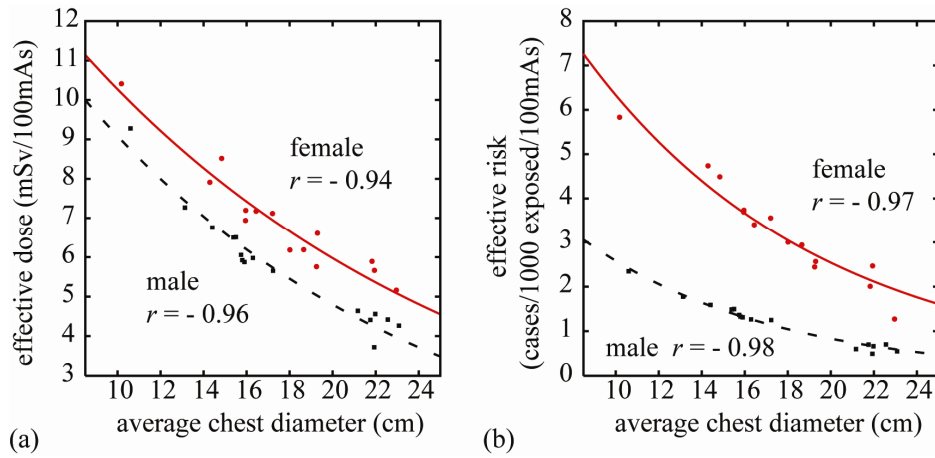


Figure 20: Normalized effective dose and effective risk, resultant from Protocol A. The symbols represent effective dose and effective risk estimated for individual patients. The lines are exponential fits $y = \exp(ax + b)$ to the data. The quantity r is the Pearson sample correlation coefficient.

Table 16: Protocol A (120 kVp, pediatric body scan FOV, small bowtie filter, 1.375 pitch, 40 mm collimation): correlations of organ dose, effective dose, cancer risk to individual organs, and effective risk with three body size indices: average chest diameter, total scan length (a surrogate for chest height), and weight, and the results of exponential fits $y = \exp(ax + b)$ to the relationships between dose/risk estimates and average chest diameter.

	Pearson correlation coefficient (r)			fitting parameters ^ε		
	average chest diameter	total scan length	weight	a	b	rms of residuals
Dose						
lungs	-0.98	-0.85	-0.88	-0.050213	3.424470	0.320426
heart	-0.96	-0.81	-0.88	-0.040762	3.298130	0.588495
thymus	-0.93	-0.79	-0.78	-0.046599	3.364670	0.710623
thyroid	-0.44	-0.26	-0.28	-0.015940	2.758440	1.321500
breasts	-0.64	-0.71	-0.66	-0.038467	3.015030	1.988640
esophagus	-0.95	-0.77	-0.80	-0.047221	3.254310	0.524667
trachea-bronchi	-0.91	-0.75	-0.74	-0.045364	3.270980	0.741304
eyes	-0.79	-0.65	-0.67	-0.179066	1.717530	0.085230
brain	-0.88	-0.74	-0.77	-0.152745	1.699850	0.072215
pharynx-larynx	-0.80	-0.66	-0.65	-0.095600	3.500940	1.398750
liver	-0.89	-0.75	-0.78	-0.063523	3.390750	1.024030
gall bladder	-0.70	-0.61	-0.62	-0.125766	4.059540	3.018020
kidneys	-0.64	-0.43	-0.53	-0.091337	3.257740	1.580800
adrenals	-0.80	-0.59	-0.68	-0.065704	3.236350	1.211950
spleen	-0.88	-0.71	-0.77	-0.062840	3.326460	0.957355
stomach	-0.78	-0.69	-0.75	-0.052395	3.196190	1.497510
pancreas	-0.68	-0.63	-0.67	-0.101094	3.500790	2.445100
small intestine	-0.79	-0.67	-0.68	-0.200268	3.963150	0.831160
large intestine	-0.80	-0.68	-0.69	-0.204325	4.006260	0.896225
urinary bladder	-0.78	-0.72	-0.73	-0.163335	1.012290	0.091516
prostate	-0.83	-0.82	-0.79	-0.174920	1.193390	0.086215
testes	-0.86	-0.82	-0.78	-0.249787	1.795040	0.033419
ovaries	-0.82	-0.65	-0.74	-0.156647	1.004470	0.083983
uterus	-0.82	-0.66	-0.74	-0.151782	0.782001	0.071510
vagina	-0.82	-0.68	-0.76	-0.145742	0.353936	0.051563
residual soft tissue	-0.90	-0.79	-0.83	-0.102597	2.876290	0.391693
bone surface	-0.93	-0.79	-0.85	-0.081877	3.247690	0.567448
red bone marrow	-0.86	-0.67	-0.72	-0.069637	2.468830	0.433789
skin	-0.77	-0.65	-0.68	-0.096130	2.340340	0.479150
effective dose (male)	-0.96	-0.90	-0.90	-0.063847	2.845030	0.307285
effective dose (female)	-0.94	-0.73	-0.79	-0.054230	2.871750	0.388341

Table 16: Continued.

Risk - male						
lung cancer	-0.99	-0.96	-0.97	-0.080395	0.343639	0.023308
thyroid cancer	-0.97	-0.92	-0.94	-0.084693	-0.839721	0.008674
liver cancer	-0.97	-0.94	-0.95	-0.093961	-1.314180	0.005442
stomach cancer	-0.92	-0.92	-0.94	-0.082348	-1.268850	0.010092
colon cancer	-0.87	-0.80	-0.77	-0.244130	1.219350	0.016805
bladder cancer	-0.85	-0.83	-0.80	-0.190044	-2.333970	0.001845
prostate cancer	-0.84	-0.83	-0.80	-0.185120	-3.375750	0.000766
leukemia	-0.98	-0.93	-0.92	-0.117654	-0.692436	0.005561
other cancer	-0.98	-0.95	-0.94	-0.129258	1.402370	0.043734
effective risk	-0.98	-0.94	-0.94	-0.113074	2.079540	0.082711
Risk - female						
lung cancer	-0.99	-0.85	-0.90	-0.080169	1.174350	0.044444
thyroid cancer	-0.95	-0.87	-0.89	-0.091652	0.977005	0.081984
breast cancer	-0.78	-0.87	-0.80	-0.062672	1.153540	0.239272
liver cancer	-0.92	-0.72	-0.79	-0.090786	-2.181240	0.002830
stomach cancer	-0.85	-0.69	-0.77	-0.071884	-1.219400	0.016119
colon cancer	-0.74	-0.57	-0.61	-0.199068	-0.057783	0.023101
bladder cancer	-0.84	-0.69	-0.76	-0.165243	-3.139700	0.001235
ovary cancer	-0.84	-0.67	-0.74	-0.173008	-3.385040	0.000826
uterus cancer	-0.84	-0.68	-0.74	-0.165492	-4.383140	0.000334
leukemia	-0.91	-0.69	-0.75	-0.138717	-0.704148	0.008501
other cancer	-0.94	-0.75	-0.79	-0.141490	1.972610	0.094100
effective risk	-0.97	-0.88	-0.89	-0.091331	2.759070	0.331453

^ξ The unit of a is cm^{-1} and b is unitless. "rms of residuals" stands for the root-mean-square of the residuals; it represents the average discrepancy between dose/risk values predicted by the fitting function and the dose/risk results estimated by the Monte Carlo method. The unit of "rms of residuals" is mGy/100 mAs or mSv/100mAs for dose estimates and cases/1000 exposed/100 mAs for risk estimates.

Table 17: Protocol B (120 kVp, medium body scan FOV, medium bowtie filter, 1.375 pitch, 40 mm collimation): correlations of organ dose, effective dose, cancer risk to individual organs, and effective risk with three body size indices: average chest diameter, total scan length (a surrogate for chest height), and weight, and the results of exponential fits $y = \exp(ax + b)$ to the relationships between dose/risk estimates and average chest diameter.

	Pearson correlation coefficient (r)			fitting parameters ^ε		
	average chest diameter	total scan length	weight	a	b	rms of residuals
Dose						
lungs	-0.98	-0.85	-0.89	-0.043172	3.428470	0.345270
heart	-0.95	-0.81	-0.88	-0.036262	3.309100	0.598506
thymus	-0.93	-0.79	-0.78	-0.042842	3.372050	0.724682
thyroid	-0.40	-0.21	-0.24	-0.014066	2.789810	1.395710
breasts	-0.57	-0.67	-0.62	-0.031546	3.077840	2.318010
esophagus	-0.95	-0.77	-0.80	-0.043919	3.262510	0.522698
trachea-bronchi	-0.91	-0.74	-0.74	-0.041855	3.271910	0.747469
eyes	-0.78	-0.65	-0.67	-0.176483	1.791700	0.095791
brain	-0.89	-0.75	-0.78	-0.146438	1.729320	0.080993
pharynx-larynx	-0.80	-0.66	-0.65	-0.091188	3.501120	1.473710
liver	-0.88	-0.74	-0.78	-0.056565	3.390360	1.109860
gall bladder	-0.69	-0.61	-0.62	-0.117870	4.031250	3.263220
kidneys	-0.62	-0.41	-0.51	-0.084550	3.274220	1.780840
adrenals	-0.79	-0.57	-0.67	-0.061159	3.246640	1.311110
spleen	-0.88	-0.70	-0.77	-0.056292	3.369680	1.067390
stomach	-0.75	-0.67	-0.72	-0.046744	3.221080	1.699710
pancreas	-0.68	-0.62	-0.66	-0.096816	3.520820	2.611330
small intestine	-0.79	-0.67	-0.69	-0.192540	3.944980	0.908965
large intestine	-0.80	-0.68	-0.69	-0.198105	4.026540	1.010440
urinary bladder	-0.78	-0.72	-0.73	-0.160570	1.090020	0.102656
prostate	-0.83	-0.83	-0.80	-0.170154	1.228230	0.093875
testes	-0.87	-0.83	-0.79	-0.239570	1.736730	0.038188
ovaries	-0.81	-0.63	-0.73	-0.153007	1.061640	0.095429
uterus	-0.81	-0.67	-0.75	-0.149600	0.871050	0.081901
vagina	-0.82	-0.68	-0.76	-0.143634	0.424179	0.057295
residual soft tissue	-0.90	-0.80	-0.84	-0.095085	2.901240	0.448163
bone surface	-0.93	-0.79	-0.86	-0.076011	3.289240	0.646910
red bone marrow	-0.85	-0.67	-0.71	-0.064290	2.506380	0.483272
skin	-0.75	-0.65	-0.67	-0.087711	2.383820	0.566310
effective dose (male)	-0.96	-0.91	-0.91	-0.058780	2.869570	0.324615
effective dose (female)	-0.94	-0.73	-0.80	-0.047391	2.880170	0.410536

Table 17: Continued.

Risk - male						
lung cancer	-0.98	-0.96	-0.97	-0.074204	0.362256	0.027418
thyroid cancer	-0.97	-0.92	-0.94	-0.082441	-0.813721	0.009583
liver cancer	-0.97	-0.94	-0.96	-0.088457	-1.290110	0.006197
stomach cancer	-0.91	-0.92	-0.94	-0.077568	-1.230830	0.011508
colon cancer	-0.87	-0.81	-0.78	-0.237918	1.245770	0.019229
bladder cancer	-0.85	-0.84	-0.80	-0.188100	-2.241860	0.002037
prostate cancer	-0.84	-0.84	-0.80	-0.179680	-3.355950	0.000850
leukemia	-0.98	-0.93	-0.93	-0.113076	-0.641574	0.006477
other cancer	-0.98	-0.95	-0.95	-0.125316	1.426860	0.049340
effective risk	-0.98	-0.95	-0.95	-0.108157	2.102770	0.094117
Risk - female						
lung cancer	-0.99	-0.86	-0.91	-0.073090	1.176510	0.053519
thyroid cancer	-0.95	-0.88	-0.89	-0.090355	1.017130	0.085040
breast cancer	-0.75	-0.87	-0.80	-0.055558	1.216340	0.280440
liver cancer	-0.92	-0.74	-0.80	-0.083027	-2.196910	0.003027
stomach cancer	-0.82	-0.68	-0.76	-0.065764	-1.201470	0.018447
colon cancer	-0.74	-0.57	-0.61	-0.192561	-0.050197	0.025822
bladder cancer	-0.83	-0.69	-0.75	-0.161291	-3.087470	0.001385
ovary cancer	-0.83	-0.65	-0.74	-0.171284	-3.304740	0.000937
uterus cancer	-0.84	-0.68	-0.74	-0.163941	-4.281150	0.000375
leukemia	-0.91	-0.70	-0.75	-0.133366	-0.667036	0.009631
other cancer	-0.94	-0.76	-0.80	-0.137541	1.995210	0.103552
effective risk	-0.97	-0.89	-0.90	-0.084814	2.775810	0.377755

^ξ The unit of a is cm^{-1} and b is unitless. "rms of residuals" stands for the root-mean-square of the residuals; it represents the average discrepancy between dose/risk values predicted by the fitting function and the dose/risk results estimated by the Monte Carlo method. The unit of "rms of residuals" is $\text{mGy}/100 \text{ mAs}$ or $\text{mSv}/100\text{mAs}$ for dose estimates and $\text{cases}/1000 \text{ exposed}/100 \text{ mAs}$ for risk estimates.

Table 18: Protocol C (120 kVp, large body scan FOV, large bowtie filter, 1.375 pitch, 40 mm collimation): correlations of organ dose, effective dose, cancer risk to individual organs, and effective risk with three body size indices: average chest diameter, total scan length (a surrogate for chest height), and weight, and the results of exponential fits $y = \exp(ax + b)$ to the relationships between dose/risk estimates and average chest diameter.

	Pearson correlation coefficient (r)			fitting parameters ^ε		
	average chest diameter	total scan length	weight	a	b	rms of residuals
Dose						
lungs	-0.98	-0.85	-0.90	-0.034711	3.191130	0.291553
heart	-0.95	-0.80	-0.88	-0.030329	3.094860	0.484088
thymus	-0.93	-0.79	-0.78	-0.037559	3.163880	0.566816
thyroid	-0.41	-0.23	-0.26	-0.012918	2.646380	1.124350
breasts	-0.48	-0.60	-0.56	-0.024142	2.887650	2.082900
esophagus	-0.95	-0.78	-0.81	-0.038692	3.065170	0.411794
trachea-bronchi	-0.91	-0.75	-0.75	-0.037296	3.079350	0.589214
eyes	-0.78	-0.65	-0.67	-0.165546	1.587690	0.090570
brain	-0.89	-0.76	-0.79	-0.137534	1.561900	0.076760
pharynx-larynx	-0.80	-0.67	-0.66	-0.087027	3.325440	1.281910
liver	-0.87	-0.73	-0.77	-0.048238	3.155470	0.971865
gall bladder	-0.68	-0.60	-0.62	-0.108739	3.778200	2.836500
kidneys	-0.59	-0.38	-0.49	-0.073279	3.012380	1.604990
adrenals	-0.76	-0.55	-0.65	-0.054139	3.030420	1.164040
spleen	-0.86	-0.69	-0.76	-0.047423	3.154330	0.960472
stomach	-0.70	-0.62	-0.68	-0.039783	3.011260	1.543950
pancreas	-0.67	-0.62	-0.66	-0.090717	3.321010	2.279030
small intestine	-0.79	-0.68	-0.70	-0.181283	3.685260	0.805247
large intestine	-0.80	-0.69	-0.70	-0.187742	3.775840	0.902279
urinary bladder	-0.78	-0.72	-0.74	-0.156983	1.013260	0.098748
prostate	-0.85	-0.84	-0.81	-0.170107	1.205690	0.082654
testes	-0.87	-0.83	-0.79	-0.239195	1.703810	0.034472
ovaries	-0.81	-0.65	-0.74	-0.147410	0.929825	0.088773
uterus	-0.81	-0.67	-0.75	-0.141755	0.717792	0.078423
vagina	-0.82	-0.68	-0.75	-0.145301	0.467446	0.058464
residual soft tissue	-0.90	-0.81	-0.85	-0.086085	2.681370	0.409274
bone surface	-0.93	-0.79	-0.86	-0.067967	3.073630	0.587449
red bone marrow	-0.84	-0.65	-0.70	-0.057298	2.326970	0.444775
skin	-0.73	-0.63	-0.66	-0.077943	2.158370	0.522363
effective dose (male)	-0.96	-0.91	-0.92	-0.052091	2.662840	0.277358
effective dose (female)	-0.94	-0.73	-0.81	-0.039689	2.661950	0.351419

Table 18: Continued.

Risk - male						
lung cancer	-0.98	-0.97	-0.98	-0.066631	0.139302	0.025670
thyroid cancer	-0.97	-0.92	-0.95	-0.080882	-0.960416	0.008792
liver cancer	-0.96	-0.95	-0.96	-0.081231	-1.506060	0.005700
stomach cancer	-0.89	-0.92	-0.93	-0.070996	-1.436470	0.010675
colon cancer	-0.88	-0.82	-0.79	-0.227266	0.993084	0.017346
bladder cancer	-0.85	-0.84	-0.81	-0.182040	-2.355800	0.001974
prostate cancer	-0.86	-0.86	-0.82	-0.179336	-3.380300	0.000754
leukemia	-0.98	-0.94	-0.94	-0.107034	-0.804353	0.006303
other cancer	-0.99	-0.96	-0.95	-0.120022	1.239140	0.046444
effective risk	-0.98	-0.95	-0.95	-0.101972	1.903790	0.089009
Risk - female						
lung cancer	-0.99	-0.87	-0.93	-0.064916	0.943610	0.051920
thyroid cancer	-0.95	-0.89	-0.91	-0.087620	0.845797	0.073790
breast cancer	-0.71	-0.86	-0.79	-0.048403	1.030150	0.257782
liver cancer	-0.92	-0.75	-0.82	-0.074296	-2.439050	0.002604
stomach cancer	-0.80	-0.66	-0.74	-0.059581	-1.396770	0.016683
colon cancer	-0.73	-0.57	-0.62	-0.182293	-0.302708	0.022992
bladder cancer	-0.83	-0.68	-0.75	-0.159393	-3.135910	0.001346
ovary cancer	-0.84	-0.68	-0.75	-0.166119	-3.434790	0.000850
uterus cancer	-0.83	-0.68	-0.74	-0.157882	-4.416900	0.000374
leukemia	-0.91	-0.70	-0.76	-0.126274	-0.848473	0.009116
other cancer	-0.94	-0.77	-0.81	-0.131242	1.788120	0.094658
effective risk	-0.97	-0.91	-0.92	-0.077740	2.567090	0.351656

^ξ The unit of a is cm^{-1} and b is unitless. "rms of residuals" stands for the root-mean-square of the residuals; it represents the average discrepancy between dose/risk values predicted by the fitting function and the dose/risk results estimated by the Monte Carlo method. The unit of "rms of residuals" is mGy/100 mAs or mSv/100mAs for dose estimates and cases/1000 exposed/100 mAs for risk estimates.

Table 19: Protocol D (120 kVp, pediatric body scan FOV, small bowtie filter, 1.375 pitch, 20 mm collimation): correlations of organ dose, effective dose, cancer risk to individual organs, and effective risk with three body size indices: average chest diameter, total scan length (a surrogate for chest height), and weight, and the results of exponential fits $y = \exp(ax + b)$ to the relationships between dose/risk estimates and average chest diameter.

	Pearson correlation coefficient (r)			fitting parameters ^ε		
	average chest diameter	total scan length	weight	a	b	rms of residuals
Dose						
lungs	-0.98	-0.83	-0.87	-0.049948	3.440250	0.378479
heart	-0.96	-0.82	-0.87	-0.041876	3.344310	0.522461
thymus	-0.92	-0.74	-0.78	-0.039413	3.255730	0.686429
thyroid	-0.52	-0.33	-0.31	-0.020362	2.830780	1.340140
breasts	-0.76	-0.70	-0.72	-0.043013	3.115090	1.475900
esophagus	-0.92	-0.73	-0.77	-0.049258	3.277310	0.669035
trachea-bronchi	-0.89	-0.71	-0.71	-0.043115	3.223680	0.813298
eyes	-0.76	-0.64	-0.66	-0.142563	0.601166	0.048691
brain	-0.90	-0.77	-0.80	-0.127323	0.914356	0.047033
pharynx-larynx	-0.77	-0.62	-0.63	-0.127029	3.647960	1.387650
liver	-0.83	-0.69	-0.74	-0.066823	3.340100	1.275570
gall bladder	-0.61	-0.52	-0.55	-0.124924	3.625740	2.708920
kidneys	-0.51	-0.27	-0.37	-0.105197	3.058180	1.462460
adrenals	-0.58	-0.33	-0.45	-0.070754	3.068990	1.768260
spleen	-0.74	-0.53	-0.61	-0.066597	3.287810	1.527220
stomach	-0.68	-0.62	-0.65	-0.056670	3.147170	1.896660
pancreas	-0.59	-0.53	-0.55	-0.117721	3.285570	2.103140
small intestine	-0.78	-0.69	-0.71	-0.147626	2.513230	0.392850
large intestine	-0.71	-0.61	-0.62	-0.185912	3.030920	0.549034
urinary bladder	-0.77	-0.72	-0.73	-0.154700	0.461175	0.061158
prostate	-0.83	-0.83	-0.79	-0.165430	0.644765	0.057053
testes	-0.87	-0.83	-0.79	-0.238459	1.147250	0.019776
ovaries	-0.80	-0.64	-0.74	-0.142162	0.342258	0.055380
uterus	-0.80	-0.66	-0.75	-0.140158	0.192700	0.049478
vagina	-0.79	-0.67	-0.75	-0.132421	-0.290593	0.036492
residual soft tissue	-0.89	-0.78	-0.82	-0.093950	2.587510	0.346522
bone surface	-0.92	-0.78	-0.86	-0.068741	2.905490	0.506205
red bone marrow	-0.83	-0.63	-0.68	-0.055158	2.106100	0.352718
skin	-0.75	-0.63	-0.67	-0.090715	2.170380	0.437774
effective dose (male)	-0.94	-0.89	-0.88	-0.060846	2.708210	0.322329
effective dose (female)	-0.89	-0.63	-0.72	-0.053110	2.765170	0.524768

Table 19: Continued.

Risk - male						
lung cancer	-0.98	-0.95	-0.96	-0.080468	0.362521	0.022997
thyroid cancer	-0.97	-0.93	-0.94	-0.090324	-0.768955	0.008107
liver cancer	-0.97	-0.94	-0.95	-0.099456	-1.289650	0.005103
stomach cancer	-0.89	-0.91	-0.89	-0.091355	-1.220140	0.010899
colon cancer	-0.79	-0.70	-0.68	-0.289688	1.166400	0.009839
bladder cancer	-0.84	-0.83	-0.80	-0.182227	-2.870710	0.001248
prostate cancer	-0.85	-0.85	-0.81	-0.175623	-3.927180	0.000518
leukemia	-0.98	-0.94	-0.94	-0.106831	-0.999674	0.003920
other cancer	-0.98	-0.94	-0.93	-0.128982	1.257560	0.033559
effective risk	-0.98	-0.94	-0.94	-0.108975	1.916760	0.069177
Risk - female						
lung cancer	-0.99	-0.84	-0.90	-0.080058	1.194870	0.044447
thyroid cancer	-0.94	-0.85	-0.86	-0.096085	1.071380	0.082099
breast cancer	-0.90	-0.84	-0.81	-0.085772	1.480420	0.183132
liver cancer	-0.86	-0.65	-0.73	-0.091197	-2.330250	0.003451
stomach cancer	-0.71	-0.57	-0.66	-0.070770	-1.384440	0.020746
colon cancer	-0.70	-0.59	-0.66	-0.134970	-1.803890	0.009816
bladder cancer	-0.83	-0.69	-0.75	-0.157793	-3.681890	0.000830
ovary cancer	-0.83	-0.67	-0.75	-0.158918	-4.048740	0.000539
uterus cancer	-0.85	-0.72	-0.78	-0.155701	-4.919840	0.000232
leukemia	-0.91	-0.70	-0.76	-0.125249	-1.048670	0.006647
other cancer	-0.93	-0.73	-0.78	-0.143454	1.866890	0.081297
effective risk	-0.97	-0.83	-0.86	-0.097723	2.815270	0.300244

^ξ The unit of a is cm^{-1} and b is unitless. "rms of residuals" stands for the root-mean-square of the residuals; it represents the average discrepancy between dose/risk values predicted by the fitting function and the dose/risk results estimated by the Monte Carlo method. The unit of "rms of residuals" is mGy/100 mAs or mSv/100mAs for dose estimates and cases/1000 exposed/100 mAs for risk estimates.

Table 20: Protocol E (120 kVp, pediatric body scan FOV, small bowtie filter, 0.984 pitch, 40 mm collimation): correlations of organ dose, effective dose, cancer risk to individual organs, and effective risk with three body size indices: average chest diameter, total scan length (a surrogate for chest height), and weight, and the results of exponential fits $y = \exp(ax + b)$ to the relationships between dose/risk estimates and average chest diameter.

	Pearson correlation coefficient (r)			fitting parameters ^ε		
	average chest diameter	total scan length	weight	a	b	rms of residuals
Dose						
lungs	-0.98	-0.84	-0.88	-0.049646	3.735480	0.467958
heart	-0.97	-0.82	-0.88	-0.041880	3.642260	0.672268
thymus	-0.93	-0.76	-0.79	-0.039732	3.562330	0.880948
thyroid	-0.50	-0.27	-0.25	-0.017278	3.079450	1.633080
breasts	-0.92	-0.81	-0.85	-0.050118	3.529680	1.087480
esophagus	-0.94	-0.75	-0.79	-0.048086	3.570960	0.800027
trachea-bronchi	-0.89	-0.71	-0.71	-0.042526	3.521070	1.048170
eyes	-0.79	-0.66	-0.68	-0.157761	1.482170	0.089681
brain	-0.89	-0.76	-0.79	-0.138904	1.623720	0.080546
pharynx-larynx	-0.78	-0.64	-0.64	-0.108499	3.854190	1.902350
liver	-0.87	-0.72	-0.76	-0.064590	3.673370	1.531580
gall bladder	-0.68	-0.57	-0.61	-0.120715	4.092270	3.630650
kidneys	-0.60	-0.38	-0.47	-0.101841	3.537240	2.040430
adrenals	-0.71	-0.48	-0.59	-0.065703	3.425250	1.906730
spleen	-0.81	-0.62	-0.71	-0.057780	3.499370	1.598760
stomach	-0.77	-0.69	-0.75	-0.053350	3.460950	1.997910
pancreas	-0.65	-0.59	-0.63	-0.104563	3.660430	3.100240
small intestine	-0.79	-0.68	-0.71	-0.172264	3.569790	0.828685
large intestine	-0.78	-0.67	-0.68	-0.193039	3.864710	0.975360
urinary bladder	-0.79	-0.73	-0.74	-0.160714	1.124670	0.104714
prostate	-0.83	-0.83	-0.79	-0.170835	1.268790	0.096816
testes	-0.87	-0.83	-0.79	-0.239959	1.779390	0.036921
ovaries	-0.81	-0.65	-0.74	-0.148970	1.039980	0.100434
uterus	-0.82	-0.66	-0.74	-0.153175	0.939228	0.081071
vagina	-0.82	-0.66	-0.74	-0.154603	0.658414	0.061453
residual soft tissue	-0.90	-0.79	-0.83	-0.097931	3.036810	0.498030
bone surface	-0.93	-0.79	-0.85	-0.075313	3.386080	0.724355
red bone marrow	-0.85	-0.65	-0.70	-0.061699	2.583220	0.528251
skin	-0.76	-0.64	-0.67	-0.092188	2.545380	0.621296
effective dose (male)	-0.95	-0.90	-0.90	-0.061237	3.066110	0.415124
effective dose (female)	-0.90	-0.64	-0.74	-0.056462	3.167570	0.712865

Table 20: Continued.

Risk - male						
lung cancer	-0.99	-0.96	-0.97	-0.079901	0.653201	0.031379
thyroid cancer	-0.98	-0.94	-0.95	-0.088698	-0.491954	0.009995
liver cancer	-0.97	-0.93	-0.95	-0.095210	-1.011850	0.007231
stomach cancer	-0.90	-0.91	-0.91	-0.085490	-0.959658	0.013878
colon cancer	-0.87	-0.79	-0.77	-0.235687	1.120200	0.017903
bladder cancer	-0.85	-0.84	-0.81	-0.187365	-2.227170	0.002112
prostate cancer	-0.84	-0.84	-0.80	-0.179757	-3.322150	0.000880
leukemia	-0.98	-0.94	-0.93	-0.111787	-0.546597	0.006229
other cancer	-0.98	-0.94	-0.94	-0.127543	1.616130	0.054050
effective risk	-0.98	-0.94	-0.94	-0.109660	2.284560	0.105448
Risk - female						
lung cancer	-0.99	-0.84	-0.90	-0.079876	1.492640	0.061031
thyroid cancer	-0.95	-0.86	-0.87	-0.092584	1.308400	0.097434
breast cancer	-0.95	-0.82	-0.87	-0.089602	1.840710	0.164094
liver cancer	-0.90	-0.69	-0.76	-0.092218	-1.914900	0.004174
stomach cancer	-0.84	-0.70	-0.79	-0.070754	-0.999933	0.020910
colon cancer	-0.72	-0.56	-0.60	-0.185566	-0.236013	0.025674
bladder cancer	-0.83	-0.68	-0.75	-0.163630	-3.007200	0.001468
ovary cancer	-0.83	-0.67	-0.74	-0.164940	-3.360220	0.000979
uterus cancer	-0.84	-0.68	-0.74	-0.168463	-4.192430	0.000387
leukemia	-0.91	-0.70	-0.75	-0.131101	-0.583309	0.010310
other cancer	-0.94	-0.74	-0.79	-0.141599	2.213210	0.121516
effective risk	-0.97	-0.82	-0.86	-0.099424	3.162970	0.375630

^ξ The unit of a is cm^{-1} and b is unitless. "rms of residuals" stands for the root-mean-square of the residuals; it represents the average discrepancy between dose/risk values predicted by the fitting function and the dose/risk results estimated by the Monte Carlo method. The unit of "rms of residuals" is mGy/100 mAs or mSv/100mAs for dose estimates and cases/1000 exposed/100 mAs for risk estimates.

Table 21: Protocol F (80 kVp, pediatric body scan FOV, small bowtie filter, 1.375 pitch, 40 mm collimation): correlations of organ dose, effective dose, cancer risk to individual organs, and effective risk with three body size indices: average chest diameter, total scan length (a surrogate for chest height), and weight, and the results of exponential fits $y = \exp(ax + b)$ to the relationships between dose/risk estimates and average chest diameter.

	Pearson correlation coefficient (r)			fitting parameters ^ε		
	average chest diameter	total scan length	weight	a	b	rms of residuals
Dose						
lungs	-0.97	-0.83	-0.86	-0.063462	2.536650	0.146916
heart	-0.96	-0.81	-0.87	-0.052969	2.382060	0.232868
thymus	-0.92	-0.77	-0.77	-0.060010	2.458280	0.297985
thyroid	-0.37	-0.16	-0.17	-0.016835	1.644020	0.549094
breasts	-0.63	-0.71	-0.66	-0.041528	1.985920	0.740595
esophagus	-0.93	-0.75	-0.77	-0.061486	2.323910	0.223605
trachea-bronchi	-0.89	-0.71	-0.70	-0.057418	2.324210	0.318231
eyes	-0.77	-0.62	-0.64	-0.218024	0.889993	0.022365
brain	-0.86	-0.71	-0.73	-0.182367	0.772328	0.019690
pharynx-larynx	-0.79	-0.63	-0.61	-0.105387	2.483570	0.465037
liver	-0.90	-0.75	-0.78	-0.076774	2.486630	0.354924
gall bladder	-0.72	-0.62	-0.63	-0.142793	3.205910	1.051210
kidneys	-0.68	-0.46	-0.56	-0.116099	2.482500	0.516251
adrenals	-0.83	-0.63	-0.71	-0.085295	2.367620	0.390450
spleen	-0.88	-0.71	-0.77	-0.076637	2.421200	0.340358
stomach	-0.83	-0.73	-0.78	-0.063848	2.258590	0.510010
pancreas	-0.70	-0.64	-0.67	-0.115219	2.564090	0.823272
small intestine	-0.79	-0.66	-0.67	-0.227053	3.185460	0.277861
large intestine	-0.80	-0.67	-0.68	-0.225529	3.190280	0.310236
urinary bladder	-0.79	-0.71	-0.71	-0.192890	0.054631	0.024118
prostate	-0.83	-0.82	-0.78	-0.201708	0.190615	0.021486
testes	-0.84	-0.78	-0.74	-0.279734	0.866746	0.008866
ovaries	-0.83	-0.63	-0.71	-0.190138	0.113190	0.021227
uterus	-0.83	-0.65	-0.72	-0.184704	-0.154013	0.017507
vagina	-0.84	-0.66	-0.74	-0.181083	-0.529184	0.012174
residual soft tissue	-0.90	-0.78	-0.81	-0.113835	1.939140	0.133376
bone surface	-0.93	-0.78	-0.83	-0.095437	2.412990	0.209686
red bone marrow	-0.87	-0.68	-0.72	-0.084335	1.477790	0.132000
skin	-0.77	-0.65	-0.68	-0.103666	1.404410	0.168862
effective dose (male)	-0.95	-0.89	-0.89	-0.076431	1.914600	0.114666
effective dose (female)	-0.94	-0.72	-0.78	-0.064777	1.923790	0.132803

Table 21: Continued.

Risk - male						
lung cancer	-0.98	-0.95	-0.96	-0.092431	-0.564218	0.007397
thyroid cancer	-0.96	-0.89	-0.91	-0.087663	-1.933890	0.002712
liver cancer	-0.97	-0.94	-0.94	-0.105342	-2.251090	0.001787
stomach cancer	-0.93	-0.93	-0.94	-0.093968	-2.200800	0.003316
colon cancer	-0.85	-0.78	-0.75	-0.265742	0.411306	0.005817
bladder cancer	-0.84	-0.81	-0.77	-0.218536	-3.294320	0.000475
prostate cancer	-0.84	-0.83	-0.79	-0.211610	-4.376920	0.000207
leukemia	-0.97	-0.91	-0.90	-0.130684	-1.713270	0.001541
other cancer	-0.98	-0.93	-0.92	-0.141298	0.447407	0.012633
effective risk	-0.97	-0.93	-0.92	-0.124872	1.132810	0.024186
Risk - female						
lung cancer	-0.99	-0.81	-0.87	-0.092825	0.277892	0.013808
thyroid cancer	-0.93	-0.84	-0.85	-0.097412	-0.049013	0.028927
breast cancer	-0.78	-0.86	-0.78	-0.065023	0.118852	0.087236
liver cancer	-0.91	-0.70	-0.77	-0.104302	-3.075610	0.000976
stomach cancer	-0.87	-0.70	-0.78	-0.080568	-2.203500	0.005519
colon cancer	-0.74	-0.55	-0.60	-0.220222	-0.876045	0.007959
bladder cancer	-0.86	-0.68	-0.74	-0.195792	-4.086010	0.000291
ovary cancer	-0.84	-0.65	-0.72	-0.198745	-4.384050	0.000212
uterus cancer	-0.85	-0.68	-0.73	-0.189813	-5.429230	0.000088
leukemia	-0.90	-0.68	-0.73	-0.152091	-1.713700	0.002451
other cancer	-0.93	-0.73	-0.77	-0.155316	1.053460	0.028945
effective risk	-0.97	-0.86	-0.87	-0.098944	1.777070	0.108806

^ξ The unit of a is cm^{-1} and b is unitless. “rms of residuals” stands for the root-mean-square of the residuals; it represents the average discrepancy between dose/risk values predicted by the fitting function and the dose/risk results estimated by the Monte Carlo method. The unit of “rms of residuals” is $\text{mGy}/100 \text{ mAs}$ or $\text{mSv}/100\text{mAs}$ for dose estimates and $\text{cases}/1000 \text{ exposed}/100 \text{ mAs}$ for risk estimates.

Table 22: Protocol G (100 kVp, pediatric body scan FOV, small bowtie filter, 1.375 pitch, 40 mm collimation): correlations of organ dose, effective dose, cancer risk to individual organs, and effective risk with three body size indices: average chest diameter, total scan length (a surrogate for chest height), and weight, and the results of exponential fits $y = \exp(ax + b)$ to the relationships between dose/risk estimates and average chest diameter.

	Pearson correlation coefficient (r)			fitting parameters ^ε		
	average chest diameter	total scan length	weight	a	b	rms of residuals
Dose						
lungs	-0.98	-0.84	-0.88	-0.054949	3.045070	0.230135
heart	-0.96	-0.81	-0.88	-0.045173	2.909220	0.397718
thymus	-0.93	-0.78	-0.78	-0.051293	2.976490	0.491413
thyroid	-0.43	-0.23	-0.25	-0.016788	2.305320	0.898477
breasts	-0.64	-0.71	-0.66	-0.039733	2.577500	1.296160
esophagus	-0.94	-0.76	-0.79	-0.052337	2.860010	0.360308
trachea-bronchi	-0.90	-0.73	-0.73	-0.050212	2.879370	0.520952
eyes	-0.78	-0.64	-0.65	-0.196468	1.412150	0.049986
brain	-0.88	-0.73	-0.76	-0.163328	1.311140	0.042878
pharynx-larynx	-0.80	-0.66	-0.64	-0.098644	3.066100	0.879306
liver	-0.90	-0.75	-0.78	-0.068211	3.004190	0.658692
gall bladder	-0.71	-0.62	-0.63	-0.131810	3.691200	1.938600
kidneys	-0.66	-0.44	-0.54	-0.099964	2.915860	0.992906
adrenals	-0.81	-0.61	-0.70	-0.072826	2.866160	0.759118
spleen	-0.88	-0.71	-0.77	-0.067802	2.940430	0.622094
stomach	-0.80	-0.71	-0.76	-0.056522	2.799110	0.955405
pancreas	-0.69	-0.63	-0.67	-0.106282	3.106880	1.558390
small intestine	-0.79	-0.67	-0.68	-0.209756	3.624980	0.529137
large intestine	-0.80	-0.68	-0.69	-0.211658	3.649390	0.575760
urinary bladder	-0.79	-0.72	-0.72	-0.175713	0.639431	0.053409
prostate	-0.83	-0.83	-0.79	-0.179924	0.704330	0.049425
testes	-0.85	-0.80	-0.76	-0.265582	1.474780	0.020251
ovaries	-0.82	-0.65	-0.73	-0.168606	0.611197	0.048362
uterus	-0.82	-0.66	-0.74	-0.163246	0.391595	0.040829
vagina	-0.85	-0.69	-0.75	-0.166824	0.118553	0.028938
residual soft tissue	-0.90	-0.79	-0.82	-0.106694	2.478510	0.249933
bone surface	-0.93	-0.78	-0.84	-0.086925	2.903190	0.378352
red bone marrow	-0.86	-0.68	-0.72	-0.075032	2.053350	0.266064
skin	-0.77	-0.65	-0.68	-0.099017	1.943490	0.309355
effective dose (male)	-0.95	-0.90	-0.90	-0.068363	2.450300	0.202539
effective dose (female)	-0.94	-0.73	-0.79	-0.058185	2.471050	0.247829

Table 22: Continued.

Risk - male						
lung cancer	-0.99	-0.96	-0.96	-0.084689	-0.043046	0.014487
thyroid cancer	-0.97	-0.91	-0.93	-0.085352	-1.300900	0.005320
liver cancer	-0.97	-0.94	-0.95	-0.097956	-1.712300	0.003441
stomach cancer	-0.92	-0.93	-0.94	-0.086611	-1.662690	0.006362
colon cancer	-0.86	-0.80	-0.77	-0.251133	0.858596	0.010823
bladder cancer	-0.85	-0.83	-0.79	-0.202301	-2.706460	0.001059
prostate cancer	-0.84	-0.83	-0.80	-0.189702	-3.879670	0.000440
leukemia	-0.97	-0.92	-0.92	-0.122320	-1.120870	0.003298
other cancer	-0.98	-0.94	-0.93	-0.133693	1.001230	0.026323
effective risk	-0.98	-0.94	-0.93	-0.117276	1.678620	0.050036
Risk - female						
lung cancer	-0.99	-0.83	-0.89	-0.084698	0.791818	0.027364
thyroid cancer	-0.95	-0.86	-0.87	-0.094684	0.563086	0.051507
breast cancer	-0.78	-0.87	-0.79	-0.063771	0.714130	0.154072
liver cancer	-0.92	-0.71	-0.78	-0.095671	-2.564760	0.001807
stomach cancer	-0.85	-0.70	-0.78	-0.074906	-1.635390	0.010313
colon cancer	-0.74	-0.56	-0.61	-0.206614	-0.411578	0.014823
bladder cancer	-0.84	-0.67	-0.74	-0.178454	-3.515130	0.000707
ovary cancer	-0.84	-0.65	-0.72	-0.181674	-3.825340	0.000472
uterus cancer	-0.83	-0.66	-0.73	-0.184981	-4.664500	0.000192
leukemia	-0.91	-0.69	-0.74	-0.143666	-1.125960	0.005125
other cancer	-0.94	-0.75	-0.78	-0.146152	1.577540	0.058239
effective risk	-0.98	-0.87	-0.88	-0.094390	2.347270	0.206522

^ξ The unit of a is cm^{-1} and b is unitless. "rms of residuals" stands for the root-mean-square of the residuals; it represents the average discrepancy between dose/risk values predicted by the fitting function and the dose/risk results estimated by the Monte Carlo method. The unit of "rms of residuals" is mGy/100 mAs or mSv/100mAs for dose estimates and cases/1000 exposed/100 mAs for risk estimates.

Table 23: Protocol H (140 kVp, pediatric body scan FOV, small bowtie filter, 1.375 pitch, 40 mm collimation): correlations of organ dose, effective dose, cancer risk to individual organs, and effective risk with three body size indices: average chest diameter, total scan length (a surrogate for chest height), and weight, and the results of exponential fits $y = \exp(ax + b)$ to the relationships between dose/risk estimates and average chest diameter.

	Pearson correlation coefficient (r)			fitting parameters ^ε		
	average chest diameter	total scan length	weight	a	b	rms of residuals
Dose						
lungs	-0.98	-0.86	-0.89	-0.046484	3.720160	0.412886
heart	-0.95	-0.81	-0.88	-0.037523	3.605640	0.801768
thymus	-0.93	-0.79	-0.78	-0.043058	3.670600	0.952684
thyroid	-0.46	-0.28	-0.31	-0.015156	3.109020	1.748370
breasts	-0.63	-0.71	-0.66	-0.037318	3.351490	2.765920
esophagus	-0.95	-0.78	-0.80	-0.043852	3.573270	0.705186
trachea-bronchi	-0.92	-0.75	-0.75	-0.042510	3.592990	0.974573
eyes	-0.79	-0.65	-0.67	-0.170444	2.016270	0.127488
brain	-0.89	-0.75	-0.78	-0.145018	2.000940	0.107869
pharynx-larynx	-0.80	-0.67	-0.66	-0.092292	3.821680	2.003510
liver	-0.89	-0.75	-0.78	-0.059993	3.694870	1.447470
gall bladder	-0.69	-0.61	-0.62	-0.121219	4.349570	4.274030
kidneys	-0.62	-0.41	-0.51	-0.085165	3.532330	2.274420
adrenals	-0.79	-0.57	-0.67	-0.060685	3.534990	1.757420
spleen	-0.88	-0.71	-0.77	-0.059533	3.638210	1.354630
stomach	-0.77	-0.68	-0.74	-0.049185	3.506870	2.133070
pancreas	-0.68	-0.62	-0.66	-0.097517	3.814170	3.491330
small intestine	-0.79	-0.67	-0.69	-0.193434	4.232610	1.186740
large intestine	-0.80	-0.69	-0.69	-0.198861	4.287090	1.267790
urinary bladder	-0.78	-0.73	-0.74	-0.156617	1.340810	0.136641
prostate	-0.82	-0.82	-0.79	-0.160938	1.399030	0.129873
testes	-0.87	-0.83	-0.79	-0.239824	2.067730	0.050088
ovaries	-0.81	-0.65	-0.74	-0.144849	1.244610	0.128035
uterus	-0.81	-0.66	-0.75	-0.142130	1.061600	0.111794
vagina	-0.82	-0.68	-0.76	-0.138110	0.647321	0.077720
residual soft tissue	-0.90	-0.80	-0.83	-0.099373	3.186810	0.556973
bone surface	-0.93	-0.79	-0.85	-0.077848	3.503770	0.769883
red bone marrow	-0.85	-0.67	-0.71	-0.065552	2.794100	0.635944
skin	-0.76	-0.65	-0.68	-0.093936	2.652970	0.677215
effective dose (male)	-0.96	-0.91	-0.91	-0.060424	3.154790	0.424351
effective dose (female)	-0.94	-0.73	-0.79	-0.051087	3.182790	0.546317

Table 23: Continued.

Risk - male						
lung cancer	-0.98	-0.96	-0.97	-0.077069	0.646028	0.033808
thyroid cancer	-0.97	-0.93	-0.95	-0.083099	-0.497132	0.013268
liver cancer	-0.97	-0.94	-0.95	-0.090964	-1.000600	0.007786
stomach cancer	-0.91	-0.92	-0.94	-0.079275	-0.956394	0.014505
colon cancer	-0.87	-0.81	-0.78	-0.238675	1.500090	0.023768
bladder cancer	-0.85	-0.84	-0.81	-0.184637	-1.990580	0.002713
prostate cancer	-0.84	-0.84	-0.81	-0.170647	-3.180210	0.001168
leukemia	-0.98	-0.93	-0.93	-0.114086	-0.358147	0.008366
other cancer	-0.98	-0.95	-0.94	-0.126083	1.719420	0.065099
effective risk	-0.98	-0.95	-0.95	-0.109829	2.392860	0.122638
Risk - female						
lung cancer	-0.99	-0.86	-0.91	-0.076514	1.470970	0.065568
thyroid cancer	-0.95	-0.88	-0.90	-0.089492	1.301090	0.114578
breast cancer	-0.79	-0.87	-0.80	-0.061667	1.491020	0.332848
liver cancer	-0.91	-0.73	-0.79	-0.087197	-1.879120	0.004009
stomach cancer	-0.84	-0.69	-0.77	-0.069273	-0.898909	0.022910
colon cancer	-0.74	-0.57	-0.62	-0.193838	0.226065	0.032695
bladder cancer	-0.83	-0.69	-0.76	-0.157169	-2.828240	0.001894
ovary cancer	-0.84	-0.68	-0.75	-0.161788	-3.146080	0.001238
uterus cancer	-0.83	-0.68	-0.75	-0.157815	-4.083350	0.000522
leukemia	-0.91	-0.70	-0.75	-0.134834	-0.375924	0.012581
other cancer	-0.94	-0.76	-0.80	-0.137884	2.281310	0.137163
effective risk	-0.98	-0.89	-0.90	-0.088927	3.078850	0.473637

^ξ The unit of a is cm^{-1} and b is unitless. “rms of residuals” stands for the root-mean-square of the residuals; it represents the average discrepancy between dose/risk values predicted by the fitting function and the dose/risk results estimated by the Monte Carlo method. The unit of “rms of residuals” is $\text{mGy}/100 \text{ mAs}$ or $\text{mSv}/100\text{mAs}$ for dose estimates and cases/1000 exposed/100 mAs for risk estimates.

5.3.2 Effects of Scan Parameters

The exponential relationships reported in Table 16 to Table 23 allowed the effects of bowtie filter, collimation, helical pitch, and peak tube potential to be studied for all dose and risk estimates. Examples are illustrated in Figure 21 for lung dose, large intestine dose, effective dose, and effective risk. As expected, the effects of bowtie filter

and collimation were generally smaller compared to the effects of helical pitch and peak tube potential, an exception being dose to the large intestine, an organ on the periphery or outside the chest scan coverage, for which the effect of collimation was greater than that of the helical pitch.

With all other scan parameters kept the same, using the medium bowtie filter resulted in higher dose/risk than the other two bowtie filters. Compared with using the small bowtie filter, using the large bowtie filter resulted in lower dose for small patients and higher dose in large patients. The dose difference associated with the different choices of bowtie filters was not reflected by the corresponding $CTDI_{vol}$ values; the $CTDI_{vol}$ values for the medium and the large bowtie filters were substantially lower than that for the small bowtie filter.

Beam collimation had little effect on dose to the lung, an organ inside the chest scan coverage, although lung dose was slightly higher at 20-mm collimation. In contrast, dose to the large intestine was higher at 40-mm collimation, and the difference between the two collimation settings decreased with increasing patient size. Effective dose and effective risk were also slightly higher at the wider beam collimation. The difference in $CTDI_{vol}$ between the two collimation settings was indicative of the difference observed for lung dose.

For the size range (10-23 cm) of pediatric patients in this study, the ratio of lung dose between pitch of 0.984 and pitch of 1.375 ranged from 1.37-1.38, close to but slightly

lower than the theoretical prediction of 1.40 (1.375/0.984), as represented by the $CTDI_{vol}$ ratio between the two pitch settings. The ratio, however, was much lower for dose to the large intestine, ranging 0.97-1.13. For the effective dose and effective risk of male patients, the ratio ranged 1.28-1.32 and 1.27-1.33, respectively.

All dose and risk estimates depended strongly on peak tube potential. For the size range of pediatric patients in this study (10-23 cm), the ratio of dose and risk estimates between 120 kVp and 100 kVp ranged between 1.53-1.63, 1.54-1.69, 1.55-1.65, and 1.56-1.64 for lung dose, large intestine dose, effective dose (male), and effective risk (male), respectively, increasing with patient size. In contrast, the $CTDI_{vol}$ ratio between the two kVp settings was 1.70.

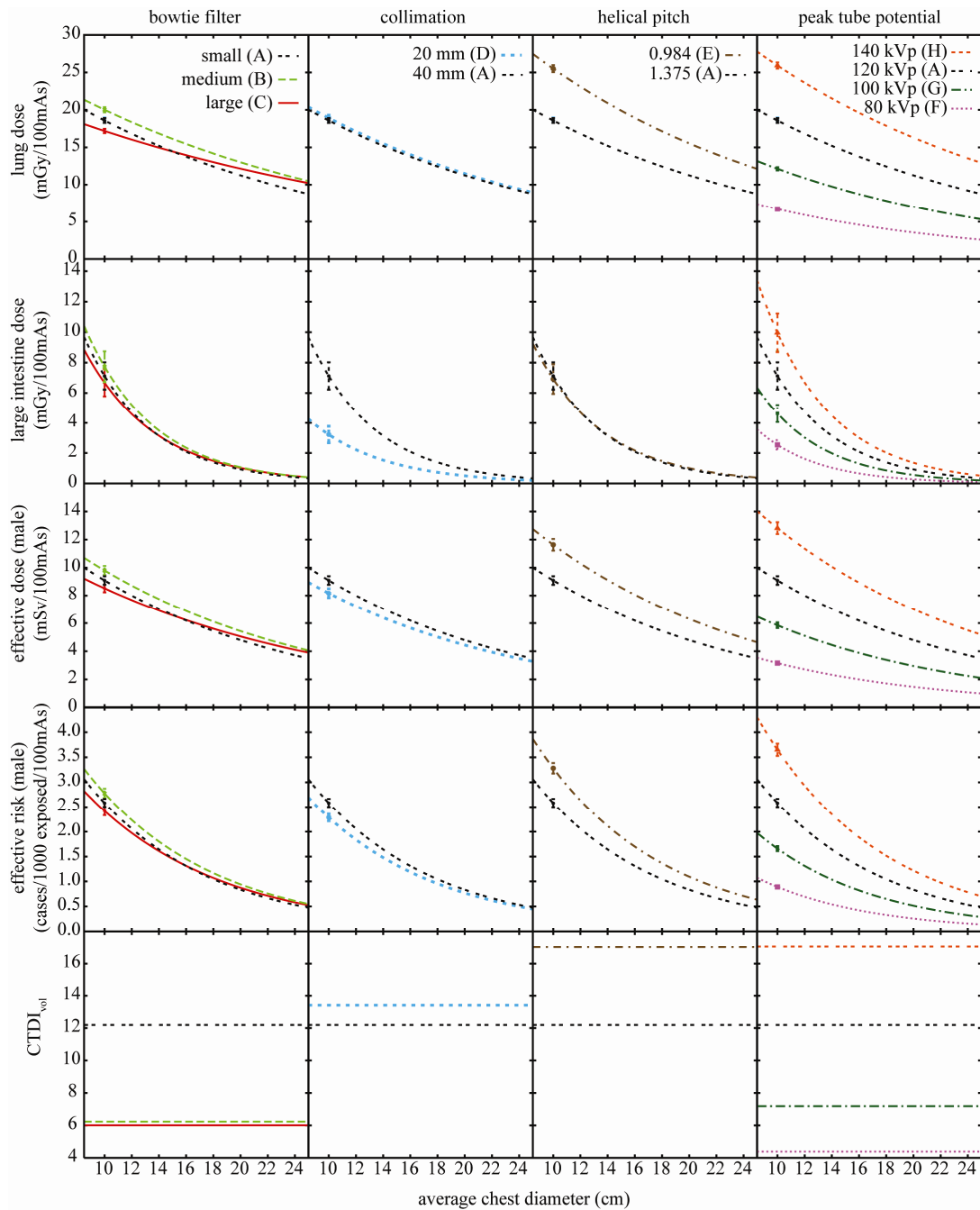


Figure 21: Effects of scan parameters (bowtie filter, collimation, helical pitch, and peak tube potential) on radiation dose and cancer risk, using lung dose, large intestine dose, effective dose (male), and effective risk (male) as examples. The error bar on each curve reflects the root-mean-square of the residuals associated with the exponential fit; it represents the average discrepancy between dose/risk values predicted by the fitting function and the dose/risk results estimated by the Monte Carlo method. Volume-weighted CTDI ($CTDI_{vol}$) were shown for comparison. The letters A-H refer to Protocols A-H.

5.4 Discussions

In this study, we combined patient-specific computer models of a population of pediatric CT patients with a validated Monte Carlo technique to systematically evaluate the effects of patient size and scan parameters on radiation dose and cancer risk. In a prior study of seven pediatric patients (16-20 cm chest diameter)¹⁰³, we showed that normalized dose to centrally-located large organs in the chest scan coverage (e.g., lung and heart) correlated strongly, decreasing linearly, with chest diameter. In the current study, we confirmed the strong correlations and found the relationships to be exponential over a larger range of body diameters (10-23 cm) (Figure 18a), consistent with the exponential dependence of CTDI on cylindrical phantom diameter reported by Nickoloff et al.⁹². In addition to centrally-located large organs, normalized dose to centrally-located small tubular organs (e.g., esophagus) also correlated well with average chest diameter (Figure 18a). These strong relationships suggest that patient-specific dose to these organs can be accurately estimated for any patient in this size range who undergoes a chest scan from a simple measurement of the patient's chest diameter or circumference, thus obviating the need to construct a computer model for every patient.

For some organs, the correlation between dose and average chest diameter was less than ideal. We attributed the weak correlation ($r = -0.64$) of breast dose in Protocol A with average chest diameter (Figure 18b) to the high helical pitch of 1.375 in Protocol

A, which left gaps of tissues un-irradiated by the primary radiation beam. This was especially the case for organs on the surface of a patient, such as the breast. Depending on how much of the breast volume was irradiated by the primary beam, the dose to the breast could vary considerably. In fact, the correlation of breast dose with average chest diameter was much stronger ($r = -0.92$) in Protocol E, which employed a lower helical pitch of 0.984. The weak correlation of thyroid dose with average chest diameter ($r = -0.44$) was not surprising, considering that the thyroid is in the neck region, the dose of which would more likely be affected by neck thickness than chest size. Despite these weak correlations and the generally weak correlations found for organs on the periphery or outside of the chest scan coverage (Figure 18c) and for distributed organs (Figure 18d), the relationships could still be represented by exponential equations, which may be used to broadly estimate patient-specific dose to these organs.

Our results reflect strong effects of age and gender on CT radiation dose. While the lung dose of a 10-cm diameter patient was about twice that of a 23-cm diameter patient (Figure 18a), the risk of lung cancer incidence was three times higher in the smaller patient (Figure 19a), due to the patient's younger age. Furthermore, with the same lung dose, the risk to a female patient was about double that to a male patient of the same size (Figure 19a), a direct result of the dramatically different risk coefficients for the two genders. As in the case of organ dose, the exponential relationship between cancer risk and average chest diameter may be used to infer risk information for any

patient in the size range who undergoes a chest scan. Such dose and risk estimates, when documented in a patient's dosimetry and medical records, could have significant implications in patient management, potentially providing guidance in decisions for image utilization, including the situation in which multiple examinations have been performed or are being considered.

Our study further illustrated the difference between effective dose and radiation risk. While the effective dose of a 10-cm diameter patient was about twice that of a 23-cm diameter patient (Figure 20a), the effective risk was three to four times higher in the smaller patient (Figure 20b). As mentioned earlier, effective dose is defined for a reference hermaphrodite person; the tissue weighting factors are mean values representing averages over many individuals of different genders and age groups²¹. However, the concept has been widely applied to patients of various sizes, ages, and genders^{30, 31, 38, 98} as a surrogate for radiation risk. In particular, dose-length product (DLP) to effective dose conversion coefficients have been developed for various patient ages (e.g. 0, 1, 5, 10 years, adult)¹⁰. The limitations of these applications have been discussed recently by several authors^{71, 102, 110}. In this study, we calculated effective dose for individual patients because it is a concept that the medical imaging community is familiar with. Our results help to quantify the age and gender deficiencies of the effective dose concept; the difference in effective dose does not represent the risk difference between the two age groups, nor does the difference in effective dose fully

capture the risk difference between two genders. While effective dose may still be useful for comparing between scan techniques and imaging devices, when risk is compared across ages and genders, effective risk is a more useful concept.

At our institution, pediatric patients are assigned to different protocol groups based on weight, body length, or age. However, the results of this study demonstrate that chest diameter/circumference is a stronger predictor of dose and risk than weight and body length and should perhaps replace the other body size indices for the purpose of protocol design and assignment. This is in line with the recommendation of Haaga et al., who advocated the use of patient diameter to determine parameters such as tube current^{111, 112}.

Our study of the effect of bowtie filter showed that, on the LightSpeed VCT scanner, the medium bowtie filter was associated with the highest radiation dose, and compared with using the small bowtie filter, using the large bowtie filter resulted in lower dose for small patients and higher dose in large patients. These results may appear counter-intuitive, but can be understood by knowing that (1) the medium bowtie filter has the same materials and thicknesses as the small bowtie filter at the center, but is thinner than the small bowtie filter on the periphery, and (2) the large bowtie filter is the thinnest on the periphery, but contains an additional layer of copper. These results can aid in the design of CT protocols. For example, if one determines that changing from the small to the medium bowtie filters would result in more uniform X-ray intensity at

the detector for patients of a certain size, then one may need to reduce tube current at the same time to compensate for the dose increase due to the bowtie filter change. Furthermore, we found that the dose differences associated with the different choices of bowtie filters were not reflected by the corresponding differences in the $CTDI_{vol}$ value. This is due to the fact that $CTDI_{vol}$ reported by the manufacturer is for a 32-cm diameter acrylic phantom when the medium bowtie filter (medium body scan FOV) and the large bowtie filter (large body scan FOV) are used, but for a 16-cm diameter acrylic phantom when the small bowtie filter (pediatric body scan FOV) is used. As such, if the medium bowtie filter is used for any patient (10-23 cm in diameter) in our study, the reported $CTDI_{vol}$ value represents a gross underestimation of patient dose.

Our study of the effect of beam collimation showed that dose to the lung was slightly higher at 20-mm collimation than at 40-mm collimation. This may be explained by the effect of the penumbra; at a narrower beam collimation, more rotations were needed to cover the same image volume, resulting in more contribution from the penumbra. The higher dose to the large intestine at 40-mm collimation could be attributable to the longer over-ranging distance and hence longer total scan length at this collimation setting, which, for small patients, caused a larger volume of the large intestine to be directly irradiated by the primary radiation beam and, for large patients, caused more scattered radiation to reach the large intestine. For the same reason, effective dose and effective risk were also slightly larger at the wider beam collimation.

As for the effect of helical pitch, we found that the dose and risk ratios between pitch of 0.984 and pitch of 1.375 were universally smaller than the theoretical prediction of 1.40 ($1.375/0.984$). This may be explained by the longer overranging distance associated with the larger helical pitch. The ratio was close to unity (0.97-1.13) for dose to the large intestine, most likely because the large intestine was either partially irradiated by the primary radiation beam or only irradiated by scattered radiation.

Our study of the effect of the peak tube potential showed that the dose/risk ratio between two kVp settings was a function of patient size. In other words, the same kVp increase entails different dose and risk increases to patients of different sizes. Recently, a number of studies explored the feasibility of reducing peak tube potential to increase image contrast^{18, 113-115}. The resulting increase in image noise was often compensated by an increase in tube current. The dose and risk data provided in our study can facilitate such efforts by informing the healthcare providers of the tradeoff in patient dose and risk as a consequence of using a lower-kVp and higher-mA technique.

One limitation of our study was that we did not study the effect of tube current modulation (TCM). As the thirty patients in our study underwent CT examinations between 2005 and 2006 using fixed-tube-current techniques, the TCM profiles could not be readily obtained. However, as the design of a TCM protocol requires specifying the maximum tube current of the scan, the results of our study can be used to estimate the maximum dose associated with a TCM examination. Furthermore, other authors have

shown, for a reference adult patient, that the normalized organ dose values estimated by Monte Carlo methods, when multiplied by the mean tube current of a TCM scan, may serve as conservative estimates of the dose associated with the TCM scan¹¹⁶. This may equally apply to pediatric patients, but further verification is required. Despite having thirty patients in this study, the sample size in our study was still relatively small (~ 15 patients in each gender). As such, we did not treat patient size and patient age as two separate factors affecting patient risk. With a larger sample size, the same average chest diameter would likely correspond to a larger range of patient ages and thus more variable risk estimates. Lastly, in this investigation, we estimated cancer risk for individual patients by combining patient-specific dose estimates with risk coefficients that are tissue-, age-, and gender-specific. We note, however, that as the risk coefficients are still statistical averages over many individuals of the same gender and similar age, they can not reflect individual vulnerability due to genetic factors. As such, the cancer risks we reported do not represent the true risk of an individual from his/her CT examination but rather our current best knowledge of the potential risk to a patient from his/her CT examination, knowing the patient's age and gender. Therefore, care should be exercised when interpreting the risk results. Nevertheless, the patient-specific risk information, as presented by our study, represents a step forward beyond effective dose towards personalized patient care.

Part II: Tool Development

6. Three-Dimensional Simulation of Lung Nodules for Pediatric Multidetector Array CT*

6.1 Introduction

Detection of even one small lung nodule may have profound implications in the prognosis and treatment of pediatric cancer. Owing to the superior resolutions of modern multi-detector array computed tomography (MDCT), CT of the chest is often standard for pediatric cancer staging and surveillance. However, compared with other imaging modalities, CT delivers higher radiation dose to the patients¹⁶, and children are especially sensitive to the detrimental effect of radiation. Therefore, care must be taken to optimize radiation dose while maintaining diagnostic accuracy. The influence of dose reduction on lung nodule detection has been studied for adult patients by performing repeated CT scans on the same subjects at different tube current levels^{28, 117}. Such an approach is not suitable for the pediatric population. An alternative approach is to develop techniques to simulate lung nodules for pediatric chest MDCT.

Three types of techniques have been developed in the past to simulate lung nodules. Type I technique adds synthetic nodules into a phantom^{118, 119} and has the obvious disadvantage of using unrealistic backgrounds, making it difficult to generalize research results to patients. Type II technique digitally inserts nodules segmented from

* This chapter is based on an article with the same title published in the *British Journal of Radiology*.

clinical images into clinical images^{48, 120}, thus may be optimal in terms of image/nodule realism. However, the occurrence of solitary small lung nodules in the pediatric population is low, limiting the available nodule morphologies and making repeated use problematic. Type III technique adds computer-generated nodule-like objects to clinical images⁴⁴⁻⁴⁷. It offers the maximum flexibility and is also capable of achieving high degree of realism as demonstrated by two recent studies^{46, 47}. Nodule characteristics modeled in these two studies, however, were typical of nodules larger than those of interest in pediatric MDCT (3-5 mm); lung nodules larger than 5 mm are rarely missed by radiologists in pediatric MDCT. The purpose of our investigation was to develop and validate a technique of type III for modeling small lung nodules in three dimensions on pediatric MDCT images and to provide a framework by which focal lesions in other organs can be simulated for dose and technique optimization research in MDCT.

6.2 Materials and Methods

Our institutional review board determined that the study was in compliance with the Health Insurance Portability and Accountability Act, and did not require informed consent.

6.2.1 Image Selection

Images of 21 patients were retrospectively selected from our clinical (teaching) database to represent infants or children up to 18 years old who underwent unenhanced MDCT (LightSpeed 16, LightSpeed QX/i, or LightSpeed VCT; GE Healthcare, Waukesha,

WI) examinations. All patient identifiers had been removed from the images prior to the study. Sixteen of the patients had sarcomas or Wilms tumor, and nodules were presumed to represent metastatic disease. The images were acquired using tube potentials of 100-140 kVp, tube currents of 44-211 mA, helical pitches of 0.75 or 1.375, gantry rotation periods of 0.4-0.8 second, slice thicknesses of 5 mm, reconstruction intervals of 2.5 mm or 5 mm, and in-plane resolutions of 0.41-0.66 mm. Those imaging parameters were typical of the current clinical protocols for pediatric MDCT at our institution. Thirty-four small (real) lung nodules were identified by a pediatric radiologist who had 15 years of experience with pediatric CT.

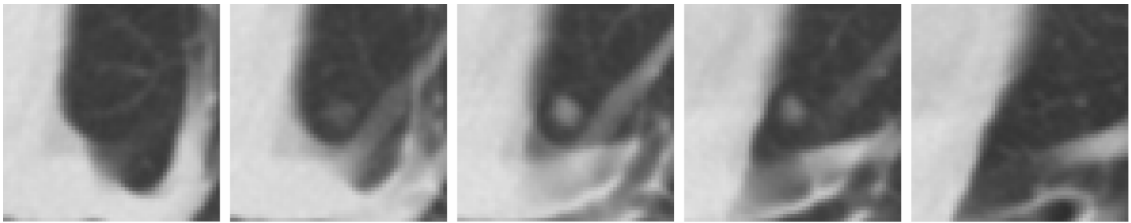


Figure 22: Three-dimensional characteristics of small lung nodules on pediatric MDCT images as exemplified by a nodule in our study. The nodule was clearly visible on 3 contiguous CT slices with slice thickness of 5 mm and reconstruction interval of 2.5 mm. The regions of interest (ROIs) are 30 mm in size with the nodule located centrally.

6.2.2 Nodule Characterization

The real nodules in our study had diameters between 2.5 and 6 mm and were clearly visible on 1-4 contiguous MDCT slices. Nodule size and contrast varied across slices; frequently, a central slice with maximum nodule size and contrast was accompanied by adjacent slices with reduced sizes and contrasts (Figure 22). Although

small nodules tended to appear round, a variety of shapes existed that deviated clearly from a perfect sphere (Figure 23). The shape of a nodule varied from slice to slice, but strong resemblance in shape was often observed across slices (Figure 22). The margin of a nodule varied from well-defined margin to diffused/hazy margin (Figure 23).

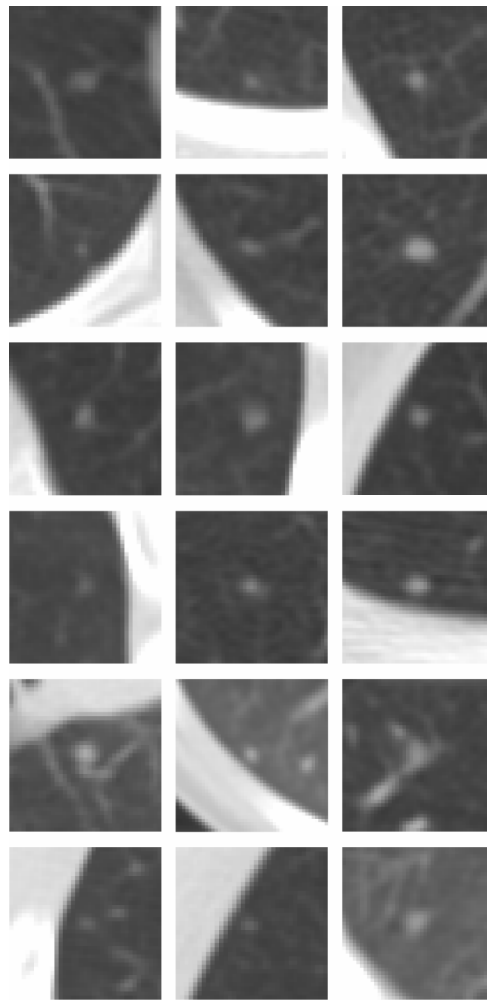


Figure 23: A variety of nodule appearances existed as exemplified by 18 real nodules in our study. Only the central slice of each nodule is shown. All ROIs are 20 mm in size with nodules located centrally.

6.2.3 Nodule Simulation Method

We developed a technique to simulate lung nodules with realistic characteristics. A 3-D nodule was modeled as multiple 2-D masks on sequential MDCT slices. All computer codes were written in an interactive program (Matlab, R2007a; Mathworks, Natick, MA).

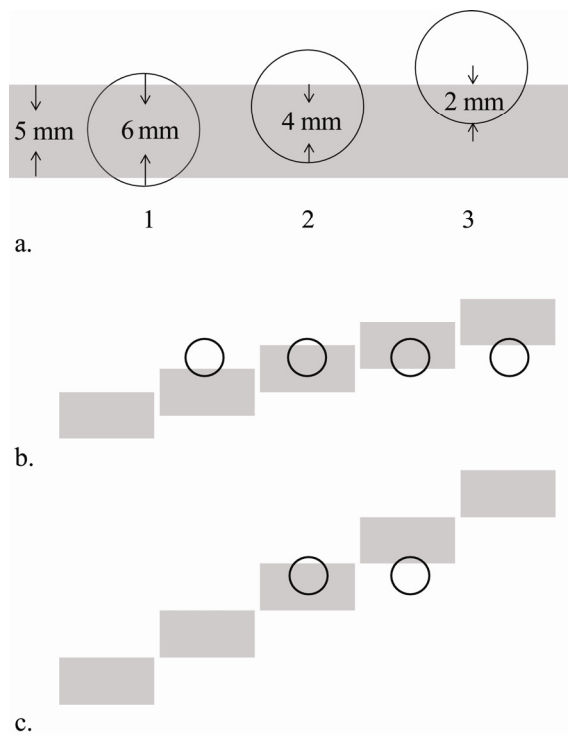


Figure 24: (a) For a 3-D nodule with diameter $2R_0$ of 6 mm, its radii on a 5-mm thick CT slice are 3, 3, and 2.83 mm for the vertical (z-direction) locations 1, 2, and 3, respectively. Assuming the peak contrast of the nodule to be proportional to its diameter subtended by the CT slice and defining its peak contrast at vertical location 1 as C_0 , its peak contrasts at vertical locations 2 and 3 are $4C_0/5$ and $2C_0/5$, respectively. When changing reconstruction interval from (b) half of the slice thickness to (c) one slice thickness, the occupation and the appearance of a nodule on contiguous CT slices also change.

For a given 3-D nodule, its radii and peak contrasts on contiguous CT slices can vary, depending on the vertical (z-direction) offsets of the nodule center relative to the CT slices (Figure 24). On each CT slice, the 2-D mask can be defined by a contrast profile equation proposed by Samei et al¹²¹ and reformulated by Burgess et al¹²² as

$$c(r) = C \left(1 - \left(\frac{r}{R} \right)^2 \right)^n \quad (17)$$

where R and C are the radius and peak contrast of the 2-D mask, and exponent n is a positive number inversely related to the steepness of the contrast profile, reflective of edge characteristics. Due to its radial symmetry, Equation (17) defines perfectly circular masks and has been adopted by Hoe et al¹²³ to model small liver lesions on pediatric MDCT images.

To reflect the variability of real nodule shapes, we introduced radial asymmetry by defining radius as a function of polar angle and exponent as a function of radius, i.e.

$$c(r, \theta) = C \left(1 - \left(\frac{r}{R_\theta} \right)^2 \right)^{n(R_\theta)} \quad (18)$$

$$n(R_\theta) = n \frac{R_\theta}{R}$$

where R_θ is a pre-defined *nodule shape function*, rescaled so that its average across all polar angles equals R , nodule radius on current CT slice obtained from initial geometric calculation. We chose $n(R_\theta)$ as a linearly increasing function of R_θ to improve the smoothness of nodule border; the roughness induced by increasing nodule size from one

polar angle to another is ameliorated by a corresponding decrease in the steepness of the nodule contrast profile. Because the steepness of the contrast profile of a spherical nodule can be shown to increase with the fraction of its diameter contained by a CT slice, f , we assumed a linear relationship between n and f as

$$n = \frac{n_{1/6} - n_1}{1/6 - 1}(f - 1) + n_1 \quad (19)$$

where n_1 and $n_{1/6}$ are exponents corresponding to conditions when all or one-sixth of the nodule diameter is contained by a CT slice, respectively.

To determine n_1 , Equation (17) was used to simulate spherical nodules fully enclosed by a CT slice with a sequence of n_1 values between 1.0 and 2.0. An experienced pediatric radiologist examined the nodule images and determined that $n_1 = 1.8 - 2.0$ yielded the most realistic appearances. Subsequently, Equations (17) and (19) were used to create 3-D nodules visible on multiple contiguous CT slices with a sequence of $n_{1/6}$ values between 2.0 and 2.6 and an n_1 value of 2.0. The 3-D nodule images were examined by the same radiologist, who determined that $n_{1/6} = 2.4$ yielded the most realistic appearances. $n_1 = 2.0$ and $n_{1/6} = 2.4$ were used to calculate n in our subsequent simulations.

Because shape variability contributes greatly to the difficulties associated with nodule detection, any realistic nodule simulation must reflect the variety of real nodule

shapes. We developed an algorithm which generated a nodule shape function R_θ from 12 manually-specified base radii at evenly spaced polar angles with linearly interpolated values in between. A nodule shape function was first designed for the central CT slice containing the nodule center. Slight variations were then added to 4 of the base radii, 90 degrees apart, to create nodule shape functions for the inferior and superior CT slices. Using this method, a library of 60 sets of nodule shape functions was created.

Lastly, we modeled nodules with diffused edges by adding a second component to Equation (18) as

$$c(r, \theta) = \alpha C \left(1 - \left(\frac{r}{R_\theta^{(1)}} \right)^2 \right)^{n(R_\theta^{(1)})} + (1 - \alpha) C \left(1 - \left(\frac{r}{R_\theta^{(2)}} \right)^2 \right)^{n(R_\theta^{(2)})} \quad (20)$$

where

$$\begin{aligned} n(R_\theta^{(1)}) &= n \frac{R_\theta^{(1)}}{R^{(1)}} \\ n(R_\theta^{(2)}) &= \left(\frac{n}{\gamma} \right) \frac{R_\theta^{(2)}}{R^{(2)}} \end{aligned} \quad (21)$$

$$R^{(1)} = \frac{R}{\beta}$$

$$R^{(2)} = R$$

Here, $R_\theta^{(1)}$ and $R_\theta^{(2)}$ are two nodule shape functions, rescaled so that their averages equal $R^{(1)}$ and $R^{(2)}$, respectively. Peak contrast C is shared between the two components in a $\alpha : (1 - \alpha)$ ratio. Relative to the first component, the exponent of the second component is reduced by γ fold, while the average radius of the second component is increased by

β fold. Both C and n were derived from the radius of the first component $R^{(1)}$. Simulations were performed for sequences of α , β , and γ over the ranges of 0.2-0.8, 1.1-1.5, and 0.5-1.6, respectively. We found that $\alpha=0.4$, $\beta=1.3-1.4$, and $\gamma=1.3$ provided the most realistic nodule appearances. Equations (20) and (21) with $\alpha=0.4$, $\beta=1.4$, and $\gamma=1.3$ were subsequently used to create double-component nodules, each of which adopted two sets of nodule shape functions, randomly sampled from the library. Sixty pairs of function sets were selected by an experienced pediatric radiologist and added to the library, bringing the total number of designs to 120 (i.e. 60 single-component and 60 double-component designs). Figure 25 illustrates an example simulated nodule in 3-D.

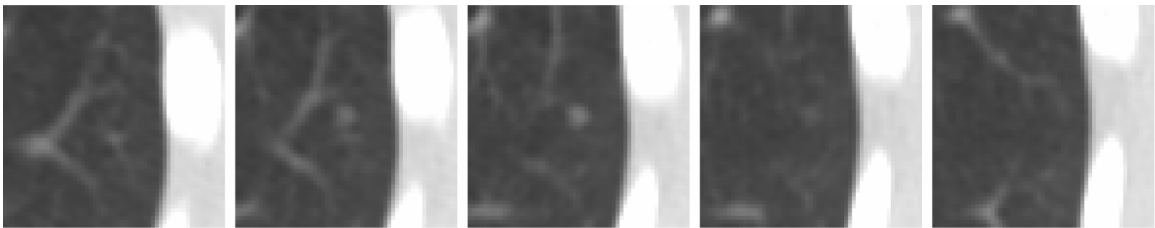


Figure 25: An example simulated (single-component) nodule in three dimensions. The nodule was simulated with $2R_0 = 5$ mm and $C_0 = 350$ HU on 5 contiguous CT slices with slice thickness of 5 mm and reconstruction interval of 2.5 mm. All ROIs are 30 mm in size with the nodule located centrally.

6.2.4 Comparison between Real and Simulated Nodules: Physical Characteristics

We compared real and simulated nodules in terms of measured shape and contrast profile irregularities.

For the comparison, twenty real nodules with diameters of 4-6 mm were selected, excluding nodules that were too small to demonstrate contrast profiles or too close to vessels to allow accurate segmentation. The largest/brightest 2-D mask of each nodule was segmented with a method described by Hoe et al¹²³. Using the maximum pixel value as peak contrast and the corresponding pixel as origin, we derived six contrast profiles from each mask by plotting average pixel value as a function of radial distance for six evenly divided angular bins. The contrast profiles were then normalized to the peak contrast and fitted to the normalized version of Equation (17) as

$$c'(r) = \left(1 - \left(\frac{r}{R'} \right)^2 \right)^{n'} \quad (22)$$

where $c'(r) = c(r)/C$ is normalized contrast. For each nodule, six R' and six n' values were extracted from the fits. In a few cases where Equation (22) did not provide a good fit, we further attempted double-component fits.

The visual span of a contrast profile was measured in terms of $R'_{0.05}$, the distance at which normalized contrast $c'(r)$ equals 0.05, i.e.

$$R'_{0.05} = R' \sqrt{1 - \sqrt[n']{0.05}} \quad (23)$$

Accordingly, the visual steepness of a contrast profile was measured by

$$\eta = \frac{R'_{0.05}}{R'_{0.5}} = \frac{\sqrt{1 - \sqrt[n']{0.05}}}{\sqrt{1 - \sqrt[n']{0.5}}} \quad (24)$$

The dimensionless quantity η is a slowly increasing function of n' , and thus is inversely related to the steepness of the contrast profile. Furthermore, to describe shape and contrast profile irregularities, *coefficients of intra-nodule variation* were calculated for the six $R'_{0.05}$ and six η values of each nodule as

$$\begin{aligned} \text{cov}(R'_{0.05}) &= \frac{\sigma(R'_{0.05})}{\bar{R}'_{0.05}} 100\% \\ \text{cov}(\eta) &= \frac{\sigma(\eta)}{\bar{\eta}} 100\% \end{aligned} \tag{25}$$

To compare with real nodule masks, the 120 designs in our library were used to simulate 60 single-component and 60 double-component 2-D masks on a zero background with nodule centers assuming random vertical (z-direction) locations inside the background. Radius R_0 and peak contrast C_0 were randomly sampled from ranges determined to match that of the real masks. The same fitting method was applied to the simulated masks to extract R' and n' values for the calculation of $\text{cov}(R'_{0.05})$ and $\text{cov}(\eta)$.

Two-sample t -tests were performed to compare shape and contrast profile irregularities of simulated and real masks. Commercial software (JMP, version 6; SAS Institute, Cary, NC) was used to perform the tests at a significance level of 0.05.

6.2.5 Comparison between Real and Simulated Nodules: Observer Experiment

The quality and clinical utility of simulated nodules were evaluated in terms of the ability of radiologists to distinguish between simulated and real nodules.

Sample Preparation. Sixteen of the patients had one or more lung nodules. Images with more than one nodule were rendered multiple times, and each time, all but one nodule was digitally removed using a method described in Reference¹²³. This process provided 34 image sets, each containing 4-6 contiguous CT slices with a single real nodule visible on 1-4 slices.

Another 55 image sets of 4-6 slices, clear of nodules, were identified from images of all 21 patients and used as backgrounds for nodule simulation. A single simulated 3-D nodule with simulation diameter $2R_0$ of 3-7 mm (corresponding to visual diameter of 2.5-6 mm) was inserted into each of the 55 backgrounds at randomly selected locations in the pulmonary parenchyma, not immediately adjacent to the chest wall. A peak contrast C_0 range of 200-600 Hounsfield units (HU) was used to match the contrasts of real nodules. Figure 26 illustrates examples of simulated nodules in this sample. The ratio of single-component to double-component nodules was 5:4, but they were otherwise grouped and analyzed together to enlarge the scale of the study. Another 4 image sets of 4-6 slices, clear of nodules, were combined with the real and simulated nodule samples, yielding a total of 93 image sets for the observer experiment.

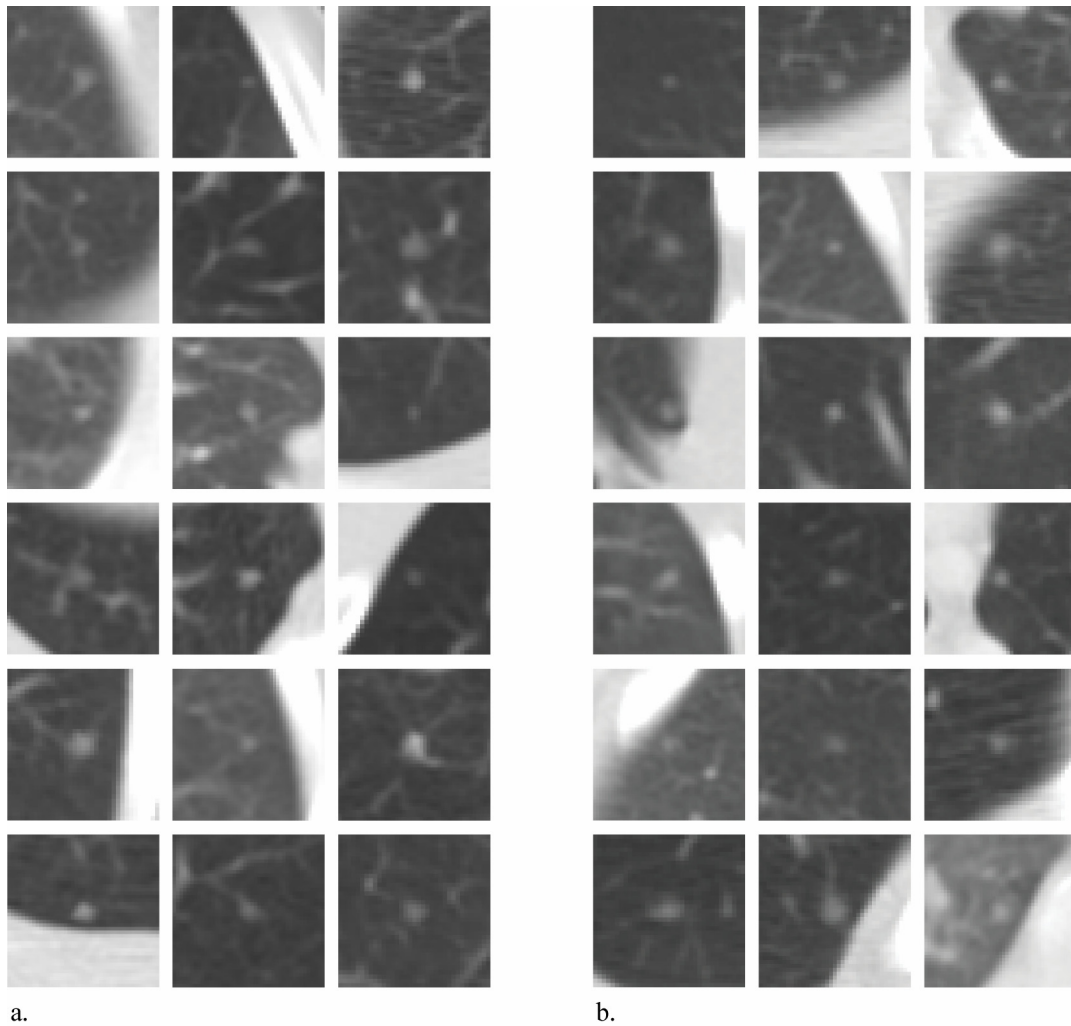


Figure 26: Examples of simulated nodules used in the observer experiment: the central slices of (a) 18 single-component and (b) 18 double-component nodules. All ROIs are 20 mm in size with nodules located centrally.

Observer Experiment. The 93 image sets were randomized and displayed as independent series on a GE Advantage Workstation (GE Healthcare, Waukesha, WI) set to the standard lung window (window center = -500 HU, window width = 1500 HU) in a controlled reviewing environment. Four experienced pediatric radiologists (with 3-12 years of experience with pediatric CT) independently rated the image sets for nodule

appearance on a continuous scale between 0 (definitely not real) and 100 (definitely real). All observers were told that there was zero or one nodule in each image set; they were not told how many of image sets had no nodule or how many were real. The observers were encouraged to use the full scale for assigning scores. They had no time limit in rating each image set, but they were not allowed to return to an image set once rated. To minimize the effect of learning period, the image sets were shown in numerical order to two observers, but in reverse numerical order to the other two. Each observer was first asked about the presence of nodule, and if a nodule was found, the observer was asked to point to the location before rating on a score sheet.

Data Analysis. The detection rates and the rates of false (spurious nodule) detection were computed for the real and simulated nodules. As the goal of the experiment was to evaluate the appearances of the known nodules in the images, scores given to spurious (non-existing) nodules were discarded from further analysis.

ROC analysis was performed to test each observer's ability to distinguish between simulated and real nodules. ROC software (ROCKIT, version 1.1 B 2; Charles E. Metz, University of Chicago, IL) was used. Simulated nodules were defined as positive cases; true-positive fraction (TPF) was the likelihood of a simulated nodule being identified as simulated, while false-positive fraction (FPF) was the likelihood of a real nodule being identified as simulated. As our objective was to determine whether simulated nodules could emulate the appearances of real ones, our ROC analysis was

targeted to determine how close the areas under the ROC curves were to the chance value of 0.5. In that way, our objective in this use of the ROC analysis, precedent by an earlier study¹²⁴, was somewhat different from that in the standard use of the ROC methodology, in which one aims to assess the *difference* (and not the similarity) between two alternatives (e.g. disease present versus disease absent).

Two-sample *t*-test was also performed for each observer to test the null hypothesis that the difference in population mean score between simulated and real nodules ($\Delta\bar{\mu} = \bar{\mu}_{\text{simulated}} - \bar{\mu}_{\text{real}}$) was zero. Commercial software (JMP, version 6; SAS Institute, Cary, NC) was used to perform the *t*-tests at a significance level of 0.05.

Lastly, equivalence tests were performed based on the confidence intervals of $\Delta\bar{\mu}$. We defined the zone of equivalence as $\pm <\sigma(\chi_{\text{real}})>_{\text{observer}}$, the standard deviation of real nodule scores averaged across observers. As a graphical depiction of the quality of simulated nodules, histograms of the frequencies of score assignments for both types of nodules were derived for each observer.

6.3 Results

6.3.1 Physical Characteristics

Among the 120 contrast profiles derived from the 20 real nodule masks, 105 profiles (87.5%) fitted well to Equation (22) as exemplified by Figure 27a and Figure 27b, 5 (4.2%) profiles had apparent two-component appearance resembling that in Figure 27c, and 10 (8.3%) profiles had apparent flat tops resembling that in Figure 27d. For the 120

simulated nodule masks, the goodness-of-fit resembled that in Figure 27a and Figure 27b. Ten (1.4%) profiles had slight two-component appearance similar to that in Figure 27c, but not as obvious. Equation (22) was found to provide generally reasonable fit for both real and simulated nodule masks.

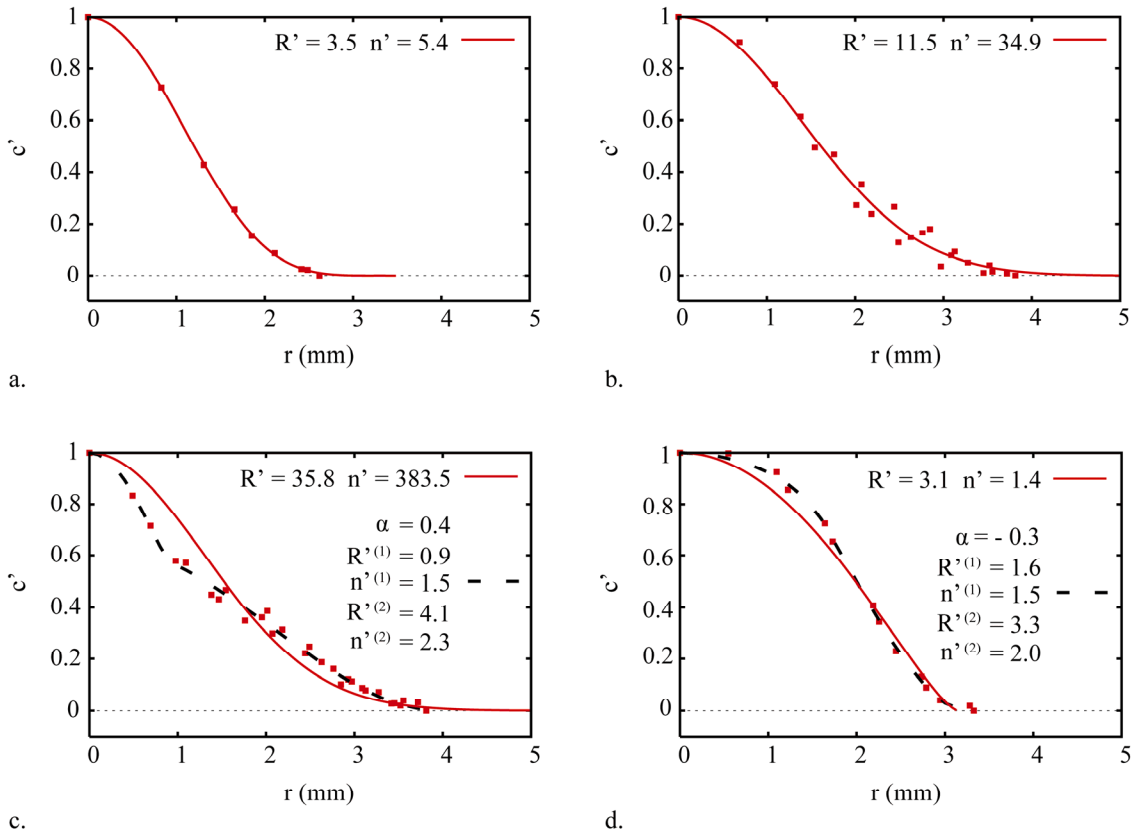


Figure 27: Sample results of curve fitting performed for normalized contrast profiles of 20 real nodule masks. Contrast profiles are represented by symbols, and their fits to Equation (22) are represented by solid lines. All R' , $R'^{(1)}$, and $R'^{(2)}$ values are in the unit of mm. (a) An excellent fit with small residues. (b) Another excellent fit, where the general trend of the contrast profile was well described by Equation (22), despite the relatively large residues. (b) is also an example fit that yielded large R' and n' values. The corresponding $R'_{0.05}$ and η values were 3.3 mm and 2.1, respectively, more suitable to describe the visual radius and steepness of this contrast profile than the original R' and n' values. (c) and (d) are two examples of not excellent, but acceptable fits to Equation (22). Excellent fits, however, were obtained when fitting these two contrast profiles to the double-component version of Equation (22), as demonstrated by the thick dashed lines.

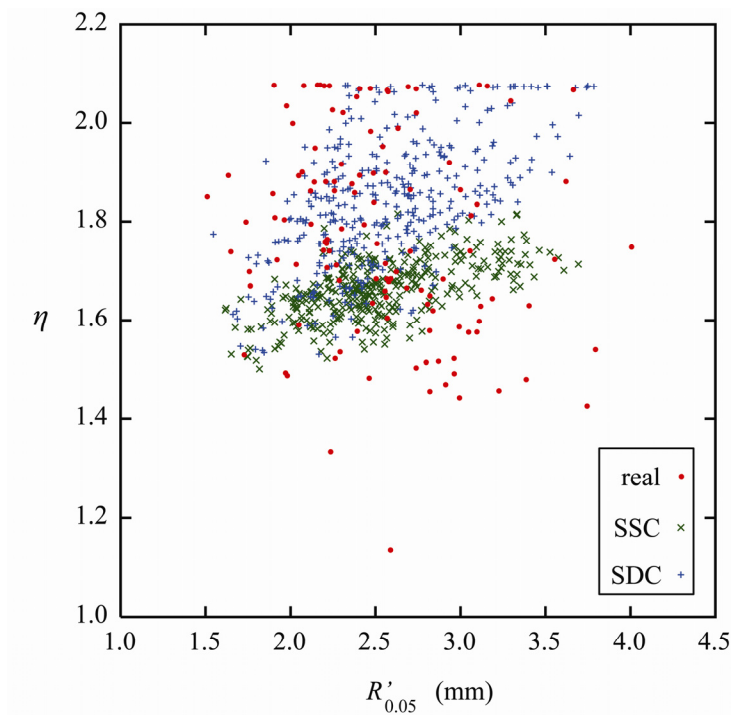


Figure 28: Scatter plots of visual steepness (inversely related to η) versus visual radius $R'_{0.05}$ for real, simulated single-component (SSC), and simulated double-component (SDC) nodule masks.

When comparing scatter plots of visual steepness versus visual radius (Figure 28), excellent match was found between simulated and real masks except for the lower right corner ($R'_{0.05} > \sim 2.75$ mm or visual diameter $> \sim 5.5$ mm) of the real mask scatter plot, where the sharp steepness (small η values) of some contrast profiles was not captured by the simulation. Although marginally significant differences in shape irregularity and significant differences in contrast profile irregularity were found between the two types of simulated masks and the real ones (Table 24), the three types of masks had comparable shape irregularities, and simulated double-component masks had comparable contrast profile irregularities to the real ones.

Table 24: Summary of *t*-test results for comparing real and simulated nodule masks in terms of shape and contrast profile irregularities

Case	Sample Size	Mean (\pm sd ^a)	Difference (95% CI ^b)	<i>p</i> -value ^c
Shape irregularity $\text{cov}(R'_{0.05})$ ^d				
Real	20	14.1 (\pm 5.2)		
SSC ^e	60	11.0 (\pm 3.8)		
SDC ^e	60	11.5 (\pm 4.4)		
SSC – Real			-3.0 (-5.6, -0.4)	0.02
SDC – Real			-2.6 (-5.2, 0.1)	0.06
Contrast profile irregularity $\text{cov}(\eta)$ ^d				
Real	20	8.1 (\pm 2.2)		
SSC	60	3.2 (\pm 1.2)		
SDC	60	6.3 (\pm 3.0)		
SSC – Real			-4.9 (-6.0, -3.9)	< 0.0001
SDC – Real			-1.8 (-3.1, -0.5)	0.01

^a sd = standard deviation.

^b CI = confidence interval.

^c The null hypothesis was that the difference in population mean shape/contrast profile irregularity between simulated single/double-component masks and real masks was zero.

^d $\text{cov}(R'_{0.05})$ and $\text{cov}(\eta)$ are coefficients of intra-nodule variation in radius and steepness of contrast profile, respectively.

^e SSC = simulated single-component, SDC = simulated double-component.

6.3.2 Observer Experiment

The real and simulated nodules had similar and high detection rates, 86.8% and 78.2%, respectively, with similar rates of false (spurious nodule) detection, 2.2% and 1.4%, respectively (Table 25). At these similar detection rates, the observers could not reliably distinguish simulated nodules from real ones. All ROC curves (Figure 29) were close to the chance line. No significant difference in population mean score was found between simulated and real nodules for any observer (Table 25). Although three of the

observers assigned slightly lower scores to simulated nodules, the lower limits of all confidence intervals of $\Delta\bar{\mu}$ ($\bar{\mu}_{\text{simulated}} - \bar{\mu}_{\text{real}}$) were well contained within the zone of equivalence (Figure 30), indicating that the two types of nodules were perceptually equivalent within the normal variation of real nodule appearances. The histograms of score assignments (Figure 31) showed that the distributions of scores were similar for the two types of nodules for all observers.

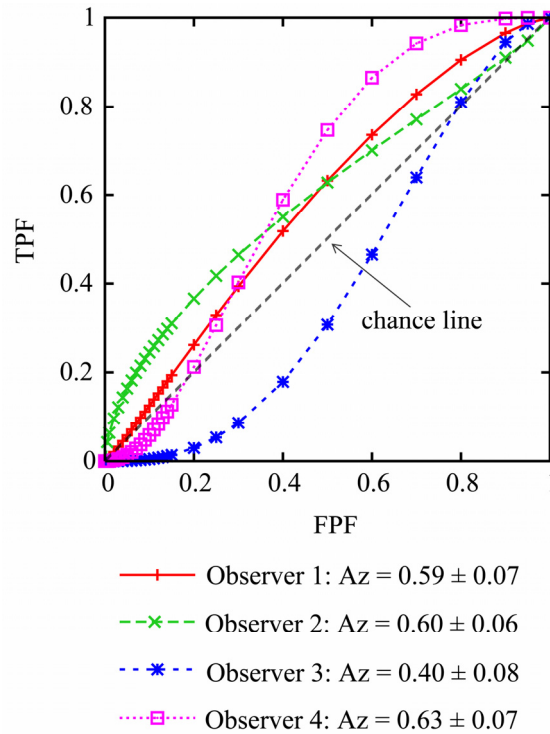


Figure 29: Results of ROC analysis. Simulated nodules were defined as positive cases; true-positive fraction (TPF) was the likelihood of a simulated nodule being identified as simulated, while false-positive fraction (FPF) was the likelihood of a real nodule being identified as simulated. Error figures refer to standard errors.

Table 25: Summary of *t*-test results for comparing real and simulated nodule scores

Observer and Case	Detection Rate ^a	Mean Score (\pm sd ^b)	Difference (95% CI ^c)	<i>p</i> -value ^d
Observer 1				
Real	97.1%	59.7 (\pm 25.7)		
Simulated	81.8%	51.7 (\pm 24.3)		
Simulated-Real			-8.0 (-19.5, 3.5)	0.17
Observer 2				
Real	91.2%	69.2 (\pm 23.4)		
Simulated	83.6%	58.2 (\pm 27.5)		
Simulated-Real			-11.0 (-22.6, 0.7)	0.06
Observer 3				
Real	76.5%	49.5 (\pm 38.5)		
Simulated	69.1%	62.1 (\pm 29.6)		
Simulated-Real			12.5 (-5.5, 30.6)	0.17
Observer 4				
Real	82.4%	83.2 (\pm 15.0)		
Simulated	78.2%	79.3 (\pm 13.1)		
Simulated-Real			-3.9 (-10.9, 3.0)	0.26

^a The detection rates averaged across observers were 86.8% and 78.2% for the real and simulated nodules, respectively. The rates of missed nodules, for which no scores were given or scores were given to spurious (non-existing) nodules, equaled one minus the corresponding detection rates. The rates of false (spurious nodule) detection averaged across observers were 2.2% and 1.4% for the real and simulated cases, respectively. Scores given to spurious nodules were not included in the analysis.

^b sd = standard deviation.

^c CI = confidence interval.

^d The null hypothesis was that the difference in population mean score between simulated and real nodules was zero.

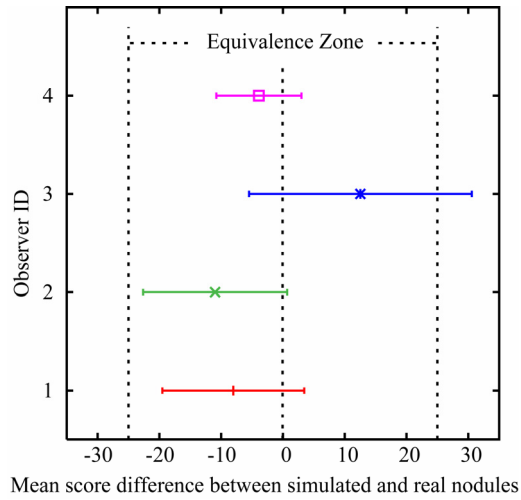


Figure 30: Results of equivalence tests based on confidence intervals of the differences in population mean score between simulated and real nodules ($\Delta\bar{\mu} = \bar{\mu}^{\text{simulated}} - \bar{\mu}^{\text{real}}$). The zone of equivalence was defined as $\langle\sigma(x_{\text{real}})\rangle_{\text{observer}}$, the standard deviation of real nodule scores averaged across observers.

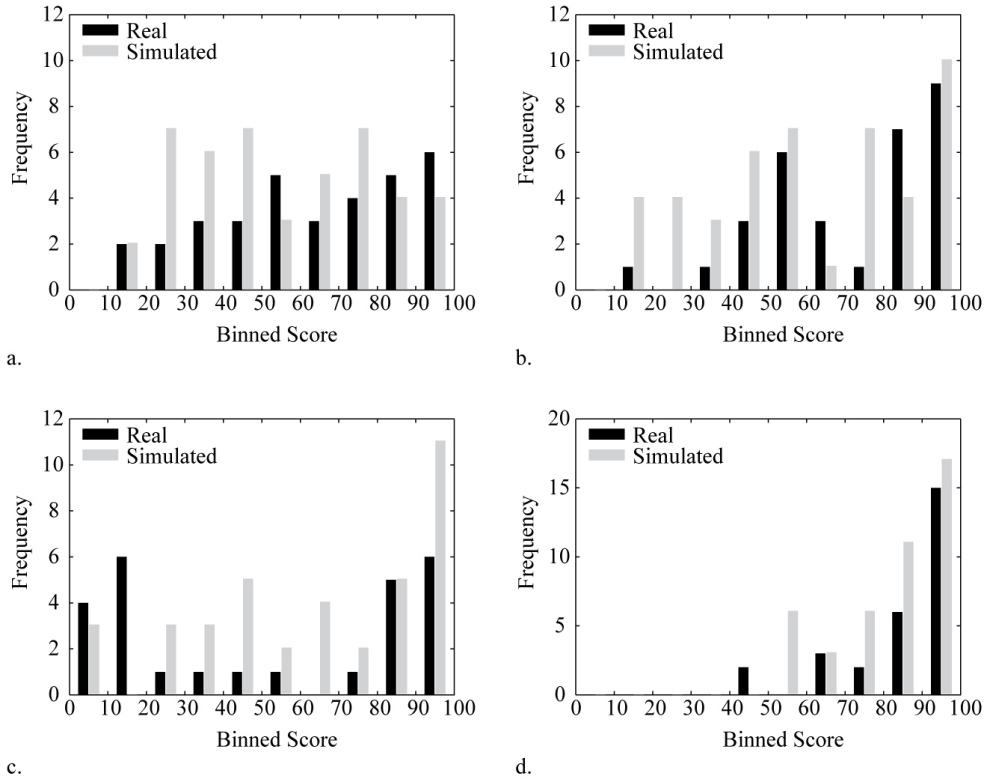


Figure 31: Histograms of score assignments for (a) observer 1, (b) observer 2, (c) observer 3, and (d) observer 4. Scores of 100 were included in the last bin of each histogram.

6.4 Discussions

Computer modeling of lung nodules has been an important area of investigation in CT⁴⁴⁻⁴⁸. Most prior studies have not aimed to emulate the features of real lung nodules, validated by observer studies of nodule appearances. Two recent studies have offered an exception^{46, 47}; however, the modeled nodule characteristics were typical of large (> 5 mm) nodules, a range that is larger than what would be subtle enough for most technique optimization studies in MDCT, particularly in pediatric applications^{48, 125}. Most recently, in an investigation focused on the pediatric population⁴⁸, a single real nodule extracted from a pediatric chest MDCT image was digitally resized and inserted back into the image to study the effects of added noise on nodule detection. The nodule was presented and reviewed on a single slice only, was not validated as representing a standard nodule, and did not vary in terms of shape or contrast, making the nodule detection study less reflective of the actual clinical paradigm in which nodules with variable appearances need to be detected.

In this work, we developed *and* validated a technique for computer modeling of small lung nodules in 3-D. Our study focused on pediatric MDCT because of the fact that the pediatric population is more sensitive to radiation-induced cancer, making investigations in dose reduction more important, at the same time, limiting our ability to systematically investigate lower dose techniques due to ethical concerns with multiple MDCT scans on the same patients with technique variations.

Our work also represents, to our knowledge, the first detailed characterization of small lung nodules in terms of shape and contrast profile irregularities. The contrast profiles of most small lung nodules on pediatric MDCT images fitted well to an exponential equation originally proposed for nodules in chest radiography. In those cases where fitting to this original equation was unsatisfactory, the double-component version could be used to achieve excellent fits. These findings supported our application of this equation to simulate small lung nodules. With the introduction of radial asymmetry, the simulation nearly matched the shape irregularities of real nodules.

Even though the objective of our study was to compare real and simulated nodules in terms of their appearances, not of their detection rates, it is interesting to examine their detection rates and the reason for missed nodules. The real nodules yielded a higher detection rate, which is not surprising given the fact that they were pre-selected, i.e. they had been detected (in the sample selection process) in the first place before they could be included in the study. Nevertheless, the detection rates of the two types of nodules were similar. Therefore, the subtlety of the simulated nodules (determined by size, shape, contrast, and location) adequately resembled that of the real nodules, and would be appropriate for studies aiming at comparing nodule detection rates between different CT techniques. Revisiting the cases with missed real/simulated nodules revealed that most of the nodules that were missed by more than two observers were close to vessels and thus looked like parts of the vessels. This highlights the

importance of nodule location in detection studies that employ nodule simulation techniques.

One limitation of our study is that we did not fully model the contrast profile irregularities of real nodules. We assumed a linear increase of exponent n with radius R_g . As a result, contrast profile steepness (inversely related to η) of simulated nodules showed a decreasing trend with nodule radius (Figure 28). The behaviors of real nodules, however, were more complex and variable. Closer match was found between simulated double-component and real masks because the superimposition of two components of different sizes and shapes introduced more variations. This physical discrepancy, however, did not seem to have provided strong visual clues to our observers as demonstrated by the results of the observer experiment. Another limitation is that our 3-D nodule model did not fully account for the effects of respiratory and cardiac motions, which could further depend on nodule locations in the lung parenchyma. By adding nodules directly to reconstructed CT slices, we have assumed that the noise characteristics of the images remain the same with or without the nodules. For the small nodule sizes modeled in our study, this is a valid assumption, because the perturbations of the small nodules to the attenuation properties of the images are negligible. Lastly, our evaluation of the technique was limited to the ranges of scan protocols, slice thickness, reconstruction intervals used for the pediatric MDCT patients

at our institution only. However, our method can be readily adapted to simulate small lung nodules on images acquired with other scan and reconstruction protocols.

Our simulation method may also enable the modeling of large nodules, which often have flat-topped contrast profiles. A few real nodules in our study exhibited such contrast profiles, which did not fit well to the single-component contrast profile equation (as exemplified by the solid line Figure 27d) and contributed to the lower right corner of the real mask scatter plot (combinations of small η with $R'_{0.05} > \sim 2.75$ mm or visual diameter $> \sim 5.5$ mm). However, a double-component contrast profile equation in which a small component is subtracted from a large component can model such contrast profiles (thick dashed line in Figure 27d), thus extending our method to simulate larger nodules, provided that the nodule sizes are small enough ($< \sim 1$ cm) to still consider the perturbations to the noise backgrounds negligible.

In conclusion, our results demonstrated that mathematical simulation is a feasible technique for creating small lung nodules that resemble real nodules in physical characteristics and detection rate, and are perceptually indistinguishable from real nodules to experienced pediatric radiologists. The nodule simulation technique can find applications in several areas of research. When used in conjunction with noise (tube current reduction) simulation techniques operating on either projection or reconstructed CT images^{50, 51, 53, 125}, simulated 3-D nodules can be used in dose reduction studies. As opposed to the virtually impractical process of collecting nodules from pediatric

patients, simulated nodules can be inserted to normal MDCT images, allowing quick generation of a large database of images with established truth. Our technique may also prove useful in the optimization of other CT imaging parameters and in the training and evaluation of computer-aided diagnosis systems. Lastly, we believe that the simulation technique can be extended to model nodules and lesions in other organs, facilitating not only research investigations but potentially education and training of medical professionals¹²⁶.

7. Comparison of Patient Size Based Methods for Estimating Quantum Noise in CT Images of the Lung^{*}

7.1 Introduction

To assess the effect of reduced radiation dose on image quality in computed tomography (CT), one frequently needs to ascertain the level of quantum noise in the image^{107, 111, 127}. Knowledge of the noise can guide CT protocol designs to provide acceptable noise levels with minimum dose to the patient. However, it is often difficult to reliably and accurately measure the quantum noise in actual patient images due to the underlying anatomy (structured noise). An example is quantum noise in images of the lung, which is impossible to be measured directly. Therefore, methods are needed to estimate the noise indirectly. One method is to reconstruct the noise in each CT pixel using a modified filter backprojection formulation that includes the square of the reconstruction kernel¹²⁸⁻¹³⁰. While accurate, this method requires proprietary knowledge of the reconstruction kernel and the availability of sinogram data, which are cumbersome to store and transfer and are poorly archived (deleted by most sites after image reconstruction). Another method is to acquire two copies of the same patient image at exactly the same setting and divide the subtraction image by $\sqrt{2}$ to yield the noise image^{131, 132}. While simple to perform, this image-subtraction method requires

^{*} This chapter is based on an article with the same title published in the journal *Medical Physics*.

scanning the same patient twice and is unacceptable due to the additional radiation burden to the patient.

An alternative approach is to estimate noise based on patient size. It is well-established that object size (d) is a factor that influences quantum noise (σ) in CT: $\sigma^2 \propto e^{\mu d}$, where μ is the energy-dependent X-ray attenuation coefficient of the object³⁹. For a specific CT system and scan protocol, the exact relationship between σ and d can be determined for cylindrical phantoms of uniform materials¹⁰⁷. If an effective diameter can be established for a patient, this relationship can then be used to estimate quantum noise in the patient image.

The goal of this technical note is to compare different patient size based methods for estimating quantum noise in CT images of the lung. The relationship between noise and diameter is determined on a 64-slice CT system for a series of water phantoms. Using noise measured by the image-subtraction method as a gold standard, four patient size based methods are compared for their suitability to estimate quantum noise in CT images of the lung.

7.2 Materials and Methods

7.2.1 Noise-Diameter Relationship in Water Phantoms

To estimate quantum noise in the patient image based on patient size, we first determined the relationship between noise and diameter in water phantoms. Six cylindrical water phantoms with diameters of 12.7, 15.3, 17.8, 20.0, 23.3, and 27.0 cm

were used to represent body size ranging from infant, to adolescent, to small adult (Figure 32).



a.



b.

Figure 32: Six water phantoms representing body size ranging from infant, to adolescent, to young adult: (a) five custom-built phantoms with diameters of 12.7, 15.3, 17.8, 23.3, and 27.0 cm, and (b) 20-cm-diameter GE quality-assurance water phantom.

Each phantom was scanned on a clinical 64-slice CT scanner (LightSpeed VCT, GE Healthcare, Waukesha, WI) at four tube potentials of 80, 100, 120, 140 kVp and eleven tube currents of 200, 180, 160, 140, 120, 100, 80, 60, 40, 20, 10 mA with 40-mm beam collimation and 0.4-second gantry rotation period. Other scan parameters were summarized in Table 26 and were chosen to emulate our size-based clinical MDCT protocols.

Table 26: Scan parameters used to acquire noise images from six water phantoms.

Bowtie Filter	Water Phantom Diameter (cm)	Pitch	Slice Thickness ^a (mm)
small	12.7	0.984	3.75
	15.3	0.984	3.75
	17.8	1.375	5
	20.0	1.375	5
medium	17.8	1.375	5
	20.0	1.375	5
	23.3	1.375	5
	27.0	1.375	5
large	20.0	1.375	5
	23.3	1.375	5
	27.0	1.375	5

^a Same as reconstruction interval.

At each combination of bowtie filter, phantom size, kVp, and mA, three to five contiguous CT slices were selected from the middle of the scanned section. On each selected CT slice, noise was measured as standard deviation of pixel values within a central region-of-interest (ROI), which was free of image artifact and had an area larger than a quarter of the total cross-sectional area of the phantom. The noise thus measured was averaged across contiguous CT slices to yield a single noise figure for the combination of bowtie filter, phantom size, kVp, and mA. At extremely low kVp and/or mA and for large phantom sizes, severe photon starvation shifted CT numbers of the images. The standard deviations measured from such images no longer represented noise and were not included in subsequent analysis.

At each combination of bowtie filter and kVp, the measured noise data were fitted to a second-order polynomial equation as

$$\ln(\sigma) = \alpha_0 + \alpha_1 d + \alpha_2 \ln(mA) + \alpha_3 d^2 + \alpha_4 \ln^2(mA) + \alpha_5 d \ln(mA), \quad (26)$$

where σ is the measured noise, mA is tube current, and d is phantom diameter. Commercial software (OriginPro 8, v8.0725, OriginLab Corporation, MA) was used to perform the fits.

7.2.2 Noise in the Lung Measured Using Image-Subtraction Method

Quantum noise in the lung images of an anthropomorphic phantom (ATOM, adult female, Model 702, CIRS, Norfolk, VA) was measured using the image-subtraction method and served as a gold standard. The chest section of the phantom without breast inserts was scanned on the CT scanner at a tube voltage of 120 kVp, tube currents of both 95 and 20 mA, pitch of 1.375, gantry rotation period of 0.4 second, beam collimation of 20 mm, and medium body scan field-of-view (corresponding to medium bowtie filter) with slice thickness of 5 mm at 5 mm interval. At each tube current, the phantom was scanned twice, and the difference in pixel value between the two scans was divided by $\sqrt{2}$ to yield the noise map of each CT slice (Figure 33). Twenty-eight contiguous CT slices were selected covering most volume of the lung. On the noise map of each selected CT slice, six 50-pixel-diameter ROIs, evenly distributed in the lung, were identified (Figure 33). Noise values (standard deviations of pixel values) in the six ROIs were averaged to yield a single noise figure for the CT slice. The coefficient of variation¹⁰⁴ for

the six noise values was used to quantify noise variation in the lung within a CT slice. The coefficient of variation was also calculated for the twenty-eight average noise figures to quantify noise variation across the lung volume.

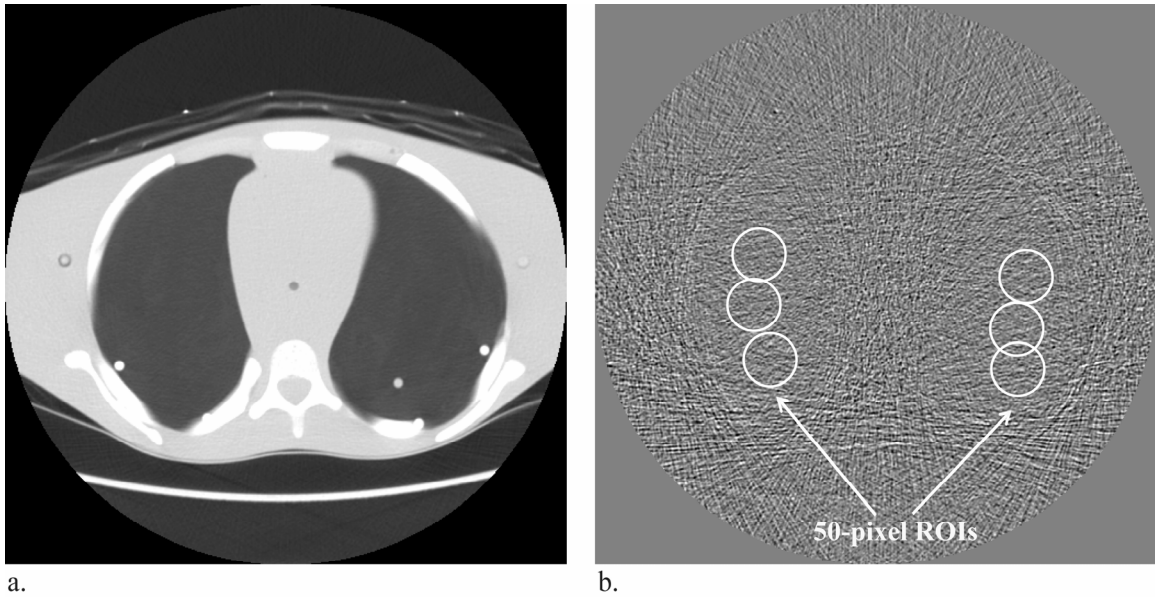


Figure 33: (a) A CT slice from the chest section of the anthropomorphic phantom acquired at 95 mA. (b) The noise map of (a) obtained by subtracting two copies of (a) and dividing the subtraction image by $\sqrt{2}$. Standard deviations of pixel values within six 50-pixel-diameter ROIs evenly distributed in the lung region were averaged to yield a single noise figure for the CT slice.

7.2.3 Noise in the Lung Estimated Using Patient Size Based Methods

Quantum noise in the lung was estimated for the aforementioned 28 CT slices of the anthropomorphic phantom using four methods, each based on a different definition of patient size, characterized in terms of water-equivalent diameter (d_w).

Chest Area Method: A patient's chest was assumed to be composed entirely of water with $d_w^{(CA)}$ defined as the diameter of a circle having the same circumference/area

as the circumference/area of the patient's chest in the image. This definition has been used by Boone et al.⁹³ to determine the equivalent-diameters of patients from abdomen CT images, who found that the equal-circumference criterion and the equal-area criterion produced similar results. The equal-area criterion was used in this study for the ease of computation. The chest area was calculated as the total area of all pixels in the image with CT numbers greater than -900 HU to reduce the contribution from the patient bed in the reconstruction field-of-view. For each of the 28 CT slices, $d_w^{(CA)}$ was used to estimate quantum noise in the lung at both 95 and 20 mA using the relationship in Equation (26).

Water-Equivalent Area Method: To take into account the difference in X-ray attenuation property between tissue and water, patient size was characterized by $d_w^{(WEA)}$, the diameter of a circle having the same area as the water-equivalent area of the patient's chest in the CT slice. The water-equivalent area was calculated as $\sum (CT/1000 + 1)a$, in which CT and a were the CT number and the area of each pixel, respectively, and the summation was over all pixels in the reconstruction field-of-view. Because the bulk of the patient bed has very low X-ray attenuation, contribution from the patient bed in the reconstruction field-of-view was minimal. A similar definition of d_w has been adopted by Menke¹³³ who calculated d_w from the average image of a patient's scanned section and used it to summarize the x-ray attenuation properties of the scanned section for patient-specific dose adaptation purposes. Patient size defined this way has also been used in

the algorithm of z-axis automatic tube current modulation¹³². For each of the 28 CT slices, $d_w^{(WEA)}$ was used to estimate quantum noise in the lung at both 95 and 20 mA using the relationship in Equation (26).

Non-lung Area Method: As a variant of the preceding method, the linear attenuation coefficients of lung were assumed to be zero, and that of the bone and soft tissue to be water-equivalent. Patient size was thus characterized by $d_w^{(NLA)}$, the diameter of a circle having the same area as the non-lung area of the patient's chest in the CT slice. The non-lung area was calculated as the total area of all pixels in the reconstruction field-of-view with CT numbers greater than -200 HU. For each of the 28 CT slices, $d_w^{(NLA)}$ was used to estimate quantum noise in the lung at both 95 and 20 mA using the relationship in Equation (26).

Water-Equivalent Path Length Method: Considering the facts that noise at a location in the CT slice is a result of back-projecting the noise in all CT projections that interrogate that location, and the noise in a projection is determined by the attenuation that X-ray traces through in that projection, patient size was characterized by $d_w^{(WEPL)}$, the water-equivalent path length of X-ray through a location of interest in the image averaged over all X-ray incident angles. To determine $d_w^{(WEPL)}$ for a pixel location, the CT numbers (CT) of all pixels in the image were first converted to linear attenuation coefficients ($\mu = CT/1000 + 1$), normalized by μ_{water} . Radon transform (Matlab, Mathworks, Natick, MA) was then employed to calculate the line integral (i.e., water-

equivalent path length) through the pixel location of interest for X-ray incident angles between 0° and 180° . The average of those line integrals was $d_w^{(WEPL)}$. For each of the 28 CT slices, $d_w^{(WEPL)}$ was calculated for ten evenly distributed pixel locations in the lung, and the results were averaged to yield a single $d_w^{(WEPL)}$ for the CT slice. The $d_w^{(WEPL)}$ was used to estimate quantum noise in the lung region of the CT slice at both 95 and 20 mA using the relationship in Equation (26).

Error Evaluation: The accuracies of the four patient size based methods were evaluated against the gold standard of image-subtraction method. For each of the 28 CT slices, percent errors were calculated for the quantum noise estimated by $d_w^{(CA)}$, $d_w^{(WEA)}$, $d_w^{(NLA)}$, and $d_w^{(WEPL)}$ at both the 95 and 20 mA settings.

Table 27: Coefficients of polynomial equation describing the relationship between quantum noise and diameter in water phantoms on a LightSpeed VCT scanner.

Bowtie Filter	kVp	Coefficients						Adjusted R ²
		α_0	α_1	α_2	α_3	α_4	α_5	
small	80	4.42809	0.01476	-0.63593	0.00742	0.05724	-0.02681	0.990
	100	4.05954	-0.00583	-0.52538	0.00490	0.01714	-0.00877	0.993
	120	3.97994	-0.02059	-0.52299	0.00471	0.01276	-0.00576	0.995
	140	3.94392	-0.02886	-0.52743	0.00440	0.00723	-0.00249	0.996
medium	80	1.64157	0.26954	-0.42099	-0.00048	0.03194	-0.02331	0.975
	100	1.54965	0.28661	-0.61874	-0.00187	0.05493	-0.02037	0.986
	120	1.24914	0.27993	-0.55677	-0.00275	0.03529	-0.01306	0.990
	140	1.26746	0.25753	-0.51762	-0.00282	0.02260	-0.00886	0.993
large	80	10.17070	-0.12202	-1.94568	0.00783	0.18631	-0.02452	0.998
	100	5.52959	-0.05413	-0.56413	0.00526	0.05182	-0.02125	0.999
	120	4.96463	-0.03127	-0.54763	0.00382	0.03951	-0.01467	0.999
	140	4.66454	-0.01537	-0.56091	0.00271	0.02667	-0.00824	0.999

7.3 Results

The relationship between noise and diameter measured from images of the water phantoms fitted well to Equation (26) with adjusted R^2 values close to unity (Table 27). The coefficients $\alpha_i (i = 0, 1, \dots, 5)$ extracted from the fits are also summarized in Table 27.

Quantum noise in the lung measured using the image-subtraction method is illustrated in Figure 34 for the 28 CT slices of the anthropomorphic phantom's chest section at 95 and 20 mA. Noise variation within a CT slice ranged from 2.1% to 9.9% at 95 mA and from 3.7% to 11.4% at 20 mA. Noise variation across the lung volume was 22.7% at 95 mA and 28.8% at 20 mA.

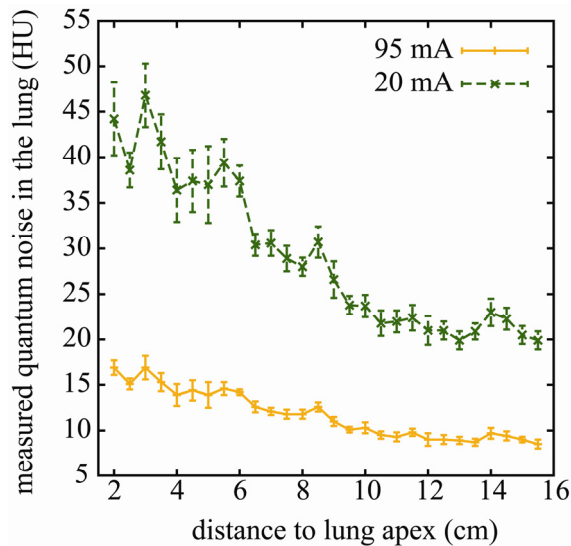


Figure 34: Quantum noise in the lung measured using the image-subtraction method from the 28 contiguous CT slices of the anthropomorphic phantom's chest section at 95 and 20 mA. The error bar reflects the standard deviation of the six measurements on each CT slice. The distance to lung apex was calculated as the z-distance between a given CT slice and the CT slice associated with the most superior position of the lung.

The $d_w^{(CA)}$, $d_w^{(WEA)}$, $d_w^{(NLA)}$, and $d_w^{(WEPL)}$ values calculated for the 28 CT slices are illustrated in Figure 35. Their averages across the chest section were 24.6, 21.0, 18.1, and 14.1 cm, respectively. The accuracies of the noise estimated by the d_w 's are shown in Figure 36a and Figure 36b for 95 mA and 20 mA, respectively. Noise estimated by $d_w^{(NLA)}$ had the highest accuracy with maximum percent error of around 30%, comparable to the magnitudes of noise variation across lung volume. In contrast, noise estimated by $d_w^{(CA)}$, $d_w^{(WEA)}$, and $d_w^{(WEPL)}$ had maximum percent error of 229%, 93%, and 57%, respectively.

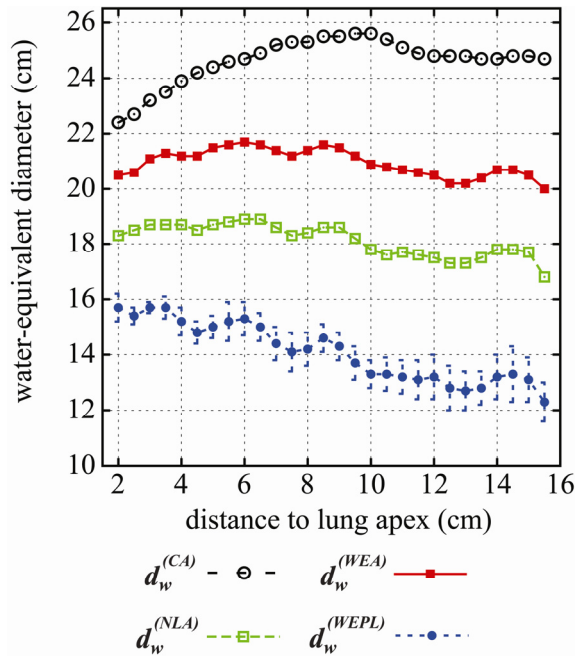


Figure 35: Four definitions of patient size calculated for the 28 contiguous CT slices of the anthropomorphic phantom's chest section, including water-equivalent diameters derived from chest area ($d_w^{(CA)}$), water-equivalent area ($d_w^{(WEA)}$), non-lung area ($d_w^{(NLA)}$), and water-equivalent path length ($d_w^{(WEPL)}$). The error bar on $d_w^{(WEPL)}$ reflects the standard deviation of the ten $d_w^{(WEPL)}$'s calculated for each CT slice. The distance to lung apex was calculated as the z-distance between a given CT slice and the CT slice associated with the most superior position of the lung.

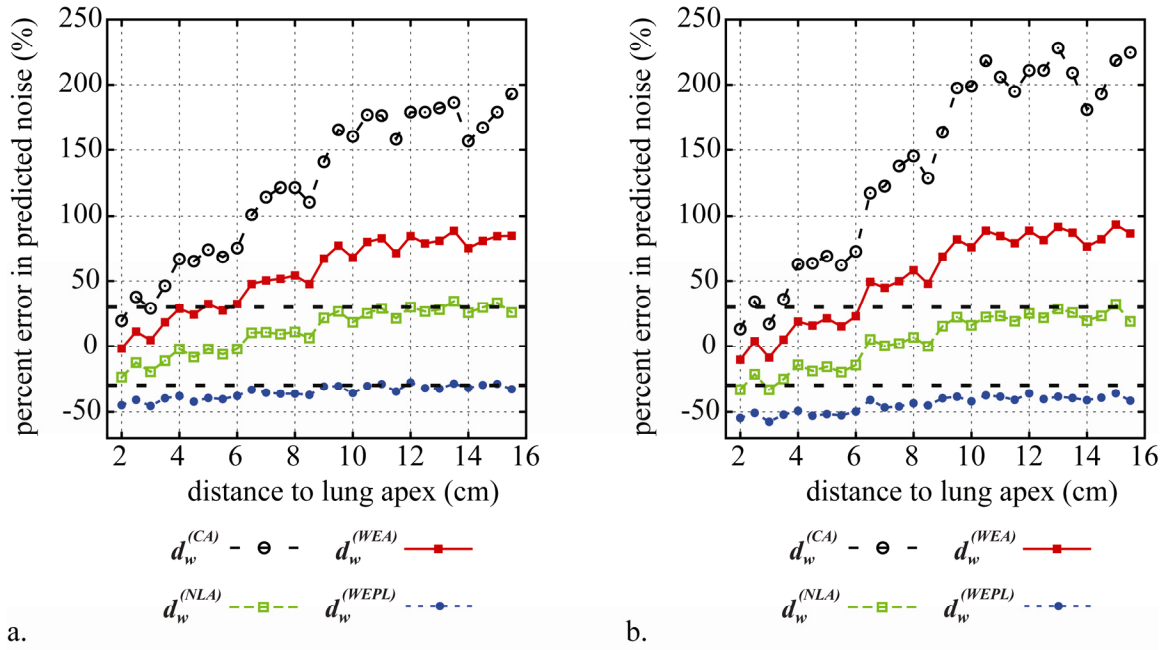


Figure 36: Accuracies of quantum noise in the lung estimated by $d_w^{(CA)}$, $d_w^{(WEA)}$, $d_w^{(NLA)}$, and $d_w^{(WEPL)}$ for the 28 contiguous CT slices of the anthropomorphic phantom's chest section at (a) 95-mA and (b) 20-mA scans. Errors of $\pm 30\%$, the magnitude of noise variation across the lung volume, are indicated by thick dashed lines.

7.3 Discussions

In studies that evaluate the effect of dose reduction on the diagnosis of pulmonary abnormalities, diagnostic accuracy is frequently evaluated at different tube current levels^{49, 52, 134}. Ideally, such evaluations should be performed at different noise levels to allow the generalization of study results to other CT systems and scan protocols. However, this ideal approach has not been used due to the difficulty with ascertaining noise level in the lung. In this study, we explored four methods for estimating quantum noise in the lung, each based on a different definition of patient size and the relationship between noise and diameter determined in water phantoms.

While patient size is commonly characterized based on cross-sectional circumference/area ($d_w^{(CA)}$)⁹³ or water-equivalent area ($d_w^{(WEA)}$)¹³², the results of our study show that such definitions of patient size are not suitable for estimating quantum noise in the lung and result in gross overestimations, presumably because they do not consider the anatomical and attenuation variation across an image. Considering that the technique of z-axis tube current modulation is based on patient size derived from water-equivalent area¹³², the noise index associated with the technique¹⁹ is likely not representative of the actual noise in the lung.

Anatomical/attenuation variation across an image is taken into account when patient size is derived from water-equivalent path length ($d_w^{(WEPL)}$); $d_w^{(WEPL)}$ (and noise) in the lung is in general smaller than that in the mediastinum. Furthermore, the anatomical/attenuation variation across the lung volume is also reflected by $d_w^{(WEPL)}$; the magnitude of $d_w^{(WEPL)}$ (Figure 35) and, hence, the noise it predicted showed a clearly decreasing trend with increasing distance to lung apex, consistent with the decreasing trend of measured noise (Figure 34). Therefore, the noise prediction error of $d_w^{(WEPL)}$, while large, had the lowest variance across the lung volume among all four methods (Figure 36). We attribute the poor accuracy of this method to its neglect of the effect of bowtie filter attenuation on noise. Bowtie filters preferentially attenuate X-ray on the periphery. As a result, at a peripheral location in the lung with $d_w^{(WEPL)}$, the noise is higher than that measured from the center of a water phantom with diameter $d_w^{(WEPL)}$.

In this study, we determined empirically that patient size derived from non-lung chest area has noise prediction errors comparable to the noise variation across lung volume, and thus can be used for a broad estimation of lung noise. Furthermore, the continuous variation of quantum noise from top to bottom of the lung suggests that the average noise level in the lung may be estimated using the non-lung area diameter calculated from a single CT slice at the middle of the chest (half-way between lung apex and lung base).

Our study was limited to a single CT scanner model and an associated clinical protocol in place at our institution. Applicability of our finding to other CT systems and scan protocols requires further validation. Ideally, the accuracies of the different size-based methods should be evaluated using actual patient images. However, because gold standards cannot be established without scanning a patient twice, we chose to perform the study using an anthropomorphic phantom, assuming that the construction of the phantom is representative of actual patient anatomy. A further verification of our finding may be useful if repeated images of patient cadavers are available.

Part III: Diagnostic Accuracy Studies

8. Pediatric MDCT: Towards Assessing the Diagnostic Influence of Dose Reduction on the Detection of Small Lung Nodules*

8.1 Introduction

Owing to the superior resolutions of modern multi-detector array computed tomography (MDCT), chest CT examination for the detection of lung nodules is often standard for pediatric cancer staging and surveillance. In such examinations, the presence of even one small lung nodule may have tremendous prognostic and therapeutic implications⁴⁰. However, a chest MDCT involves the irradiation of many radiosensitive organs, including the thyroids, lungs, breasts, stomach, esophagus, and bone marrow; these organs are at risk for radiation-induced cancer later in life^{16, 135}. Therefore, reducing radiation dose from chest CT is an important area of investigation¹³⁶.

Several previous studies on the pediatric population⁴¹⁻⁴³ have suggested that diagnostic-quality images of the lung could be obtained at significantly reduced tube-current levels. However, those studies were preference-based; reduced-tube-current images were evaluated by assigning subjective image quality scores to known anatomical structures. The results of such studies do not necessarily reflect the actual performance of radiologists in terms of lung nodule detection at reduced tube current

* This chapter is based on an article with the same title published in the journal *Academic Radiology*.

levels. Performance-based evaluations have been hindered by two major challenges: (a) the low occurrence of isolated small lung nodules in the pediatric population makes it difficult to research with real lung nodules, and (b) ethical concerns prohibit repeated scans to be taken on the same patients at different tube current levels.

The former challenge may be overcome by the simulation of lung nodules^{44-46, 48, 137}. However, most prior nodule simulation studies have not aimed to emulate the characteristics of real nodules, validated by observer studies of nodule appearances. In two recent studies which have offered an exception^{46, 47}, the modeled nodule characteristics were typical of large (> 5 mm) nodules, a size range that is not subtle enough for most technique optimization studies in MDCT, particularly in pediatric applications⁴⁸. To overcome the second challenge, one may add virtual noise to existing CT data to simulate reduced tube current conditions⁴⁸⁻⁵⁶. However, most noise simulation software operates on raw projection data, which are cumbersome to store and transfer and often require scanner processors for image reconstruction. In addition, prior software has not been validated in terms of both magnitude and texture of the simulated noise.

The goal of our study was to evaluate the influence of reduced tube current levels on the detection of small lung nodules using hybrid images, real pediatric CT images with added simulated noise and lung nodules. As radiation dose is proportional to tube current, we will refer to “reduced tube current” as “reduced dose” hereafter. Our

study was distinct from prior efforts in that it was performance-based, as opposed to preference-based⁴¹⁻⁴³, used a realistic model of noise with proper texture and calibrated magnitude, and used a validated, realistic, and variable model of three-dimensional lung nodules¹³⁸.

8.2 Materials and Methods

This study was approved by our institutional review board (IRB), who determined that it was in compliance with the Health Insurance Portability and Accountability Act, and did not require informed consent.

8.2.1 Clinical Cases

Normal chest CT examinations of 13 patients (median age, 3 years old; age range, 1-7 years old; median weight, 14 kg; weight range, 11-23 kg) were retrospectively selected from our clinical database of children who underwent 64-slice MDCT examinations (LightSpeed VCT, GE Healthcare, Waukesha, WI). Images were obtained according to our size-based clinical protocols with tube currents of 70-180 mA, tube potential of 100 or 120 kVp (lower kVp in smaller children), effective beam width of 20 or 40 mm, pitch of 1.375, and a slice thickness of 3.75 mm at 3.75-mm interval or 5 mm at 5-mm interval (thinner slice thickness in smaller children). Each examination was reviewed by a radiologist with 18 years of experience in pediatric CT to reconfirm that the CT data were free of any lung nodule.

8.2.2 Noise Simulation

Reduced-dose images were simulated using a noise addition software tool (GE Noise Addition Tool, Version 1.1, GE Healthcare, Waukesha, WI). The software accepts DICOM (Digital Imaging and Communications in Medicine) images acquired on the LightSpeed VCT scanner and adds noise to axial slice data to simulate either a reduced tube current (mA) or an increased noise index.

Principles of Noise Simulation

The noise addition tool is based on the automatic-exposure-control algorithm used on the LightSpeed VCT scanner ¹³⁹ and performs noise simulation in three steps. In the first step, the noise tool estimates the overall noise magnitude in the input image. A single scout projection of the input image is calculated and used to estimate noise in the input image. The estimate is based on a pre-determined noise model for a reference scanning technique in which noise (in the reconstructed image) is a function of projection area and amplitude. The noise magnitude is then scaled based on the relationship between the reference technique and the actual technique of the input image.

Once the overall noise magnitude is ascertained, the next step addresses the noise variability across the image. The input image is re-projected at four degree increments over 360 degrees to obtain patient attenuations. Bowtie filter attenuations are then added to the patient attenuations to yield total projection attenuations. Random

noise projections are generated, and their relative intensities are modulated according to the total projection attenuations so that noise is related to the square root of the number of photons in each projection according to Poisson statistics. The weighted noise is then filtered and back projected to produce a spatially variable noise field image. The filtering and backprojection processes applied to the simulated noise are identical to that applied to the real noise. This ensures the accurate spatial correlation of the simulated noise.

In the final step, the noise field image is scaled based on the relationship between the original tube current (or noise index) and the desired tube current (or noise index) and added to the input image.

Evaluation of Simulated Noise

The accuracy of the GE noise addition tool was evaluated using images of six cylindrical water phantoms with diameters of 12.7, 15.3, 17.8, 20.0, 23.3, and 27.0 cm to represent pediatric body sizes. Each phantom was scanned on a clinical 64-slice scanner (LightSpeed VCT, GE Healthcare, Waukesha, WI) at four tube potentials of 80, 100, 120, 140 kVp and eleven tube currents of 200, 180, 160, 140, 120, 100, 80, 60, 40, 20, 10 mA with 40-mm effective beam width and 0.4-second gantry rotation period. Other scan parameters were summarized in Table 28 and were chosen to emulate our size-based clinical pediatric MDCT protocols. Using the noise addition tool, noise was added to the original images acquired at 200 mA to simulate images at each of the ten reduced tube

current levels. Simulated images were validated against real images in terms of both noise magnitude and noise texture.

Table 28: Scan parameters used to acquire images from six water phantoms*.

Bowtie Filter	Diameter (cm)	Pitch	Slice Thickness ^η (mm)	DFOV ^ξ (cm)
small	12.7	0.984	3.75	20
	15.3	0.984	3.75	25
	17.8	1.375	5	25
	20.0	1.375	5	25
medium	17.8	1.375	5	25
	20.0	1.375	5	25
	23.3	1.375	5	36
	27.0	1.375	5	32
large	20.0	1.375	5	25
	23.3	1.375	5	36
	27.0	1.375	5	32

* The same phantoms and scan parameters were also used in another study that relates image noise with phantom size¹⁴⁰.

^ηSame as reconstruction interval.

^ξDFOV = display (reconstruction) field of view.

Noise magnitude was validated for all combinations of bowtie filter, phantom size, kVp, and mA. At each combination, three to five contiguous CT slices were selected from the middle of the scanned section of the phantom. On each CT slice, noise magnitude was measured as the standard deviation of pixel values within a central region-of-interest (ROI). The results were averaged across contiguous CT slices to yield a single noise figure for that combination of bowtie filter, phantom size, kVp, and mA.

Noise texture, a reflection of the spatial correlation of noise, was measured by the spectral shape of the noise power spectrum¹⁴¹. Comparison was made between real and simulated images of the 20-cm water phantom at all combinations of kVp and mA using the small bowtie filter. On each selected CT slice of the 20-cm phantom, sixteen ROIs, 64 × 64 pixels in size, were identified covering most area of the phantom image and used to calculate radial normalized noise power spectrum (NNPS) using an established technique¹⁴². After averaging across contiguous CT slices, the radial NNPS was further normalized relative to its peak value to allow a comparison of spectral shape, hence noise texture, between real and simulated images. While noise texture may exhibit spatial dependence, in this study we assumed this dependence as a secondary effect and focused on the global noise texture.

Calibration of Simulated Noise

To correct for any possible discrepancy in noise magnitude between simulated and real noise, a *tube current (mA) calibration* was performed. At each combination of bowtie filter and kVp, noise magnitude data were fitted to second-order polynomial equations as

$$\ln(\sigma_{real}) = \alpha_0 + \alpha_1 d + \alpha_2 \ln(mA_{real}) + \alpha_3 d^2 + \alpha_4 \ln^2(mA_{real}) + \alpha_5 d \ln(mA_{real}), \quad (27)$$

and

$$\ln(\sigma_{sim}) = \beta_0 + \beta_1 d + \beta_2 \ln(mA_{sim}) + \beta_3 d^2 + \beta_4 \ln^2(mA_{sim}) + \beta_5 d \ln(mA_{sim}), \quad (28)$$

using commercial surface fitting software (OriginPro 8, v8.0725, OriginLab Corporation,

Mass). In above Equations, $\sigma_{real/sim}$ is the real/simulated noise magnitude, $mA_{real/sim}$ is the real/simulated mA, and d is phantom diameter. Coefficients α_i and β_i ($i = 0, 1, \dots, 5$) extracted from the fits were then used to calculate the nominal simulation mA that provided the same noise magnitude as that at the desired actual mA, or conversely, to calculate the actual mA that was represented by a nominal simulation mA inputted to the noise tool. After mA calibration, the accuracy of the simulated noise magnitude was re-evaluated.

Noise Simulation

Using the noise addition tool, noise was added to the original images of the 13 patients to create 13 cases at 70 mA (the lowest original mA), 13 cases at 35 mA (50% reduction), and 13 cases at 17.5 mA (75% reduction). The three mA values here referred to the nominal tube currents inputted to the noise addition tool. The corresponding actual mA values, reflective of noise levels in the simulated images, were calculated using the calibration method described above. To apply the calibration method to patient images, the water-equivalent diameters of the 13 patients were estimated using the method of non-lung area described in Chapter 7 and ranged between 11-16 cm (median: 14 cm). To enlarge the scale of our study, three copies of each case were made to create a total of 117 series (13 patients \times 3 dose levels \times 3 copies) to serve as background for nodule simulation.

8.2.3 Nodule Simulation

Simulated nodules were added to the series. The nodule simulation technique is based on a mathematical model of three-dimensional small lung nodules in MDCT reported earlier¹³⁸. The technique can create 3-D nodule masks with a large variety of shapes, allowing the user to control for nodule size, contrast density, margin characteristics (well defined or diffused), and location. It has been shown that this technique simulates pediatric lung nodules that reflect physical attributes of real lung nodules and are perceptually indistinguishable by experienced pediatric radiologists from real nodules¹³⁸.

Using this technique, small lung nodules with diameters of 3-5 mm and peak contrasts of 250-550 HU were inserted into the 117 series. The lung volume in each series was divided into three anatomical zones: upper lung (lung apex to bottom of aortic arch), middle lung (aortic arch to level of aortic valve), and lower lung (aortic valve to diaphragm). Simulated nodules were added such that each of the three lung zones randomly contained 0 or 1 nodule for a total of 5 nodules in the nine lung zones associated with the three copies of each case (Figure 37). Nodule locations were randomly selected in the pulmonary parenchyma to ensure that the distribution of nodule locations was similar for the three dose levels. For examinations free of motion artifact, nodules masks included those with well-defined edges and diffused edges, in equal proportions. For examinations where respiratory motion related artifacts were

present as determined by an experienced pediatric radiologist (usually in children ≤ 6 years of age), only nodule masks with diffused edges were used. To minimize the likelihood of nodule detection due to the recognition of a repeated mask, the total of 195 nodule masks (5 nodules/case \times 39 cases) in this study were randomly selected from a library of 120 three-dimensional nodule masks. Each nodule mask was rotated through a random angle around the axial direction (Z-axis) before insertion into the lung images.

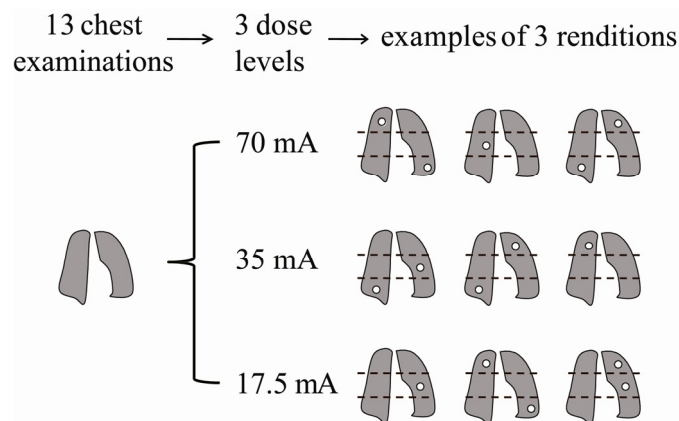


Figure 37: Diagram showing the preparation of image samples used for the ROC observer experiment.

8.2.4 Observer Experiment

The 117 series were randomized and displayed as independent series on a clinical workstation (Advantage Workstation, GE Healthcare, Waukesha, WI) with the display device (MultiSync LCD 1980SXi, NEC Display Solutions, Ltd, Tokyo, Japan) set to the standard lung window (window center = -500 HU, window width = 1500 HU) in a controlled viewing environment. With no study parameters displayed, three pediatric

radiologists (3-12 years of experience in pediatric CT) independently rated the presence of a nodule in each lung zone on a continuous scale from 0 (definitely not present) to 100 (definitely present). All observers were informed that there was 0 or 1 nodule in each lung zone; they were not told how many lung zones had nodules. Observers were encouraged to use the full scale for assigning scores. They had no time limit in rating each series, but they were not allowed to return to a series once rated. To minimize the effect of learning period, the first observer read all the series in numerical order, the second observer read all the series in reverse numerical order, and the third observer read the second half of the series in numerical order followed by the first half in reverse numerical order. Each observer was asked to point to the location of a possible nodule before rating nodule presence on the score sheet.

8.2.5 Data Analysis

As the goal of the observer experiment was to evaluate the detection accuracy of the *known* nodules in the images, if the known nodule in a lung zone was missed, and a score was given to a “nodule” that did not actually exist in the lung zone, that score was not included in further analysis. In lung zones where no known nodule was present, any suspicious “nodule” identified by an observer was included as a false positive.

The Dorfman-Berbaum-Mets (DBM) method for analyzing multi-observer multi-treatment ROC data with case split-plot design^{143, 144} was used to test the null hypothesis that dose had no effect on the detection accuracy of small lung nodules. Specifically, the

area under the ROC curve (AUC) was calculated for each observer at each dose level using the Wilcoxon-Mann-Whitney (WMW) statistic. The AUC values were then jackknifed, and their pseudovalues were fitted to a standard linear mixed-design analysis of variance (ANOVA) model¹⁴⁵ in which dose, zone location, and observer were fixed effects, and case (background image) and rendition were random effects. Commercial statistical software (SAS, version 9.1; SAS Institute, Cary, NC) was used to perform the ANOVA at a significant level of 0.05. Inter-observer variability in AUC was estimated from the mixed linear model as the standard deviation of AUC among observers averaged across different dose levels.

The Williams trend test for analyzing a monotone decreasing dose-response relationship¹⁴⁶ was also performed in which the null hypothesis was that dose had no effect on AUC, and the alternative hypothesis was that AUC decreased monotonically with dose. Commercial statistical software (SAS, version 9.1; SAS Institute, Cary, NC) was used to perform the test at a significant level of 0.05.

8.3 Results

8.3.1 Evaluation and Calibration of Noise Addition Software

A close match in noise texture was found between the simulated and real low-dose CT images of the 20-cm water phantom, as demonstrated by both visual appearance (Figure 38a and Figure 38b) and by the spectral shape of the noise power spectra (Figure 38c).

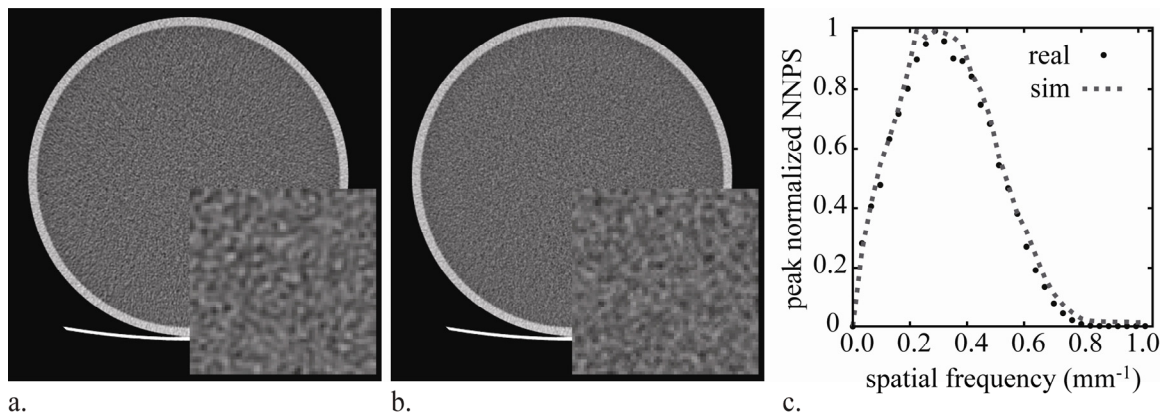
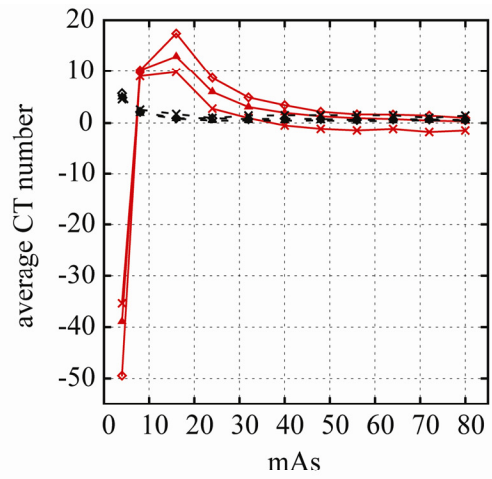
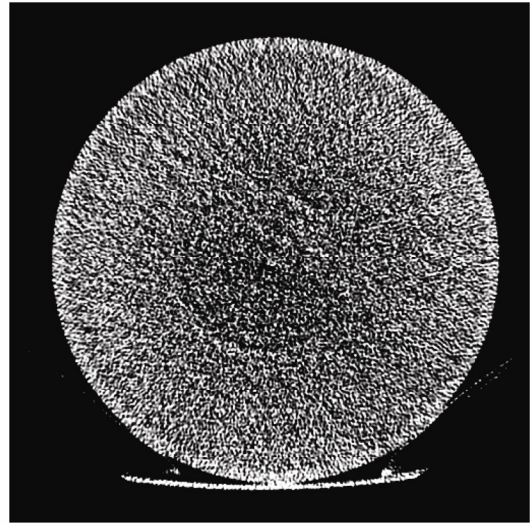


Figure 38: Noise texture of (a) real (small bowtie filter, 120 kVp, 60 mA) and (b) simulated (small bowtie filter, 120 kVp, nominal simulation tube current of 60 mA, simulated from an actual image acquired at 200 mA) CT images of the 20-cm water phantom. A 64-pixel ROI from the center of each image was blown up by 4 times and displayed at the lower right hand corner of each image to allow a close view of the noise texture. (c) Normalized noise power spectra (NNPS) of real and simulated CT images of the 20-cm water phantom acquired using the small bowtie filter at tube potential of 120 kVp and tube current of 100 mA. The NNPS were further normalized relative to their respective peak values in order to compare spectral shapes. The spectral shapes of NNPS at other kVp and mA settings were similar.



80 kVp-Small —x— 140 kVp-Small - -x- -
 80 kVp-Medium —▲— 140 kVp-Medium - -▲- -
 80 kVp-Large —◇— 140 kVp-Large - -◇- -

a.



b.

Figure 39: (a) Average CT number as a function of mAs measured from real images of the 20-cm water phantom at 80 kVp and 140 kVp for the small, medium and large bowtie filters. The average CT number was calculated as the average of mean pixel values within central ROIs of the selected CT slices. (b) An image of the 20-cm water phantom acquired at 80 kVp and 4 mAs (i.e. 10 mA, 0.4-second gantry rotation period) using the medium bowtie filter. Severe photon starvation caused a shift in CT number of ~ 40 HU at the center of the image which would otherwise look uniform as in Figure 38.

Table 29: Minimum tube-current-time product (mAs)*

bowtie filter	diameter (cm)	kVp			
		80	100	120	140
small	12.7	4	4	4	4
	15.3	8	4	4	4
	17.8	8	8	4	4
	20.0	16	8	4	4
medium	17.8	16	8	4	4
	20.0	24	8	4	4
	23.3	24	16	8	4
	27.0	56	16	8	4
large	20.0	32	16	8	4
	23.3	32	16	8	4
	27.0	56	24	8	8

* Below the minimum mAs, severe photon starvation caused shifts in CT number of more than ~10 HU, leading to apparent artifact in the image. If such artifact was not present in images acquired at 4 mAs (10 mA, 0.4-second gantry rotation period), 4 mAs was used as the minimum mAs.

At low X-ray tube outputs (low kVp and/or mA) and for large phantom sizes, severe photon starvation shifted CT numbers of the actual images as illustrated in Figure 39. Table 29 summarizes the minimum tube-current-time product (mAs) for each combination of kVp, bowtie filter, and phantom size; below the minimum mAs, the shift in CT number was greater than ~ 10 HU, leading to apparent artifact in the image (Figure 39b), and the measured standard deviation no longer represented noise in the image. Such data were not included in the calibration of tube currents.

Table 30: Coefficients of polynomial equations (27) and (28) describing real and simulated noise in images of water phantoms as functions of phantom diameter and tube current.

Noise	Bowtie Filter	kVp	Coefficients					Adjusted R ²	
real*			α_0	α_1	α_2	α_3	α_4	α_5	
	small	80	4.42809	0.01476	-0.63593	0.00742	0.05724	-0.02681	0.990
		100	4.05954	-0.00583	-0.52538	0.00490	0.01714	-0.00877	0.993
		120	3.97994	-0.02059	-0.52299	0.00471	0.01276	-0.00576	0.995
		140	3.94392	-0.02886	-0.52743	0.00440	0.00723	-0.00249	0.996
	medium	80	1.64157	0.26954	-0.42099	-0.00048	0.03194	-0.02331	0.975
		100	1.54965	0.28661	-0.61874	-0.00187	0.05493	-0.02037	0.986
		120	1.24914	0.27993	-0.55677	-0.00275	0.03529	-0.01306	0.990
		140	1.26746	0.25753	-0.51762	-0.00282	0.02260	-0.00886	0.993
	large	80	10.17070	-0.12202	-1.94568	0.00783	0.18631	-0.02452	0.998
		100	5.52959	-0.05413	-0.56413	0.00526	0.05182	-0.02125	0.999
		120	4.96463	-0.03127	-0.54763	0.00382	0.03951	-0.01467	0.999
		140	4.66454	-0.01537	-0.56091	0.00271	0.02667	-0.00824	0.999
simulated			β_0	β_1	β_2	β_3	β_4	β_5	
	small	80	5.32980	-0.09420	-0.76424	0.00530	0.02829	0.00722	0.993
		100	5.07604	-0.07876	-0.61616	0.00394	-0.00854	0.01022	0.995
		120	4.63546	-0.05051	-0.61640	0.00314	-0.00548	0.00891	0.994
		140	4.47683	-0.05519	-0.64763	0.00343	0.00350	0.00791	0.994
	medium	80	5.03943	0.03963	-0.99079	-0.00007	0.02920	0.01576	0.993
		100	2.76751	0.18154	-0.72131	-0.00265	0.01716	0.00602	0.996
		120	2.17034	0.21300	-0.70031	-0.00336	0.01650	0.00520	0.997
		140	3.25378	0.13269	-0.84735	-0.00227	0.02278	0.01020	0.997
	large	80	7.45078	-0.22402	-0.93278	0.00613	0.05620	0.01045	0.997
		100	4.80621	0.00321	-0.86714	0.00105	0.05076	0.00580	0.999
		120	4.18627	0.02800	-0.79986	0.00060	0.04929	0.00331	0.999
		140	3.77092	0.04403	-0.79241	0.00027	0.05152	0.00289	0.999

* The real coefficients were also reported in another study that relates image noise with phantom diameter¹⁴⁰.

Without mA calibration, percent errors up to ~ 50% existed in simulated noise magnitude; percent errors ranged (-45%, 15%), (-45%, 1%), and (-54%, 3%) for the small, medium, and large bowtie filters, respectively. The simulated and real noise data fitted

well to Equations (27) and (28) with adjusted R-square values close to 1 (Table 30). After applying mA calibration, percent errors in simulated noise magnitude reduced to be within $\pm 10\%$; percent errors ranged (-9%, 9%), (-10%, 9%), and (-10%, 7%) for the small, medium, and large bowtie filters, respectively.

8.3.2 Observer Experiment

For all observers, the AUC value was the greatest at the nominal tube current of 70 mA (Figure 40), although only the AUC of observer 2 showed a monotonically decreasing trend with dose, and dose seemed to have little effect on the AUC of observer 3.

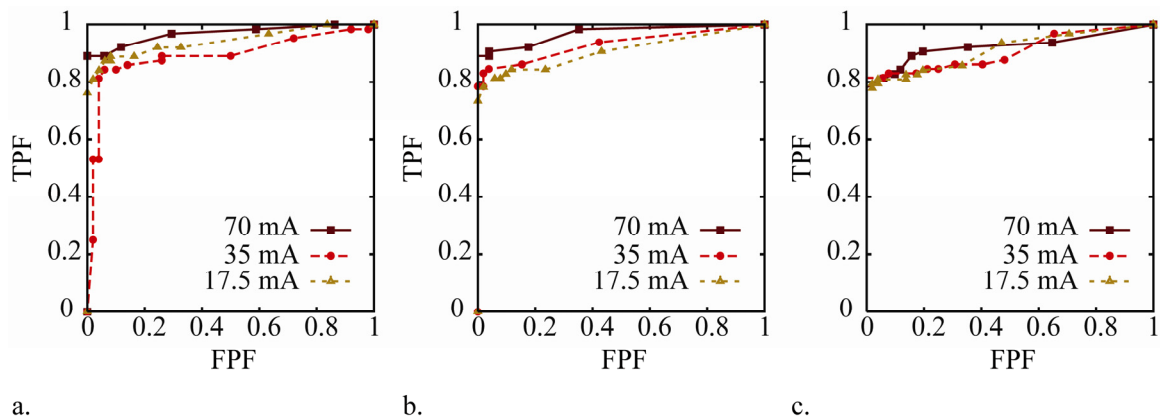


Figure 40: ROC curves for (a) observer 1, (b) observer 2, and (c) observer 3 at three nominal tube current (dose) levels: 70 mA, 35 mA, and 17.5 mA.

Table 31 summarizes the AUC values for all observers and tube current (dose) levels and the averages across observers. Using the DBM method, the effect of dose was not statistically significant, but close to being significant ($p = 0.09$). The effect of observer

was not significant ($p = 0.64$). The effect of location in the lung was significant ($p = 0.02$); the average AUC values for the upper, middle, and lower lung zones were 0.93, 0.96, and 0.90, respectively, with standard errors of 0.02. Inter-observer variability in AUC was 0.02.

Using the Williams trend test, the effect of dose was barely significant ($p = 0.05$), just rejecting the null hypothesis (no effect) against the alternative of a monotonically decreasing AUC with dose.

Table 31: Areas under the ROC Curves (AUC \pm 0.02).

	Observer			Average
	1	2	3	
70 mA	0.97	0.97	0.92	0.95
35 mA	0.89	0.93	0.91	0.91
17.5 mA	0.94	0.91	0.91	0.92

8.4 Discussions

The influence of dose reduction on the detection of lung nodules has been studied extensively for adult CT patients^{28, 45, 134, 147, 148} mainly by performing repeated CT scans on the same subjects at different dose levels. Similar studies are difficult to conduct in children, however, not only because of the low occurrence of lung nodules in this population, but also because of the fact that children are more sensitive to radiation-induced cancer, making repeated scans in children ethically unacceptable. In this study, we addressed these difficulties by using computer-simulated lung nodules and noise

that have been validated or calibrated. We focused on nodules of 3-5 mm diameters, i.e., small nodules compared with what is seen clinically, because nodules of this size range are likely to be missed by radiologists especially at reduced dose (increased noise) conditions, yet they have significant implications for the diagnosis and treatment of pediatric cancer. To our knowledge, this work represents the first controlled, systematic, and task-specific assessment of the influence of dose reduction in pediatric chest MDCT.

The results of our study revealed that the influence of tube current (dose) on the detection of small lung nodules in children was marginally significant, i.e. dose had a weak effect on detection accuracy. On one hand, the effect of dose was measurable since all observers had the highest accuracy at the highest dose. This effect would likely be confirmed in a larger scale study. On the other hand, however, with a dose saving of 75%, the decrease in detection accuracy was only ~ 3% (i.e. average AUC dropped from 0.95 to 0.92). One may question whether such a small difference is *clinically* significant. One may hypothesize that there exists a clinical zone of equivalence; if the change in accuracy due to dose falls inside such a zone, then one can conclude that the detection accuracies at different dose levels are equivalent and dose reduction is justified. One way to define the clinical zone of equivalence is to use the particular difference in AUC at which decreased accuracy, hence increased mortality, is fully offset by the number of lives saved through dose reduction. However, relating the difference in AUC to that in mortality requires a large-scale long-term clinical study and is beyond the scope of our

current work. We noted that the difference in detection accuracy due to dose (~ 0.03) was comparable to that due to inter-observer variability (~ 0.02). Thus, an alternative method for defining the clinical zone of equivalence may be to use the magnitudes of the effects on detection accuracy of other contributing factors, assuming that these effects can be reliably measured by using large sample sizes. Although no conclusion regarding equivalence could be made at this point due to the limited power of our study, the equivalence test framework proposed here can guide future larger scale observer studies.

Unlike previous nodule detection studies^{28, 45, 134, 147, 148}, where a single (sensitivity, specificity) pair was used as a measure of detection accuracy, our choice of a ROC study allowed us to measure sensitivity and specificity at all decision criteria of an observer (i.e. how strict or lax the observer is when deciding whether a nodule is present)¹⁴⁹; the resulting AUC values were free from the influence of decision criterion which could vary among observers and even from time to time for the same observer. Thus, our method is more sensitive to the change in detection accuracy induced by dose reduction and is a preferred method.

By adding computer-simulated noise to existing clinical images, there was no additional radiation burden for the patients. Simulated noise also enabled the investigation of nodule conspicuity at systematically reduced dose levels, thus allowing the determination of threshold dose levels. Because the noise in a CT image is uniquely

dependent on the noise content of the patient's projection measurements and the reconstruction process, adding noise to raw projection data can be very accurate^{49, 53}. However, there are practical difficulties with handling raw projection data; raw data are cumbersome to store and transfer, most sites delete raw data after image reconstruction, and modified raw data may only be reconstructed on the scanner reconstruction processor. In contrast, reconstructed images are easier to transfer, well archived, and do not require any post-processing following noise addition. For these reasons, techniques that add noise directly to reconstructed CT slices can be very valuable⁵¹. In this study, we evaluated and calibrated the GE Noise Addition Tool which adds noise directly to reconstructed CT images. We showed that not only can this new software emulate the actual noise texture, after appropriate calibrations, the actual noise magnitudes can be accurately simulated as well.

An interesting finding of our study was the fact that nodule detection accuracies were significantly different in different lung zones (i.e. upper, middle, lower zones): $AUC_{middle} > AUC_{upper} > AUC_{lower}$. The poorest accuracy in the lower lung zone might be a result of satisfaction of search¹⁵⁰, observer fatigue, or more pronounced motion artifacts in the lower lung zone. The relatively lower accuracy in the upper lung zone may be attributable to the higher levels of noise and streak artifact around the shoulders. The effect of location in the lung deserves further investigation in future larger scale studies.

Our study had several limitations. It was limited to a single type of MDCT scanner and the associated pediatric CT protocols in effect at our institution. In addition, tube current was the only dose-related imaging parameter considered in our study. However, as the equipment and the protocol were representative of current clinical practice, the findings are applicable to similar clinical settings. Our future study will assess nodule detection accuracy at selected (fixed) noise levels. This will allow the study results to be applicable to other CT scanner models and tube-current modulation techniques. We note that the prevalence of nodules in our study was much higher than their actual prevalence in pediatric patients undergoing CT examinations. An earlier study revealed elevated diagnostic accuracy with increased disease prevalence¹⁵¹. In addition, as the clinical task in this study was the detection of lung nodules, the observers were less distracted by the search for other abnormalities. Therefore, the AUC values reported in our study may be higher than the actual clinical values. Nevertheless, our findings provided objective and task-based guidelines for dose reduction in pediatric MDCT.

9. Lung Nodule Detection in Pediatric CT: Quantitative Relationship between Image Quality and Radiologist Performance*

9.1 Introduction

In pediatric patients with primary cancer, the number and distribution of lung nodules have been shown to significantly associate with metastatic disease and patient outcome⁴⁰. Unlike in adult patients, where small lung nodules (< 5 mm) tend to be benign, studies in pediatric patients have shown that small lung nodules are equally likely to be benign and malignant^{152, 153}. Due to the superior resolution of modern multi-detector array CT systems, CT is more sensitive than MRI for the detection of lung nodules^{154, 155} and is often the standard for staging and surveillance of pediatric cancer. As CT examinations involve the use of ionization radiation and children are especially sensitive to radiation¹⁴, it is essential that scan protocols are formulated to achieve the best nodule detection accuracy at the minimum possible radiation dose.

In the past, protocol designs in pediatric CT have mainly focused on determining the combination of scan parameters that provide the best tradeoff between radiation dose and image quality, expressed in terms of physical quantities such as noise, contrast, and contrast-to-noise ratio^{93, 106, 107, 156}. Few studies have investigated how these physical quantities influence the diagnostic performance of radiologists, the endpoint of protocol optimization. In a recent study⁴⁸, the radiologists' sensitivity and specificity in detecting

* This chapter is based on a manuscript to be submitted to the journal *Radiology*.

lung nodules were assessed at various ranges of signal-to-noise ratios. However, the study used simulated nodules resized from a single real nodule mask and Gaussian monochromatic noise, making the detection task less reflective of the actual clinical scenario, in which nodules with various appearances must be detected on highly correlated noise backgrounds. To assess radiologist performance in a more realistic setting, we recently conducted a pilot receiver operating characteristic (ROC) study¹⁵⁷, in which a realistic model of noise with proper texture and calibrated magnitude was used in combination with a validated and variable model of three-dimensional lung nodules¹³⁸. However, similar to many other dose reduction studies^{28, 45, 50, 52, 134}, our pilot study evaluated observer performance at different tube current levels, making it difficult to generalize research results to other scan protocols and CT scanner models.

The goal of this work was to extend our pilot study to quantitatively assess the protocol- and scanner-independent relationships between image quality and radiologist performance in detecting lung nodules in pediatric CT.

9.2 Materials and Methods

This study was partially funded by GE Healthcare. The authors had complete control over the data and information submitted in this article. Our institutional review board determined that the study was in compliance with the Health Insurance Portability and Accountability Act and did not require informed consent.

9.2.1 Clinical Cases

Chest CT examinations of 30 patients (median age, 4 years old; age range, 0-16 years old; median weight, 17 kg; weight range, 2-52 kg) were retrospectively selected from our clinical database of children who underwent 64-slice CT examinations (LightSpeed VCT, GE Healthcare, Waukesha, WI) between 2005 and 2006. The images were obtained according to our size-based clinical protocols during the two-year period that employed fixed-tube techniques with tube currents of 55-180 mA, peak tube potentials of 100-140 kVp (lower kVp in smaller children), beam collimations of 20 or 40 mm, helical pitches of 0.985 or 1.375, and slice thicknesses of 3.75 mm at 3.75-mm interval or 5 mm at 5-mm interval (generally thinner slice thickness in smaller children). The images were either free of lung nodule or had a small number of lung nodules. The real lung nodules were identified by a radiologist (20 years of experience in pediatric CT) and were digitally removed using a technique reported earlier¹²³.

9.2.2 Noise Simulation

Noise Addition Software

Tube current-reduced images were simulated using a noise addition software tool (GE Noise Addition Tool, Version 1.1, GE Healthcare, Waukesha, WI)^{139, 158}. The software accepts DICOM (Digital Imaging and Communications in Medicine) images acquired on the LightSpeed VCT scanner and adds noise to axial slice data to simulate either a reduced tube current (mA) or an increased noise index condition. We previously

evaluated and calibrated the accuracy of this software in terms of both noise texture and magnitude¹⁵⁷. The texture of the simulated noise, as represented by the noise power spectrum, was found to match very well with that of the real noise. Discrepancies up to ~50%, however, existed between the magnitudes of the simulated and real noise. A calibration procedure was developed to correct for the discrepancies in noise magnitude using noise measured from real and simulated images of six cylindrical water phantoms with diameters of 12.7-27.0 cm.

Extended Calibration of Noise Addition Software

In this study, the calibration procedure was extended to a wider range of body sizes by including an 8.2-cm diameter water phantom to represent a newborn patient and by increasing the number of phantoms scanned with each bowtie filter. Each phantom was scanned on a clinical 64-slice scanner (LightSpeed VCT, GE Healthcare, Waukesha, WI) at four tube potentials of 80, 100, 120, 140 kVp and eleven tube currents of 200, 180, 160, 140, 120, 100, 80, 60, 40, 20, 10 mA with a 40-mm beam collimation and 0.4-second gantry rotation period. Other scan parameters are summarized in Table 32.

Table 32: Scan parameters used to acquire images of the water phantoms.

bowtie filter	water phantom diameter (cm)			Slice Thickness ^b (mm)	DFOV ^c (cm)
	geometric diameter	water-equivalent diameter	helical pitch ^a		
small	8.2	8.7	1.375	5	15
small	12.7	13.2	0.984	3.75	20
small	15.3	16.3	0.984	3.75	25
small	17.8	18.3	1.375	5	25
small	20.0	22.0	1.375	5	25
medium	8.2	8.7	1.375	5	15
medium	12.7	13.2	1.375	5	20
medium	15.3	16.3	1.375	5	25
medium	17.8	18.3	1.375	5	25
medium	20.0	22.0	1.375	5	25
medium	23.3	24.6	1.375	5	30
medium	27.0	27.8	1.375	5	32
large	12.7	13.2	1.375	5	20
large	15.3	16.3	1.375	5	25
large	17.8	18.3	1.375	5	25
large	20.0	22.0	1.375	5	25
large	23.3	24.6	1.375	5	30
large	27.0	27.8	1.375	5	32

^a Noise in the CT image is proportional to $\sqrt{\text{pitch}/\text{slice thickness}}$ ³⁹. Therefore, the noise at pitch of 1.375 and slice thickness of 5 differs by only 2% from the noise at pitch of 0.984 and slice thickness of 3.75.

^b Same as reconstruction interval.

^c DFOV = display (reconstruction) field of view.

Using the noise addition tool, noise was added to the original images acquired at 200 mA to simulate images at each of the ten reduced tube current levels. For both real and simulated images, noise magnitude was measured as the standard deviation of pixel values within a central region-of-interest (ROI) for all combinations of bowtie filter,

phantom size, kVp, and mA. At each combination of bowtie filter and kVp, the noise magnitude data were fitted to second-order polynomial equations as

$$\ln(\sigma_{real}) = \alpha_0 + \alpha_1 d + \alpha_2 \ln(\text{mAs}_{real}) + \alpha_3 d^2 + \alpha_4 \ln^2(\text{mAs}_{real}) + \alpha_5 d \ln(\text{mAs}_{real}), \quad (29)$$

and

$$\ln(\sigma_{sim}) = \beta_0 + \beta_1 d + \beta_2 \ln(\text{mAs}_{sim}) + \beta_3 d^2 + \beta_4 \ln^2(\text{mAs}_{sim}) + \beta_5 d \ln(\text{mAs}_{sim}), \quad (30)$$

using commercial surface fitting software (OriginPro 8, v8.0725, OriginLab Corporation, MA). In the above Equations, $\sigma_{real/sim}$ is the real/simulated noise magnitude, $\text{mAs}_{real/sim}$ is the tube current-time product of the real/simulated images, and d is the water-equivalent diameter of the water phantom (Table 32), calculated as the diameter of a circle having the same area as the water-equivalent area of the phantom in the CT image¹⁴⁰. The calculation of water-equivalent diameter was needed to convert the phantom, which was composed of water, plastic container, air bubbles, and any materials supporting the phantom, into a pure water cylinder that provided the equivalent X-ray attenuations. At low X-ray tube outputs (low kVp and/or mA) and for large phantom sizes, severe photon starvation shifted CT numbers of the real images by more than 10 HU, leading to apparent artifact in the image¹⁵⁸, and the measured standard deviation no longer represented noise in the image. Such data were not included in the calibration.

Noise Simulation

Using the noise addition tool, noise was added to the nodule-free images of the 30 patients to create 29 studies at 70 mA (the lowest original mA for all but one patient), 30 studies at 35 mA (50% reduction), and 30 studies at 17.5 mA (75% reduction). For one patient, the original tube current was 55 mA; therefore, a study at 70 mA could not be created for this patient. The three mA values here refer to the nominal tube currents inputted to the noise addition tool. The corresponding calibrated mA values, reflective of noise levels in the simulated images, ranged 44-118 mA (median: 69 mA), 19-76 mA (median: 30 mA), and 9-46 mA (median: 16 mA), respectively*. To enlarge the scale of the investigation, two copies of each study were made to create a total of 178 series ((29 + 30 + 30) studies × 2 copies) to serve as background for nodule simulation.

9.2.3 Nodule Simulation

Simulated nodules were added to the series. The nodule simulation technique was based on a mathematical model of three-dimensional small lung nodules in CT

* To apply the calibration method to patient images, it is necessary to determine the water-equivalent diameter of the patient. In this study, water-equivalent diameters of the 30 patients, estimated using the method of non-lung area described in an earlier publication¹⁴⁰, ranged between 9-22 cm (median: 15 cm). For each patient, water-equivalent diameter and calibrated tube current were estimated for each chest image and averaged over all the images. The ranges of values reported here reflect the ranges of the averaged results.

reported earlier¹³⁸. The technique can create three-dimensional nodule masks with a large variety of shapes, allowing the user to control for nodule location, size, contrast density, and margin characteristics (well defined or diffused). It has been shown that this technique simulates pediatric lung nodules that reflect the physical attributes of real lung nodules and are perceptually indistinguishable from real nodules for experienced pediatric radiologists¹³⁸.

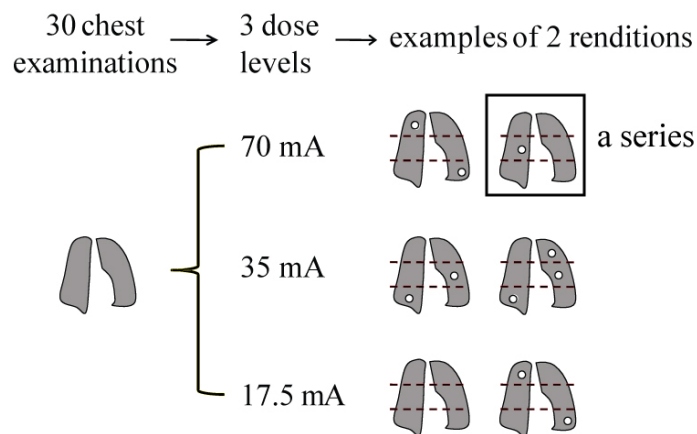


Figure 41: Diagram showing the preparation of image samples used in the ROC observer experiment. Because nodule locations and characteristics (size, shape, and contrast) were randomized, the nodules in any series were different from the nodules in any other series within a patient or cross patients.

Using this technique, simulated lung nodules were inserted into the 178 series. The lung volume in each series was divided into three anatomical zones: upper lung (lung apex to bottom of aortic arch), middle lung (aortic arch to level of aortic valve), and lower lung (aortic valve to lung base). For each lung zone, a simulated nodule was added with a 50% probability (Figure 41). As such, each series could have from zero to

three nodules, with a maximum of one in each lung zone. Nodule locations were randomly selected throughout the pulmonary parenchyma but not immediately adjacent to the chest wall. The simulation diameter of each nodule was randomly sampled between 3.9 and 6.5 mm to achieve an approximate visual diameter between 3 and 5 mm¹³⁸. The peak contrast of each nodule was randomly sampled between 200 and 500 HU. To minimize the likelihood of nodule detection due to the recognition of a repeated nodule shape, the shape of each nodule was randomly sampled from a library of 120 pre-defined three-dimensional nodule shapes, including 60 shapes for nodules with well-defined margins and 60 shapes for nodules with diffused margins¹³⁸. Each nodule shape was rotated through a random angle around the axial direction (z-axis) before being applied in nodule simulation. As the simulated nodules were created with random characteristics (size, contrast, and shape) and placed at random locations, the two copies of each study had different nodule numbers, locations, and characteristics and will be referred to as the two *renditions* of each study hereafter (Figure 41).

9.2.4 Observer Experiment

The observer experiment was conducted in two parts. In the first part, the first renditions of the 89 studies were randomized and displayed as 89 independent series on a clinical workstation (Advantage Workstation, GE Healthcare, Waukesha, WI) equipped with a LCD display device (MultiSync LCD 1980SXi, NEC Display Solutions, Ltd, Tokyo, Japan). Four pediatric radiologists (5-14 years of experience in pediatric CT)

independently rated the presence of a nodule in each lung zone on a continuous scale from 0 (definitely not present) to 100 (definitely present). All observers were informed that there was 0 or 1 nodule in each lung zone; they were not told how many lung zones had nodules. Each observer had up to eight minutes to review each series, had the freedom to scroll through a series, but was not allowed to return to a series once rated. The default window/level setting was the standard lung window (window center = -500 HU, window width = 1500 HU); however, the observers were allowed to adjust the window/level setting and manipulate the images in other ways that they normally would when reviewing clinical images. To minimize the effect of any possible learning process, the first observer read the first half of the series in reverse numerical order followed by the second half in reverse numerical order, the second observer read the second half of the series in numerical order followed by the first half in numerical order, the third observer read all the series in reverse numerical order, and the fourth observer read all the series in numerical order. Following the completion of the first part of the observer experiment, the second part was conducted, in which the second renditions of the 89 studies were randomized and reviewed in exactly the same manner as was done in the first part.

9.2.5 Data Analysis

ROC analysis was performed, treating the 534 lung zones (178 series \times 3 lung zones) as independent cases. ROC software (ROCKIT, version 1.1 B 2; Charles E. Metz,

University of Chicago, Chicago, IL) was used to calculate the area under of the ROC curve, A_z , as a measure of diagnostic accuracy.

9.2.5.1 Relationship between nodule detectability and diagnostic accuracy

Diagnostic accuracy was presumed to be only a function of nodule detectability¹⁵⁹, which we defined, based on the Rose model¹⁶⁰, as

$$CDNR_{\text{display}} = \frac{C \cdot D_{\text{display}}}{N}, \quad (31)$$

where C and D_{display} are the peak contrast and display diameter of a nodule, and N is the noise in the lung zone where the nodule is located.

The display diameter of a nodule was defined as

$$D_{\text{display}} = \frac{D}{\Delta x} \cdot \Delta x_{\text{display}}, \quad (32)$$

where D is the physical of a nodule and ranged between 3-5 mm in this study, Δx is the physical dimension of each pixel in a CT image and is equal to

$$\Delta x = \frac{\text{reconstruction field-of-view size (mm)}}{512}, \quad (33)$$

and $\Delta x_{\text{display}}$ is the display pixel size determined as

$$\Delta x_{\text{display}} = \frac{\text{image dimension on display device (mm)}}{512}. \quad (34)$$

D_{display} was used in Equation (31) to account for the effect of pixel size, Δx , on nodule detectability. As all CT images are 512×512 in size, the pixel size increases with the

reconstruction/display field-of-view (FOV) size, which is usually larger for larger patients. Therefore, if a newborn patient and a teenager patient both have a 4-mm diameter nodule, the nodule would be depicted by a larger number of pixels in the images of the newborn patient, whose small body size enables a small reconstruction FOV and hence a smaller pixel size. As such, the nodule in the newborn patient would have a larger display size and is more likely to be detected. In our study, the image pixel size, Δx , ranged between 0.29-0.65 mm. The display pixel size was 0.58 mm.

For the 89 studies, noise in the lung region of each chest CT image was estimated using a patient size based method reported earlier¹⁴⁰. The effects on noise of helical pitch and slice thickness were accounted for by using the relationship of noise $\propto \sqrt{\text{pitch} / \text{slice thickness}}$ ³⁹. The noise values in individual images were then averaged to obtain the noise in each lung zone.

The positive cases (i.e., cases with a nodule present) in the observer experiment were sorted based on the value of $CDNR_{\text{display}}$ and divided into five bins with equal number of cases in each bin. The positive cases in each bin were then combined with all the negative cases to perform the ROC analysis.

The A_z values calculated for each bin were averaged across the four observers. The standard error (SE) of the averaged A_z was calculated using the method described in Swets and Pickett¹⁶¹ and formulated as

$$SE = \left(S_{c+wr}^2 + \frac{S_{br+wr}^2}{l} - S_{wr}^2 \right)^{1/2}, \quad (35)$$

where S^2 values are variances associated with case sample c , between-reader br , and within-reader wr variability, and l is the number of observers. S_{c+wr}^2 was calculated as the observer-averaged square of the standard error associated with the A_z of each observer. As no repeated reading was performed in the observer experiment, the within-reader variance term S_{wr}^2 was not included. This only led to a conservative overestimation of the resultant SE , i.e., the averaged A_z values were more accurate than reflected by their standard errors.

To test if the difference in A_z between any two bins of $CDNR_{\text{display}}$ was statistically significant, the standard error for the difference in A_z was first calculated using the method described in Swets and Pickett¹⁶¹ and formulated as

$$SE_{\text{diff}} = 2^{1/2} \left[S_{c+wr}^2 (1 - r_{c-wr}) + \frac{S_{br+wr}^2}{l} (1 - r_{br-wr}) - S_{wr}^2 \right]^{1/2}, \quad (36)$$

where r_{c-wr} and r_{br-wr} are the correlations between A_z values in the two bins due to case sample and observer correlations, respectively, and S_{c+wr}^2 and S_{br+wr}^2 are the corresponding values in Equation (35) averaged across all the bins. Again, the within-reader variance term S_{wr}^2 was not included, leading to a conservative overestimation of SE_{diff} . The z-score for the statistical test was then calculated as

$$z = \frac{A_z^{bin_i} - A_z^{bin_j}}{SE_{diff}}, \quad (37)$$

from which the p -value was determined. Bonferroni adjustment¹⁰⁴ was employed for multiple comparisons.

9.2.5.2 Effect of location in the lung

In the pilot study we reported earlier¹⁵⁷, diagnostic accuracy was found to be significant different in different lung zones. The effect of nodule location in the lung was re-examined in this larger-scale study. The 534 cases were binned based on location in the lung into upper, middle, and lower lung zone bins. The data in each lung zone bin was then used to calculate A_z . To test if the difference in A_z between any two lung zones was statistically significant, the method described above for testing differences between $CDNR_{display}$ bins was used.

9.2.5.3 Relationship between noise and diagnostic accuracy

Considering that CT examinations are increasingly being performed with tube-current-modulation techniques, which aim to provide a target noise in the image, we lastly examined the relationship between noise and diagnostic accuracy for representative nodule diameter and contrast values. The image pixel size was fixed at $\Delta x = 0.48$ mm, the average pixel size of all the chest images in this study. For a nodule with a diameter D of 4 mm (the average diameter of all the nodules in this study), A_z as a function of noise was derived at four peak contrast values: 200, 300, 400, and 500

HU. Specifically, noise was incremented between 7 and 32 HU at a 0.5 HU interval. At each noise value, $CDNR_{\text{display}}$ was calculated using Equation (31). If the $CDNR_{\text{display}}$ value fell in between the centers of the first and last $CDNR_{\text{display}}$ bins, it was used to determine A_z by linearly interpolating the relationship between A_z and the center location of the $CDNR_{\text{display}}$ bin. Similarly, A_z as a function of noise was derived for a nodule with a peak contrast of 350 HU (the average peak contrast of all the nodules in this study) and a diameter of 3, 4, or 5 mm.

9.3 Results

9.3.1 Extended Calibration of Noise Addition Software

The simulated and real noise data fitted well to Equations (29) and (30) with adjusted R-square values close to 1 (Table 33).

Table 33 also tabulated the coefficients α_i and β_i ($i = 0, 1, \dots, 5$) extracted from the fits. They were used to calculate the nominal simulation mAs that provided the same noise magnitude as that at the desired actual mAs, or conversely, to calculate the actual mAs that was represented by a nominal simulation mAs inputted to the noise tool.

Table 33: Coefficients of polynomial Equations (29) and (30) describing real and simulated noise in images of the water phantoms as functions of phantom diameter and tube current-time product (mAs).

bowtie filter tube potential		coefficient						adjusted R ²
		real noise						
		α_0	α_1	α_2	α_3	α_4	α_5	
small	80	2.84448	0.14125	-0.58035	0.00087	0.03742	-0.01489	0.998
	100	2.58080	0.12434	-0.52498	-0.00012	0.01389	-0.00555	0.999
	120	2.47005	0.11510	-0.53298	-0.00027	0.01165	-0.00327	0.999
	140	2.43375	0.10618	-0.53797	-0.00033	0.00745	-0.00113	1.000
medium	80	3.09812	0.12501	-0.65923	0.00086	0.04042	-0.01002	0.995
	100	2.53207	0.12076	-0.48219	0.00037	0.01476	-0.00852	0.997
	120	2.40700	0.11447	-0.49727	0.00009	0.01354	-0.00606	0.998
	140	2.41142	0.10877	-0.54230	-0.00013	0.01515	-0.00354	0.998
large	80	3.72322	0.12024	-0.91608	0.00097	0.07744	-0.01069	0.992
	100	2.66605	0.10998	-0.44749	0.00057	0.01136	-0.00878	0.997
	120	2.44186	0.11499	-0.47405	0.00009	0.01342	-0.00708	0.997
	140	2.37880	0.11009	-0.48698	-0.00016	0.00881	-0.00418	0.998
		simulated noise						
		β_0	β_1	β_2	β_3	β_4	β_5	
small	80	3.47053	0.06395	-0.69398	0.00023	0.02431	0.00704	0.999
	100	3.56248	0.04668	-0.58157	0.00004	-0.01790	0.00985	0.999
	120	3.27701	0.05338	-0.57671	-0.00008	-0.01331	0.00817	0.999
	140	3.06415	0.05384	-0.60361	0.00002	-0.00216	0.00719	0.999
medium	80	4.48714	-0.00719	-0.76384	0.00141	0.00598	0.01418	0.997
	100	3.68025	0.03355	-0.66088	0.00060	0.00358	0.00845	0.998
	120	3.32943	0.04325	-0.64420	0.00044	0.00690	0.00666	0.998
	140	3.98629	-0.00741	-0.70745	0.00082	-0.00441	0.01279	0.995
large	80	3.83864	-0.00069	-0.76858	0.00190	0.05440	0.00858	0.998
	100	3.25518	0.05831	-0.78318	0.00014	0.04847	0.00698	0.998
	120	2.81619	0.07352	-0.73398	-0.00020	0.04614	0.00531	0.998
	140	2.60441	0.07038	-0.71455	-0.00008	0.04962	0.00430	0.998

9.3.2 Relationship between Image Quality and Diagnostic Accuracy

Diagnostic accuracy, A_z , increased rapidly from 0.63 ± 0.06 to 0.88 ± 0.03 when $CDNR_{\text{display}}$ increased from 44 to 99 mm, followed by a slow increase to 0.92 ± 0.03 when $CDNR_{\text{display}}$ further increased to 265 mm (Figure 42, Table 34). The differences in A_z between the first $CDNR_{\text{display}}$ bin and the third, fourth, and fifth $CDNR_{\text{display}}$ bins were statistically significant after adjustment for multiple comparisons with p values of $2e^{-5}$, $5e^{-6}$ and $8e^{-7}$, respectively.

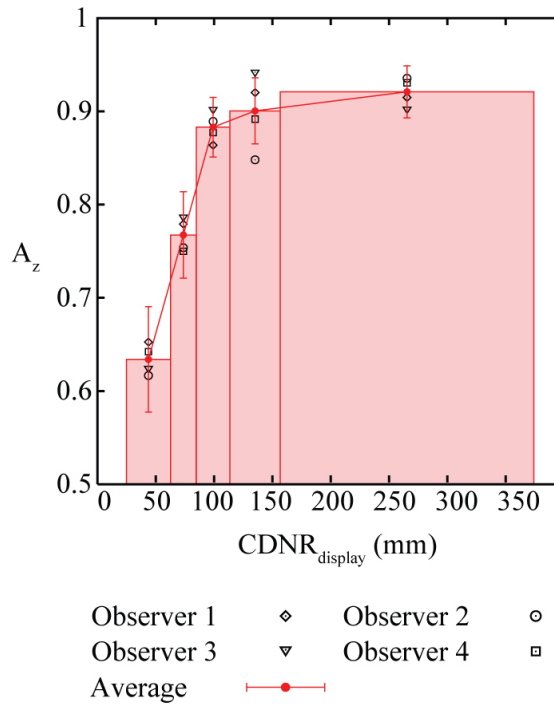


Figure 42: Diagnostic accuracy, A_z , as a function of nodule detectability, $CDNR_{\text{display}}$.

Table 34: A_z and associated errors as a function of $CDNR_{display}$, and results of testing the statistical significance of difference between $CDNR_{display}$ bins.

	CDNR _{display} bin 1 (24.8 - 62.6) mm		CDNR _{display} bin 2 (62.6 - 84.6) mm		CDNR _{display} bin 3 (84.6 - 113.6) mm		CDNR _{display} bin 4 (113.6 - 156.7) mm		CDNR _{display} bin 5 (156.7 - 374.2) mm	
	$A_z^{(1)}$	S_{c+wr}	$A_z^{(2)}$	S_{c+wr}	$A_z^{(3)}$	S_{c+wr}	$A_z^{(4)}$	S_{c+wr}	$A_z^{(5)}$	S_{c+wr}
Observer 1	0.65	0.04	0.78	0.04	0.86	0.03	0.92	0.02	0.91	0.03
Observer 2	0.62	0.06	0.75	0.05	0.89	0.03	0.85	0.04	0.94	0.02
Observer 3	0.62	0.07	0.79	0.05	0.90	0.03	0.94	0.03	0.90	0.04
Observer 4	0.64	0.05	0.75	0.04	0.88	0.03	0.89	0.03	0.93	0.02
average	0.63	0.06	0.77	0.05	0.88	0.03	0.90	0.04	0.92	0.03
S_{br+wr}	0.01		0.02		0.01		0.04		0.01	
<i>p</i> -value ^a										
	$A_z^{(1)} - A_z^{(2)}$	0.02	$A_z^{(1)} - A_z^{(3)}$	2.E-05	$A_z^{(1)} - A_z^{(4)}$	5.E-06	$A_z^{(1)} - A_z^{(5)}$	8.E-07	$A_z^{(2)} - A_z^{(3)}$	0.05
	$A_z^{(2)} - A_z^{(4)}$	0.02	$A_z^{(2)} - A_z^{(5)}$	0.01	$A_z^{(3)} - A_z^{(4)}$	0.76	$A_z^{(3)} - A_z^{(5)}$	0.52	$A_z^{(4)} - A_z^{(5)}$	0.73

^a The significance level was 0.005 after Bonferroni adjustment. Significant differences are highlighted in bold.

Table 35: A_z and associated errors as a function of location in the lung, and results of testing the statistical significance of difference between lung zones.

	upper lung zone		middle lung zone		lower lung zone	
	$A_z^{(U)}$	S_{c+wr}	$A_z^{(M)}$	S_{c+wr}	$A_z^{(L)}$	S_{c+wr}
Observer 1	0.80	0.03	0.87	0.03	0.81	0.03
Observer 2	0.78	0.05	0.87	0.03	0.76	0.05
Observer 3	0.84	0.04	0.89	0.03	0.69	0.06
Observer 4	0.82	0.03	0.91	0.02	0.65	0.05
average	0.81	0.04	0.88	0.03	0.73	0.06
S_{br+wr}	0.02		0.02		0.06	
<i>p</i> -value ^a						
	$A_z^{(U)} - A_z^{(M)}$	0.26	$A_z^{(U)} - A_z^{(L)}$	0.19	$A_z^{(M)} - A_z^{(L)}$	0.01

^a The significance level was 0.017 after Bonferroni adjustment. Significant differences are highlighted in bold.

For all observers, A_z was the highest in the middle lung zone and lowest in the lower lung zone (Table 35). The difference between the middle and the lower lung zones

was statistically significant after adjustment for multiple comparisons with a p value of 0.01.

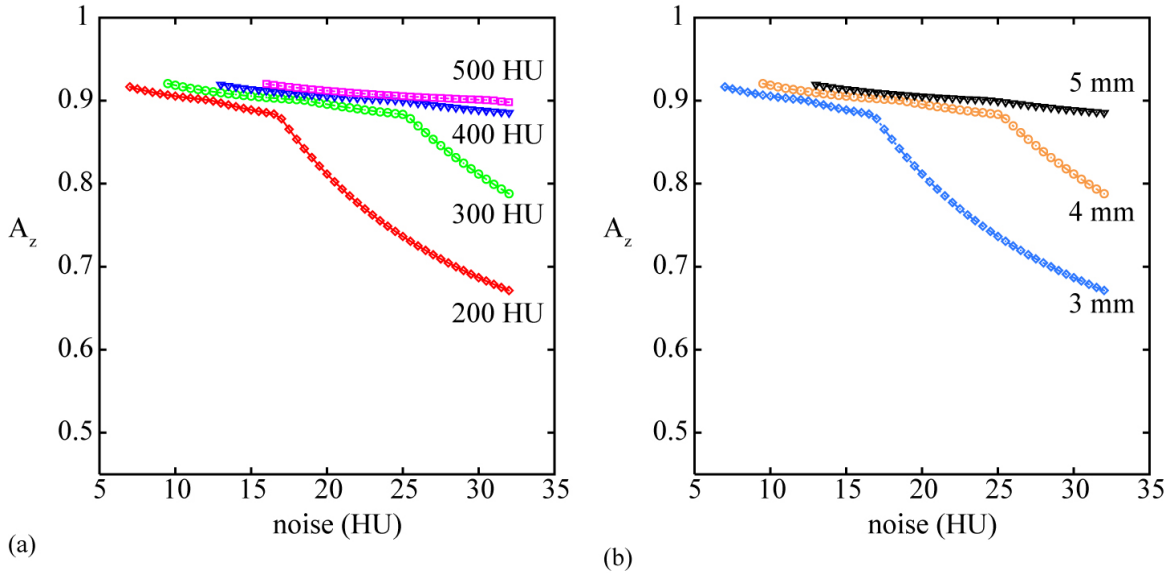


Figure 43: Diagnostic accuracy, A_z , as a function of noise for (a) a nodule with a diameter of 4 mm and a peak contrast of 200-500 HU and (b) a nodule with a peak contrast of 350 HU and a diameter of 3-5 mm.

For a 4-mm diameter nodule with a peak contrast between 200-300 HU, A_z initially increased rapidly with decreasing noise and then reached a plateau beyond a threshold noise value (Figure 43a). The threshold value increased with increasing nodule contrast. However, for a nodule of the same size with a peak contrast above 400 HU, A_z increased very slowly with decreasing noise, appearing to have reached a plateau at noise of 32 HU. Similarly, for a 350-HU nodule with a diameter between 3-4 mm, A_z first increased rapidly with decreasing noise and then reached a plateau beyond a threshold noise value (Figure 43b). The threshold value increased with

increasing nodule size. However, for a nodule of the same peak contrast with a diameter of 5 mm, A_z increased very slowly with decreasing noise, appearing to have reached a plateau at noise of 32 HU.

9.4 Discussions

Combining real clinical CT images with realistically simulated nodules and noise, we conducted a ROC observer study to evaluate the diagnostic influence of image quality (nodule detectability and noise) on the detection of small lung nodules in pediatric CT. We showed that diagnostic accuracy, A_z , increased with nodule detectability, $CDNR_{\text{display}}$, but reached a plateau beyond a threshold $CDNR_{\text{display}}$ value (~ 99 mm). The relationship was analogous with the well-known theoretical relationship between A_z and signal-to-noise ratio (SNR)¹⁵⁹, expressed as

$$A_z = \frac{1}{2} \left(1 + \operatorname{erf} \left(\frac{SNR}{2} \right) \right), \quad (38)$$

where erf is the error function; Equation (38) has the same shape as an integrated Gaussian distribution function or a sigmoidal curve. The relationship implies that the performance of the radiologists saturates beyond a threshold nodule detectability level; further reducing noise or increasing contrast to improve $CDNR_{\text{display}}$ beyond this threshold would result in little gain in diagnostic accuracy. The saturation behavior may be explained by the presence of anatomical background variation (also termed anatomical noise)⁵⁷, which prevents the radiologists from achieving a perfect diagnostic

accuracy even when quantum noise is reduced to a negligible amount. Even at the highest $CDNR_{\text{display}}$, A_z does not exceed 0.92, 0.08 value lower than the ideal value of unity. Because $CDNR_{\text{display}}$ beyond the saturation threshold may be achieved by many different combinations of scan parameters, protocol design in CT should aim to determine the combination of scan parameters that results in the minimum radiation dose to the patient.

Our study also indicates that diagnostic accuracy are different in different lung zones (i.e., upper, middle, lower zones): $A_z^M > A_z^U > A_z^L$. This is consistent with the results of our pilot study in 13 patients¹⁵⁷. As the noise in the three lung zones was similar, an average of 17, 16, and 17 HU for the upper, middle, and lower lung zones, respectively, the difference in diagnostic accuracy cannot be explained by noise. The poorest accuracy in the lower lung zone might be a result of satisfaction of search¹⁵⁰, observer fatigue¹⁶², or more pronounced motion artifacts in the lower lung zone. The relatively lower accuracy in the upper lung zone may be attributable to the higher level of streak artifact around the shoulders.

The relationship between A_z and $CDNR_{\text{display}}$ can be used to examine the effect of a single image quality index, such as noise, by keeping other indices constant. We showed that, for given nodule size and contrast, A_z increased rapidly with decreasing noise, but reached a plateau beyond a threshold noise, the value of which increased with increasing nodule size and contrast (Figure 43). The transition point (threshold noise)

was a direct result of the transition point (threshold $CDNR_{\text{display}}$) in the relationship of A_z versus $CDNR_{\text{display}}$ (Figure 42). The dependence of the threshold noise on nodule size and contrast indicates that the noise required to achieve a given diagnostic accuracy varies with the conspicuity of the target. Typically, the nodule diameter and contrast of interest spread over a range. Thus, A_z as a function of noise may be determined for the centers of the diameter and contrast ranges. A conservative alternative would be to determine A_z as a function of noise for the smallest nodule with the lowest contrast. With either approach, the dependence of A_z with noise informs the compromise (i.e., reduction in accuracy) associated with reducing tube current/dose or increasing noise. It might be argued that certain compromise is clinically acceptable, if for instance the compromise has no consequence in patient management. Thus, the relationship between A_z and noise may be used to determine the optimal tube current or tube current modulation scheme that provides the desired diagnostic accuracy at the lowest radiation dose.

We note that the radiologist's maximum diagnostic accuracy in this study ($A_z \sim 0.92$) was lower than that in our pilot study¹⁵⁷ ($A_z \sim 0.97$), which had a very similar study design. This decrease in performance can be explained by (1) the nodules in this study had slightly lower contrast (200-500 HU) than those in the pilot study (250-550 HU) and (2) all the 13 patients in the pilot study aged between 1-7 years old, whereas nearly half of the 30 patients in this study were older than 6 years old, for whom the overall noise

and the pixel size were larger than those for the younger patients. In fact, the average $CDNR_{display}$ was 143 mm (range: 52-374 mm) and 82 mm (range: 25-271 mm) for patients younger and older than 6 years old, respectively. We chose a lower range of nodule contrasts in this study because the influence of image quality is more likely to be demonstrated when the observers are challenged by more difficult detection tasks.

One limitation of our study was that the prevalence of nodules in our study was much higher than their actual prevalence in pediatric patients undergoing CT examinations. An earlier study revealed heightened diagnostic accuracy with increased disease prevalence¹⁵¹. In addition, as the clinical task in this study was the detection of lung nodules, the observers were less distracted by the search for other abnormalities. Furthermore, in an actual clinical setting, the radiologist may request to have the CT images reconstructed at thinner slices and smaller intervals or reformatted into coronal and sagittal slices to facilitate the identification of a nodule. These could not be performed in our observer experiment. As such, the A_z values reported in our study may deviate somewhat from the actual clinical values. Nevertheless, the change in A_z caused by the change in image quality was indicative of the actual performance change of the radiologist in a clinical setting and could serve as a guidance to the design and optimization of CT scan protocols.

In summary, It is feasible to quantify the relationship between image quality and radiologist performance for the task of lung nodules in pediatric CT. Diagnostic

accuracy increases with nodule detectability (contrast-diameter product to noise ratio), but reaches a plateau beyond a threshold detectability level. This quantitative relationship can be used to examine the effect of any single image quality index, such as noise, by controlling for other indices. The relationship is independent of scan protocols and CT scanner models. It can guide the design of CT protocols to achieve the desired diagnostic accuracy at the minimum radiation dose.

10. Lung Nodule Detection in Pediatric CT: the Tradeoff between Diagnostic Accuracy and Radiation Dose or Cancer Risk^{*}

10.1 Introduction

Since its inception in the 1970's, computed tomography (CT) has revolutionized the practice of medicine and evolved into an essential tool for diagnosing numerous diseases not only in adults but also in children^{5,6}. The clinical utility of CT examinations has led to a rapid expansion in CT use and a corresponding increase in the radiation burden to patients¹⁶. CT radiation is of particular concern to children, whose rapidly growing tissues are more susceptible to radiation-induced cancer and who have longer life spans during which cancerous changes might occur¹⁴. In recent years, the increasing awareness of CT radiation risk to children has brought about growing efforts to reduce CT dose to the pediatric population⁶⁰. The key of all dose reduction efforts is to reduce radiation dose (hence cancer risk) while maintaining diagnostic accuracy. Achieving the desired diagnostic accuracy at the minimum radiation dose requires knowledge of the tradeoff between the two.

The goal of this work is to substantiate the tradeoff between diagnostic accuracy and radiation dose and further between diagnostic accuracy and cancer risk for the task of lung nodule detection in pediatric CT. In pediatric patients with primary cancer, the

^{*} This chapter is based on a manuscript to be submitted to *Medical Physics*.

detection of even one small lung nodule may have tremendous prognostic and therapeutic implications⁴⁰. Owing to the superior resolution of modern multi-detector array CT systems, chest CT examination for the detection of lung nodules is often the standard for pediatric cancer staging and surveillance. To examine the impact of dose reduction on diagnostic accuracy, we recently conducted a receiver operating characteristic (ROC) observer experiment¹⁶³, in which diagnostic accuracy (characterized in terms of the area under the ROC curve, A_z) was measured as a function of nodule detectability (the product of nodule peak contrast and display diameter to noise ratio, $CDNR_{\text{display}}$). For a 64-slice CT system, we have also studied noise, radiation dose, and cancer risk as functions of patient size and scan parameters^{140, 164}. The purpose of this work was to draw correlation between scan parameters, radiation dose/cancer risk, and diagnostic accuracy so as to substantiate the tradeoff between diagnostic accuracy and radiation dose or cancer risk.

10.2 Materials and Methods

For a 64-slice CT system (LightSpeed VCT, GE Healthcare, Waukesha, WI), we have shown that quantum noise in the lung region of the CT image is related with patient size and scan parameters as^{140, 163}

$$\sigma = \sqrt{\frac{t}{5} \cdot \frac{1.375}{p}} \exp(\alpha_0 + \alpha_1 d_w^{(NLA)} + \alpha_2 \ln(\text{mAs}) + \alpha_3 (d_w^{(NLA)})^2 + \alpha_4 \ln^2(\text{mAs}) + \alpha_5 (d_w^{(NLA)}) \ln(\text{mAs})), \quad (39)$$

where t is slice thickness in millimeter, p is helical pitch, $d_w^{(NLA)}$ is the water-equivalent diameter of a patient calculated from the non-lung chest area¹⁴⁰, and coefficients α_i ($i = 0, 1, \dots, 5$) are functions of tube potential and bowtie filter (determined by the choice of scan field-of-view). It can be shown that the effect of bowtie filter on noise was negligible¹⁶³. Therefore, Equation (39) is reduced to

$$\sigma = \sigma(\text{kVp}, p, t, \text{mAs}, d_w^{(NLA)}). \quad (40)$$

For the task of lung nodule detection in pediatric CT, we have also measured the performance of pediatric radiologists as a function of nodule detectability,

$$A_z = A_z(CDNR_{\text{display}}), \quad (41)$$

where A_z is the area under the ROC curve and $CDNR_{\text{display}}$ is the product of nodule peak contrast and display diameter to noise ratio¹⁶³. Equation (41) was ascertained over a noise range of 7 to 32 HU and a $CDNR_{\text{display}}$ range of 25 to 374 mm¹⁶³. Thus, for given nodule characteristics (i.e., given contrast, diameter, and pixel size), diagnostic accuracy is a function of noise and can be expressed as

$$A_z = A_z(\text{kVp}, p, t, \text{mAs}, d_w^{(NLA)}). \quad (42)$$

For the aforementioned CT system, we have also shown, through a Monte Carlo study¹⁶⁴, that the effective dose (D) and effective risk (R) associated with a chest examination decrease exponentially with increasing patient size, i.e.,

$$D = \exp(\beta_0 d + \beta_1) \cdot \text{mAs}, \text{ and} \quad (43)$$

$$R = \exp(\gamma_0 d + \gamma_1) \cdot \text{mAs}, \quad (44)$$

where d is the average chest diameter of a patient and coefficients β_i and γ_i ($i = 0,1$) are functions of bowtie filter, collimation, helical pitch, and tube potential¹⁶⁴. As the effects of bowtie filter and collimation on dose and risk are small compared with the effects of kVp and pitch¹⁶⁴, Equations (43) and (44) may be expressed as

$$D = D(\text{kVp}, p, \text{mAs}, d), \text{ and} \quad (45)$$

$$R = R(\text{kVp}, p, \text{mAs}, d). \quad (46)$$

Equations (42), (45), and (46) suggest that, for a given patient size and a chosen set of scan parameters (tube potential, helical pitch, and slice thickness), each mAs value corresponds to an A_z value, an effective dose value, and an effective risk value. Thus, by eliminating mAs from Equations (42), (45), and (46), the dependence of diagnostic accuracy on effective dose and effective risk can be derived.

To combine Equations (42), (45), and (46), the relationship between $d_w^{(NLA)}$ and d was first determined using the chest images of the 30 patients in our prior ROC study¹⁶³. For each patient, the non-lung area diameter and chest area diameter¹⁴⁰ were calculated for each CT slice between lung apex and lung base. The results were averaged across CT slices to obtain one pair of average non-lung area diameter $d_w^{(NLA)}$ and average chest diameter d for each patient. $d_w^{(NLA)}$ was correlated with d by regression analysis.

Diagnostic accuracy as a function of effective dose and effective risk was determined for the detection of lung nodules with a typical peak contrast and physical diameter product (CD) of 1400 HU·mm, corresponding to the peak location of the CD distribution in the prior ROC study¹⁶³. A representative pixel size of 0.48 mm was assumed, corresponding to the average pixel size of all the chest images in the prior ROC study¹⁶³. A set of scan parameters (tube potential of 120 kVp, helical pitch of 1.375, slice thickness of 5 mm, and gantry rotation period of 0.4 second) most commonly used for imaging children on the aforementioned CT system was considered. Four representative average chest diameters (d of 10, 14, 18, 22 cm) were selected from the pediatric diameter range of 10-23 cm¹⁶⁴. For each d , effective dose and effective risk of male patients were calculated using Equations (45) and (46) for a range of tube currents between 10 and 180 mA with a 10-mA interval. At each tube current value, noise was also calculated using Equation (40), where $d_w^{(NLA)}$ was estimated from d using the correlation relationship between the two. If the noise value fell in between 7-32 HU (the noise over which Equation (41) was obtained) and the resultant $CDNR_{display}$ value fell in between the centers of the first and last $CDNR_{display}$ bins, A_z was determined by linearly interpolating the relationship between A_z and the center location of the $CDNR_{display}$ bin.

10.3 Results

The average non-lung area diameter $d_w^{(NLA)}$ of a patient was a linear function of the patient's average chest diameter d (Figure 44). For a given patient size, A_z increased with increasing effective dose, but reached a plateau beyond a threshold dose value (Figure 45a). The threshold dose increased with increasing patient size. At a given effective dose, A_z increases with decreasing patient size. The effective dose required to achieve an A_z of 0.90 was approximately 0.3, 0.6, 0.9, and 1.3 mSv for male patients with average chest diameters of 10, 14, 18, and 22 cm, respectively. Similar trends were also observed for the relationship between A_z and effective risk (Figure 45b). The effective risk required to achieve an A_z of 0.90 was approximately 1.0, 1.3, 1.7, and 2.0 in 10000 exposed male patients with average chest diameters of 10, 14, 18, and 22 cm, respectively.

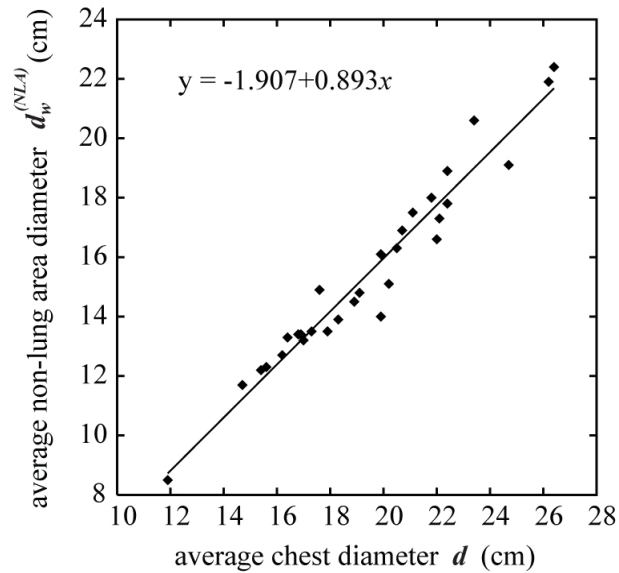


Figure 44: The relationship between average non-lung area diameter $d_w^{(NLA)}$ and average chest diameter d .

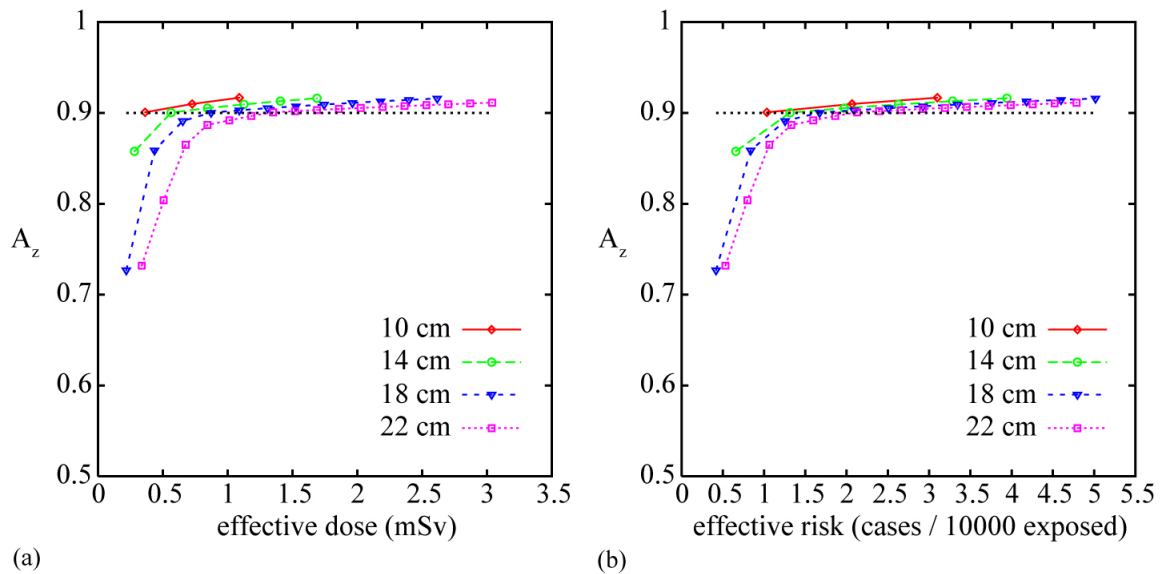


Figure 45: For the detection of lung nodules with a typical contrast-diameter product of 1400 HU·mm, diagnostic accuracy A_z as a function of (a) effective dose and (b) effective risk of male patients from a chest examination. The chest examination employed tube potential of 120 kVp, helical pitch of 1.375, slice thickness of 5 mm, and gantry rotation period of 0.4 second. A typical pixel size of 0.48 mm was assumed. The effects of bowtie filter and collimation on dose and risk were assumed to be small¹⁶⁴.

10.4 Discussions

Substantiating the tradeoff between diagnostic accuracy and radiation dose/risk is an important yet challenging area of research. Due to the time- and labor-consuming nature of observer experiments, the lack of clinical patient images with isolated abnormalities, and the difficulty in ascertaining actual patient dose, most prior studies have been based on phantom images¹⁶⁵⁻¹⁶⁸ or have only evaluated diagnostic accuracy as a function of tube current^{28, 45, 134}. In addition, the effect of patient size was usually not considered. In this work, we combined the results of a ROC observer study⁹⁸ that employed hybrid images (clinical patient images with simulated noise and abnormalities) and experienced radiologists with dose and risk estimated for actual pediatric patients of a wide range of body sizes¹⁶⁴. Thus, our work represents an improvement over prior efforts in that the tradeoff between diagnostic accuracy and radiation dose/risk is reflective of actual patients and is patient size/age dependent.

For a typical product of nodule contrast and diameter and a set of most commonly used scan parameters, we found that diagnostic accuracy first increased rapidly with effective dose/risk and then reached a plateau. Taking a 18-cm diameter patient for example, raising A_z from 0.85 to 0.90 requires additional dose of approximately 0.5 mSv, whereas further raising A_z to 0.91 requires a dose increase of nearly 1 mSv. The saturation behavior is a direct result of the saturation behavior exhibited by the relationship of A_z versus $CDNR_{display}$ ¹⁶³. If it could be shown that

decreasing A_z from 0.91 to 0.90 has no consequence in patient management, then substantial dose saving could be achieved.

The dose needed to achieve the same noise and hence diagnostic accuracy increases with patient size. To achieve an A_z of 0.90, the dose needed for a 22-cm diameter patient is about quadruple of that for a 10-cm diameter patient. This is consistent with the fact that, when designing tube-current-modulated protocols, higher noise index is often used for larger patients to avoid over-dosing the patients. Thus, if nodules with the same characteristics are being considered, the diagnostic accuracy for larger patients can be compromised. It should be noted that there are other considerations for selecting higher noise index in larger patients. One consideration is that larger patients generally have larger anatomical structures, which presumably can be discerned at higher noise levels. Another consideration is that images of larger (older) patients are less prone to breathing artifact; larger (older) patients are more capable of taking a deep breath and holding the breath. Therefore, the inherent contrast of the lung is likely higher in larger patients, which puts less demand on noise in the image. On the other hand, as images of patients with different body sizes are displayed with the same display size (512×512 matrices), a nodule of the same physical size has a smaller display size in images of larger patients, which may require lower noise to discern. Therefore, the choice of noise index for larger patients requires careful consideration of multiple factors.

While the risk associated with achieving the same diagnostic accuracy also increases with patient size, the risk required to achieve an A_z of 0.90 for a 22-cm diameter patient is only twice that for a 10-cm diameter patient. This is because, given the same dose, the risk to a larger (older) patient is smaller than that for a smaller (younger) patient. As the end goal of dose reduction is to reduce risk, this result suggests that risk is a more useful quantity than dose for the purposes of CT protocol design and optimization.

We note that the decision of what A_z is adequate or how much A_z can be compromised is a difficult clinical question. Such decisions may only be substantiated in clinical trials and are beyond the scope of our investigation. Nevertheless, the area under the ROC curve, A_z , has an intuitive explanation; it is often equated to the percentage correct in a two-alternative force choice (2AFC) experiment¹⁶⁹⁻¹⁷¹. Therefore, the tradeoff of A_z with dose and risk reported in this study may guide protocol designs to prevent large medical errors such as significant over-dosing of a patient or substantial degradation of diagnostic accuracy.

In summary, by combining the relationships of diagnostic accuracy with image quality, image quality with scan parameters, and scan parameter with radiation dose/risk, we assessed the tradeoff between diagnostic accuracy and radiation dose or cancer risk for the task of lung nodule in pediatric CT. For a typical lung nodule in pediatric CT and a common set of scan parameters, diagnostic accuracy increases with

radiation dose and cancer risk, but reaches a plateau beyond a threshold dose/risk values. The threshold values increase with patient size. The relationships can guide CT protocol design to achieve the desired diagnostic accuracy at the minimum dose/risk. As the end goal of dose reduction is to reduce risk, risk is a more useful quantity than dose for the purposes of CT protocol design and optimization.

11. Conclusions, Implications, and Future Directions

11.1 Summary and Conclusions

This dissertation addressed two important aspects of pediatric CT: radiation dose and diagnostic accuracy and assessed the tradeoff between the two for the task of lung nodule detection in pediatric cancer.

To obtain dose results related to actual patient risk, a Monte Carlo technique was developed to simulate organ dose of pediatric patients from CT examination. Our work demonstrated that Monte Carlo simulation is a powerful tool for modeling modern CT systems. Provided that the geometry and filtration of a CT system are accurately reproduced in the simulation, the simulated dose results do not deviate from experimental measurements on average by more than around 10%. However, as the filtration data are rarely known exactly, validation against experiments is essential to ensure the accuracy of the simulation results.

To address the patient-generic nature of the current dose estimation/reporting methods, the developed Monte Carlo technique was combined with computer models of pediatric patients created from clinical CT data to estimate patient-specific organ dose. The results showed that volume-weighted CT dose index ($CTDI_{vol}$) cannot serve as a surrogate for patient dose in CT (underestimations of 30-48% were found for two representative pediatric patients). We further showed that effective dose derived from the dose-length product (DLP) can differ considerably from that calculated using

patient-specific organ dose (discrepancies of -30 to 42% were found for the two representative patients).

Considering that the same dose delivered to two patients may entail substantially different risks due to age and gender differences, patient-specific dose was further combined with age-, gender-, and tissue-specific risk coefficients to estimate patient-specific cancer risk. Although cancer risk estimated in this way does not represent the true risk of an individual due to the limitations of the risk coefficients, they represent our current best knowledge of the potential radiation detriment to a patient associated with his/her CT examination.

To facilitate the ongoing efforts of the medical imaging community to better manage patient dose, the patient-specific method was used to evaluate factors that affect dose and risk, including patient size, age, gender, and scan parameters. For pediatric patients in the same weight/protocol group, organ dose variation across patients was found to be generally small for large organs in the scan coverage (< 10%), larger for small organs in the scan coverage (1-18%), and the largest for organs partially or completely outside the scan coverage (6-77%). Across the entire pediatric population, dose and risk associated with a chest scan protocol was found to decrease exponentially with increasing patient size, with average chest diameter being a stronger predictor of dose and risk than weight and total scan length. Our results also helped to quantify the age and gender deficiencies of the effective dose concept; the difference in effective dose

does not represent the risk difference between the two age groups, nor does the difference in effective dose fully capture the risk difference between two genders. While effective dose may still be useful for comparing scan techniques and imaging devices, when risk is compared across ages and genders, effective risk is a more suitable concept to use.

Our study of the effects of scan parameters showed that the effects of bowtie filter and beam collimation on dose and risk are small compared to the effects of helical pitch and tube potential. The effects of any scan parameter were found to depend on patient size, which cannot be reflected by the difference in $CTDI_{vol}$.

While it is important to minimize dose and risk to pediatric patients, dose and risk reduction should not come at the expense of deteriorated diagnostic accuracy. In this dissertation, the influence of dose reduction on diagnostic accuracy was investigated for the task of lung nodule detection.

To overcome the limitation of the real lung nodules, a technique was developed to simulate small lung nodules in three dimensions by adding random asymmetry to a mathematical model initially proposed for lung nodules on chest radiographs and by considering the size and contrast variations across sequential CT slices. Simulated lung nodules were found to resemble real nodules in physical characteristics and detection rate, and to be perceptually indistinguishable from real nodules for experienced pediatric radiologists.

Because it is not feasible to scan the same patients at multiple dose levels, noise addition software was used to emulate image quality at reduced dose conditions. After proper calibrations of the input tube currents, simulated noise was found to match real noise in term of both texture and magnitude.

In view of the fact that noise-base dose reduction studies can provide results independent of scan protocols and scanner models, a method was developed to estimate quantum noise in the CT image based on patient size. We showed that when noise-diameter relationships determined in water phantoms were combined with water-equivalent diameter of a patient estimated from non-lung chest area, noise in the lung region of the CT images can be estimated with errors ($< \sim 30\%$) comparable to the noise variation across the lung volume.

Simulated noise and nodules were added to real clinical images to create hybrid images, which allowed the diagnostic performance of radiologists to be assessed in a realistic setting. We found that, over a range of relatively high nodule detectability levels (product of nodule peak contrast and display diameter to noise ratio or $CDNR_{\text{display}}$ of approximately 52-374 mm), tube current or dose has a weak effect on the diagnostic accuracy of lung nodules. The effect of 75% dose reduction was shown to be comparable to inter-observer variability, suggesting a potential for dose reduction.

Over a wider range of nodule detectability ($CDNR_{\text{display}}$ of 25-374 mm), diagnostic accuracy was found to increase with increasing nodule detectability and

reached a plateau beyond a threshold detectability level. Considering that CT examinations are increasingly being performed with tube-current-modulation techniques, which aim to provide a target noise in the image, the relationship between diagnostic accuracy and nodule detectability was used to derive the dependence of accuracy on noise for representative nodule diameter and contrast values. We found that, for given nodule size and contrast, diagnostic accuracy increases rapidly with decreasing noise, but reaches a plateau beyond a threshold noise, the value of which increased with increasing nodule size and contrast.

Lastly, we combined the relationships between diagnostic accuracy and image quality, between image quality and scan parameters, and between scan parameter and radiation dose/risk to provide the tradeoff between diagnostic accuracy and radiation dose or cancer risk. For typical values of nodule size and contrast and for a set of most commonly used scan parameters, diagnostic accuracy was found to increase with effective dose and effective risk for a given patient size and reach a plateau beyond a threshold dose/risk value. To achieve the same diagnostic accuracy, higher dose is needed to image a larger patient. Although the associated risk is also higher in a larger patient, the risk ratio between two patient sizes was found to be much lower than the dose ratio, a result of the older age of the larger patient. As the end goal of dose reduction is to reduce risk, risk is a more useful quantity than dose for the purposes of CT protocol design and optimization.

11.2 Clinical Implications

The research in this dissertation has two important clinical implications. First, the quantitative relationships between patient dose/risk and patient size, between patient dose/risk and scan parameters, between diagnostic accuracy and image quality, and between diagnostic accuracy and radiation dose can guide the design and optimization of CT protocols to achieve the desired diagnostic accuracy at the minimum radiation dose/risk.

Second, patient-specific dose and risk information, when included in a patient's dosimetry and medical records, can inform healthcare providers of prior radiation exposure and aid in decisions for image utilization, including the situation where multiple examinations are being considered. Patient-specific dose and risk information may also be extremely helpful for institutional review of scientific investigations using CT examinations. Lastly, patient-specific dose and risk results afford more individualized and expanded application of dose tracking from medical radiation exposures.

11.3 Future Directions

The Monte Carlo method developed in this dissertation work was limited to a single scanner model and to fixed-tube-current techniques. Future work can extend the method to other scanner models and to tube-current-modulated techniques including both longitudinal and angular modulations. Other authors have shown, with small

numbers of patient and scanner models, that when organ dose estimates are normalized by CTDI values appropriate for the patient size (e.g., $CTDI_{vol}$ in a cylindrical phantom with the same circumference as the patient), the variations across CT scanner models are small. Thus, the Monte Carlo method may be extended to provide patient-specific normalized dose and risk estimates independent of scanner models, although this requires further testing and validation.

Our study of patient-specific dose and risk was limited to the pediatric population only. With the development of a library of adult computer models for both normal and obese patients, our dose and risk estimation method can be extended to the entire patient population to enable a patient-specific dose reporting system, potentially replacing the current CTDI-based dose reporting system.

The utility of our Monte Carlo method can be further expanded by developing a user-friendly software interface to enable not only medical physicists but also physicians, CT technologists, and other healthcare professionals to estimate radiation dose and cancer risk from a patient's CT image with a few mouse clicks. The development of such a software application is pending on the automation of image segmentation and model creation process, but should become feasible in the foreseeable future.

One limitation of our nodule simulation technique is that the asymmetric shape of a nodule is created in the axial slice, i.e., in two dimensions. Thus, if the axial CT slices

were to be reformatted into coronal or sagittal planes, discontinuities may appear around nodule borders. Future work can create asymmetric (irregular-shaped) nodule models in three dimensions and insert a nodule into each CT slice based on both the partial-volume effect and the modulation transfer property of the CT system. Similar approaches can also be used to model other focal lesions and abnormalities of other nature, such as fracture. Computer models of abnormalities created in three dimensions may also be correlated with physical properties of actual abnormalities, thus offering a database of disease truth, by which the quantitative accuracy of an imaging system can be evaluated.

To apply the quantitative relationship between diagnostic accuracy and image quality in the design and optimization of CT protocols, image quality as a function of scanner acquisition parameters needs to be ascertained as well. The only image quality index that we studied was noise. Future work is needed to measure nodule contrast as a function of scan parameters for each nodule size range of interest. For a given actual nodule size (as determined by pathology), the visual size on the CT image may also depend on scan and reconstruction parameters. While contrast as a function of scan parameters has been studied by many authors, most studies have focused on iodine contrast or soft-tissue contrast such as the contrast between muscle and fat. The contrast and size of lung nodules as functions of scan parameters are topics of interest in the emerging area of quantitative imaging.

Apart from quantifying the dependence of image quality and diagnostic accuracy on scan parameters and radiation dose, optimizations in CT can be greatly facilitated by the development of a realistic image simulation tool. The noise addition software employed in this dissertation work is only capable of emulating image quality at reduced tube currents. The image quality at various tube potentials, for example, cannot be simulated. With computer modeling of human anatomy becoming increasingly sophisticated, computer-simulated CT images may become sufficiently realistic in the future for not only image quality assessment but also the evaluation of human observer performances.

References

1. G. N. Hounsfield, "Computerized transverse axial scanning (tomography). 1. Description of system," *The British journal of radiology* **46**, 1016-1022 (1973).
2. I. Mori, "Computerized tomographic apparatus utilizing a radiation source," US Patent 4,630,202 (1986).
3. H. Nishimura and O. Miyazaki, "CT system for spirally scanning subject on a movable bed synchronized to X-ray tube revolution," US Patent 4,789,929 (1988).
4. W. A. Kalender, W. Seissler and P. Vock, "Single-breath-hold spiral volumetric CT by continuous patient translation and scanner rotation," *Radiology* **173**, 414 (1989).
5. M. J. Siegel, "Pediatric Multislice Computed Tomography of the Chest," in *Multidetector-Row CT of the Thorax, Part 1*, edited by U. J. Schoepf (Springer Berlin Heidelberg, 2005), pp. 375-394.
6. E. Yekeler, "Pediatric abdominal applications of multidetector-row CT," *European journal of radiology* **52**, 31-43 (2004).
7. R. G. Evens and F. A. Mettler, "National CT use and radiation exposure: United States 1983," *Ajr* **144**, 1077-1081 (1985).
8. B. Bahador, *Trends in diagnostic imaging to 2000*. London: Financial Times Pharmaceuticals and Healthcare Publishing, 1996.
9. IMV 2006 CT Market Summary Report. Des Plaines, IL: IMV Medical Information Division, 2006.
10. P. C. Shrimpton, D. Hart, M. C. Hiller, B. F. Wall and K. Faulkner, *Survey of CT practice in the UK. 1. Aspects of examination frequency and quality assurance*. Chilton, England: National Radiological Protection Board, 1991. NRPB report 248.
11. UNSCEAR (United Nations Scientific Committee on the Effects of Atomic Radiation). *Sources and effects of ionizing radiation*. New York: United Nations, 1993. UN publication E.94.IX.2.
12. F. A. Mettler, Jr., P. W. Wiest, J. A. Locken and C. A. Kelsey, "CT scanning: patterns of use and dose," *J Radiol Prot* **20**, 353-359 (2000).

13. A. S. Brody, D. P. Frush, W. Huda and R. L. Brent, "Radiation risk to children from computed tomography," *Pediatrics* **120**, 677-682 (2007).
14. NRC. Health Risks from Exposure to Low Levels of Ionizing Radiation — BEIR VII. Washington, DC: The National Academies Press; 2006.
15. D. Brenner, C. Elliston, E. Hall and W. Berdon, "Estimated risks of radiation-induced fatal cancer from pediatric CT," *Ajr* **176**, 289-296 (2001).
16. D. J. Brenner and E. J. Hall, "Computed tomography--an increasing source of radiation exposure," *The New England journal of medicine* **357**, 2277-2284 (2007).
17. A. Paterson and D. P. Frush, "Dose reduction in paediatric MDCT: general principles," *Clinical radiology* **62**, 507-517 (2007).
18. D. Marin, R. C. Nelson, S. T. Schindera, S. Richard, R. S. Youngblood, T. T. Yoshizumi and E. Samei, "Low-tube-voltage, high-tube-current multidetector abdominal CT: improved image quality and decreased radiation dose with adaptive statistical iterative reconstruction algorithm--initial clinical experience," *Radiology* **254**, 145-153 (2010).
19. M. K. Kalra, M. M. Maher, T. L. Toth, L. M. Hamberg, M. A. Blake, J. A. Shepard and S. Saini, "Strategies for CT radiation dose optimization," *Radiology* **230**, 619-628 (2004).
20. ICRP, *Managing Patient Dose in Multi-Detector Computed Tomography (MDCT)*, ICRP Publication 102 (International Commission on Radiological Protection).
21. ICRP, *The 2007 Recommendations of the International Commission on Radiological Protection*, ICRP Publication 103 (International Commission on Radiological Protection, Essen, Germany).
22. D. Brenner and W. Huda, "Effective dose: a useful concept in diagnostic radiology?," *Radiat Prot Dosimetry* **128**, 503-508 (2008).
23. B. Axelsson, J. Persliden and P. Schuwert, "Dosimetry for computed tomography examination of children," *Radiat Prot Dosim* **64**, 221-226 (1996).
24. C. L. Chapple, S. Willis and J. Frame, "Effective dose in paediatric computed tomography," *Physics in medicine and biology* **47**, 107-115 (2002).

25. M. Zankl, W. Panzer, N. Petoussihenss and G. Drexler, "Organ Doses for Children from Computed Tomographic Examinations," *Radiation Protection Dosimetry* **57**, 393-396 (1995).
26. M. Caon, G. Bibbo and J. Pattison, "An EGS4-ready tomographic computational model of a 14-year-old female torso for calculating organ doses from CT examinations," *Physics in medicine and biology* **44**, 2213-2225 (1999).
27. M. Caon, G. Bibbo and J. Pattison, "Monte Carlo calculated effective dose to teenage girls from computed tomography examinations," *Radiation Protection Dosimetry* **90**, 445-448 (2000).
28. N. Karabulut, M. Toru, V. Gelebek, M. Gulsun and O. M. Ariyurek, "Comparison of low-dose and standard-dose helical CT in the evaluation of pulmonary nodules," *European radiology* **12**, 2764-2769 (2002).
29. I. A. Castellano, D. R. Dance and P. M. Evans, "CT dosimetry: Getting the best from the adult cristy phantom," *Radiation Protection Dosimetry* **114**, 321-325 (2005).
30. J. J. DeMarco, C. H. Cagnon, D. D. Cody, D. M. Stevens, C. H. McCollough, M. Zankl, E. Angel and M. F. McNitt-Gray, "Estimating radiation doses from multidetector CT using Monte Carlo simulations: effects of different size voxelized patient models on magnitudes of organ and effective dose," *Physics in medicine and biology* **52**, 2583-2597 (2007).
31. C. Lee, C. Lee, R. J. Staton, D. E. Hintenlang, M. M. Arreola, J. L. Williams and W. E. Bolch, "Organ and effective doses in pediatric patients undergoing helical multislice computed tomography examination," *Medical physics* **34**, 1858-1873 (2007).
32. C. Lee, D. Lodwick, J. L. Williams and W. E. Bolch, "Hybrid computational phantoms of the 15-year male and female adolescent: Applications to CT organ dosimetry for patients of variable morphometry," *Medical Physics* **35**, 2366-2382 (2008).
33. J. J. DeMarco, C. H. Cagnon, D. D. Cody, D. M. Stevens, C. H. McCollough, J. O'Daniel and M. F. McNitt-Gray, "A Monte Carlo based method to estimate radiation dose from multidetector CT (MDCT): cylindrical and anthropomorphic phantoms," *Physics in medicine and biology* **50**, 3989-4004 (2005).

34. R. J. Staton, C. Lee, C. Lee, M. D. Williams, D. E. Hintenlang, M. M. Arreola, J. L. Williams and W. E. Bolch, "Organ and effective doses in newborn patients during helical multislice computed tomography examination," *Physics in medicine and biology* **51**, 5151-5166 (2006).
35. P. Deak, M. van Straten, P. C. Shrimpton, M. Zankl and W. A. Kalender, "Validation of a Monte Carlo tool for patient-specific dose simulations in multi-slice computed tomography," *European radiology* **18**, 759-772 (2008).
36. P. Shrimpton, Assessment of patient dose in CT. NRPB-PE/1/2004. NRPB, Chilton. (2004).
37. W. Huda and K. M. Ogden, "Computing effective doses to pediatric patients undergoing body CT examinations," *Pediatric radiology* **38**, 415-423 (2008).
38. K. E. Thomas and B. Wang, "Age-specific effective doses for pediatric MSCT examinations at a large children's hospital using DLP conversion coefficients: a simple estimation method," *Pediatric radiology* **38**, 645-656 (2008).
39. M. Kachelriess, S. Schaller and W. A. Kalender, "Strategies for Dose Reduction and Improved Image Quality in MSCT," in *Multidetector-Row CT of the Thorax*, Part 1, edited by U. J. Schoepf (Springer Berlin Heidelberg, 2005), pp. 35-45.
40. M. J. Absalon, M. B. McCarville, T. Liu, V. M. Santana, N. C. Daw and F. Navid, "Pulmonary nodules discovered during the initial evaluation of pediatric patients with bone and soft-tissue sarcoma," *Pediatric blood & cancer* **50**, 1147-1153 (2008).
41. P. Rogalla, B. Stover, I. Scheer, R. Juran, G. Gaedicke and B. Hamm, "Low-dose spiral CT: applicability to paediatric chest imaging," *Pediatric radiology* **29**, 565-569 (1999).
42. J. Lucaya, J. Piqueras, P. Garcia-Pena, G. Enriquez, M. Garcia-Macias and J. Sotil, "Low-dose high-resolution CT of the chest in children and young adults: dose, cooperation, artifact incidence, and image quality," *Ajr* **175**, 985-992 (2000).
43. R. Shah, A. K. Gupta, M. M. Rehani, A. K. Pandey and S. Mukhopadhyay, "Effect of reduction in tube current on reader confidence in paediatric computed tomography," *Clinical radiology* **60**, 224-231 (2005).

44. S. E. Seltzer, P. F. Judy, D. F. Adams, F. L. Jacobson, P. Stark, R. Kikinis, R. G. Swensson, S. Hooton, B. Head and U. Feldman, "Spiral CT of the chest: comparison of cine and film-based viewing," *Radiology* **197**, 73-78 (1995).
45. H. Rusinek, D. P. Naidich, G. McGuinness, B. S. Leitman, D. I. McCauley, G. A. Krinsky, K. Clayton and H. Cohen, "Pulmonary nodule detection: low-dose versus conventional CT," *Radiology* **209**, 243-249 (1998).
46. H. O. Shin, M. Blietz, B. Frericks, S. Baus, D. Savellano and M. Galanski, "Insertion of virtual pulmonary nodules in CT data of the chest: development of a software tool," *European radiology* **16**, 2567-2574 (2006).
47. X. Zhang, E. Olcott, P. Raffy, N. Yu and H. Chui, "Simulating solid lung nodules in MDCT images for CAD evaluation: modeling, validation, and applications," *Proceedings of SPIE: Medical Imaging-Computer-Aided Diagnosis*, Vol 6514, Page 65140Z.
48. S. Punwani, J. Zhang, W. Davies, R. Greenhalgh and P. Humphries, "Paediatric CT: the effects of increasing image noise on pulmonary nodule detection," *Pediatric radiology* **38**, 192-201 (2008).
49. J. R. Mayo, K. P. Whittall, A. N. Leung, T. E. Hartman, C. S. Park, S. L. Primack, G. K. Chambers, M. K. Limkeman, T. L. Toth and S. H. Fox, "Simulated dose reduction in conventional chest CT: validation study," *Radiology* **202**, 453-457 (1997).
50. D. P. Frush, C. C. Slack, C. L. Hollingsworth, G. S. Bisset, L. F. Donnelly, J. Hsieh, T. Lavin-Wensell and J. R. Mayo, "Computer-simulated radiation dose reduction for abdominal multidetector CT of pediatric patients," *Ajr* **179**, 1107-1113 (2002).
51. A. J. Britten, M. Crotty, H. Kiremidjian, A. Grundy and E. J. Adam, "The addition of computer simulated noise to investigate radiation dose and image quality in images with spatial correlation of statistical noise: an example application to X-ray CT of the brain," *The British journal of radiology* **77**, 323-328 (2004).
52. J. R. Mayo, K. I. Kim, S. L. MacDonald, T. Johkoh, P. Kavanagh, H. O. Coxson and S. Vedal, "Reduced radiation dose helical chest CT: effect on reader evaluation of structures and lung findings," *Radiology* **232**, 749-756 (2004).
53. D. A. Sennst, M. Kachelriess, C. Leidecker, B. Schmidt, O. Watzke and W. A. Kalender, "An extensible software-based platform for reconstruction and evaluation of CT images," *Radiographics* **24**, 601-613 (2004).

54. D. Tack, V. De Maertelaer, W. Petit, P. Scillia, P. Muller, C. Suess and P. A. Gevenois, "Multi-detector row CT pulmonary angiography: comparison of standard-dose and simulated low-dose techniques," *Radiology* **236**, 318-325 (2005).
55. M. H. Brem, A. A. Zamani, R. Riva, K. H. Zou, Z. Rumboldt, F. F. Hennig, R. Kikinis, A. M. Norbash and U. J. Schoepf, "Multidetector CT of the paranasal sinus: potential for radiation dose reduction," *Radiology* **243**, 847-852 (2007).
56. J. Wessling, R. Esseling, R. Raupach, S. Fockenberg, N. Osada, J. Gerss, W. Heindel and R. Fischbach, "The effect of dose reduction and feasibility of edge-preserving noise reduction on the detection of liver lesions using MSCT," *European radiology* **17**, 1885-1891 (2007).
57. E. Samei, M. J. Flynn and W. R. Eyler, "Detection of subtle lung nodules: relative influence of quantum and anatomic noise on chest radiographs," *Radiology* **213**, 727-734 (1999).
58. NCRP, Ionizing radiation exposure of the population of the United States, NCRP Report No. 160 (National Council on Radiation Protection and Measurements, Bethesda, MD, 2009).
59. AAPM Task Group 23, The measurement, reporting, and management of radiation dose in CT, AAPM Report No. 96 (American Association of Physicists in Medicine, College Park, MD, 2008).
60. M. J. Goske, K. E. Applegate, J. Boylan, P. F. Butler, M. J. Callahan, B. D. Coley, S. Farley, D. P. Frush, M. Hernanz-Schulman, D. Jaramillo, N. D. Johnson, S. C. Kaste, G. Morrison, K. J. Strauss and N. Tuggle, "The 'Image Gently' campaign: increasing CT radiation dose awareness through a national education and awareness program," *Pediatr Radiol* **38**, 265-269 (2008).
61. E. S. Amis, Jr., P. F. Butler, K. E. Applegate, S. B. Birnbaum, L. F. Brateman, J. M. Hevezi, F. A. Mettler, R. L. Morin, M. J. Pentecost, G. G. Smith, K. J. Strauss and R. K. Zeman, "American College of Radiology white paper on radiation dose in medicine," *J Am Coll Radiol* **4**, 272-284 (2007).
62. <http://rpop.iaea.org/RPOP/RPoP/Content/News/smart-card-project.htm>.
63. T. B. Shope, R. M. Gagne and G. C. Johnson, "A method for describing the doses delivered by transmission x-ray computed tomography," *Medical physics* **8**, 488-495 (1981).

64. L. M. Hurwitz, T. T. Yoshizumi, P. C. Goodman, R. C. Nelson, G. Toncheva, G. B. Nguyen, C. Lowry and C. Anderson-Evans, "Radiation dose savings for adult pulmonary embolus 64-MDCT using bismuth breast shields, lower peak kilovoltage, and automatic tube current modulation," *Ajr* **192**, 244-253 (2009).
65. M. Cristy and K. F. Eckerman, "Specific absorbed fractions of energy at various ages from internal photon sources," ORNL/TM-8381/Volumes I-VII (Oak Ridge National Laboratory, Oak Ridge, TN, 1987) (1987).
66. N. Petoussi-Henss, M. Zanki, U. Fill and D. Regulla, "The GSF family of voxel phantoms," *Physics in medicine and biology* **47**, 89-106 (2002).
67. C. Lee, J. L. Williams and W. E. Bolch, "Whole-body voxel phantoms of paediatric patients--UF Series B," *Physics in medicine and biology* **51**, 4649-4661 (2006).
68. C. Lee, D. Lodwick, J. Hurtado, D. Pafundi, J. L. Williams and W. E. Bolch, "The UF family of reference hybrid phantoms for computational radiation dosimetry," *Physics in medicine and biology* **55**, 339-363 (2010).
69. V. F. Cassola, V. J. Lima, R. Kramer and H. J. Khoury, "FASH and MASH: female and male adult human phantoms based on polygon mesh surfaces: I. Development of the anatomy," *Physics in medicine and biology* **55**, 133-162 (2010).
70. A. Christ, W. Kainz, E. G. Hahn, K. Honegger, M. Zefferer, E. Neufeld, W. Rascher, R. Janka, W. Bautz, J. Chen, B. Kiefer, P. Schmitt, H. P. Hollenbach, J. Shen, M. Oberle, D. Szczerba, A. Kam, J. W. Guag and N. Kuster, "The Virtual Family--development of surface-based anatomical models of two adults and two children for dosimetric simulations," *Physics in medicine and biology* **55**, N23-38 (2010).
71. D. J. Brenner, "Effective dose: a flawed concept that could and should be replaced," *Br J Radiol* **81**, 521-523 (2008).
72. J. Baro, J. Sempau, J. M. Fernandezvarea and F. Salvat, "Penelope - an Algorithm for Monte-Carlo Simulation of the Penetration and Energy-Loss of Electrons and Positrons in Matter," *Nucl Instrum Meth B* **100**, 31-46 (1995).
73. J. Sempau, J. M. Fernandez-Varea, E. Acosta and F. Salvat, "Experimental benchmarks of the Monte Carlo code PENELOPE," *Nucl Instrum Meth B* **207**, 107-123 (2003).

74. T. L. Toth and W. W. Hampel, "Collimator for reducing patient x-ray dose," US Patent 5,644,614 (1997).
75. S. J. Gibbs, A. Pujol, Jr., T. S. Chen, A. W. Malcolm and A. E. James, Jr., "Patient risk from interproximal radiography," *Oral Surg Oral Med Oral Pathol* **58**, 347-354 (1984).
76. G. Williams, M. Zankl, W. Abmayr, R. Veit and G. Drexler, "The calculation of dose from external photon exposures using reference and realistic human phantoms and Monte Carlo methods," *Physics in medicine and biology* **31**, 449-452 (1986).
77. W. P. Segars, M. Mahesh, T. J. Beck, E. C. Frey and B. M. W. Tsui, "Realistic CT simulation using the 4D XCAT phantom," *Medical Physics* **35**, 3800-3808 (2008).
78. J. Sempau and P. Andreo, "Configuration of the electron transport algorithm of PENELOPE to simulate ion chambers," *Physics in medicine and biology* **51**, 3533-3548 (2006).
79. G. M. Sturgeon, X. Li, S. Mendonca, D. P. Frush, E. Samei and W. P. Segars, "Series of anatomically detailed NURBS-based phantoms for pediatric CT research," *Medical Physics*. In Review.
80. W. E. Lorensen and H. E. Cline, "Marching cubes: A high resolution 3D surface construction algorithm," *Proceedings of the 14th annual conference on Computer graphics and interactive techniques*, 163-169 (1987).
81. W. Schroeder, K. W. Martin and B. Lorensen, *The visualization toolkit : an object-oriented approach to 3D graphics, 3rd ed.* (Kitware Inc., New York, 2006).
82. A. J. van der Molen and J. Geleijns, "Overranging in multisection CT: quantification and relative contribution to dose--comparison of four 16-section CT scanners," *Radiology* **242**, 208-216 (2007).
83. W. P. Segars, B. M. W. Tsui, E. C. Frey and E. K. Fishman, "Extension of the 4D NCAT phantom to dynamic x-ray CT simulation," *Conference Record of the 2003 Medical Imaging Conference and Nuclear Science Symposium*, October 19-25, Portland, OR (2003).
84. ICRP, *Basic anatomical and physiological data for use in radiological protection: reference values*, ICRP Publication 89 (International Commission on Radiological Protection, New York, New York, 2002).

85. ICRU, *Photon, electron, proton and neutron interaction data for body tissues*, Report 46 (International Commission on Radiation Units and Measurements, Bethesda, MD, 1992).
86. C. Lee, A. P. Shah and W. E. Bolch, "An assessment of bone marrow and bone endosteum dosimetry methods for photon sources," *Physics in medicine and biology* **51**, 5391-5407 (2006).
87. W. Huda, "Computing effective doses from dose-length product in CT," *Radiology* **248**, 321; author reply 321-322 (2008).
88. M. F. McNitt-Gray, E. Angel, A. C. Turner, D. M. Stevens, A. N. Primak, C. H. Cagnon, D. D. Cody, J. J. DeMarco and C. H. McCollough, "CTDI Normalized to Measured Beam Width as an Accurate Predictor of Dose Variations for Multidetector Row CT (MDCT) Scanners Across all Manufacturers," *Radiological Society of North America, 94th Scientific Assembly and Annual Meeting*, 2008.
89. G. Jarry, J. J. DeMarco, U. Beifuss, C. H. Cagnon and M. F. McNitt-Gray, "A Monte Carlo-based method to estimate radiation dose from spiral CT: from phantom testing to patient-specific models," *Physics in medicine and biology* **48**, 2645-2663 (2003).
90. D. Zhang, M. Zankl, J. J. DeMarco, C. H. Cagnon, E. Angel, A. C. Turner and M. F. McNitt-Gray, "Reducing radiation dose to selected organs by selecting the tube start angle in MDCT helical scans: a Monte Carlo based study," *Medical physics* **36**, 5654-5664 (2009).
91. S. Utrup, D. M. E. Bardo, D. Smith, J. Asamoto, S. Glasberg and J. H. Yanof, "Reduction of Helical "Over-ranging" Radiation Dose with Dynamic Collimation on 256-Slice CT " *Radiological Society of North America, 95th Scientific Assembly and Annual Meeting*, 2009.
92. E. L. Nickoloff, A. K. Dutta and Z. F. Lu, "Influence of phantom diameter, kVp and scan mode upon computed tomography dose index," *Medical physics* **30**, 395-402 (2003).
93. J. M. Boone, E. M. Geraghty, J. A. Seibert and S. L. Wootton-Gorges, "Dose reduction in pediatric CT: a rational approach," *Radiology* **228**, 352-360 (2003).
94. ICRP, *The 1990 Recommendations of the International Commission on Radiological Protection*, ICRP Publication 60 (International Commission on Radiological Protection, Pergamon, Oxford, 1991).

95. A. Turner, M. Zankl, J. J. Demarco, E. Angel, D. Zhang and M. F. McNitt-Gray, "A Method to Estimate Organ Doses from Multidetector Row CT Abdominal Exams from Patient Sized Corrected CT Dose Index (CTDI) Values: A Monte Carlo Study," Radiological Society of North America, 95th Scientific Assembly and Annual Meeting, 2009.
96. O. W. Linton and F. A. Mettler, Jr., "National conference on dose reduction in CT, with an emphasis on pediatric patients," *AJR Am J Roentgenol* **181**, 321-329 (2003).
97. M. E. Arch and D. P. Frush, "Pediatric body MDCT: a 5-year follow-up survey of scanning parameters used by pediatric radiologists," *AJR Am J Roentgenol* **191**, 611-617 (2008).
98. A. Khursheed, M. C. Hillier, P. C. Shrimpton and B. F. Wall, "Influence of patient age on normalized effective doses calculated for CT examinations," *British Journal of Radiology* **75**, 819-830 (2002).
99. W. P. Segars, J. Sandberg, X. Li, E. Samei, R. P. Jones and D. P. Frush, "Transformable Digital Phantom for Modeling Patient Populations in Pediatric CT Research," Radiological Society of North America, 93rd Scientific Assembly and Annual Meeting, 2007.
100. S. D. King and F. W. Spiers, "Photoelectron enhancement of the absorbed dose from X rays to human bone marrow: experimental and theoretical studies," *Br J Radiol* **58**, 345-356 (1985).
101. X. Li, E. Samei, T. T. Yoshizumi, J. G. Colsher, R. P. Jones and D. P. Frush, "Experimental benchmarking of a Monte Carlo dose simulation code for pediatric CT," *Proceedings of SPIE: Medical Imaging-Physics of Medical Imaging*, Vol 6510, Page 65102A.
102. C. J. Martin, "Effective dose: how should it be applied to medical exposures?," *Br J Radiol* **80**, 639-647 (2007).
103. X. Li, E. Samei, W. P. Segars, G. M. Sturgeon, J. G. Colsher and D. P. Frush, "Patient-specific dose estimation for pediatric chest CT," *Medical physics* **35**, 5821-5828 (2008).
104. B. Rosner, *Fundamentals of biostatistics*, 6th ed. (Thomson-Brooks/Cole, Belmont, CA, 2006).

105. M. J. Goske, K. E. Applegate, J. Boylan, P. F. Butler, M. J. Callahan, B. D. Coley, S. Farley, D. P. Frush, M. Hernanz-Schulman, D. Jaramillo, N. D. Johnson, S. C. Kaste, G. Morrison, K. J. Strauss and N. Tuggle, "The Image Gently campaign: working together to change practice," *Ajr* **190**, 273-274 (2008).
106. D. D. Cody, D. M. Moxley, K. T. Krugh, J. C. O'Daniel, L. K. Wagner and F. Eftekhari, "Strategies for formulating appropriate MDCT techniques when imaging the chest, abdomen, and pelvis in pediatric patients," *Ajr* **182**, 849-859 (2004).
107. M. J. Siegel, B. Schmidt, D. Bradley, C. Suess and C. Hildebolt, "Radiation dose and image quality in pediatric CT: effect of technical factors and phantom size and shape," *Radiology* **233**, 515-522 (2004).
108. X. Li, E. Samei, W. P. Segars, G. M. Sturgeon, J. G. Colsher, G. Toncheva, T. T. Yoshizumi and D. P. Frush, "A Monte Carlo method for estimating patient-specific radiation dose and cancer risk in CT " *Medical Physics*. In Review.
109. ICRP, Basic anatomical and physiological data for use in radiological protection: reference values, ICRP Publication 89 (International Commission on Radiological Protection, New York, NY, 2002).
110. C. J. Martin, "The application of effective dose to medical exposures," *Radiat Prot Dosimetry* **128**, 1-4 (2008).
111. J. R. Haaga, F. Miraldi, W. MacIntyre, J. P. LiPuma, P. J. Bryan and E. Wiesen, "The effect of mAs variation upon computed tomography image quality as evaluated by in vivo and in vitro studies," *Radiology* **138**, 449-454 (1981).
112. J. R. Haaga, "Radiation dose management: weighing risk versus benefit," *Ajr* **177**, 289-291 (2001).
113. A. B. Sigal-Cinquabre, R. Hennequin, H. T. Abada, X. Chen and J. F. Paul, "Low-kilovoltage multi-detector row chest CT in adults: feasibility and effect on image quality and iodine dose," *Radiology* **231**, 169-174 (2004).
114. C. M. Heyer, P. S. Mohr, S. P. Lemburg, S. A. Peters and V. Nicolas, "Image quality and radiation exposure at pulmonary CT angiography with 100- or 120-kVp protocol: prospective randomized study," *Radiology* **245**, 577-583 (2007).
115. D. Marin, R. C. Nelson, E. Samei, E. K. Paulson, L. M. Ho, D. T. Boll, D. M. DeLong, T. T. Yoshizumi and S. T. Schindera, "Hypervascular liver tumors: low

- tube voltage, high tube current multidetector CT during late hepatic arterial phase for detection--initial clinical experience," *Radiology* **251**, 771-779 (2009).
116. M. van Straten, P. Deak, P. C. Shrimpton and W. A. Kalender, "The effect of angular and longitudinal tube current modulations on the estimation of organ and effective doses in x-ray computed tomography," *Medical physics* **36**, 4881-4889 (2009).
 117. D. P. Naidich, C. H. Marshall, C. Gribbin, R. S. Arams and D. I. McCauley, "Low-dose CT of the lungs: preliminary observations," *Radiology* **175**, 729-731 (1990).
 118. J. P. Ko, R. Marcus, E. Bomsztyk, J. S. Babb, C. Stefanescu, M. Kaur, D. P. Naidich and H. Rusinek, "Effect of blood vessels on measurement of nodule volume in a chest phantom," *Radiology* **239**, 79-85 (2006).
 119. H. Bolte, S. Muller-Hulsbeck, C. Riedel, T. Jahnke, N. Inan, M. Heller and J. Biederer, "Ex-vivo injection technique for implanting solid pulmonary nodules into porcine lungs for multi-slice CT," *Rofo* **176**, 1380-1384 (2004).
 120. M. T. Madsen, K. S. Berbaum, A. N. Ellingson, B. H. Thompson, B. F. Mullan and R. T. Caldwell, "A new software tool for removing, storing, and adding abnormalities to medical images for perception research studies," *Academic radiology* **13**, 305-312 (2006).
 121. E. Samei, M. J. Flynn and W. R. Eyler, "Simulation of subtle lung nodules in projection chest radiography," *Radiology* **202**, 117-124 (1997).
 122. A. E. Burgess, X. Li and C. K. Abbey, "Nodule detection in two component noise: toward patient structure," *Proceedings of SPIE: Medical Imaging-Image Perception*, Vol 3036, Page 2-13.
 123. C. L. Hoe, E. Samei, D. P. Frush and D. M. DeLong, "Simulation of liver lesions for pediatric CT," *Radiology* **238**, 699-705 (2006).
 124. R. Saunders, E. Samei, J. Baker and D. DeLong, "Simulation of mammographic lesions," *Academic radiology* **13**, 860-870 (2006).
 125. X. Li, E. Samei, D. M. DeLong, R. P. Jones, J. G. Colsher and D. P. Frush, "Towards assessing the diagnostic influence of dose reduction in pediatric CT: a study based on simulated lung nodules," *Proceedings of SPIE: Medical Imaging-Physics of Medical Imaging*, Vol 6913, Page 69131L; **6916**, 69131L (2008).

126. G. J. Becker, "Simulation and the coming transformation of medical education and training," *Radiology* **245**, 7-9 (2007).
127. G. Starck, L. Lonn, A. Cederblad, M. Alpsten, L. Sjostrom and S. Ekholm, "Radiation dose reduction in CT: application to tissue area and volume determination," *Radiology* **209**, 397-403 (1998).
128. A. C. Kak and M. Slaney, *Principles of computerized tomographic imaging*. (Society for Industrial and Applied Mathematics, Philadelphia, 2001).
129. N. M. Alpert, D. A. Chesler, J. A. Correia, R. H. Ackerman, J. Y. Chang, S. Finklestein, S. M. Davis, G. L. Brownell and J. M. Taveras, "Estimation of the local statistical noise in emission computed tomography," *IEEE Trans Med Imaging* **1**, 142-146 (1982).
130. L. D. Nickerson, S. Narayana, J. L. Lancaster, P. T. Fox and J. H. Gao, "Estimation of the local statistical noise in positron emission tomography revisited: practical implementation," *Neuroimage* **19**, 442-456 (2003).
131. N. R. Fefferman, E. Bomsztyk, A. M. Yim, R. Rivera, J. B. Amodio, L. P. Pinkney, N. A. Strubel, M. E. Noz and H. Rusinek, "Appendicitis in children: low-dose CT with a phantom-based simulation technique--initial observations," *Radiology* **237**, 641-646 (2005).
132. T. Toth, Z. Ge and M. P. Daly, "The influence of patient centering on CT dose and image noise," *Medical physics* **34**, 3093-3101 (2007).
133. J. Menke, "Comparison of different body size parameters for individual dose adaptation in body CT of adults," *Radiology* **236**, 565-571 (2005).
134. S. Diederich, H. Lenzen, R. Windmann, Z. Puskas, T. M. Yelbuz, S. Henneken, T. Klaiber, M. Eameri, N. Roos and P. E. Peters, "Pulmonary nodules: experimental and clinical studies at low-dose CT," *Radiology* **213**, 289-298 (1999).
135. D. Tack and P. A. Gevenois, "Radiation dose in computed tomography of the chest," *Jbr-Btr* **87**, 281-288 (2004).
136. T. Kubo, P. J. Lin, W. Stiller, M. Takahashi, H. U. Kauczor, Y. Ohno and H. Hatabu, "Radiation dose reduction in chest CT: a review," *Ajr* **190**, 335-343 (2008).
137. X. Zhang, E. Olcott, P. Raffy, N. Yu and H. Chui, presented at the Proceedings of SPIE: Medical Imaging-Computer-Aided Diagnosis, Vol 6514, Page 65140Z,, San

- Diego, CA, USA; Bellingham, Wash: International Society for Optical Engineering, 2007 (unpublished).
138. X. Li, E. Samei, D. M. Delong, R. P. Jones, A. M. Gaca, C. L. Hollingsworth, C. M. Maxfield, C. W. Carrico and D. P. Frush, "Three-dimensional simulation of lung nodules for paediatric multidetector array CT," *The British journal of radiology* **82**, 401-411 (2009).
 139. T. Toth, R. Castellanos, A. Horst, L. Tuszynski and A. Thomas, "A method to determine optimum CT automatic exposure control scan parameter settings," *Radiological Society of North America, 92nd Scientific Assembly and Annual Meeting*, 2006.
 140. X. Li and E. Samei, "Comparison of patient size-based methods for estimating quantum noise in CT images of the lung," *Medical Physics* **36**, 541-546 (2009).
 141. J. Beutel, H. L. Kundel and R. L. Van Matter, Editors, *Handbook of medical imaging. Vol. 1, Physics and psychophysics*. (SPIE Press, 2000, pp. 190-202).
 142. M. J. Flynn and E. Samei, "Experimental comparison of noise and resolution for 2k and 4k storage phosphor radiography systems," *Medical physics* **26**, 1612-1623 (1999).
 143. D. D. Dorfman, K. S. Berbaum and C. E. Metz, "Receiver operating characteristic rating analysis. Generalization to the population of readers and patients with the jackknife method," *Investigative radiology* **27**, 723-731 (1992).
 144. D. D. Dorfman, K. S. Berbaum, R. V. Lenth and Y. F. Chen, "Monte Carlo validation of a multireader method for receiver operating characteristic discrete rating data: split-plot experimental design," *Proceedings of SPIE: Medical Imaging-Image Perception and Performance*, Vol 3663, Page 91 (1999).
 145. B. J. Winer, *Statistical principles in experimental design*, 2d ed. (McGraw-Hill, New York,, 1971).
 146. D. A. Williams, "A test for differences between treatment means when several dose levels are compared with a zero dose control," *Biometrics* **27**, 103-117 (1971).
 147. D. Wormanns, K. Ludwig, F. Beyer, W. Heindel and S. Diederich, "Detection of pulmonary nodules at multirow-detector CT: effectiveness of double reading to improve sensitivity at standard-dose and low-dose chest CT," *European radiology* **15**, 14-22 (2005).

148. X. J. Xu, F. L. Lou, M. M. Zhang, Z. M. Pan and L. Zhang, "Usefulness of low-dose CT in the detection of pulmonary metastasis of gestational trophoblastic tumours," *Clinical radiology* **62**, 998-1003 (2007).
149. C. E. Metz, "ROC methodology in radiologic imaging," *Investigative radiology* **21**, 720-733 (1986).
150. K. S. Berbaum, E. A. Franken, Jr., D. D. Dorfman, S. A. Rooholamini, M. H. Kathol, T. J. Barloon, F. M. Behlke, Y. Sato, C. H. Lu, G. Y. el-Khoury and et al., "Satisfaction of search in diagnostic radiology," *Investigative radiology* **25**, 133-140 (1990).
151. T. K. Egglin and A. R. Feinstein, "Context bias. A problem in diagnostic radiology," *Jama* **276**, 1752-1755 (1996).
152. P. L. Robertson, D. W. Boldt and J. F. De Campo, "Paediatric pulmonary nodules: a comparison of computed tomography, thoracotomy findings and histology," *Clinical radiology* **39**, 607-610 (1988).
153. M. B. McCarville, H. M. Lederman, V. M. Santana, N. C. Daw, S. J. Shochat, C. S. Li and R. A. Kaufman, "Distinguishing benign from malignant pulmonary nodules with helical chest CT in children with malignant solid tumors," *Radiology* **239**, 514-520 (2006).
154. T. Schroeder, S. G. Ruehm, J. F. Debatin, M. E. Ladd, J. Barkhausen and S. C. Goehde, "Detection of pulmonary nodules using a 2D HASTE MR sequence: comparison with MDCT," *Ajr* **185**, 979-984 (2005).
155. M. Regier, S. Kandel, M. G. Kaul, B. Hoffmann, H. Ittrich, P. M. Bansmann, J. Kemper, C. Nolte-Ernsting, M. Heller, G. Adam and J. Biederer, "Detection of small pulmonary nodules in high-field MR at 3 T: evaluation of different pulse sequences using porcine lung explants," *European radiology* **17**, 1341-1351 (2007).
156. C. J. Kotre and S. P. Willis, "A method for the systematic selection of technique factors in paediatric CT," *The British journal of radiology* **76**, 51-56 (2003).
157. X. Li, E. Samei, D. M. DeLong, R. P. Jones, A. M. Gaca, C. L. Hollingsworth, C. M. Maxfield, J. G. Colsher and D. P. Frush, "Pediatric MDCT: towards assessing the diagnostic influence of dose reduction on the detection of small lung nodules," *Academic radiology* **16**, 872-880 (2009).

158. X. Li, E. Samei, D. M. DeLong, R. P. Jones, A. M. Gaca, C. L. Hollingsworth, C. Maxfield, J. G. Colsher and D. P. Frush, "Pediatric MDCT: Towards Assessing the Diagnostic Influence of Dose Reduction on the Detection of Small Lung Nodules," *Acad Radiol*, In Press.
159. H. H. Barrett, C. K. Abbey and E. Clarkson, "Objective assessment of image quality. III. ROC metrics, ideal observers, and likelihood-generating functions," *J Opt Soc Am A Opt Image Sci Vis* **15**, 1520-1535 (1998).
160. A. Rose, "The sensitivity performance of the human eye on an absolute scale," *J Opt Soc Am* **38**, 196-208 (1948).
161. J. A. Swets and R. M. Pickett, *Evaluation of diagnostic systems : methods from signal detection theory*. (Academic Press, New York, 1982).
162. E. A. Krupinski and K. S. Berbaum, "Measurement of visual strain in radiologists," *Academic radiology* **16**, 947-950 (2009).
163. X. Li, E. Samei, H. Barnhart, A. M. Gaca, C. L. Hollingsworth, C. M. Maxfield, C. W. T. Carrico, J. G. Colsher and D. P. Frush, "Lung nodule detection in pediatric CT: quantitative relationship between image quality and radiologist performance," *Radiology*. In Submission.
164. X. Li, E. Samei, W. P. Segars, G. M. Sturgeon, J. G. Colsher and D. P. Frush, "Patient-specific radiation dose and cancer risk in pediatric chest CT: a systematic evaluation of the effects of patient size and scan parameters," *Radiology*. In Submission.
165. K. D. Eggli, S. H. King, D. K. B. Boal and T. Quiogue, "Low-Dose Ct of Developmental Dysplasia of the Hip after Reduction - Diagnostic-Accuracy and Dosimetry," *American Journal of Roentgenology* **163**, 1441-1443 (1994).
166. T. Svahn, B. Hemdal, M. Ruschin, D. P. Chakraborty, I. Andersson, A. Tingberg and S. Mattsson, "Dose reduction and its influence on diagnostic accuracy and radiation risk in digital mammography: an observer performance study using an anthropomorphic breast phantom," *British Journal of Radiology* **80**, 557-562 (2007).
167. J. D. Silverman, N. S. Paul and J. H. Siewerdsen, "Investigation of lung nodule detectability in low-dose 320-slice computed tomography," *Med Phys* **36**, 1700-1710 (2009).

168. N. S. Paul, J. H. Siewerdsen, D. Patsios and T. B. Chung, "Investigating the low-dose limits of multidetector CT in lung nodule surveillance," *Med Phys* **34**, 3587-3595 (2007).
169. D. Bamber, "Area above Ordinal Dominance Graph and Area Below Receiver Operating Characteristic Graph," *Journal of Mathematical Psychology* **12**, 387-415 (1975).
170. D. M. Green and J. A. Swets, *Signal detection theory and psychophysics*. (Wiley, New York,, 1966).
171. J. A. Hanley and B. J. McNeil, "The meaning and use of the area under a receiver operating characteristic (ROC) curve," *Radiology* **143**, 29-36 (1982).

Biography

Name

Xiang Li

Place of Birth

Jilin City, Jilin Province, China

Education

Duke University, USA
Ph.D. Medical Physics 2010

University of British Columbia, Canada
M.Sc. Physics 2005

Nankai University, China
B.Sc. Physics 2002

Honors and Awards

2009 – Award for Excellence in Research, Medical Physics Graduate Program, Duke University

2008 – Conference Finalist of the Michael B. Merickel Best Student Paper Award, SPIE Medical Imaging Symposium

2007 – Carey E. Floyd Jr. Graduate Fellowship, Medical Physics Graduate Program, Duke University

2007 – Award for Excellence in Academic Performance, Medical Physics Graduate Program, Duke University

2007 – Honorable Mention Poster Award, SPIE Medical Imaging Symposium

2006 – Award for Excellence in Academic Performance, Medical Physics Graduate Program, Duke University

2003 – Graduate Entrance Scholarship, University of British Columbia

2002 – Cheng Jing Theoretical Physics Scholarship, Nankai University

2001 – Chinese Academy of Sciences Scholarship, Nankai University

2000 – Chinese Academy of Sciences Scholarship, Nankai University

2000-2002 – Outstanding student of Nankai University, Nankai University

Book Chapters

- Ehsan Samei and **Xiang Li**. “Logistical issues in designing perception experiments”, in *The Handbook of Medical Image Perception and Techniques* (Cambridge Press, Cambridge, UK, 2010).

Peer-Reviewed Publications

- **Xiang Li**, Ehsan Samei, W. Paul Segars, Gregory M. Sturgeon, James G. Colsher, Greta Toncheva, Terry T. Yoshizumi, Donald P. Frush. “A Monte Carlo Method for Estimating Patient-Specific Radiation Dose and Cancer Risk in CT,” *Medical Physics*, In Review.
- **Xiang Li**, Ehsan Samei, W. Paul Segars, Gregory M. Sturgeon, James G. Colsher, Donald P. Frush. “Patient-Specific Radiation Dose and Cancer Risk in Pediatric Chest CT: a Systematic Evaluation of the Effects of Patient Size and Scan Parameters,” *Radiology*, In Submission.
- **Xiang Li**, Ehsan Samei, Huiman Barnhart, Ana M. Gaca, Caroline L. Hollingsworth, Charles M. Maxfield, Caroline W.T. Carrico, James G. Colsher, Donald P. Frush. “Lung Nodule Detection in Pediatric CT: Quantitative Relationship between Image Quality and Radiologist Performance,” *Radiology*, In Submission.
- **Xiang Li**, Ehsan Samei, Donald P. Frush. “Lung Nodule Detection in Pediatric CT: the Tradeoff between Diagnostic Accuracy and Radiation Dose or Cancer Risk,” *Medical Physics*, In Preparation.
- Gregory M. Sturgeon, **Xiang Li**, Shawn Mendonca, Donald P. Frush, Ehsan Samei, W. Paul Segars. “Series of Whole Body NURBS-based Phantoms for Pediatric CT Research,” *Medical Physics*, In Review.
- **Xiang Li**, Ehsan Samei, David M. DeLong, Robert P. Jones, Ana M. Gaca, Caroline L. Hollingsworth, Charles M. Maxfield, Caroline W.T. Carrico, Donald P. Frush.

“Three-dimensional Simulation of Lung Nodules for Pediatric Multi-detector Array CT,” *British Journal of Radiology*, 82: 401-411 (2009).

- **Xiang Li**, Ehsan Samei, David M. DeLong, Robert P. Jones, Ana M. Gaca, Caroline L. Hollingsworth, Charles M. Maxfield, James G. Colsher, Donald P. Frush. “Pediatric MDCT: Towards Assessing the Diagnostic Influence of Dose Reduction on the Detection of Small Lung Nodules,” *Academic Radiology*, 16: 872-880 (2009).
- **Xiang Li**, Ehsan Samei. “Comparison of Patient Size Based Methods for Estimating Quantum Noise in CT Images of the Lung,” *Medical Physics*, 36 (2), 541-546 (2009).
- **Xiang Li**, Philip T. Eles, Carl A. Michal. “Water Permeability of Spider Dragline Silk,” *Biomacromolecules*, 10(5): 1270-1275 (2009).
- **Xiang Li**, Ehsan Samei, W. Paul Segars, Gregory M. Sturgeon, James G. Colsher, Donald P. Frush. “Patient-Specific Dose Estimation for Pediatric Chest CT,” *Medical Physics*, 35, 5821-5828 (2008).

Conference Proceedings

- **Xiang Li**, Ehsan Samei, W. Paul Segars, Gregory M. Sturgeon, James G. Colsher, Donald P. Frush. “Patient-specific Dose Estimation for Pediatric Abdomen-Pelvis CT,” *Proc. SPIE* Vol. 7258, 725804 (2009).
- **Xiang Li**, Ehsan Samei, David M. DeLong, Robert P. Jones, James G. Colsher, Donald P. Frush. “Towards Assessing the Diagnostic Influence of Dose Reduction in Pediatric CT: A Study Based on Simulated Lung Nodules,” *Proc. SPIE* Vol. 6913, 69131L (2008).
- **Xiang Li**, Ehsan Samei, Terry Yoshizumi, James G. Colsher, Robert P. Jones, Donald P. Frush. “Experimental Benchmarking of a Monte Carlo Dose Simulation Code for Pediatric CT,” *Proc. SPIE* Vol. 6510, 65102A (2007).

Oral Presentations

- “Noise-based Radiation Dose Reduction Paradigm for Lung Nodule Detection in Pediatric Chest CT”, Annual Meeting of the Radiological Society of North America (RSNA), November 2009.
- “Three-Dimensional Simulation of Lung Nodules for Pediatric CT”, Medical Image Perception Conference XIII, October 2009

- “Patient-Specific Dose Estimation for Pediatric MDCT”, SPIE Medical Imaging Symposium – Physics of Medical Imaging, February 2009.
- “Patient-Specific Dose Estimation for Pediatric Chest MDCT”, Annual Meeting of the Radiological Society of North America (RSNA), November 2008.
- “Towards Assessing the Diagnostic Influence of Dose Reduction in Pediatric MDCT: Lung Nodule Detection”, SPIE Medical Imaging Symposium – Physics of Medical Imaging, February 2008.
- “Developing a Monte Carlo Code to Simulate Organ Dose for Pediatric CT Patients”, Student Presentation at the Annual Meeting of the Southeastern Chapter of the American Association of Physicists in Medicine (SEAAPM), March 2007.

Poster Presentations

- “Evaluation of Noise Addition Software for Simulating Low Dose MDCT Images”, Annual Meeting of the American Association of Physicists in Medicine (AAPM), July 2007.
- “Experimental Benchmarking of a Monte Carlo Dose Simulation Code for Pediatric CT”, SPIE Medical Imaging Symposium – Physics of Medical Imaging, February 2007.